The Pennsylvania State University

The Graduate School

College of Engineering

ATMOSPHERIC AEROSOL AND PARTICLE PROPERTIES USING LIDAR

A Thesis in

Electrical Engineering

by

Guangkun Li

Submitted in Partial Fulfillment
of the Requirements
for the Degree of

Doctor of Philosophy

December 2003

We approve the thesis of Guangkun LI.

Date of Signature

C. Russell Philbrick Professor of Electrical Engineering Thesis Advisor Chair of Committee	
Kultegin Aydin Professor of Electrical Engineering	
Dennis Lamb Professor of Meteorology	
John D. Mathews Professor of Electrical Engineering	
Victor Pasko Associate Professor of Electrical Engineering	
W. Kenneth Jenkins Professor of Electrical Engineering Head of the Department of Electrical Engineering	

ABSTRACT

Characterization of airborne particulate matter, both dust particles and aerosols, has been a major challenge to researchers. Lidar (light detection and ranging) techniques have been used to make remote sensing measurements of the aerosol optical extinction and other properties of optical scattering from the particles in the atmosphere. In this thesis, a range of technologies available in the area of laser remote sensing have been used to study the optical properties of atmosphere, including the techniques of Rayleigh scattering, Mie scattering and Raman scattering.

Algorithms and techniques have been developed for analysis of data to calculate the atmospheric optical extinction in the troposphere using backscatter lidar and Raman lidar instruments, and models are described which have been developed to study the optical extinction and backscatter characteristics. The data obtained by Raman lidar and backscatter lidar during several different campaigns were analyzed. An algorithm for extinction at UV wavelengths measured by Raman lidar has been developed in which the molecular scattering and ozone absorption are removed to obtain the aerosol optical extinction profile. The relationships between extinction measured by Raman lidar and surface particulate matter (PM) mass concentration measurements of the ambient particles are investigated. Model simulations have been developed to explain and quantify the relations between extinction and PM concentration. The ratio of the extinction coefficient at different wavelengths has been analyzed to show unique information on particle sizes, which can not be obtained from a single extinction profile.

Backscatter lidar has been used to study the atmospheric meteorological properties and characterize the fate (deposition and transport) of PM plumes originating from the mechanical disturbance of surface soil in one of our projects. A particle size distribution model has been developed from lidar results and measurements from particle size instruments. Model calculations of Mie scattering have been designed to simulate various features of the optical scattering from the generated dust plumes. Field measurements are used to analyze the inverse problem and describe the particulate matter properties from the scattering profiles.

Several achievements from the research work in this thesis include. 1) The ultraviolet aerosol extinction algorithm and telescope form factor for LAPS are successfully developed. 2) The relation between Raman lidar extinction, relative humidity and PM mass measurements are quantified and modeled. The results show that we can describe the vertical distribution of the airborne particulate matter using Raman lidar and thereby describe the evolution of air pollution episodes more accurately. 3) The modeling results from California Dust campaign show the rapid deposition of large (PM_{10}) particles, and the relatively longer residence time of the optical plume associated with small particles (< 2 μm). The rapid loss of PM mass may have led to overestimates of airborne particle mass in plumes and could explain the major discrepancy between the source estimate and the measured mass of soil particulates that has been recognized in California. 4) The ratio of signal from backscatter lidar and ratio of extinction profiles from Raman lidar at multiple wavelengths are used to demonstrate the unique information that can be obtained on the characteristics of airborne particles in the atmosphere.

TABLE OF CONTENTS

List of Figures……..……..…… vii

List of Tables……..... xv

Acknowledgments…..……..…..……xvi

CHAPTER 1: Introduction and Statement of Problem…….....1
1.1 Background and Objective…….……...1
1.2 Outline of Research and Hypothesis……..……...2

CHAPTER 2: Background: Atmospheric Science and Aerosols….……5
2.1 Atmospheric Science……5
2.1.1 Lower Atmospheric Structure and Processes……..……..5
2.1.2 Composition of atmosphere……..…….7
2.2 Aerosol and Dust Size Distribution……..……....8
2.2.1 Log-normal distribution……..……...…..13
2.3 Water Vapor and Clouds…….15

CHAPTER 3: Instrument Hardware and Measurement Techniques...……....19
3.1 The Laps Raman Lidar Instrument….……....19
3.3.1 Raman Lidar Telescope Form Factor.....22
3.2 Scanning Micro-Pulse Lidar……...29
3.3 Lidar Equation and Extinction Calculation..…….……..31
3.4 Ozone Calculation…….……..35

CHAPTER 4: CA-Dust Measurement Campaign.....……..……39
4.1 Introduction…….....39
4.1.1 Objective.....39
4.1.2 Approach……..……40
4.2 Measurement Approach……..40
4.2.1 Portable Digital LIDAR (Dual Wavelength with Scanner).....40
4.2.2 High Resolution Photography……..…40
4.2.3 Meteorological Sensors…….……...41
4.2.4 Real-Time Point Monitors……..….41
4.2.5 Integrated (Filter) Samplers…….....42
4.2.6 Soil Selection……..….43
4.3 Methods…….…….....44
4.3.1 Particle Entrainment System (Chamber)……..……..……44
4.3.2 Dust Generation and Test Scenario……...…...…47
4.3.3 Data Summary……..……...48
4.4 Measurement Results and Interpretation……..……..49
4.4.1 CCD camera data……..……...50
4.4.2 Lidar Vertical Profiles (Pilot Study, 2000)……..50

4.4.3 Chamber Test Results (Main Study, 2001)…..…….…..55
4.4.4 Dust generation test results…….…….....70
Pilot Study……..……....70
Main Study……..……...78
4.5 Summary…….…….…...91

CHAPTER 5: NE-OPS Measurement Campaign…….…… 93
5.1 Introduction…….....93
5.2 Extinction Profiles…….…….97
5.3 Effect of Ozone Absorption on Extinction…….. 101
5.4 Effect of Relative Humidity on Extinction……...106
5.5 A Pollution Episode Analysis……...113
5.6 Aerosol Variations at Sunrise and Sunset…….115
5.7 Correlations of Extinction with PM Measurements……..117
5.8 Ratio of Extinction of Different Wavelengths……..131
5.9 Summary...…….... 135

CHAPTER 6: Conclusions……..137
6.1 Summary of Accomplishments …….…….…….....137
6.1.1 Algorithm Development. ……...…137
6.1.2 Model Simulations. ……..….139
6.1.3 Ratio of Signals from Different Wavelengths. ……..…...140
6.2 Future Works……...141

REFERENCES……...143

APPENDIX A: MATLAB Program for Telescope Form Factor……..153

APPENDIX B: MATLAB Program for Extinction Algorithm…….155

APPENDIX C: MATLAB Program of Mie Scattering for Sphere Particles…...…158

APPENDIX D: Model Simulation and Comparison in Pilot Study……..162

APPENDIX E: Comparison of Lidar Results with Sonde Measurements……...170

APPENDIX F: Summary of PM Measurements During NEOPS Campaign……..172

APPENDIX G: Keyword Definitions…….……..175

LIST OF FIGURES

Figure 2.1. Size distribution of aerosols [Ruskin and Scott, 1974]. ..……8

Figure 2.2. Particle settling rate [Seinfeld and Pandis, 1998]. ..……....9

Figure 2.3. Atmospheric aerosol surface-area distribution [Whitby 1975]. ..……..11

Figure 2.4. Atmospheric aerosol source and size range [Farmer,2001]. ..……...12

Figure 2.5. Heavy loading dust size and mass distribution [Watson and Chow, 1999]. .12

Figure 2.6. The same particle distribution is plotted to show the character dependence upon whether the measuring instrument is sensitive to one, two or three dimensional properties. (a) particle number distribution d*n*/dlog*r* (b) particle surface area distribution d*S*/dlog*r* (c) particle volume distribution *dV/dlogr*. …….....15

Figure 3.1. Arrangement of the Telescope Receiver of the LAPS Instrument. [Jenness, 1997]. ..…….....21

Figure 3.2. Sample Raman Lidar raw return signals taken during the summer 99 NE-OPS campaign. ..…….....23

Figure 3.3. (a) The optics configuration and parameters of LAPS receiver system; (b) Locations of images near field and far field; *f* is the focus distance (*f* = 1.53 m); dm is the diameter of the mirror (dm = 0.62 m); d_f is the diameter of the fiber (d_f = 1 mm); d_t is the diameter of the laser beam (d_t = 47.5 mm); *z* is the distance of fiber position to the focus point. ..…….....24

Figure 3.4. Theoretical calculation of fiber capture efficiencies for the relative position of the fiber located at: -1 mm, 0 mm, 1 mm, 2 mm, 3 mm and 4 mm from the focal point (minus corresponds to position shorter than the focal length). …….....25

Figure 3.5. Summary of experimental fiber capture efficiency in percentage shown on log scale and linear scale. Numbers were calculated from several campaigns, including USNS Sumner, SCOS, Barrow Alaska, NEOPS 98, NEOPS 99, NEOPS 2001 and NEOPS 2002. …….....28

Figure 3.6. Comparison of experimental and theoretical fiber capture efficiency. …….29

Figure 3.7. Sample of MPL Lidar vertical profile from slant path measurement (elevation angle 70^o) during period of afternoon convection shows the top of the boundary layer near 1300 m. ……..31

Figure 3.8. Hartley band absorption cross-section of ozone is shown with wavelengths associated with the lidar's 266-nm transmission and its Raman-shifted wavelengths [Philbrick, 1998a, Inn, et. al., 1953]. ……..…....37

Figure 3.9. Example of one hour integrated ozone density and differential ozone profiles measured by LAPS on 07/02/1999 03:00 – 04:00 UTC, data is smoothed by 5 point Hanning filter. ……..…..37

Figure 4.1. Particle entrainment system schematic. ……..…….…..45

Figure 4.2. (a) View of the east side of 10-meter chamber, (b) Front (west) and north sides of test chamber where samples are injected and measurements made, the chamber is shown together with instrumented meteorological tower, (c) DustTrak optical scatter instruments and Climet particle spectrometer (16 channels - 0.5 to 10 μm). ……....46

Figure 4.3. Example of the lidar return signal as a function of time during a chamber test shows the comparison of the 1046 nm signal (red curve has been multiplied by 10) with the 523 nm signal (green curve). …….……..47

Figure 4.4. The lidar with a digital camera scans dust cloud generated by a blower, the 10 m tower is located directly behind the generator, and the target board can be seen in front of trees on the far left. …….……..48

Figure 4.5. Test 18 (12/15/2000 14:30) generate dust with vehicle, this is time sequence of CCD images along with the corresponding background removed images: (a) 14:31:37 (b) 14:32:36 (c) 14:32:49 (d) 14:33:14. …….…….……..51

Figure 4.6. Vertical profile (elevation angle 70^{o}) during period of afternoon convection shows the top of the boundary layer near 1300 m. …….…….……..52

Figure 4.7. Horizontal scan profiles of raw data plots showing dust plumes were generated by the large wind shear at the surface during the Santa Anna on 18 December 2000.…….…….…..……..53

Figure 4.8. Vertical profiles show dust plumes between surface and 700 m. The raw signals have only been range corrected and thus the signal at higher altitude appears larger due to the effect of the telescope form factor (the red channel shows an instrument artifact near 400 m). …….……..……..54

Figure 4.9. The lidar return signal at the visible wavelength resulting from a dust sample of 800mg of $CACO_3$ at size 0.7 μm during Chamber Test #35 19 December 2001. …….…….……..……....56

Figure 4.10. Summary of aerosol chamber tests on 19 December 2001 5:20-8:00. (a) Comparison of DustTrak PM measurement with Climet particle size distribution measurement, (b) Linear regression of averaged DustTrack PM measurement with Climet particle size distribution measurement. ....……..57

Figure 4.11. The Climet spectrum of the particle counts versus particle size for the several samples of different sizes of $CaCO_3$ power that were tested. Notice that the 0.7 μm case is an anomaly (see text) and the other samples do show a change that agrees with the increasing particle size in the samples. .....……..59

Figure 4.12. The Climet particle size spectra for the several different types of soil and powder tested are compared . ..……...……...60

Figure 4.13. The log-normal distributions for a two component models are fit to the Climet instrument measured result for the 0.7 μm sample of $CaCO_3$. .....…….60

Figure 4.14. The Climet spectrum for the 0.7 μm sample of the $CaCO_3$ dust corresponding to Figure 4.12 displayed as number density and mass density. .....….61

Figure 4.15. The log-normal distributions for a two component model are fit to the Climet instrument measured result for the 2 μm sample of $CaCO_3$. .....……..61

Figure 4.16. The log-normal distributions for a two component model are fit to the Climet instrument measured result for the 4 μm sample of $CaCO_3$. .....……..62

Figure 4.17. The log-normal distributions for a two component model are fit to the Climet instrument measured result for the 10 μm sample of $CaCO_3$. .....……..62

Figure 4.18. The chamber test measurements from Tests #10, #11 and #12 are shown. Upper panel shows the raw signal returns from the lidar at the range intervals corresponding to the chamber and the target board. The lower panel shows the signal from the DustTrak instruments and the normalized lidar return. .....……...64

Figure 4.19. Ratio of backscatter coefficient $\frac{\beta(\lambda_G, z)}{\beta(\lambda_R, z)} \frac{\beta_{mol}(\lambda_R)}{\beta_{mol}(\lambda_G)}$ after smoothing with a Gaussian filter assuming a clear optical path (no aerosol) . ...…….……..68

Figure 4.20. Ratio of backscatter coefficient $\frac{\beta(\lambda_G, z)}{\beta(\lambda_R, z)} \frac{\beta_{mol+aer}(\lambda_R)}{\beta_{mol+aer}(\lambda_G)}$ after smoothing with a Gaussian filter assuming that there are fine mode aerosols in the optical path. 68

Figure 4.21. Ratio of the return signal of green and red channels from chamber tests during 19 December 2001. …….....…..…...70

Figure 4.22. Examples of the raw data profiles from the lidar at the visible and NIR wavelengths during Test #4 on 14 December 2000 show the backscatter and extinction of dust plume at a range of about 500 m. .....……...71

Figure 4.23. Example of data processing to quantify the total amount of backscatter and extinction. . .....…….…..72

Figure 4.24. Simulation model of the scattering from 10 μm dust showing backscatter and extinction expected for both wavelengths at several different particle concentrations in the upper panels. The two lower panels show the same results, except they show dependence on complex index of refraction typical for crustal materials. .....…….....73

Figure 4.25. The calculations of the backscatter and extinction for the two wavelengths depending on the particle size. The upper panels show values for particle concentration of 10^7 m^{-3} and the lower panels show values for particle concentration of 10^8 m^{-3}. .....……...……..……..74

Figure 4.26. The backscatter and extinction at both visible and NIR wavelengths resulting from vehicle generated dust between 14:32:00 and 14:32:45 during Test #18 on 15 December 2000. .....……...…..75

Figure 4.27. Results from Test #1, which was from a small puff of about 0.5 kg of sieved dirt from the field. The 0^o and $+10^o$ azimuth directions show the drift of the dust cloud in the background wind. The feature at 450 m at $+10^o$ azimuth is due to scattering from a row of scrub bush and the -10^o azimuth plots show that no change is observed along a clear path. .....…….....77

Figure 4.28. Results from Test #7 show the backscatter and extinction from the white powder (calcium carbonate). .....……...78

Figure 4.29. Results of the signal returns from (a) visible channel (b) IR channel from Test #44 on 19 December 2001, which was from dust generation of about 600 g of 0.7 μm $CaCO_3$. .....……...……....81

Figure 4.30. The backscatter and extinction from dust plume at the visible wavelength are function of time from Test #44 on 19 December 2001 for 600 g of 0.7 μm $CaCO_3$. .....……...……..…..82

Figure 4.31. 3-D Contour plots of signal returns from (a) visible channel (b) IR channel from Test #44 on 19 December 2001, for 600 g of 0.7 μm $CaCO_3$. .....…….. …...82

Figure 4.32. Model simulation results based upon truncation of particle spectrum from Test #44 on 19 December 2001, for 600 g of 0.7 μm $CaCO_3$. .....……. ….83

Figure 4.33. Results of the signal returns from (a) visible channel (b) IR channel from Test #45 on 19 December 2001, for 600 g of 4 μm $CaCO_3$. .....…….. …..86

Figure 4.34. The backscatter and extinction from dust plume at visible wavelength along with time from Test #45 on 19 December 2001, for 600 g. .....……...87

Figure 4.35. 3-D Contour plots of signal returns from (a) visible channel (b) IR channel from Test #45 on 19 December 2001, for 600 g of 4 μm $CaCO_3$. .....……. …...87

Figure 4.36. Model simulation results based upon truncation of particle spectrum from Test #45 on 12/19/2001, for 600 g of 4μm $CaCO_3$. .....…. ……..…..88

Figure 4.37. Results of the signal returns from (a) visible channel (b) IR channel from Test #43 on 19 December 2001, for 600 g of 10 μm $CaCO_3$. .....……. ……..89

Figure 4.38. The backscatter and extinction from dust plume at visible wavelength along with time from Test #43 on 19 December 2001, for 600 g of 10 μm $CaCO_3$. 89

Figure 4.39. 3-D Contour plots of signal returns from (a) visible channel (b) IR channel from Test #43 on 19 December 2001, for 600 g of 10 μm $CaCO_3$. .....…… …..90

Figure 4.40. Model simulation results based upon truncation of particle spectrum from Test #43 on 19 December 2001, for 600 g of 10 μm $CaCO_3$. .....……. ……..90

Figure 5.1. (a) Examples of 60 minutes integration of range corrected raw data from lidar return signal of 607nm, 530nm and 284nm taken from NEOPS 99. (b) Examples of 60 minutes integration of extinction profiles from the same time period. .....…..99

Figure 5.2. (a) Examples of 60 minutes integration of range corrected raw data from lidar return signals of 607nm, 530nm and 284nm taken from NEOPS 2001. (b) Examples of 60 minutes integration of extinction profiles from the same time period. 100

Figure 5.3. Hartley band absorption cross-section of ozone is shown with wavelengths associated with the lidar's 266 nm transmission and its associated Raman-shifted wavelengths used to measure ozone concentration [Philbrick 1998a using the data of Inn, et. al., 1953]. 101

Figure 5.4. Raman lidar 60 minutes integration of (a) ozone, and (b) total extinction and aerosol extinction profiles at 284nm on 21 August 1998 10:00 – 11:00 UTC, (c) time sequence water vapor mixing ratio on 21 August 1998 06:00 – 12:00 UTC. 104

Figure 5.5. (a) 60 minutes integration of extinction profiles at 284nm, 530nm and 607nm on 08 July 1999 02:00 – 03:00 UTC (b) Time sequence water vapor profile on 08 July 1999 00:00 – 4:13 UTC. 105

Figure 5.6. ((a) Ground level extinction and relative humidity, and (b) Water vapor mixing ratio, (c) Relative humidity, (d)Vertical extinction profile, for the time period 07/03/99 16:20 – 07/04/99 22:00 UTC. 108

Figure 5.7. (a) Ground level extinction and relative humidity, and (b) Water vapor mixing ratio, (c) Relative humidity, (d)Vertical extinction profile, (e) Ground ozone measurement from Millersville University for the time period 08/01/99 01:10 – 08/02/99 00:40 UTC. 109

Figure 5.8. (a) Example comparing the temperature profile from the LAPS measurement with the linear model in Equation 5.1 on 20 August 1998 08:00 – 08:29 UTC. (b) Calculated relative humidity from the LAPS temperature profile and from the linear model at the same time period. 111

Figure 5.9. (a) Example comparing the temperature profile from the LAPS measurement with the linear model in Equation 5.1 on 21 August 1998 01:00 – 01:29 UTC. (b) Calculated relative humidity from the LAPS temperature profile and from the linear model at the same time period. 112

Figure 5.10. Pollution episode study for the time period from 12 hours UTC on 21 August to 12 hours UTC on 22 August 1998. …….....114

Figure 5.11. Examples of optical extinction time sequence from Raman lidar results at 284 nm which show variations in extinction near local sunrise. …….116

Figure 5.12. Examples of optical extinction time sequence from Raman lidar results at 284 nm which show variations in extinction near local sunset. ……..116

Figure 5.13. (a) Summary of PM and O3 measurements by HSPH during NEOPS 1999 summer campaign, (b) Summary of PM measurement by HSPH during NEOPS 2001 summer campaign.. …….…….....119

Figure 5.14. Tethered Sonde data shows comparison of PM measurements from Tethered Sonde at surface and at altitude 100 m, 200 m, and 300 m on two days of July 2001 [Rich Clark, Millersville University]. …….…….....120

Figure 5.15. Comparison of ambient (wet mass) and dry mass with relative humidity measurements on 23 and 24 July 2001. …….....121

Figure 5.16. Comparison of PM concentration with Extinction at 284 nm, August 15 to August 22, 1998. (a) Comparison of PM_{10}, $PM_{2.5}$ with optical extinction; (b) Linear regression of $PM_{2.5}$ with optical extinction. ……..…….....122

Figure 5.17. Comparison of PM2.5 mass concentration with optical extinction at 284 nm, July 1 to July 9, 1999. (a) Comparison of $PM_{2.5}$ with optical extinction; (b) Linear regression of $PM_{2.5}$ with optical extinction. ……..…….....123

Figure 5.18. Comparison of $PM_{2.5}$ mass concentration with optical extinction at 284 nm, July 9 to July 22, 1999. …….…….....124

Figure 5.19. Optical extinction versus particle size at several different $PM_{2.5}$ concentrations. …….....125

Figure 5.20. (a) Comparison of LAPS extinction measurements at 284nm with calculation results from Millersville University $PM_{2.5}$ ambient mass measurements at 300 meters on 9 July 2001 10:00 UTC – 10 July 2001 16:00 UTC. (b) Time sequence of LAPS ozone measurements characteristic. ……..127

Figure 5.21. (a) Comparison of extinction at 600 meters with the estimated ozone absorption coefficient, optical extinction is measured by LAPS, ozone concentration is measured by ground ozone sensor from Millersville University. (b) Comparison of $PM_{2.5}$ with optical extinction. (c) EH parameters from different references (d) Time sequence optical extinction from LAPS and model calculation results. ……..130

Figure 5.22. (a) Aerosol extinction coefficient as a function of wavelength for different atmospheric conditions. [Wright et al, 1975]. (b) Ratio of extinction coefficient of 284 nm and 530 nm as a function of particle size calculated using Mie theory. 132

Figure 5.23. Analysis of the ratio of extinction coefficient of 530 nm and 284 nm on July 11 1999 02:30 – 03:00 UTC. …….....134

Figure D.1. The dependence of the backscatter on the absorption due to increasing complex refractive index is displayed for the two wavelengths and for two particle number densities. …….....162

Figure D.2. Results from Test #1, a small puff of about 0.5 kg of sieved dirt from the field. The 0^o and $+10^o$ azimuth directions show the drift of the dust cloud to the right in the background wind. The feature at 450 m at $+10^o$ azimuth is due to scattering from a row of scrub bush and the -10^o azimuth plots show that no change is observed along a clear path. …….....165

Figure D.3. The results from Test #2 are shown for both wavelengths at azimuth scan angles of -5^o (left), -2.5^o, 0^o, $+2.5^o$, and $+5^o$ (right). The test consisted of 5.5 kg of sieved dust being released at 16:31. …….....167

Figure D.4. Results from Test #10 show a slow drift and slow dissipation of a 5 kg dust cloud. The time gap is while scans were made at higher elevation angles. 167

Figure D.5. The dust cloud generated by vehicle on an east-west path during Test #19 was irregular and most dust of small size particles being stirred up by the vehicle as evidenced by predominate backscatter signal at both wavelengths. ….....168

Figure D.6. Results from Test #7 show the backscatter and extinction from the white powder (calcium carbonate). …….....168

Figure D.7. Results from Test #13 show the response of the green and NIR channel in the upper four panels. The lower left panel shows the dust cloud at 10^{o} elevation angle being blown back over the instrument location. The lower right panel shows the ratios of the green/NIR signals that are useful in describing the changes in the particle properties, in this case it is due to changes in concentration. …….....169

Figure E.1. (a) Comparison of lidar water vapor mixing ratio and sonde measurements. (b) Time sequence plot of water vapor mixing ratio. Lidar data was taken from 03:05 UTC to 03:34 UTC of August 1, 2001; Rawinsonde was released 03:19 UTC. …….....169

Figure F.1. Summary of PM measurement by HSPH during NEOPS summer campaign 1998. ……..…….....172

Figure F.2. Summary of PM and ozone measurement during NEOPS summer campaign 1999. …….....173

Figure F.3. Summary of PM measurement during NEOPS summer campaign 2001. ..174

LIST OF TABLES

Table 2.1. Atmospheric gases [Farmer, 2001]. ..……..……..……7

Table 2.2. Thermodynamic functions for particle growth (EH). ..……..……..…17

Table 3.1. Measurements made by the LAPS lidar instrument. ..……..…….….20

Table 3.2. Characteristics of the LAPS Lidar Subsystems. ..……..…….……....20

Table 3.3. Portable Scanning Micro-Pulse Lidar System Specifications. ..……..……...30

Table 4.1. Description of Soils (Main Study). ..……..…….44

Table 5.1. List of Investigators in the NARSTO-NE-OPS Program. ..……..…….….94

Table 5.2. Deliquescence Relative Humidity of Some Chemical Species at 298K. ….107

CHAPTER 1
Introduction and Statement of Problem

1.1 Background and Objective

Characterization of airborne particulate matter, both dust particles and aerosols, has been a major challenge to researchers. Recent studies have associated increases in airborne particulate matter with increased morbidity and mortality, particularly in elderly and respiratory impaired individuals. Knowledge of aerosol optical properties assumes significant importance in the wake of studies strongly correlating airborne particulate matter with adverse health effects [Albritton and Greenbaum, 1998, Hidy, et.al 1998]. The small aerosol component, labeled $PM_{2.5}$, are referring to particles with aerodynamic size less than 2.5μm, is of most concern to human health because smaller particles can be easily inhaled deeply into the lungs. Along with health issues, aerosol particle distributions have significant implications for aesthetics of the natural environment and for climatic change [Seinfeld and Pandis, 1998 pp1113-1192]. Increases in aerosol loading of the atmosphere can lead either to an increase or decrease in the mean global temperature of Earth, depending upon their optical properties which vary in the visible and infrared portion of the spectrum according to the size distributions of aerosols. Additionally, airborne particle distributions have significant influence on the visibility that effects scheduled aircraft traffic [Kyle, 1991, Wilson and Suh, 1997]. The typically observed percentage of visual range, compared to the clean molecular atmosphere, is around 50-67 % in the western United States and 20 % in eastern United States [Albritton and Greenbaum, 1998]. This increase in optical scattering in the eastern states is due to the generally eastward transport of PM and the growth of the hydroscopic aerosols in the higher east coast humidity. Also, the changes in optical transmission of the atmosphere due to suspended airborne particulate matter alters the radiative energy balance of the Earth's environment [Seinfeld and Pandis, 1998 pp1139-1142].

Along with improved knowledge of airborne particle size and associated optical properties, evaluation of the lifetime of PM from fugitive sources in the atmosphere is also a major challenge [Watson and Suh, 1999]. Source inventories for PM_{10} and $PM_{2.5}$ for the western states show that geologic dust contributes a large portion of the $PM_{2.5}$.

Geologic material is a major component of the airborne particulate matter (approximately 50%) in the western United States [Cowherd, 1988]. The measurements of the distribution and properties of airborne dust particulate matter in the atmospheric surface layer are needed to develop improved descriptions of the physical processes, and to develop modeling schemes for atmospheric distributions of airborne particulate matter.

Lidar (light detection and ranging) techniques have been used to make remote sensing measurements of the aerosol optical extinction and other properties of optical scattering from the particles in the atmosphere [Philbrick 1998a, b, Philbrick and Lysak, 1998a, b]. In this thesis, the range of technologies available to laser remote sensing have been used to investigate the optical properties of the atmosphere, including Rayleigh scattering, Mie scattering and Raman scattering. Two types of lidar were involved in these studies, a two wavelength scanning backscatter lidar and a Raman lidar.

1.2 Outline of Research and Hypothesis

This section outlines the work which has been undertaken and the hypotheses examined in this dissertation. The primary research goals are listed below:

1) Investigate optical extinction using the Raman lidar and MPL backscatter lidar technologies to improve our understanding of optical scattering from airborne particles.
2) Describe properties of airborne particles using the ratio of extinction to backscatter measured by lidar.
3) Compare optical properties measured by lidar with particle mass concentrations measured by other techniques.
4) Construct models which are capable of relating the extinction and backscatter to particle characteristics.
5) Develop inversion techniques for interpretation of atmospheric optical properties from the lidar measurements.

The main hypotheses that have been investigated follow:

1) A relationship exists between lidar extinction profiles and PM filter measurements which can be used to interpret lidar data to provide vertical profiles of PM.

2) The field measurements of two wavelength backscatter lidar can be used to analyze the inverse problem and describe the aerosol properties from the optical scattering profiles.
3) The ratio of backscatter signal at different wavelengths can be used to describe the change of particle size in atmosphere.
4) Vertical profiles of relative humidity during nighttime can be obtained from LAPS specific humidity and temperature measurements. Furthermore, daytime relative humidity profiles can be obtained for most of the time with assumption of simple linear temperature model.
5) Extinction shows strong correlation with relative humidity, and optical extinction measurements can be used to describe the effects of water vapor on aerosol growth.
6) Variations of optical extinction associated with aerosols at several wavelengths can be used to describe changes in the particle size as a function of altitude and as a function of air mass concentration.

CHAPTER 2

Background: Atmospheric Science and Aerosols

2.1 Atmospheric Science

Five different disciplines of atmospheric science have been examined to assess the current understanding of the influence of aerosol on the optical properties of the atmosphere. These include: atmospheric physics; atmospheric chemistry; atmospheric dynamics and weather forecasting; upper atmosphere and near-Earth space environment; climate and climate change [Arya, 1999]. Atmospheric physics seeks to explain atmospheric phenomena in terms of physical processes, such as, atmospheric radiation, aerosol physics, the physics of clouds, atmospheric electricity, the physics of the atmospheric boundary layer, and small-scale atmospheric dynamics, etc. Atmospheric chemistry has rapidly expanded as a major emphasis during the last half decade. This thesis introduces lidar techniques to study problems and investigate processes related to the disciplines of atmospheric physics and chemistry, as associated with aerosols.

2.1.1 Lower Atmospheric Structure and Processes

The several regions of the atmosphere are set apart and named because of their temperature structure, such as troposphere, stratosphere, mesosphere, thermosphere and exosphere. Additional overlapping names are given to regions of the atmosphere because of the physical processes that take place there, for example, boundary layer, homosphere, tropopause and heterosphere [U.S. Standard Atmosphere, 1976].

Boundary Layer

The boundary layer, which most effects human activity, is in the lowest few kilometers of the atmosphere. The boundary layer plays a central role in the weather and climate because it couples processes at the Earth's surface such as evaporation and heat transfer with the rest of the troposphere. This transfer of energy from the Earth's surface into the atmosphere is essential in describing the dynamical behavior of the atmosphere.

It is in the boundary layer that the largest diurnal changes take place. Heating of lower atmosphere does not primarily come from the air absorbing solar radiation, but

from the ground absorption of the solar radiation, followed by convective heat transfer to the air near the ground. As the air near the ground is heated at sun rise, it becomes buoyant and rises as thermal bubbles. The convection process, together with wind shear, produce mixing through the lower atmosphere. The strong mixing is limited to the lowest couple of kilometers because turbulence falls off rapidly above the surface. This region of the atmosphere is given the name of boundary layer. After sun set, the air near the surface cools when the heat source is removed. As the air cools, the convective process and wind shear turbulence decrease. After the air near the ground cools below the temperature of air above it, the night time temperature inversion has been established, resulting in a stable layer. This layer decouples the region above the inversion, typically about 400 meters, from the surface and allows horizontal transport to occur in the "residual" nighttime layer, without viscous coupling to the surface.

Troposphere

The troposphere occupies the lowest 10 km of the atmosphere. Due to the decrease in pressure with altitude, the rising surface warm air expands and cools to lower temperature. When the rising buoyant air parcel cools to the dew point, the water contained in it condenses. The result of condensation allows the warm air bubbles rise higher due to the release of the latent heat as condensation. The troposphere, where the buoyant forces establish the temperature gradient, and daytime surface heating causes strong convection mixing, is the lowest thermal layer of the atmosphere. The troposphere extends upward to the tropopause, which is an isothermal layer caused by the temperature minimum balance between the solar heating from the surface below and heating from the ultraviolet absorption in the atmospheric ozone layer above. The height of the troposphere is typically about 10 km at mid-latitudes, but decreases to less than 2 km at the high-latitudes, and achieves altitudes above 15 km at low-latitudes. One important effect of the tropopause is its action as a barrier, where buoyant forces no longer have the effect in mixing of the atmosphere. Since temperature gradients determine the stability of the atmosphere, convection is seldom strong enough to bring air and its contents through this barrier because the temperature gradient becomes positive.

2.1.2 Composition of atmosphere

The atmosphere is composed primarily of nitrogen and oxygen, and the concentrations of the primary species remain fixed over time. Also present are a number of trace gases that occur in relatively small and sometimes highly variable amounts. One of the most important variable species is water vapor, which can exist in concentrations up to about 3%. The atmosphere is a dynamic system, with its gaseous constituents being exchanged with vegetation, the oceans and biological organisms. The average lifetime of a gas molecule can range from seconds to millions of years, depending on the effectiveness of removal processes. The important atmospheric gases are listed in Table 2.1.

The abundance of water vapor is controlled by the variation of vapor pressure of water with temperature and the state changes, both condensation and freezing that occur because the temperatures which produce phase change are in the range of normal atmospheric temperatures. Ozone concentrations are determined by the photo-chemical processes in the atmosphere. Methane, nitrous oxide and carbon monoxide concentrations are determined by atmospheric chemical processes, as well as by biological processes [Deepak,1982].

Table 2.1. Atmospheric gases [Farmer, 2001]

Gas	Molecular Weight	Average Mixing Ratio (ppm)	Cycle	Status
Ar	39.948	9340	No cycle	Accumulation during Earth's history
Ne	20.179	18		
Kr	83.80	1.1		
Xe	131.30	0.09		
N_2	28.013	780,840	Biological and microbiological	?
O_2	32	209,460		
CH_4	16.043	1.72	Biogenic and chemical	Quasi-steady-state or equilibrium
CO_2	44.010	355	Anthropogenic and biogenic	
CO	28.010	0.12 (NH) 0.06 (SH)	Anthropogenic and chemical	
H_2	2.016	0.58	Biogenic and chemical	
N_2O	44.012	0.311	Biogenic and chemical	
SO_2	64.06	10^{-3}–10^{-4}	Anthropogenic, biogenic, chemical	
NH_3	17	10^{-4}–10^{-3}	Biogenic and chemical	
NO	30.006	10^{-6}–10^{-2}	Anthropogenic, biogenic, chemical	
NO_2	46.006			
O_3	48	10^{-2}–10^{-1}	Chemical	
H_2O	18.015	Variable	Physicochemical	
He	4.003	5.2		

2.2 Aerosol and Dust Size Distribution

An aerosol is the non-gaseous substances (solid particles or liquid droplets) held in suspension in the atmosphere. Atmospheric aerosols include particle sizes that range over at least 4 orders of magnitude. Figure 2.1 shows typical size distributions of aerosols typical of continental and maritime atmospheres. The vertical axis is the number of particles per cm^3 per logarithmic radius (μm) interval. The horizontal axis is the particle size radius in μm and the aerosol size distribution shown here ranges from 10^{-3} μm to 10^3 μm. The smaller sizes, corresponding to the gas to the particle conversion range below 10 nm, are difficult to measure because they do not contribute significantly to the mass of airborne particles or much to the optical scattering. The large sizes, above 10 μm, tend to settle out of the atmosphere rapidly. The settling velocity of atmospheric particles as a function of aerodynamic size is shown in Figure 2.2. Those sizes between 10 nm and 10 μm attract our attention and are of most concern.

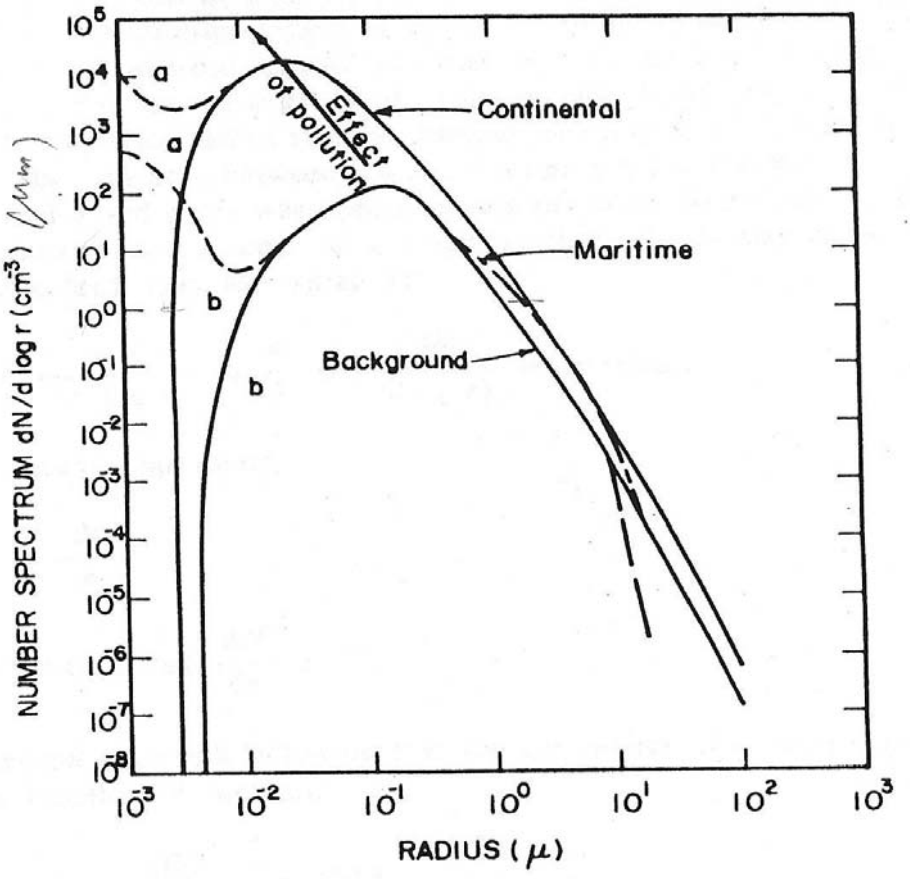

Figure 2.1. Size distribution of aerosols [Ruskin and Scott, 1974].

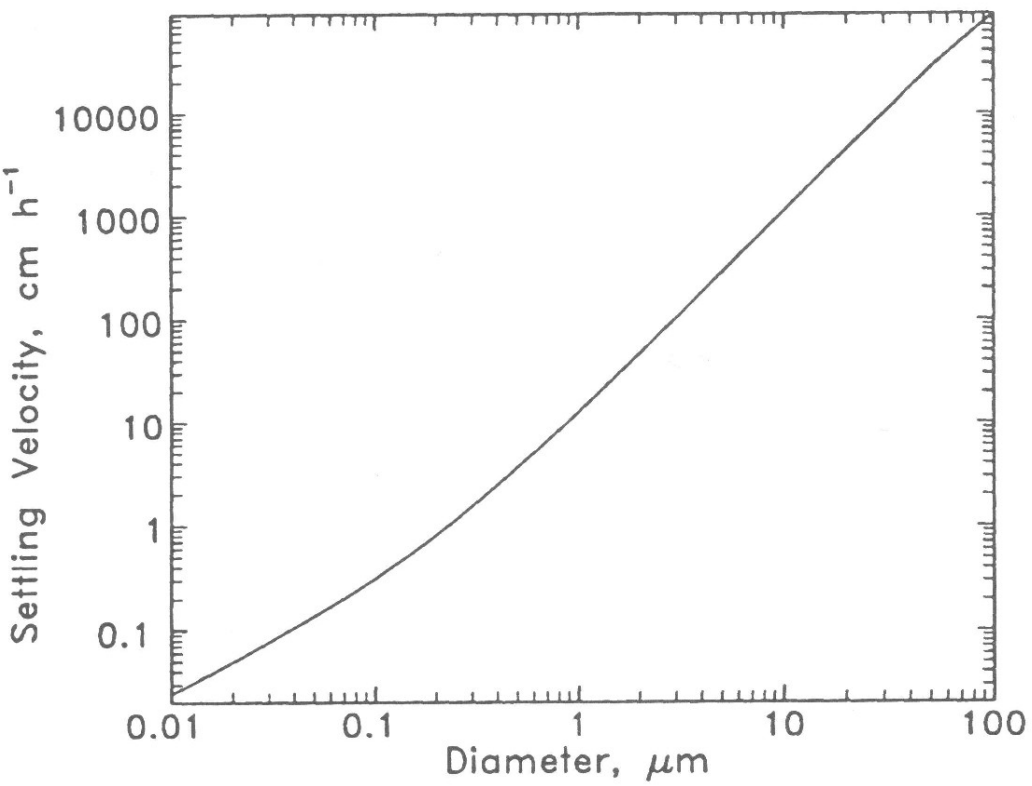

Figure 2.2. Particle settling rate [Seinfeld and Pandis, 1998].

Airborne particular matter has been approximated by three log-normal mode representations, which are classified by type of source mechanism [Shettle and Fenn,1979]. The three modes are referred to respectively as the nuclei mode, the accumulation mode and the coarse mode, and each of the modes are specified by a mass mean diameter and a geometric standard deviation. The largest numbers of particles are found at smaller sizes in the range of nuclei and in the accumulation mode. These smaller sizes are called fine particles. Particle measurements are often reported as the summation of the mass of all particles of aerodynamic size less than 10 μm, PM_{10}, or less than 2.5 μm, $PM_{2.5}$ [Rogers,1989].

Aerosol particles are produced by a number of process, including (i) gas-to-particle conversion, (ii) condensation and coagulation, (iii) ocean breaking waves, (iv) wind-blown effects, or mechanical distribution, (v) direction emissions and (vi) meteorites. The smallest particles are produced by gas-to-particle conversion processes. If the vapor concentrations are sufficiently high, particles may be formed in the free air

by ‘homogeneous nucleation’, which means the vapors cluster together and condense onto the particles if sufficient numbers of particles are present. This process is important for forming particle sizes between 0.01 μm and 0.1 μm. The composition of particles between 0.1 and 1 μm includes sulfate, nitrate, and carbonaceous aerosols, etc. When the particle size is larger than 1 μm, direct emission from vehicles, industry and wind-blown effects are more important. The processes which generate and remove particles are presented in Figure 2.3.

Figure 2.4 shows the size ranges of different aerosol types. It is possible that there is a different shape for every aerosol particle, but no computations could be carried out to make practical use of the information. The most likely use of the information on shapes would be computation of ways to parametize the shapes. For most analysis efforts, the shape problem is avoided in scattering problems by assuming a distribution of spherical particles. When all types of particles are considered, we find many are spherical in shape, or nearly so, and scattering procedures are easily described. However, the shape and ingredient features of frozen and mechanically generated particles provide the most challenging problems when describing optical scattering.

The size distribution of particles in the atmosphere is related to their residence time in the air. Small particles, which are less than 1 μm, are only slowly removed from atmosphere by rainout, or by the process of coagulation and nucleation, and their setting times are very long (see Figure 2.2). They stay in the atmosphere sufficiently long for long-distant transport to occur, the average residence time for particles of size of 1 μm is about 1 month. Large particles are removed from the atmosphere by sedimentation, the average residence time for particles of size of 10 μm is about half day, and only around 10 minutes for 100 μm particles, unless they are held aloft by high winds [Twomey, 1977].

Every air-pollution, or ‘dirty air’ problem is associated with the presence of aerosol particles. Although the large size accumulation mode and coarse mode particles, which includes dust, have relatively short residence time, they are of most concern to problems related to the visual range. Figure 2.5 shows an example of aerosol size distribution with a heavy load of coarse mode particles.

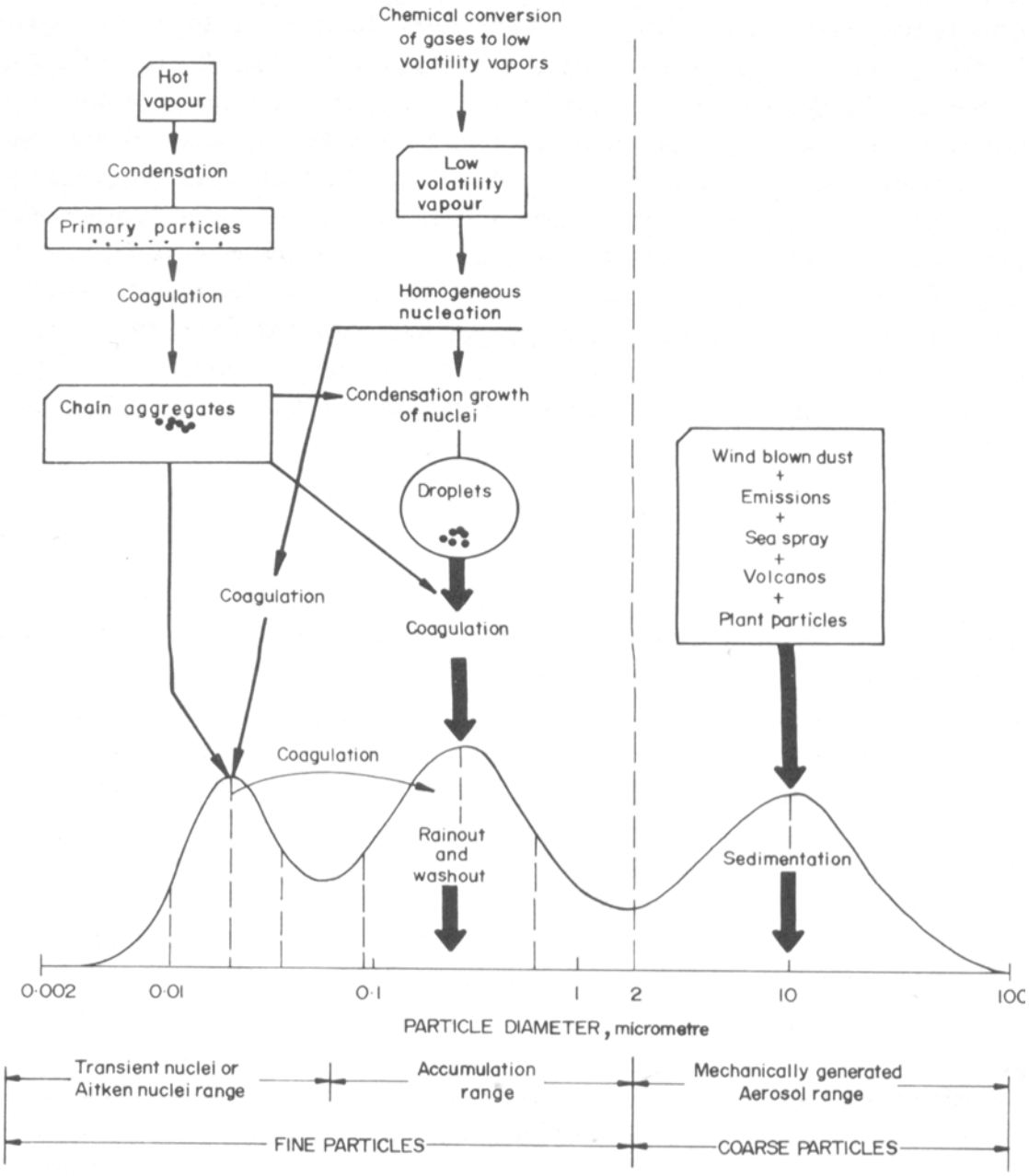

Figure 2.3. Atmospheric aerosol surface-area distribution [Whitby 1975].

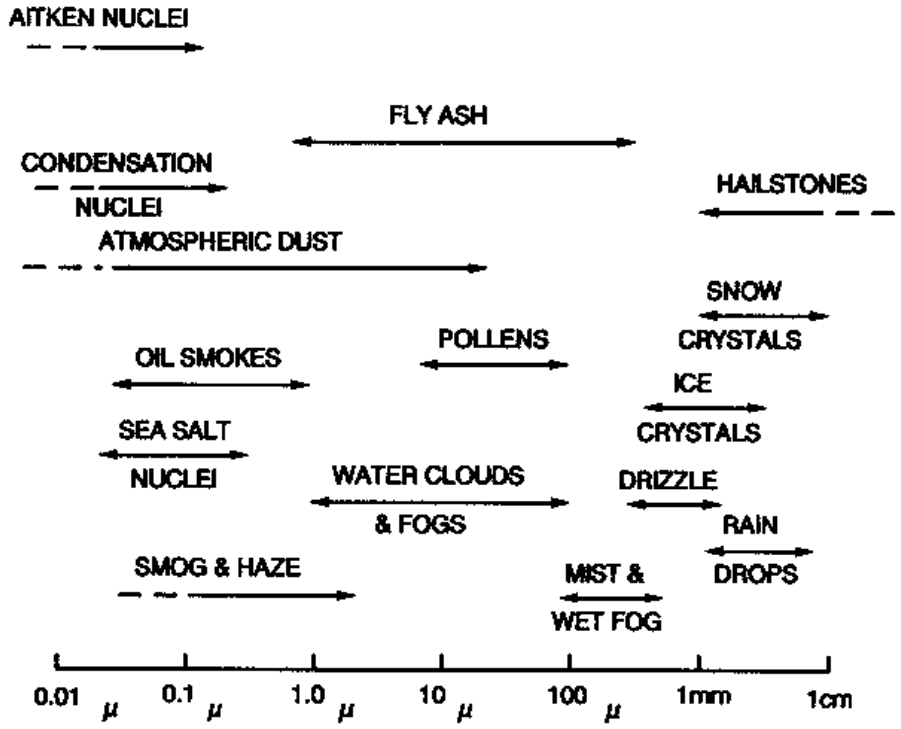

Figure 2.4. Atmospheric aerosol source and size range [Farmer,2001].

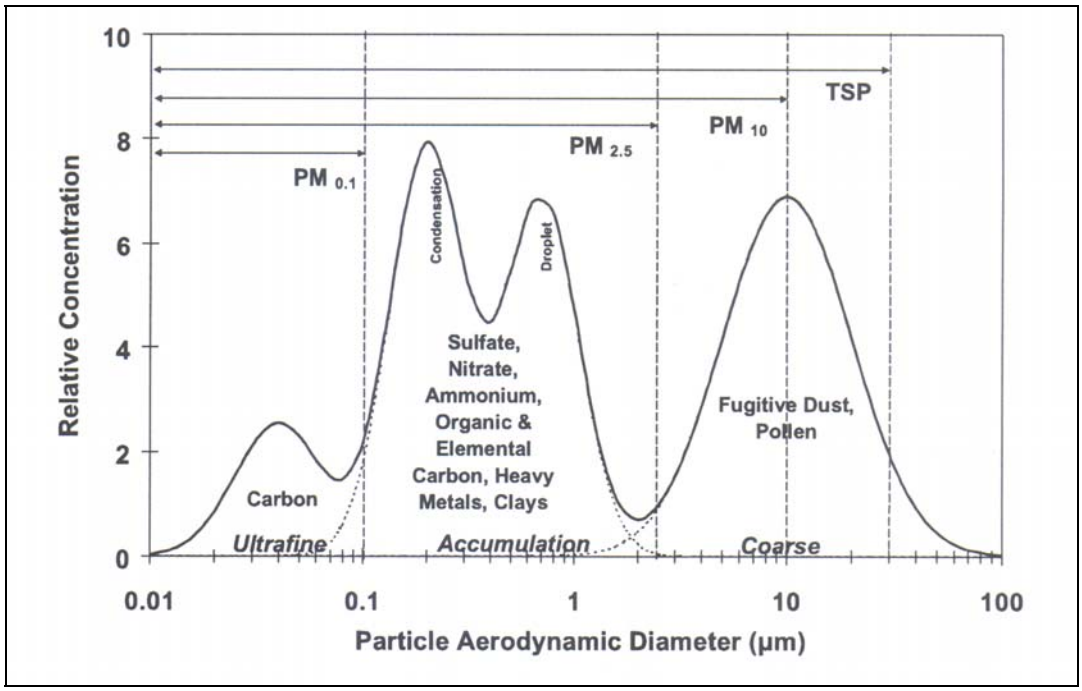

Figure 2.5. Heavy loading dust size and mass distribution [Watson and Chow, 1999].

As indicated in Figure 2.5, fugitive dust is the most common source of particles in the coarse mode range. Suspension of particles from vehicles on dirt roads, from agricultural operations, and from industrial processes are sources of atmosphere hazes and dust clouds. Source particles, which are resuspensions of surface origin particles or aerosol droplets, can remain airborne for sufficient periods of time to affect optical transmission on significant path lengths. The principal characteristics that effect airborne dust concentrations are the soil type and size, and its associated binding agent and water content. Also, meteorological conditions are important factors in governing particle formation and are important for estimating the potential of producing airborne dust. Precipitation affects on soil moisture content and wind speed are primary factors in describing dust cloud lofting and particle dispersion. The typical particle settling rate versus size shown in Figure 2.2 [Seinfeld and Pandis, 1998].

2.2.1 Log-normal distribution

The log-normal probability density distribution as function of particle radius D, used in many theoretical investigations of aerosols, is given as,

$$f(D) = \frac{1}{\ln(\sigma_g)\sqrt{2\pi}} \exp\left[-\left(\frac{\ln^2(D/D_g)}{2\ln^2(\sigma_g)} \right)^2 \right] \qquad (2.1)$$

where σ_g is the geometric standard deviation, D_g is geometric mean size. It has been suggested that multi-model log-normal distributions be chosen as representative of most dusts [Farmer, 2001, Novitsky, 2002]. In addition, surface area distribution ($dS/d\log r$) and volume density distribution ($dV/d\log r$) are also very important for the study of particle optical scattering properties and mass concentrations in atmosphere.

Figure 2.6 shows an example of atmosphere particle size, surface and volume distributions which depict some interesting information for the same set of particles. The particle number maximum occurs at a size that is different from the maximum of the surface area and volume distributions. There are numbers of different types of instruments used to measure particle properties. Particle spectrometers are used to measure number density distribution, optical instruments are sensitive to the surface area and optical scattering cross-section, and filter bases sampling instruments are used to

measure the mass, which is sensitive to volume distribution. For the optical studies using lidar techniques, we are most concerned with scattering cross-section, or surface area of particle distribution at scale sizes that are comparable with the wavelength of the scattering light.

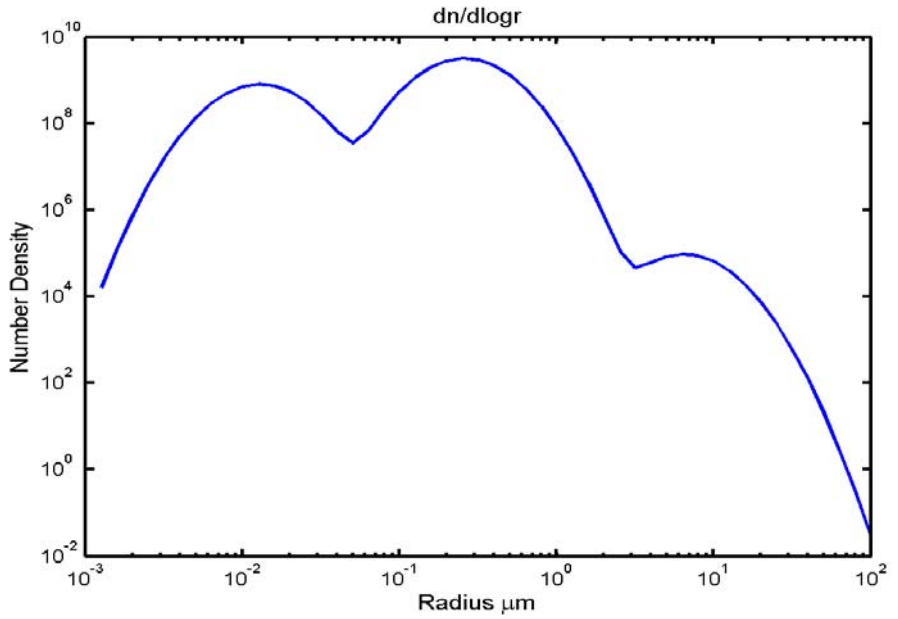

(a)

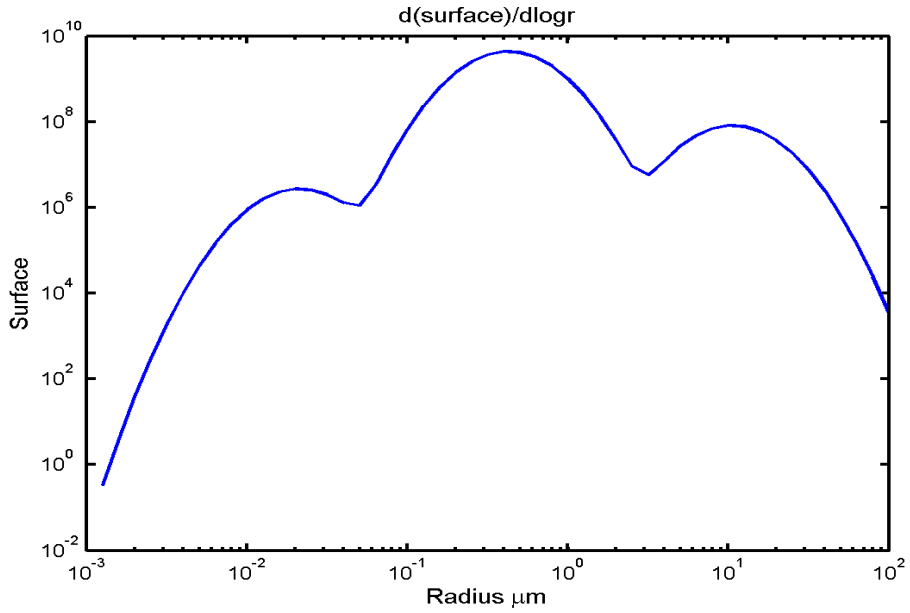

(b)

Figure 2.6. The same particle distribution is plotted to show the character dependence upon whether the measuring instrument is sensitive to one, two or three dimensional properties. (a) particle number distribution d*n*/dlog*r* (b) particle surface area distribution d*S*/dlog*r*

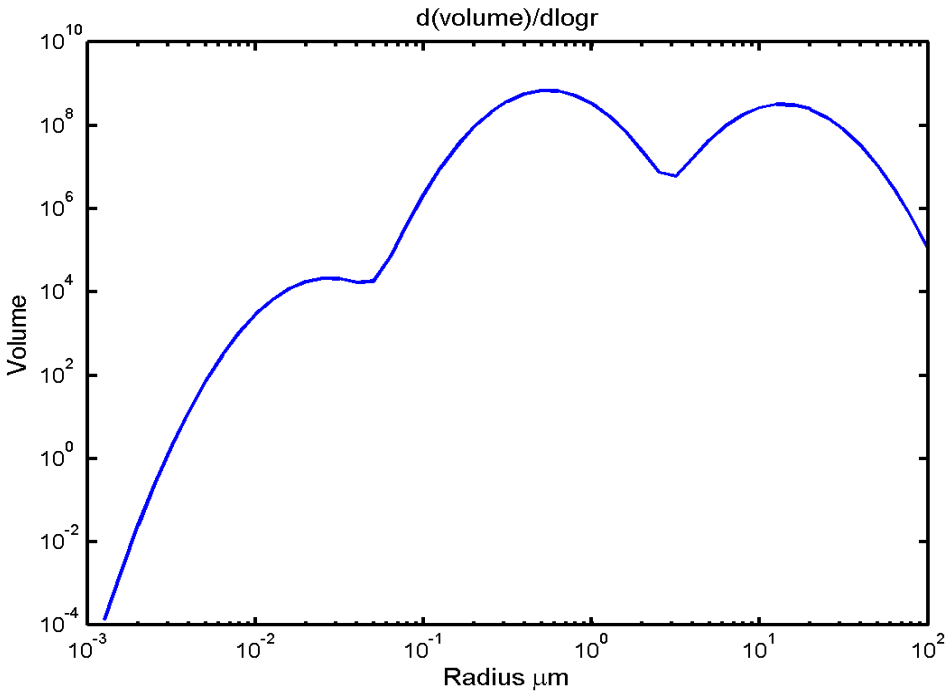

Figure 2.6. The same particle distribution is plotted to show the character dependence upon whether the measuring instrument is sensitive to one, two or three dimensional properties: (c) particle volume distribution d*V*/dlog*r*

2.3 Water Vapor and Clouds

Water vapor is distributed throughout the lower troposphere and its concentration is highly variable. It is the most important greenhouse gas and it plays the most important role in the global distribution of heat energy. The interaction of water vapor with hygroscopic particles greatly affects the optical properties in atmosphere.

It is quite common for aerosol particles to grow by absorbing a film of water from atmospheric water vapor that effects the size, shape and the reflective index of the particle. In low humidity regions where the air is usually quite clear, an increase in humidity can cause tremendous changes in visibility by increasing the average size of the already present aerosols. Even at relative humidity as low as 30%, some hygroscopic particles can still maintain a film of water. Of course, the particle's growth through absorption of water is reversible. If the humidity decreases, the water will at least partially evaporate, and the corresponding aerosol size spectrum will decrease. The absorbed film of water may dissolve any soluble materials in the aerosol. The dissolved

materials have an effect on the vapor pressure of the liquid, which is one of the mechanisms that allows a film to remain in fairly low humidity environments. Water films form more easily when hygroscopic materials, such as sea salt, sulfate and nitrate, are present in the aerosols, but films also form when no particular hygroscopic materials are involved.

Aerosol growth can be characterized as a function of relative humidity. Semi-empirical models for hygroscopic aerosol scattering and scattering efficiency have been discussed in a number of papers. These models have successfully predicted the scattering characteristics of mixed particles [Lowenthal *et al*., 1995; Zhang et al., 1994; Sloane and Wolff, 1985; Sloane, 1983; Malm and Kreidenweis, 1997].

Sloane (1986) derived following Semi-empirical growth curve:

$$\left(\frac{D}{D_0}\right)^3 = 1 + E\rho_{dry} EH\left(\frac{RH}{1-RH}\right) \tag{2.2}$$

where D is the wet Stokes diameter at a relative humidity RH; D_0 is the dry Stokes diameter; E is the soluble fraction of dry mass; ρ_{dry} is the density of dry particle. EH is defined by the composite function:

$$EH = \langle i \rangle \langle \varepsilon \rangle \frac{MW_w}{MW_s} \tag{2.3}$$

where *i* is the van'Hoff factor, which accounts for dissolution of ionic species into ions in solution, ε is the dissolved fraction of the aerosol mass, MW_S is the average molecular weight of solute, MW_W is the molecular weight of water. Variations in aerosol chemical composition can be accommodated in this model by changes in soluble fraction, in dry density, and in assumed RH-depended values of EH. The EHs vary with composition of RH, and have been determined empirically for various typical aerosol mixtures. Table 2.2 shows some typical EH values used by Sloane (1986), Malm and Kreidenweis. (1997), and Lowenthal et al. (1995).

Table 2.2. Thermodynamic functions for particle growth (EH)

Relative Humidity	*30*	*40*	*50*	*60*	*70*	*80*	*90*
Malm and Kreidenweis (1997)	0.09	0.35	0.35	0.35	0.32	0.27	0.23
Lowenthal et al. (1995)	0.09	0.12	0.13	0.13	0.17	0.27	0.23
Continental urban, Sloane(1985)	0.24	0.24	0.30	0.54	0.67	0.58	0.46
Typical urban, Sloane(1985)	0.20	0.40	0.60	0.70	0.75	0.65	0.60
NH_4HSO_4, Sloane(1985)	–	0.61	0.48	0.45	0.46	0.40	0.35

The measurements from different aerosol instruments obtained at the same time and location have been examined and modeled to study the effects of water vapor on the size increase and these results will be discussed in later chapter. The way that high relative humidity contributes to the size growth of hydroscopic particles in atmosphere has been demonstrated in this thesis.

CHAPTER 3

Instrument Hardware and Measurement Techniques

Lidar is a radar at optical wavelengths and is composed of a laser transmitter, a light collection receiver and a detector system. A lidar system transmits a pulsed laser beam at a certain wavelength into the atmosphere, and a telescope collects the return signals, including direct backscatter, vibrational Raman and rotational Raman signals, at different wavelengths which are separated and measured in a detection system. The return signals are then analyzed to obtain measurements of atmospheric properties and constituents. The measurements are range resolved and the arrival time of the backscatter light pulse provides a precise range or altitude arrangement.

3.1 The Laps Raman Lidar Instrument

Lidar Atmospheric Profile Sensor (LAPS) transmits at the 2^{nd} and 4^{th} harmonics of a 1064-nm Nd:YAG laser, 532 nm and 266 nm respectively. The return signals are measured after spectral separation and isolation, using photon counting photo-multiplier tubes (PMT). The intensity of light is measured at seven frequency shifted Raman scattering wavelengths, which are listed in Table 3.1. Table 3.2 gives information about the sub-systems that make up the LAPS lidar instrument [Philbrick, 1998].

LAPS is capable of measuring vertical profiles of water vapor, temperature, optical extinction from scattering of the 532 nm transmitted beam, and water vapor, ozone, optical extinction from scattering of the 266 transmitted beam. As shown in Table 3.1, the LAPS measures the rotational Raman backscatter signals at 530 and 528 nm and the vibrational Raman scatter signals at 660, 607, 277, 284 and 295 nm. Profiles of atmosphere ozone density are obtained by taking the ratio of vibrational Raman shifted signals of oxygen and nitrogen (277/284 nm). Measurements of atmosphere temperature are obtained by taking the ratio of the rotational Raman signals at 528 and 530 nm. Measurements of water vapor profiles are obtained by taking the ratios of water vapor to nitrogen 660/607nm and 295/284 nm, however the ultraviolet wavelength requires an additional correction for the ratio of 295/284 nm due to ozone absorption. Optical extinction, which is a measure of the total attenuation of a laser beam due to scattering

and absorption, is obtained from analysis of the slope of the profiles of Raman scatter return signals at 607, 530 and 284 nm, and the extinction is determined based upon measuring the gradient of the signal relative to the slope expected for the number density gradient of the neutral atmosphere. The neutral atmospheric density gradient can be obtained from the LAPS temperature profile and surface pressure, or by using a linear atmospheric model, which is usually accurate enough when the aerosol extinction is large.

Table 3.1. Measurements made by the LAPS lidar instrument

Property	Measurement	Altitude	Time Resolution
Water Vapor	660/607 Raman 294/285 Raman	Surface to 5 km Surface to 3 km	Night - 1 min. Day & Night - 1 min.
Temperature	528/530 Rotational Raman	Surface to 5 km	Night 30 min.
Ozone	276/285 Raman/DIAL	Surface to between 2 and 3 km	Day and Night 30 min.
Optical Extinction at 530 nm	530 nm Rotational Raman	Surface to 5 km	Night 10 to 30 min.
Optical Extinction at 607 nm	607 N_2 1st Stokes	Surface to 5 km	Night 10 to 30 min.
Optical Extinction at 285 nm	285 N_2 1st Stokes	Surface to 3 km	Day and Night 30 min.

Table 3.2. Characteristics of the LAPS Lidar Subsystems

Transmitter	Continuum 9030 -- 30 Hz 5X Beam Expander	600 mj @ 532 nm 130 mj @ 266 nm
Receiver	61 cm Diameter Telescope	Fiber optic transfer
Detector	Seven PMT channels Photon Counting	528 and 530 nm -- Temperature 660 and 607 nm -- Water Vapor 294 and 285 nm -- Daytime Water Vapor 276 and 285 nm -- Raman/DIAL Ozone
Data System	DSP 100 MHZ	75 meter range bins
Safety Radar	Marine R-70 X-Band	protects 6^o cone angle around beam

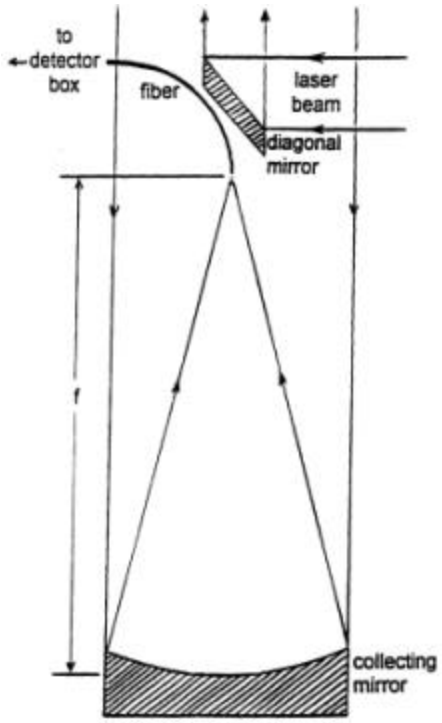

Figure 3.1. Arrangement of the Telescope Receiver of the LAPS Instrument. [Jenness, 1997]

The LAPS instrument transmitter is a Nd:YAG laser, which is pulsed at 30 Hz, with output power up to 1.6 J per pulse at the primary wavelength of 1064 nm. The laser is hosted in a weather-sealed deck unit along with an optical receiver. The 1064 nm wavelength is doubled and quadrupled to produce output wavelengths at 532 nm and 266 nm, with 8 ns and 5 ns pulses pulse widths and energies of 600 mJ and 130 mJ, respectively. The beam is expanded with a 5X beam expander before transmission into the atmosphere. The lidar receiver uses a prime focus parabolic telescope, which focuses the backscattered light onto a one millimeter diameter optical fiber. The optical fiber transfers the signal to the detector box. The lidar receiver optics are shown in Figure 3.1.

3.1.1 Raman Lidar Telescope Form Factor

A lidar receiver collects light scattered from a laser-illuminated spot at a finite distance. Figure 3.2 shows the profiles of the raw data signals which demonstrate the effect of overfilling of the fiber by the near field image of the telescope at altitudes below 800 meters. The receiver subsystem collects the signal returning through the quartz glass

window. A parabolic mirror served as a prime focus telescope and focuses the signal into the end of a 1mm diameter quartz fiber. This fiber end is mounted on a computer-controlled 3-axis positioning unit that permits remote alignment of the fiber on the optical axis of the telescope.

In order to further reduce the background during daytime operation, an automated field stop is installed in front of the fiber positioning system to reduce the telescope field of view. This field stop can be moved in and out of place by a computer command at the control console. After collecting the scattered return signal into the fiber, the light is passed from the deck unit to the detector box subsystem which is mounted on the back of the control console.

A diagonal mirror is required to transmit the coaxial laser beam from the center of the receiver axis. The diagonal mirror produces a small obstruction in the central zone of collecting mirror. The size limitation of fiber reduces the detection efficiency of the receiver system for near field signals that overfill the fiber. It also serves as a field stop to limit the transfer of background light to the detector box. For efficient capture of the convergent ray cone, the fiber's numerical aperture should be compatible with the receiver's *f*-number, and this consideration determines the receiver's size. In general, the image of a laser-illuminated spot will not be in sharp focus over the full range covered by a lidar system. Typically, when the fiber is at the infinity focus, there is a long-range interval for which the blur disk is small enough for complete capture. There is a transitional range where blur disk is approximately equal to the fiber diameter. For ranges less than about 800 meters, the blur disk is larger than the fiber, and light falls outside the fiber cross-section. At the shortest range, the obstruction of the secondary mirror further reduces the signal further. Figure 3.2 shows an example of the raw data profiles for seven wavelengths that demonstrate low altitude overfilling below 800 meters. However, the telescope form factor can be determined and used to correct the profile.

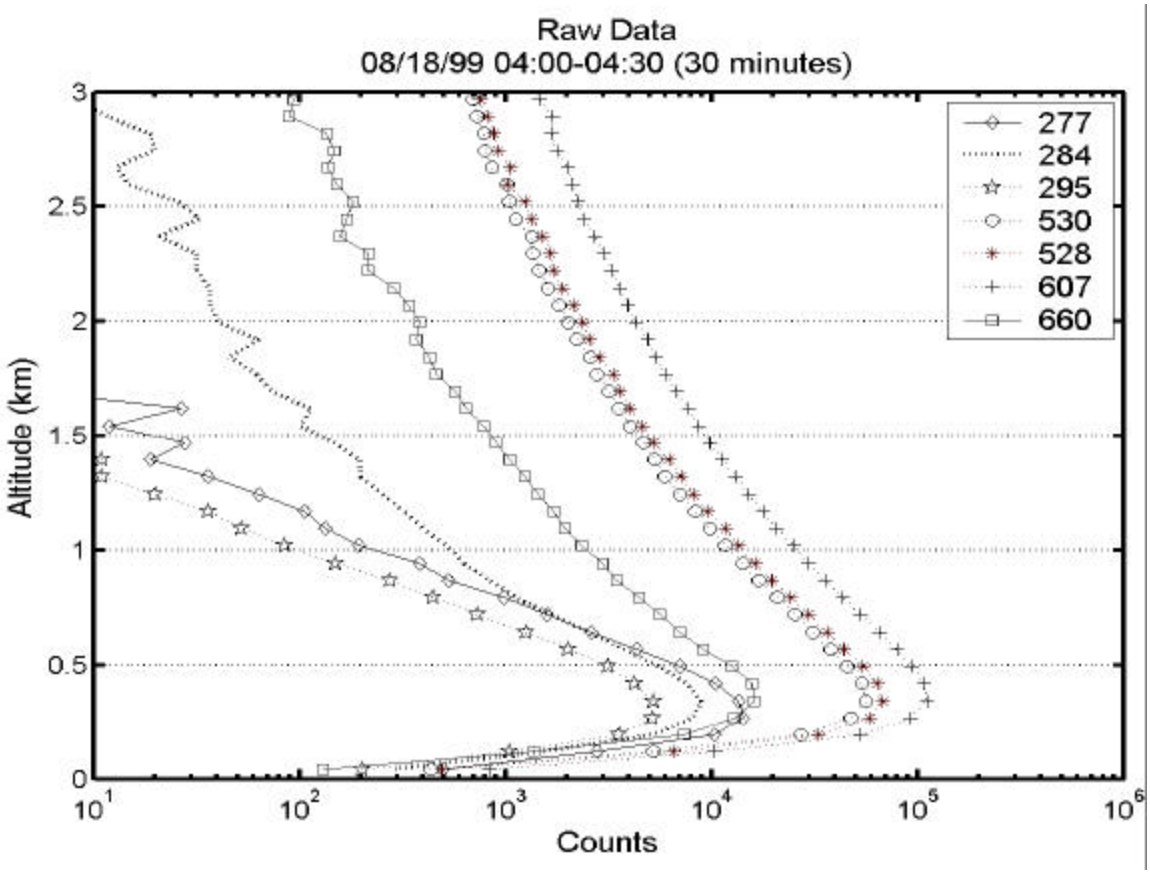

Figure 3.2. Sample Raman Lidar raw return signals taken during the summer 99 NE-OPS campaign.

We cannot simply increase the fiber size to solve the problem. As we can see from the above considerations, a smaller fiber further reduces the signal from the shortest ranges and the effect of the central obstruction becomes more severe. On the other hand, the optical fiber cannot be made sufficiently large to eliminate the near field effect. The limited the fiber cross-section is used to help improve the signal to background ratio at the higher altitudes.

The optics configuration and parameters of LAPS receiver system are shown in Figure 3.3. The signal receiving efficiency is limited by the size of the fiber diameter (d_f) and part is directly blocked by the mirror used to position the laser beam (d_t) on the receiver axis. Theoretically, the telescope form factor can be calculated depending upon the system parameters given above and assuming perfect alignment of the optical axis of the system.

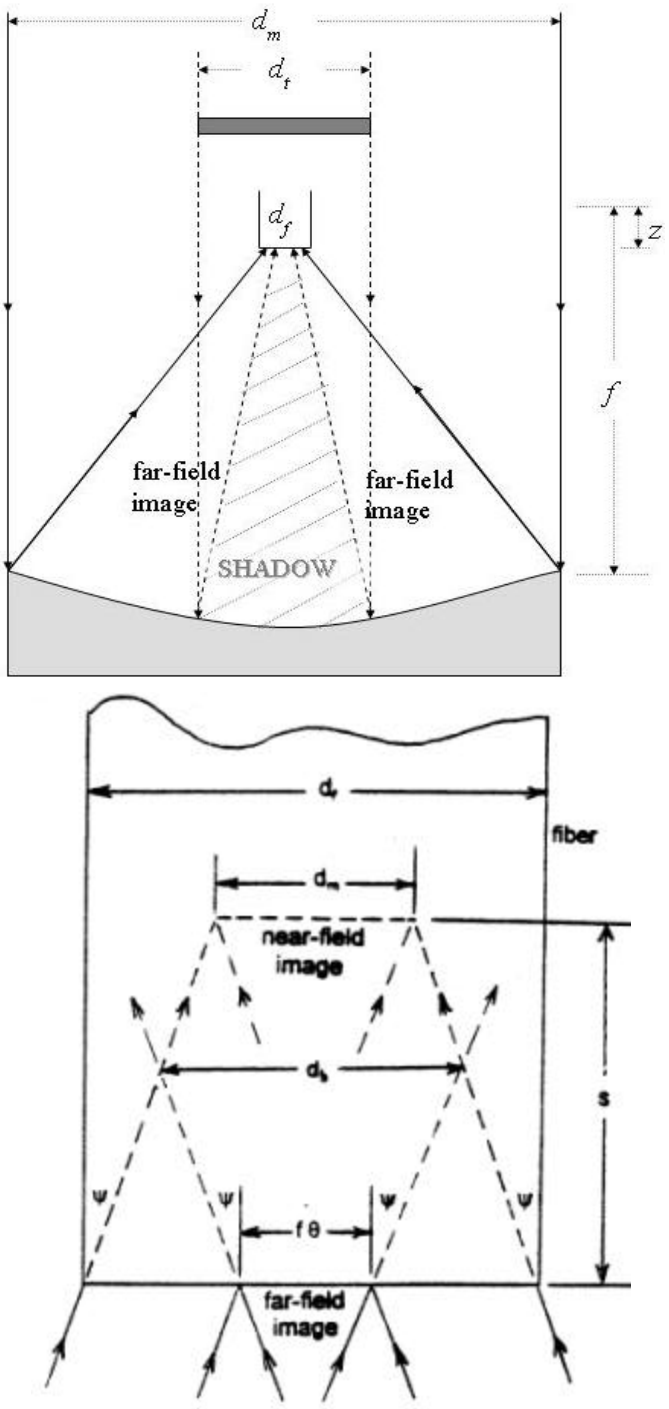

Figure 3.3. (a) The optics configuration and parameters of LAPS receiver system; (b) Locations of images near field and far field; f is the focus distance (f = 1.53 m); dm is the diameter of the mirror (dm = 0.62 m); d_f is the diameter of the fiber (d_f = 1 mm); d_t is the diameter of the laser beam (d_t = 47.5 mm); z is the distance of fiber position to the focus point.

We have both calculated the telescope form factor, and measured the form factor during clear sky conditions to aid in analyzing signals in the near field. This analysis generally uses the analytical solutions derived from the measurements because that provides a consistent result. The theoretical calculation is difficult to implement because of uncertainty about the position of the fiber surface relative to the telescope focus. The intensity of the return light is corrected by using a calibrated telescope form factor. Several efforts to properly describe the form factor have been presented [Jenness, et. al,1997, Measures 1992 pp 265-269]. A geometrical overlap correction method has been tested and used to determine the form factor of the telescope [Jenness, et.al, 1997]. In this method the overlap form factor is calculated geometrically depending on the ratio of the laser focus area to the area of the receiving fiber. We have assumed the fiber position is perfectly aligned along the central z axis and can be adjusted along the z direction to improve the reception. The comparison of fiber capture efficiencies of return signal for a range of different fiber z positions are shown in Figure 3.4.

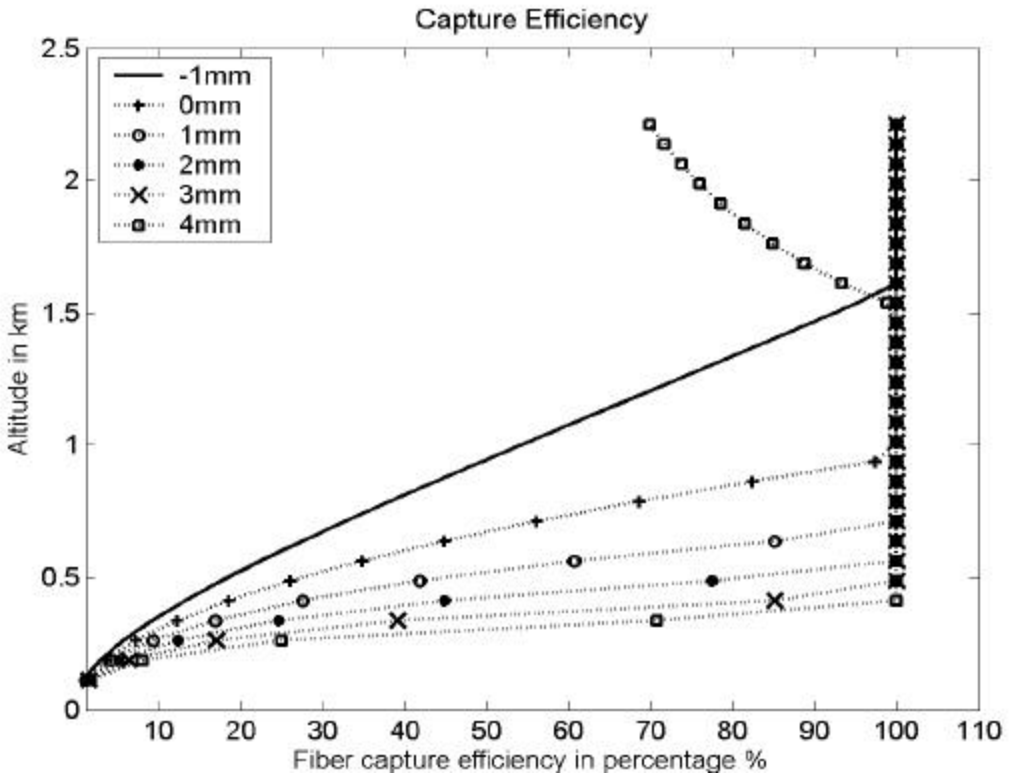

Figure 3.4. Theoretical calculation of fiber capture efficiencies for the relative position of the fiber located at: -1 mm, 0 mm, 1 mm, 2 mm, 3 mm and 4 mm from the focal point (minus corresponds to position shorter than the focal length).

As shown in the Figure 3.4, the different curves of capture efficiency represent different fiber positions on the central axis. The curve with legend of –1mm represents the fiber position that is located before the focus point, and is closer to the collecting mirror. At the point 0 mm, the fiber is positioned on the focal point, see the legend for the other curves in the figure. At the focus point, where we initially position the fiber during the measurements, we begin to observe signal loss below 800 meters. If we moved the fiber a bit behind the focus point, away from the collecting mirror, we obtain better fiber capture efficiencies, as shown in the curves at position 1 mm, 2 mm and 3 mm. However, there is a transitional range for which the laser-illuminated spot at far field is equal to the fiber diameter. If we move the fiber further behind this transition point, the light returned from far field falls outside of fiber and we cannot achieve complete capture except for a limited range altitude, as in the case of the 4 mm curve. In conclusion, the fiber should be positioned 1-3 mm beyond the infinity focus to obtain better capture efficiency and to reduce the telescope form factor distraction in future measurements. One additional point to consider when setting up this position is that lowering the altitude of the capture point will also rapidly increase the signal intensity and will require a larger dynamic range for the detection. Thus, the best arrangement in all cases is one that is stable and the position of the detector, or fiber, is only very slightly (~ 1 mm) behind the focal point. This consideration is also important for optimizing the allowance for position in x-y plane. The MATLAB program for theoretical calculation of the telescope form factor is attached in Appendix A.

This geometrical method is difficult to apply for our LAPS system because it requires the LAPS system to be perfectly aligned on the axis of the transmitter and receiver, or requires knowledge of the position. The approach is difficult because any shift in the x-y position during the system setup may cause a significant deviation of the telescope form factor from the geometrical solution.

To ease the problems in above solution, an experimental approach has been developed to obtain the telescope form factor [Li, et.al, 2000]. The experimental approach requires a time period with the weather conditions as clear and dry as possible. Under clear conditions, where the aerosol extinction and backscattering are relatively small, the laser return signal will closely approximate the profile of the neutral density

that vary exponentially with the altitude. We can model the expected lidar signal profile when clear conditions exist to examine the measured profile shape relative to this simple exponential and then calculate the telescope form factor. This form factor can be used during other periods when scattering is higher as long as the same instrument alignment is maintained during an extended measurement program. For the example data sets, we selected such time periods (9:00AM on 20 August 1998 and 5:00AM of 10 August 1999) to investigate the details of the telescope form factor. Usually, summertime conditions in urban atmospheres are not very clear and dry, so we used our lidar water vapor mixing ratio measurement, which is not affected by the form factor, to select time periods that are the most dry and clear. Additionally, the chosen periods have a uniform water vapor mixing ratio as a function of altitude, as well as a smooth profile for the optical extinction values, to eliminate periods when subvisual aerosols are present.

After the time period is chosen, the form factor can be calculate by making use of the fact that the extinction value will be uniform below 1 km during clear weather conditions. The form factor has been used to correct the profile in first kilometer range and the profile then used to obtain extinction profiles. The telescope form factor has been examined and found to provide a sufficiently accurate approach for correcting lower altitudes of the vertical signal profiles. This approach permits calculations of the extinction coefficient profiles from the ground through the troposphere. However, the form factor must be recalculated when the instrument is transported or the alignment is changed.

The experimental fiber reception percentage is shown in Figure 3.5 where the form factor results for several measurement programs are compared. The solid lines in the figure represent theoretical calculations with fiber z position at 0 mm, 1 mm, 2 mm and 3mm beyond focus point. In Figure 3.6, the form factors determined from several measurement programs are compared with the theoretical functions.

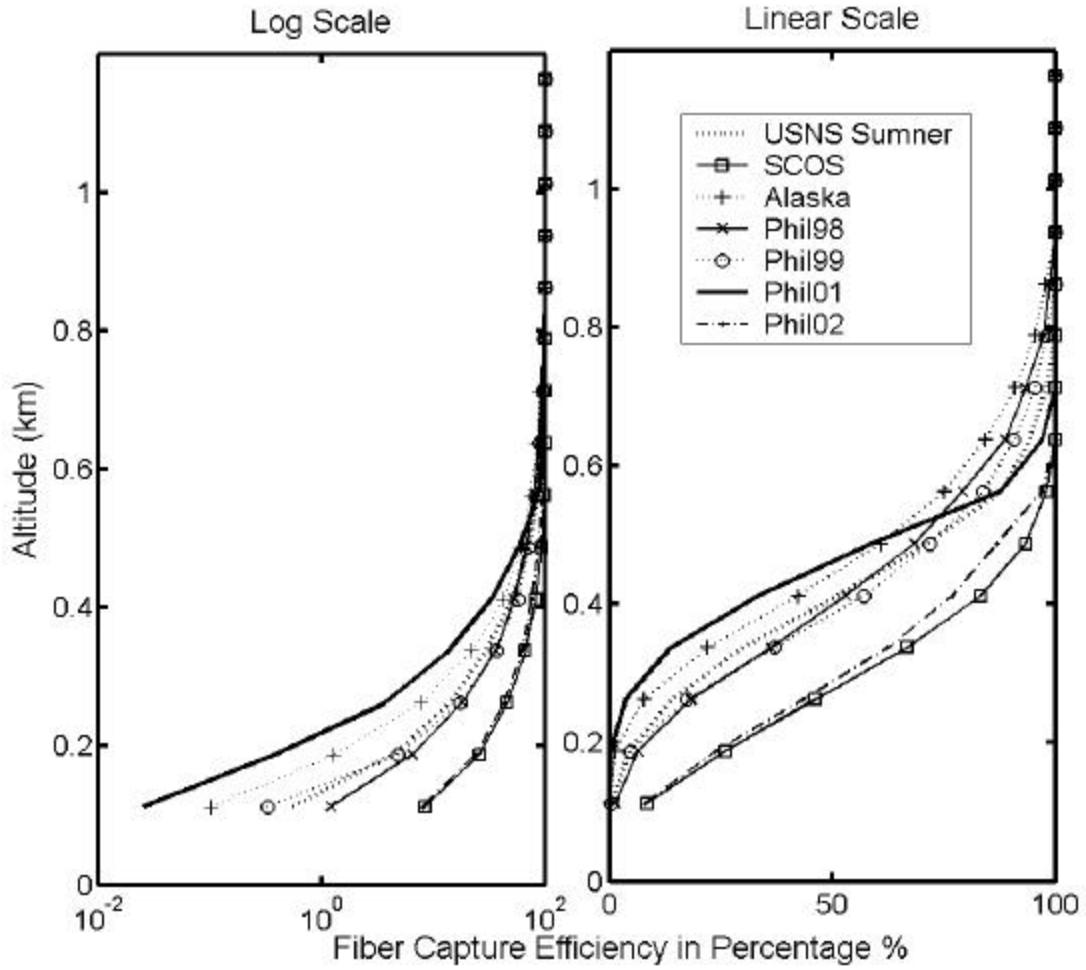

Figure 3.5. Summary of experimental fiber capture efficiency in percentage shown on log scale and linear scale. Numbers were calculated from several campaigns, including USNS Sumner, SCOS, Barrow Alaska, NEOPS 98, NEOPS 99, NEOPS 2001 and NEOPS 2002.

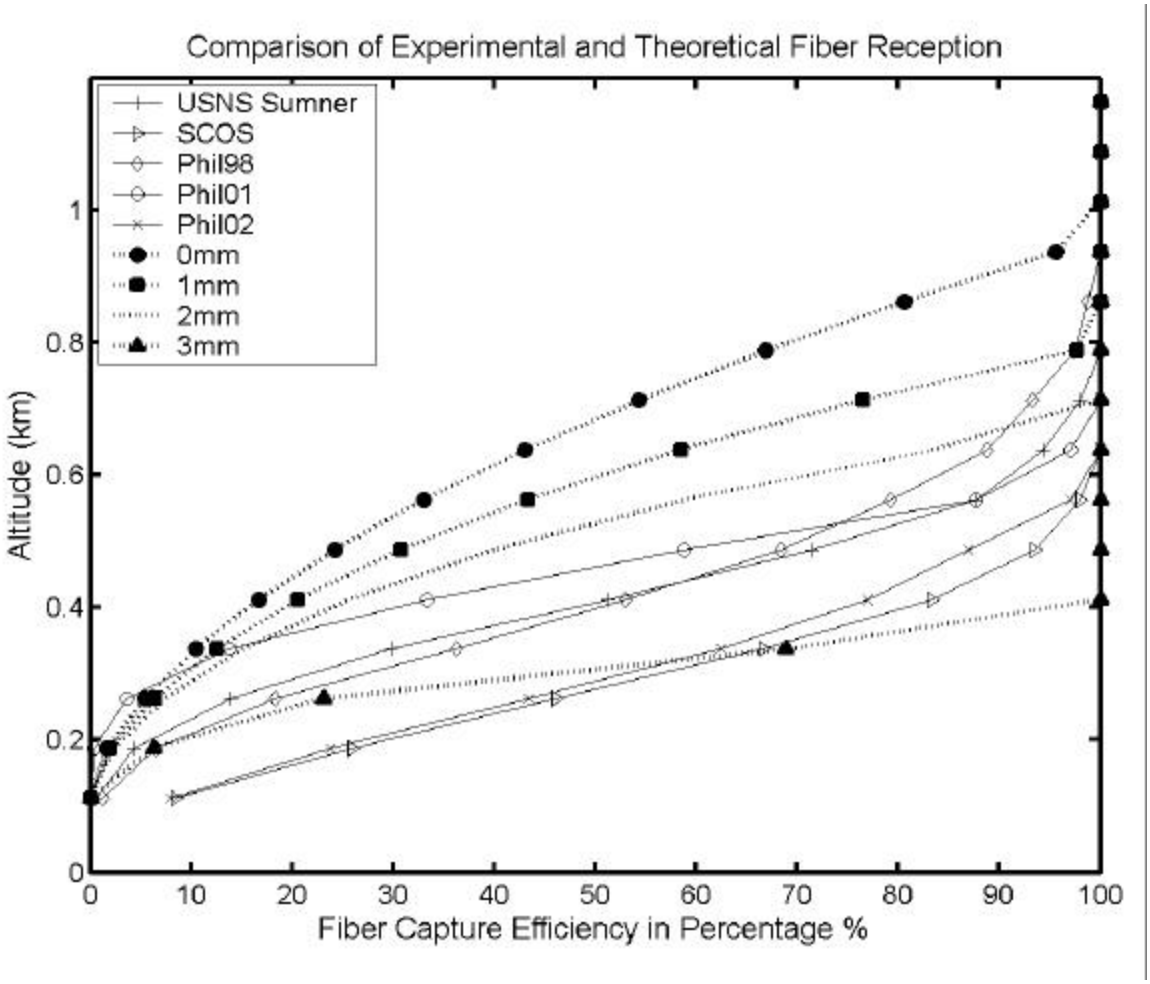

Figure 3.6. Comparison of experimental and theoretical fiber capture efficiency.

3.2 Scanning Micro-Pulse Lidar

The Portable Digital Lidar (PDL) instrument is a two wavelength, scanning, aerosol lidar system. It comprises an optical transceiver unit, a tripod and rack mounted electronics. The transceiver houses two laser transmitters at the fundamental and doubled wavelengths of the Nd:YLF laser and two detection systems. The signals are transmitted and received using the same telescope. The instrument provides the backscatter signal profiles at two wavelengths 1047 nm and 523 nm. The instrument is mounted on a platform which can be used to scan horizontally and we used that capability to map the airborne particulate matter. It has several features that make it the ideal instrument for mapping the properties of dust clouds.

The Portable Digital Lidar (PDL) instrument, which is manufactured by Science & Engineering Services, Inc (SESI) (http://www. sesi-md.com) was used in the California Dust study. The primary objective of this research activity is to conduct a field program to characterize the fate (deposition and transport) of PM emissions originating from mechanical disturbance of the soil. The results from the PDL instrument were used to determine the density distribution of airborne particles and measure the optical extinction of dust clouds. The results have been used to infer the particle size and other properties by comparisons with model calculations.

Table 3.3. Portable Scanning Micro-Pulse Lidar System Specifications

Portable Digital Lidar ***(Dual Wavelength with Scanner)***
Operating Environment Controlled Indoor
Detection Range 30 – 60 km
Laser (dual wavelength) DPSS:Nd:YLF (523.5 nm/1047 nm)
Laser Control Remote Set or RS232
Average Energy VIS: >5 μJ/pulse NIR: >10μJ/pulse
Pulse Repetition Rate (pulse duration) 1 – 10 kHz (10 ns)
Cassegrain Telescope Diameter (F.O.V.) 0.2 m (- 100μrad)
Detector APD Photon Counting Module
Scanning Mode Sweep or Stay and Stare
Horizontal Scanning (vertical swiveling) ± 90º (0º - 90º)
Scanning Speed per sec Variable from 0.1/sec to 30/sec
Optical Transceiver Dimensions (weight) 33” x 14” x 12” (40 lbs)
Computer Desktop or Laptop PC
Software Windows 95/98 based software
Dual Multichannel Scaler (dimensions) Rack-mountable (19” x 14” x 7”)
Data Averaging Time Adjustable from 1 sec to 1 hour
Range Resolution 30 m, 75 m, 150 m, 300 m

Figure 3.7 shows vertical profiles during the mid-afternoon obtained for the green and NIR channels when the instrument was pointed at an elevation angle of 70^{o}. The data has been range corrected for $1/R^2$ dependence but no other corrections have been applied and so the telescope form factor is quite noticeable for altitudes below 1 km. The top of the planetary boundary layer (PBL) is clearly evident in both the green and red channels. The green signal is large compared with the NIR signal as we would expect for the case when most of the contribution is due to the scattering by small particles. The shape of the vertical scattering profile is that expected for a well-mixed atmosphere that is relatively

clean but contains small aerosols. The increase in the signal versus altitude is due to two factors, the telescope form factor and the fact that hydroscopic particles grow larger as the temperature decreases and relative humidity increases as a function of altitude. Since the optical scattering increases ~R^6 for small particles, we expect to observe more optical scattering toward the top of the boundary layer, even small changes in size can cause significant increase in optical scattering. The micro-pulse lidar results obtained during the California Dust program will be discussed in Chapter 4.

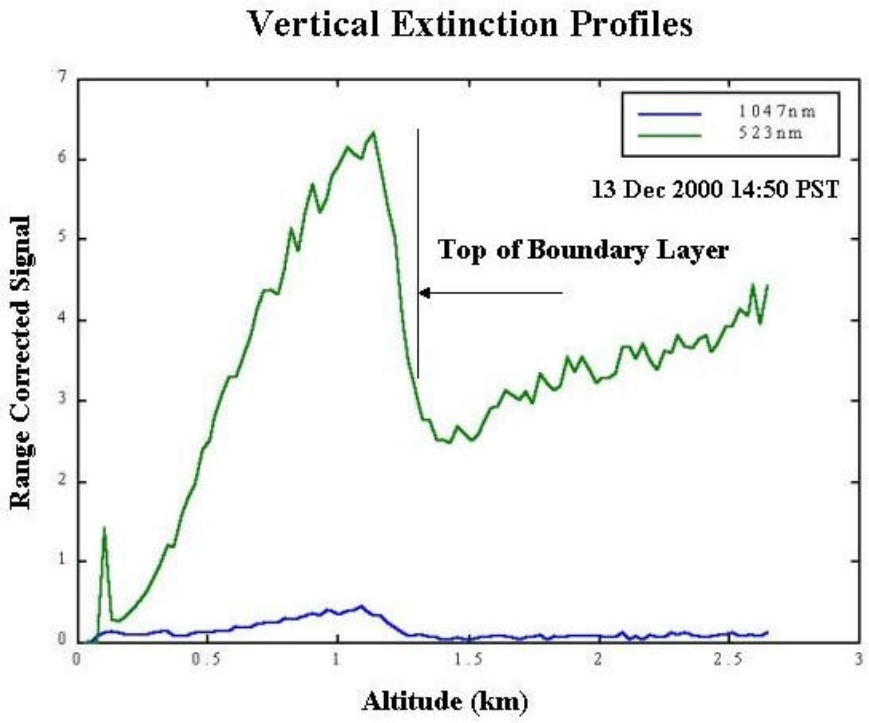

Figure 3.7. Sample of MPL Lidar vertical profile from slant path measurement (elevation angle 70°) during period of afternoon convection shows the top of the boundary layer near 1300 m.

3.3 Lidar Equation and Extinction Calculation

The LAPS instrument uses the molecular scattering properties of the species in the lower atmosphere to simultaneously measure profiles of ozone, water vapor, temperature, and optical extinction. The optical extinction profiles are obtained from the gradients in the vertical profiles of the rotational Raman molecular signal (N_2 and O_2) at 530 nm, and from the N_2 vibrational Raman signals measured at 284 nm and 607 nm. The

wavelength dependence of the optical extinction measured from the ultraviolet and visible channels can be used to interpret the variations in the particle size distribution as a function of altitude for the aerosol components of the atmosphere, after removing the known molecular scattering and absorption components. Also, these measurements can be used to determine the air mass parameter and atmospheric optical depth of the aerosol components.

In order to calculate extinction due to aerosols from Raman lidar measurements, an algorithm has been developed from the Raman lidar equation [Measures 1992 pp 237-281]. The Raman lidar equation can be written as,

$$P(l_R, z) = E_T(l_T)x_T(l_T)x_R(l_R)\frac{ct}{2}\frac{A}{z^2}b(l_T, l_R)\exp\left[-\int_0^z [a(l_T, z') + a(l_R, z')]dz'\right] \quad (3.1)$$

where z is the altitude of the scattering volume element, l_T is the wavelength transmitted, l_R is the wavelength received, $E_T(l_T)$ is the light energy per laser pulse transmitted at wavelength l_T, $x_T(l_T)$ is the net optical efficiency of all transmitting devices at wavelength l_T, $x_R(l_R)$ is the net optical efficiency of all receiving devices at wavelength l_R, c is the speed of light, t is the time duration of the laser pulse, A is the area of the receiving telescope, $b(l_T, l_R)$ is the back scattering cross section of the volume element for the laser wavelength l_T at Raman shifted wavelength l_R, and $a(l,z')$ is the extinction coefficient at wavelength λ at range z'. For vibrational Raman scattering, the backscatter coefficient $b(l_T, l_R)$ can be shown to be,

$$b(l_T, l_R, z) = N_i(z)\left\{\frac{ds(l_T, l_R, p)}{d\Omega}\right\}_i \quad (3.2a)$$

Where $N_i(z)$ represents the number density of species i, and $\left\{\frac{ds(l_T, l_R, p)}{d\Omega}\right\}_i$ is the differential Raman backscatter cross-section of the vibrational states of the gas of molecular species i, The species, i, can be nitrogen, oxygen or water vapor depending on the received wavelength of the Raman signal from different species.

Because all of the molecules of the lower atmosphere are distributed in the rotational states according to their temperature, the wavelength distribution of the rotational signal

has been used to measure the temperature profile [Haris, 1995]. For rotational Raman scattering, the backscatter coefficient $b(l_T, l_R)$ can be shown to be,

$$b(l_T, l_R, z) = N(z)\left\{\frac{ds(l_T, l_R, p)}{d\Omega}\right\} \tag{3.2b}$$

where *N(z)* represents the number density of all the molecules, and $\left\{\frac{ds(l_T, l_R, p)}{d\Omega}\right\}$ is the differential Raman backscatter cross section of the rotational Raman shift at wavelength l_R. The scattering cross-section for the rotational Raman signal near the maximum of the distribution of states, that occurs near 530 nm, is almost independent of temperature, and thus it provides an excellent molecular profile to determine the optical extinction [Philbrick, 1998, O'Brien, et. al, 1996]. The LAPS Raman lidar is used to calculate optical extinction at several wavelengths, the 284nm and 607nm profiles are derived from the Raman shift of nitrogen scattering from the 2nd and 4th harmonics of the Nd:YAG laser respectively, and the 530nm wavelength is from the rotational Raman scattering of the 2nd harmonic laser beam.

Since the number density of nitrogen is a well known fraction of the atmospheric molecules, it can represent the number density of all the molecules in atmosphere. It follows from equation (3.1), (3.2a), and (3.2b) that,

$$a(l_T, z) + a(l_R, z) = \frac{d}{dz}\left[\ln \frac{F(z)N(z)}{z^2 P(l, z)}\right] \tag{3.3}$$

l_R is the Raman shift wavelength at 284, 530 and 607nm, *N(z)* is the total molecular number density, *F(z)* is the telescope overlap function.

The extinction coefficients in equation (3) can be written as,

$$\begin{aligned} &a(l_T, z) + a(l_R, z) = \\ &a_{l_T}^{mol-sca}(z) + a_{l_T}^{aer-sca}(z) + a_{l_R}^{mol-sca}(z) + a_{l_R}^{aer-sca}(z) + a_{l_T}^{abs}(z) + a_{l_R}^{abs}(z) \end{aligned} \tag{3.4}$$

where $a_l^{mol-sca}(z)$ and $a_l^{aer-sca}(z)$ are the extinction coefficients due to molecular and aerosol scattering at the transmit and receive wavelengths, and a_l^{abs} are the molecular and aerosol extinction coefficients due to optical absorption. The ozone absorption coefficient is an important factor contributing to the total extinction calculation at the

ultraviolet wavelength, 284 nm. Molecular absorption is considered to be negligible at the mid-visible wavelengths, so the 530 nm and 607 nm signals provide measurements of the aerosol extinction. The largest absorption due to molecules at visible wavelengths is due to the Chappuis band of ozone and its absorption typically less than 1% of the extinction due to molecular scattering when the ozone density is 50 ppb.

The molecular extinction coefficients for 284, 530 and 607 nm are known from the scattering cross-sections for N_2 and O_2. The overlap function *F(z)* is equal to 1 where the path of the beam is completely within the field of view of receiver, which is the case for altitudes above 800 meters for the LAPS instrument. If we assume a wavelength dependence of the aerosol extinction is proportion to $1/\lambda$ for typical haze, then,

$$\frac{a_{l_T}^{aer}}{a_{l_R}^{aer}} = \frac{l_R}{l_T} \tag{3.5}$$

The linear response is a first order approximation to the aerosol wavelength dependence case for extinction measurements [Ansmann, 1992]. The aerosol extinction coefficient at 530 nm then can be expressed by rewriting Equation 3.1 as,

$$a_{l_R}^{aer} = \frac{\frac{d}{dz}\left[\ln \frac{N(z)}{P(z)z^2}\right] - a_{l_T}^{mol}(z) - a_{l_R}^{mol}(z)}{1+\frac{l_T}{l_R}} \approx \frac{\frac{d}{dz}\left[\ln \frac{N(z)}{P(z)z^2}\right] - a_{l_T}^{mol}(z) - a_{l_R}^{mol}(z)}{2} \tag{3.6a}$$

where the difference due to the wavelengths being at 530 and 532 nm are considered to be negligible, so no assumption about the wavelength dependence of the aerosol scatters is needed in this case. The aerosol extinction coefficient at 607 nm can be written as:

$$a_{l_R}^{aer} \approx \frac{\frac{d}{dz}\left[\ln \frac{N(z)}{P(z)z^2}\right] - a_{l_T}^{mol}(z) - a_{l_R}^{mol}(z)}{1.88} \tag{3.6b}$$

The 607 and 530 nm wavelengths are widely separated. However, when the extinction coefficient at 530nm is first determined, there is no need to assume a wavelength dependence for the aerosol scattering, because the extinction at the transmit wavelength is then known and the extinction at the receive wavelength is uniquely

calculated [O'Brien, et. al, 1996]. The ratio of the N_2 signal at 530nm and 607nm then provide a measure of the wavelength dependence of the aerosols. This ratio can be used to infer changes in size of the aerosol population, as a nepholometer measurement would.

For the 284 nm channel, the absorption at the transmit wavelength in the ultraviolet region is significant due to ozone absorption. To calculate the aerosol extinction coefficient, we have developed a method to measure the ozone density profile using the LAPS instrument. The total extinction coefficient at 284nm, which includes aerosol scattering and absorption, can be approximated as,

$$a_{l_R}^{aer} \approx \frac{\frac{d}{dz}\left[\ln \frac{N(z)}{P(z)z^2}\right] - a_{l_T}^{mol}(z) - a_{l_R}^{mol}(z)}{1.94} \tag{3.6c}$$

3.4 Ozone Calculation

Ozone profiles can be calculated directly from Raman lidar profiles by using lidar equation. A DIAL (DIfferential Absorption Lidar) analysis of the Raman shifts of N_2 (284 nm) and O_2 (277 nm), which occur on the steep side of the Hartley absorption band of ozone, is used to obtain ozone measurements. The Hartley absorption band of ozone with the Raman wavelengths indicated is shown in Figure 3.8. A measurement sensitive to atmosphere ozone density is obtained by taking the ratio of vibrational Raman shift of oxygen/nitrogen (277/284 nm) signals from the laser transmit wavelength at 266nm. The equations for the O_2 and N_2 signals,

$$P(l_{O_2}, z) = E(l_{266})x(l_{266})x_{O_2}(l_{O_2})\frac{ct}{2}\frac{A}{z^2}b(l_{266}, l_{O_2})\exp\left[-\int_0^z [a(l_{266}, z') + a(l_{O_2}, z')]dz'\right] \tag{3.7a}$$

$$P(l_{N_2}, z) = E(l_{266})x(l_{266})x_{N_2}(l_{N_2})\frac{ct}{2}\frac{A}{z^2}b(l_{266}, l_{N_2})\exp\left[-\int_0^z [a(l_{266}, z') + a(l_{N_2}, z')]dz'\right] \tag{3.7b}$$

are formed into a ratio to perform the DIAL analysis using the relationship,

$$\frac{P(l_{O_2}, z)}{P(l_{N_2}, z)} = \frac{x_{O_2}(l_{O_2})N_{O_2}(z)ds(l_{266}, l_{O_2})}{x_{N_2}(l_{N_2})N_{N_2}(z)ds(l_{266}, l_{N_2})}\exp\left[-\int_0^z [a(l_{O_2}, z') - a(l_{N_2}, z')]dz'\right] \tag{3.8}$$

Since the number densities of oxygen and nitrogen in atmosphere are well known, we can consider that $\frac{x_{O_2}(l_{O_2})N_{O_2}(z)ds(l_{266}, l_O)}{x_{N_2}(l_{N_2})N_{N_2}(z)ds(l_{266}, l_{N_2})}$ is a parameter defined by constant ratio of

oxygen to nitrogen molecules and the system, represented by k_{system}. Equation 3.8 can be simplified to the form,

$$\frac{P(l_{O_2},z)}{P(l_{N_2},z)} = k_{system}\exp\left[-\int_0^z [a(l_{O2},z') - a(l_{N2},z')]dz'\right] \\ = k_{system}\exp\left[-\int_0^z [a_{O3}(l_{O2},z') - a_{O3}(l_{N2},z')]dz'\right]\exp\left[-\int_0^z [a_{mol}(l_{O2},z') - a_{mol}(l_{N2},z')]dz'\right] \quad (3.9)$$

The number density of ozone within a scattering volume is calculated by removing the difference due to molecular scattering and then differentiating the integrated ozone number density,

$$[O_3(z)] = \frac{d}{dz}\left[\ln\left(\frac{P(l_{O_2},z)}{P(l_{N_2},z)}\frac{1}{k_{system}}\right)\left(\frac{1}{(s_{O3}(l_{N2}) - s_{O3}(l_{O2}))}\right) + \frac{(s_{mol}(l_{N2}) - s_{mol}(l_{O2}))}{(s_{O3}(l_{N2}) - s_{O3}(l_{O2}))}N(z)\right] \quad (3.10)$$

Differentiating the integrated ozone density from Equation 3.10 provides the ozone concentration profile in parts per billion (ppb) at each altitude after the first range bin. Measurements of the surface ozone from a point sensor can be used to initiate the calculation at the lowest altitude and thus extend the profile to the surface. It is interesting to note that the ozone result only depends upon the measured signal ratio and the laboratory values of cross-section of the Hartley band. Thus the primary limitation on the accuracy is the photon count level of the return signal, which can be improved with higher power laser and larger telescope. One example of ozone profile calculation result is shown in Figure 3.9.

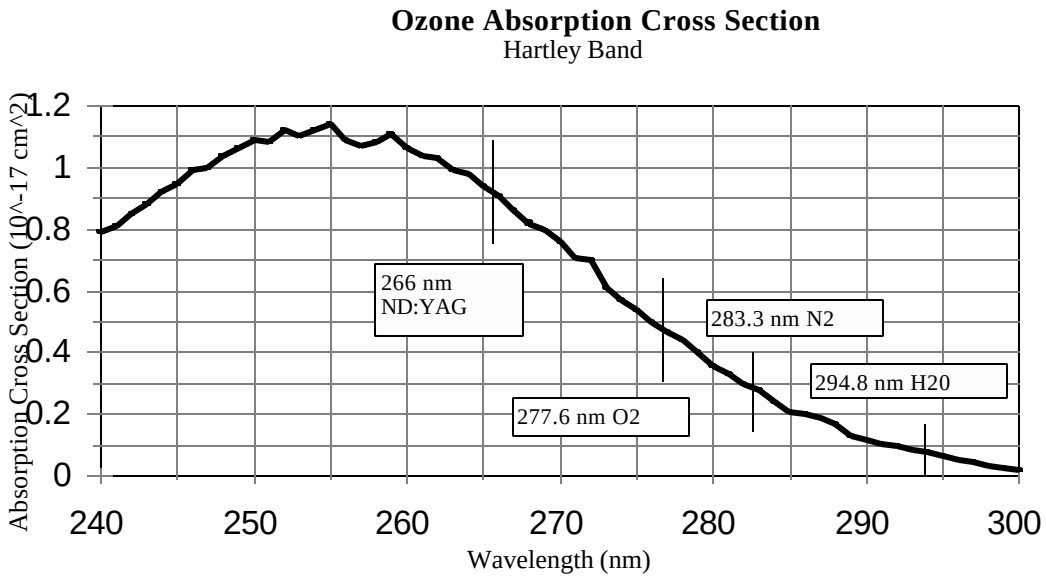

Figure 3.8. Hartley band absorption cross-section of ozone is shown with wavelengths associated with the lidar's 266-nm transmission and its Raman-shifted wavelengths [Philbrick, 1998a, Inn, et. al., 1953].

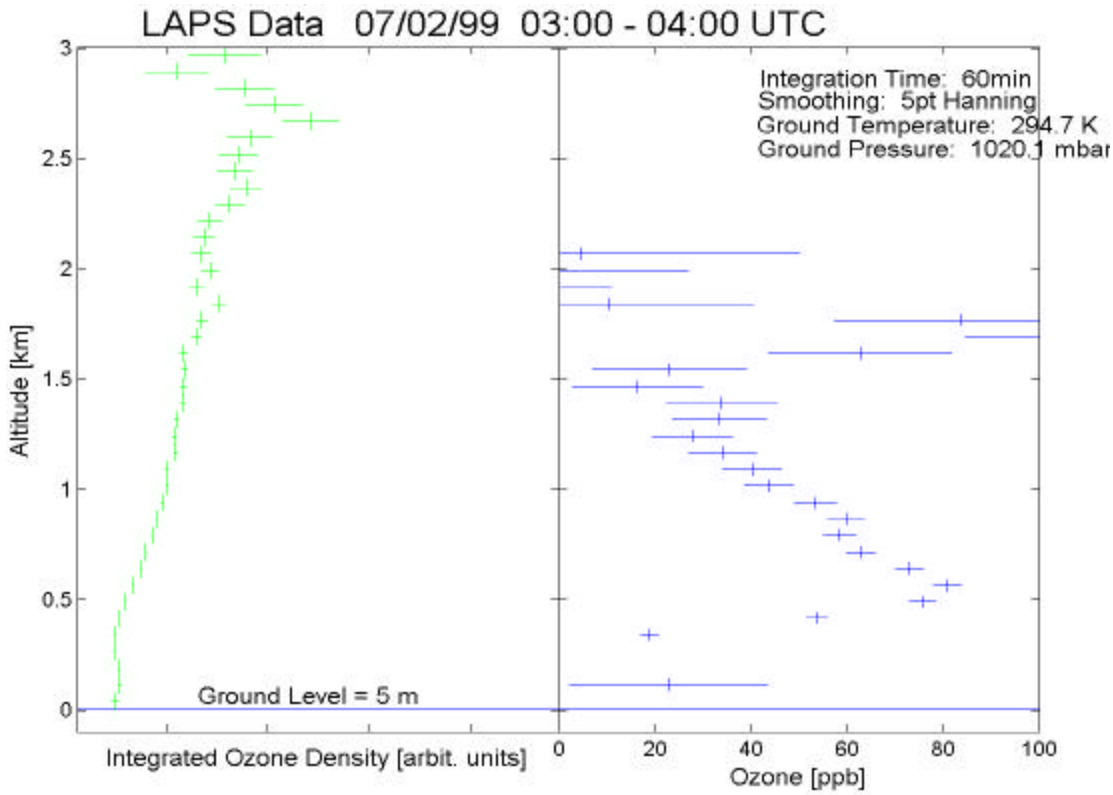

Figure 3.9. Example of one hour integrated ozone density and differential ozone profiles measured by LAPS on 07/02/1999 03:00 – 04:00 UTC, data is smoothed by 5 point Hanning filter.

CHAPTER 4

CA-Dust Measurement Campaign

4.1 Introduction

The primary objective of the California Dust Study was to carry out a field program to characterize the fate (deposition and transport) of PM emissions originating from the mechanical disturbance of surface soil. The program was undertaken because of a major discrepancy between the source estimate, and the measured mass of soil particulate. The measured mass distribution is too small compared with the source estimates. The results from the measurements were developed into a database which can be used to investigate the properties of dust plumes from soils. The tests included locally generated dust clouds to analyze optical scattering properties and the deposition algorithms for airborne particulate matter. The results from this experiment should help to resolve the existing discrepancy between the ambient measurements and source inventories of PM. The results from these measurements indicate that the discrepancy is due to the much shorter atmospheric residence time for the large mass particles than might be supposed from observing the optical scattering of dust from a source region. The results show that the optical backscatter from a dust plume provides small particle backscatters for a much longer period than the larger particle sizes remain. Since the large particles contain most of the mass, the plume image will indicate a larger source of particle mass than actually exists. The optical measurement of backscatter and extinction together with model simulations make this interpretation understandable.

4.1.1 Objective

The objectives of the study are:

- Generate and track airborne dust using lidar;
- Use several different soil samples and "quasi-monodisperse" particle samples to determine the deposition rate of soils and particles for different aerodynamic size;

- Develop algorithms to characterize the dust transport and fate.

4.1.2 Approach

The test plan included a one-week pilot study conducted in December 2000, and a two-week field measurement study in December 2001. The overall approach is to use the dust generation and airborne PM measurement methods to characterize PM emissions and their fate. Processes considered are those which are expected to be significant sources and sinks for geologic material generated as PM plumes. The project was carried out in the test area at the UCR agricultural field site near the University of California-Riverside campus because the generation conditions could be controlled. At this location, the eye safe backscatter LIDAR can be scanned without interference or obstruction over long paths to characterize the distribution of particulate matter. Tests are conducted by generating PM emissions to simulate emissions from vehicular travel on dirt roads and soil tilling operations. A series of individual test runs were conducted with data collected using real-time measurement methods.

4.2 Measurement Approach

Several instruments used for the primary and supporting measurements were transported to the UCR agricultural field site. After calibration and testing, a coordinated measurement program was conducted.

4.2.1 Portable Digital LIDAR (Dual Wavelength with Scanner)

The Portable Digital Lidar instrument, which is manufactured by Science & Engineering Services, Inc (SESI), is a two wavelength, scanning, aerosol lidar system. The detail information on this system has been described in section 3.2.

4.2.2 High Resolution Photography

A high-resolution video camera (Sony Digital DCR-VX700) was mechanically coupled to the lidar to document the distribution of the dust generated and to verify the

lidar position. Images are taken during each scanning test of lidar measurements. The camera follows the path of the laser beam to provide a clear picture of the area scanned. The scanning lidar with the camera is located at the typical position relative to the upwind generation point. The scan covers a region of about 10-30° on either side of the centerline between the lidar and the generation point. A digital inclinometer was mounted on the lidar to measure the elevation angle of the beam and its output recorded by the data computer.

4.2.3 Meteorological Sensors

Measurements for wind speed, wind direction, temperature, relative humidity and solar radiation were performed routinely through the test period. This system included an RM Young Type AQ wind speed and direction sensor mounted at a height of 10-meters. This system includes a propeller anemometer mounted with a wind vane. The wind speed and direction signals are received once per second by a Campbell CR10 data logger located at the base of the tower.

Temperature and dew point are measured using a power aspirated Climatronics sensor system at a height of 3-meters on the same tower.

Solar radiation is monitored using an Eppley model PSP radiometer. In order to locate this sensor where no shadows will pass over it, the radiometer is placed on a mast extending southward approximately 0.5 meters away from the tower at a height of three meters on the meteorological tower. The Campbell CR10 data logger located at the base of the tower also scans the signals from these sensors once per second. The Campbell data logger processes the scanned meteorological data into one-hour averages for the approximately two-month period that it operated prior to the study. During the dust measurement campaigns, the data logger processes the collected data into one-minute averages

4.2.4 Real-Time Point Monitors

An optical particle counter (OPC) is used to measure the particle count in sixteen different size ranges. The size ranges ("bins") cover a range from approximately 0.1

μm to a 20 μm using a Climet Model CI-500 instrument, which measures the particle count in the re-entrainment test chamber in real time.

Thermo Systems Inc. model 8520 DustTrak™ aerosol monitors are used to monitor the PM concentrations in the re-entrainment test chamber. Three DustTrak™ instruments are used to measure the light scattering intensity of the aerosols. These instruments provide data in 2-second intervals using inlets with particle cut points for PM_{10}, $PM_{2.5}$ and PM_1.

4.2.5 Integrated (Filter) Samplers

Two different types of PM samplers are used to measure the "total PM" and $PM_{2.5}$ (those particles less than 2.5μm effective aerodynamic diameter). For "total," a sample is drawn to the filter media without any size selecting inlet. This filter sampler operates at 16.7 L/min using a needle valve to control the flow. For $PM_{2.5}$, a Sensidyne model 240 cyclone sampling instrument with a flow of 113 L/min is used to provide the aerodynamic cutpoint. Filters used for both are ringed "stretched" Teflon filters (47mm diameter, 2 micron pore size Gelman Teflo's), selected for their low tare weight, mass stability and high collection efficiency at the sample flowrates planned for this program.

Filter weighing is performed at CE-CERT's filter weighing facility. The facility includes a room dedicated to filter weighing. There is approximately one cubic meter filter equilibration chamber which is humidity and temperature controlled in the room. A Cahn Model C-35 balance is contained in a laminar flow hood. The temperature and humidity in the laminar flow hood and equilibration chamber are controlled to 25°C and approximately 40% RH. Filters are equilibrated for 24 hours prior to the "blank" (prefield use) weighing and also prior to the "after" field use weighing. The balance used for filter weighing is calibrated with a 200mg class M NIST-traceable weight before and after each weighing session.

4.2.6 Soil Selection

The soil used for the "disking" (plowing) and "dirt road" dust generation portions of this program is the indigenous soil at the UCR Moreno Valley Agricultural Station. The soils that were entrained into the atmosphere using the centrifugal blower fall into two categories. The first category includes soils that are typical of those encountered in agricultural activities, especially those in the San Joaquin Valley (SJV). In addition to using soil from the Moreno Valley Agricultural Station, soils from three other University of California Agricultural Stations, located in different regions around the SJV were gathered to represent a cross section of soil types. A description of these soils is included in Table 4.1.

The second category is reference materials. These reference "soils" was used to characterize mixing, transport and fallout based predominantly on particle size. This category includes eight essentially monodisperse "soils" and one polydisperse indigenous test soil. The monodisperse "soils" were all calcium carbonate $CaCO_3$. $CaCO_3$ is widely used in the manufacturing of paper and paint and is crushed and ground to close tolerances for these manufacturing applications. $CaCO_3$ has a specific gravity of 2.7, which is similar to that of typical soils. For these reasons, using monodisperse $CaCO_3$ as a surrogate soil allows characterizing the mixing, transport and fallout of soil as a function of particle size. In order to aid in comparing and correlating the findings of this program to others, one soil, Arizona Road Dust, that has been used in many fugitive dust and dust entrainment studies was included in this program. A description of these materials is included in Table 4.1.

Table 4.1. Description of Soils (Main Study)

Soil Code	
1	CaCO3 with median particle diameter of 0.7 microns
2	CaCO3 with median particle diameter of 2 microns
3	CaCO3 with median particle diameter of 4 microns
4	CaCO3 with median particle diameter of 8 microns
5	CaCO3 with median particle diameter of 10 microns
6	CaCO3 with median particle diameter of 15 microns
7	CaCO3 with median particle diameter of 75 microns
8	CaCO3 with median particle diameter of 150 microns
9	Soil from UCR Moreno Valley Agricultural Station
10	Soil from UC Kearney Reseach Center, Parlier, CA; Hanford sandy loam
11	Soil from UC Shafter Reseach Center, Shafter, CA; Wasco sandy loam
12	Soil from UC West Side Reseach Center, Five Points, CA; Panoche clay loam
13	Arizona Road Dust

4.3 Methods

4.3.1 Particle Entrainment System (Chamber)

A 10 meters long resuspension chamber was constructed and used to allow measuring of the optical properties and settling times of the test soils as well as for lidar measurements of the optical scattering of the various samples, and to provide audit checks of the lidar. The particle entrainment test chamber shown in Figure 4.1 and Figure 4.2 was constructed for these tasks. Figure 4.1 shows a diagram of the setup of the experiment. Figure 4.2 shows pictures of the instruments and setup. The enclosed chamber has window openings on both ends to allow the lidar beam to pass through without obstruction. Three ports are located on the side of the chamber at different locations in the front, middle and end of chamber to permit drawing a sample from the chamber into real time integrating "point samplers" (optical particle counter, DustTrak® and "filter" samplers). A fourth port placed on the top of the chamber allowed introduction of dust samples into a blower that entrains the dust in the chamber. "Window fan" blowers placed in the chamber help keep the particulate matter entrained and maintain a homogeneous distribution in the air. Both end windows of the chamber can be closed to ensure a sealed environment while the "window fan" is on. The windows are opened after a brief mixing period to allow the

laser beam to pass through for measurements and to clean out dust samples between tests. The 10-meter chamber in Figure 4.2 (b), was oriented to align its axis with the laser beam, which is directed from a distance of 560 meters away. Three DustTrak instruments, were used to monitor the particle concentration at the front, middle and back end of the chamber with a two second resolution. The Climet particle spectrometer shown in Figures 4.2 (c) and (d) monitored the particles at the middle of the chamber, near the location where the sample was blown into the chamber.

Figure 4.3 shows changes of backscatter signal as a function of time for dust inside chamber during chamber Test #3 on December 19, 2001. The red signal has been magnified by 10 times to make the comparison. The sudden rise of signal strength indicates the time period while the chamber windows are open, after dust particles are blown into chamber. The fast drop in the red signal compared with the green signal represents the more rapid settling of the larger particles.

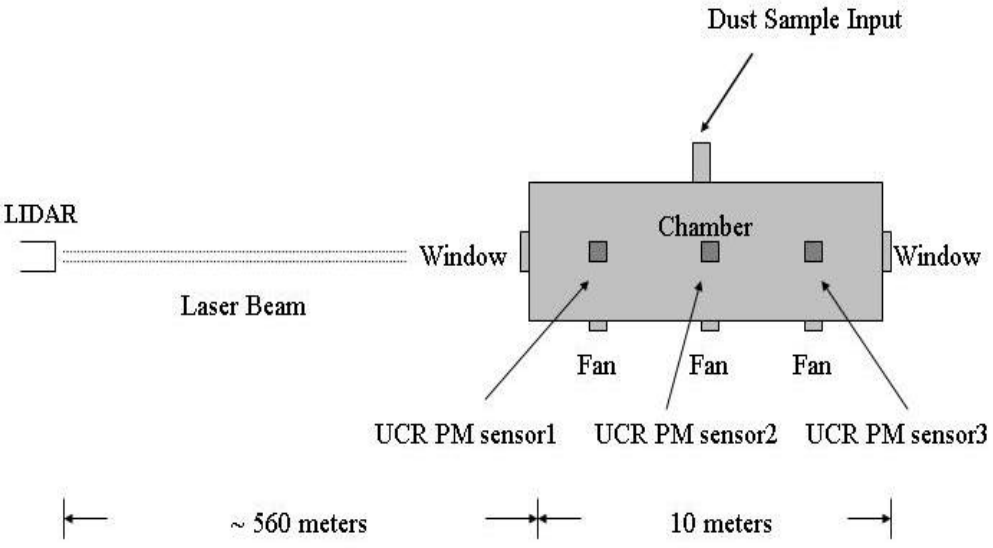

Figure 4.1. Particle entrainment system schematic .

(a)

(b) (c)

Figure 4.2. (a) View of the east side of 10 m chamber, (b) Front (west) and north sides of test chamber where samples are injected and measurements made, the chamber is shown together with instrumented meteorological tower, (c) DustTrak optical scatter instruments and Climet particle spectrometer (16 channels - 0.5 to 10 μm).

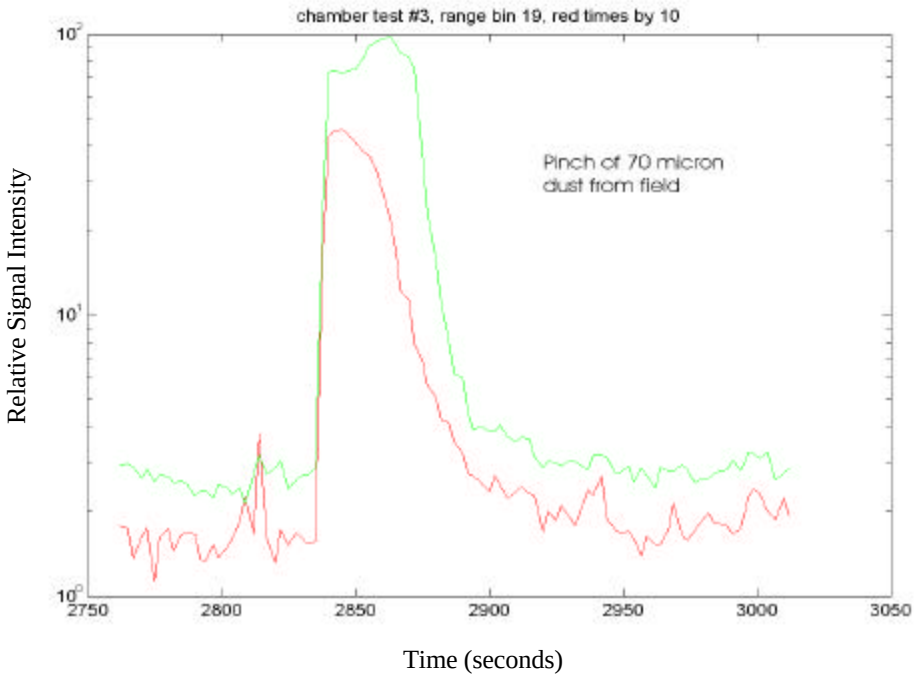

Figure 4.3 Example of the lidar return signal as a function of time during a chamber test shows the comparison of the 1046 nm signal (red curve has been multiplied by 10) with the 523 nm signal (green curve).

4.3.2 Dust Generation and Test Scenario

Several dust generation methods were used to measure plumes on open air paths during the study. The primary dust generator uses a 5 horsepower centrifugal blower to generate a dust cloud from the selected sample. Weighed amounts of selected indigenous, presieved soils and granulated materials of fine particle sizes were introduced into the blower. The blower expels these particles horizontally at a height of 1.5 meters. A second method of dust generation is to drive a vehicle in a straight line approximately 100 meters long or in tight circles ("doughnuts") approximately 30 meters in diameter. Dust plume was generated on "straight line" sections on a hard-packed dirt road, also "straight lines" and "doughnuts" were generated on the dirt field. The third method of generation includes "disking" the field with a tractor pulling a disk implement in a straight line approximately 100 meters long.

The test scenario for the blower generated dust plume is shown in Figure 4.4, where the lidar instrument with the digital video camera mounted on its top is observed

in the foreground. The dust generation equipment is located about half way between the lidar and the meteorological tower used for these measurements. The lidar was used to automatically make near horizontal scans of the test volume while the elevation angle was set to a value and could be adjusted manually.

Figure 4.4. The lidar with a digital camera scans dust cloud generated by a blower, the 10 m tower is located directly behind the generator, and the target board can be seen in front of trees on the far left.

4.3.3 Data Summary

·Pilot Study

For the initial Pilot Study, the dust generation and measurement instruments were setup on 13 December 2000. Measurements were made from 13 to 16 December 2000. Dust was generated and monitored during a total of twenty-two testing periods. Ten second average meteorological measurements, tracer gas releases, and optical measurements with digital video camera and lidar were conducted during the testing periods and meteorological data continued until 18 December 2000.

·Main Study

Lidar measurements were obtained during the Main Study from 8 December 2001 to 19 December 2001. Dust was generated and monitored for a total of 134 testing periods, which include 76 chamber tests for optical scattering investigations. Ten second average meteorological measurements, tracer gas releases and measurements with digital and video camera and with lidar were conducted on several days.

4.4 Measurement Results and Interpretation

The scanning lidar provides a unique opportunity to detect the distribution and evolution of airborne particulate matter. The optical signals from backscatter lidar are the most sensitive way of detecting the airborne particulates because the signals from accumulation mode and course mode particles have high scattering cross-sections for the visible and near infrared wavelengths. Little work has been done in the past to take advantage of the scientific benefit that can be gained from the application of laser remote sensing techniques to investigate airborne particulate matter. The advantages of optical techniques are many, however, several technical issues needed to be concluded in order to achieve results that can be properly interpreted. One challenge for modeling and interpretation of results is that the classical solutions from Mie scattering theory begin to breakdown for irregular particle sizes above about 1 μm. The analysis then requires more complicated mathematical solutions such as those associated with T-matrix analysis, Monte Carlo calculations, or other techniques. The analysis is further complicated by the range of different values for the complex index of refraction for crustal materials. The larger values of the complex index of refraction cause significant absorption of the incident radiation and lead to an even more complicated analysis. The ultimate goals of this project lead to the development of an empirical model which would be able to predict the characteristics of dust including the settling rate and dispersion, as well as the other factors effecting on the distribution of particles and their airborne lifetime for the prevailing meteorological conditions.

4.4.1 CCD camera data

The digital CCD camera provides a useful documentation of the sequence of events during a test period. The images provide a time sequence showing the early evolution of the cloud and the pointing location of the lidar. Information on the location and spatial extent of the dust cloud can be extracted from these images. In Figure 4.5, a set of example results are shown for one of the tests that uses the scene extraction techniques during the Pilot Study on 15 December, 2000. The spatial dimensions indicating growth or drift of the cloud can be extracted. It is also possible to determine the optical depth of the cloud relative to the background scene at times and locations where the path is not optically thick. Figure 4.5 shows a time sequence of CCD images of one of the tests compared with the corresponding images when the background is removed. This gives some indication of the way in which the digital images are used to determine dispersion rates.

4.4.2 Lidar Vertical Profiles (Pilot Study, 2000)

Figure 4.6 shows an example of vertical profiles obtained during the pilot study on 13 December 2000 for the green and NIR channels when the instrument was pointed on an elevation angle of 70^{o}. The data has been range corrected for $1/R^2$ dependence and translated to a vertical altitude scale, but no other corrections have been applied. The telescope form factor is observed distorting the profile at near ranges. The top of the planetary boundary layer (PBL) is clearly evident in both the green and red channels. The green signal is large compared with the NIR signal as we would expect when most of the contribution to the scattering is from small particles. The shape of the vertical scattering profile is that expected for a well-mixed atmosphere that is relatively clean, however, the low altitude signal is distorted by the telescope form factor.

Figure 4.5. Test 18 (12/15/2000 14:30) generate dust with vehicle, this is time sequence of CCD images along with the corresponding background removed images: (a) 14:31:37 (b) 14:32:36 (c) 14:32:49 (d) 14:33:14.

The increase in the signal versus altitude is due primarily to the fact that the particles grow larger by adding water as the temperature decreases at increasing altitude. Because the water vapor is uniformly mixed during the afternoon, the relative humidity must increase as a function of altitude and that increase on relative humidity causes growth in the size of the particles. The optical scattering is proportional to $\sim R^6$ for particles which are smaller than the wavelengths, and we expect that hydroscopic molecules will grow to cause more optical scattering toward the top of the boundary layer.

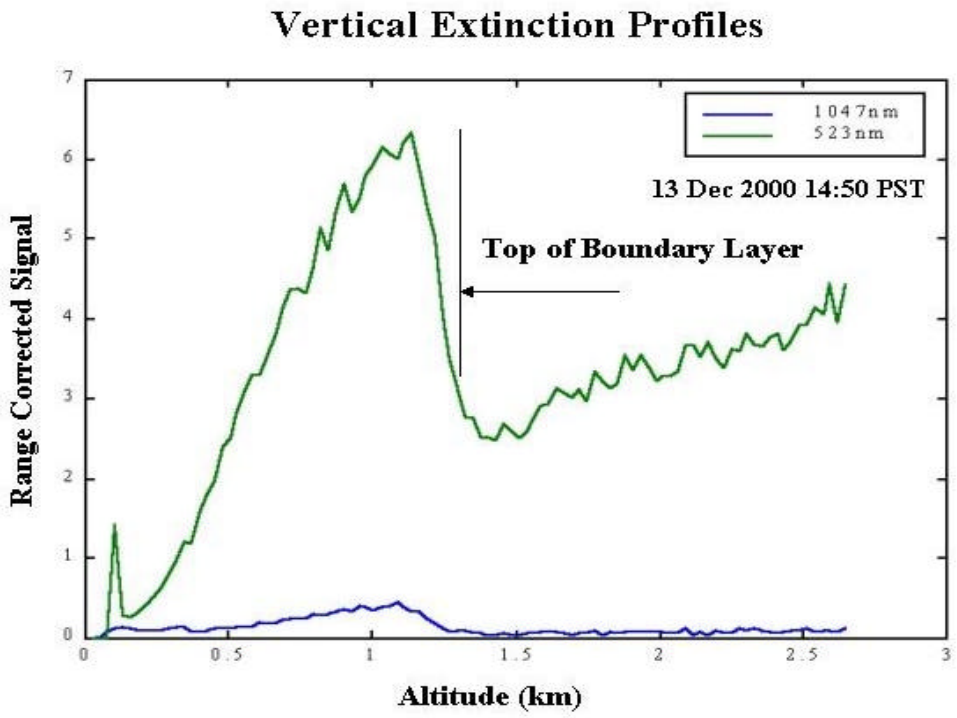

Figure 4.6. Vertical profile (elevation angle 70°) during period of afternoon convection shows the top of the boundary layer near 1300 m.

During the last couple of days of the testing period of pilot study, a Santa Anna wind storm developed. Figures 4.7 and 4.8 show the results from horizontal and vertical profiles during the Santa Anna conditions on 18 December, 2000. Both sets of figures show the effectiveness in dust being picked up by the wind shear near the surface and then being distributed up to about 700 m altitude. The fact that the visible scattering signal is so much larger than the red signal indicates that most of the scattering is associated with particles smaller than 1 μm.

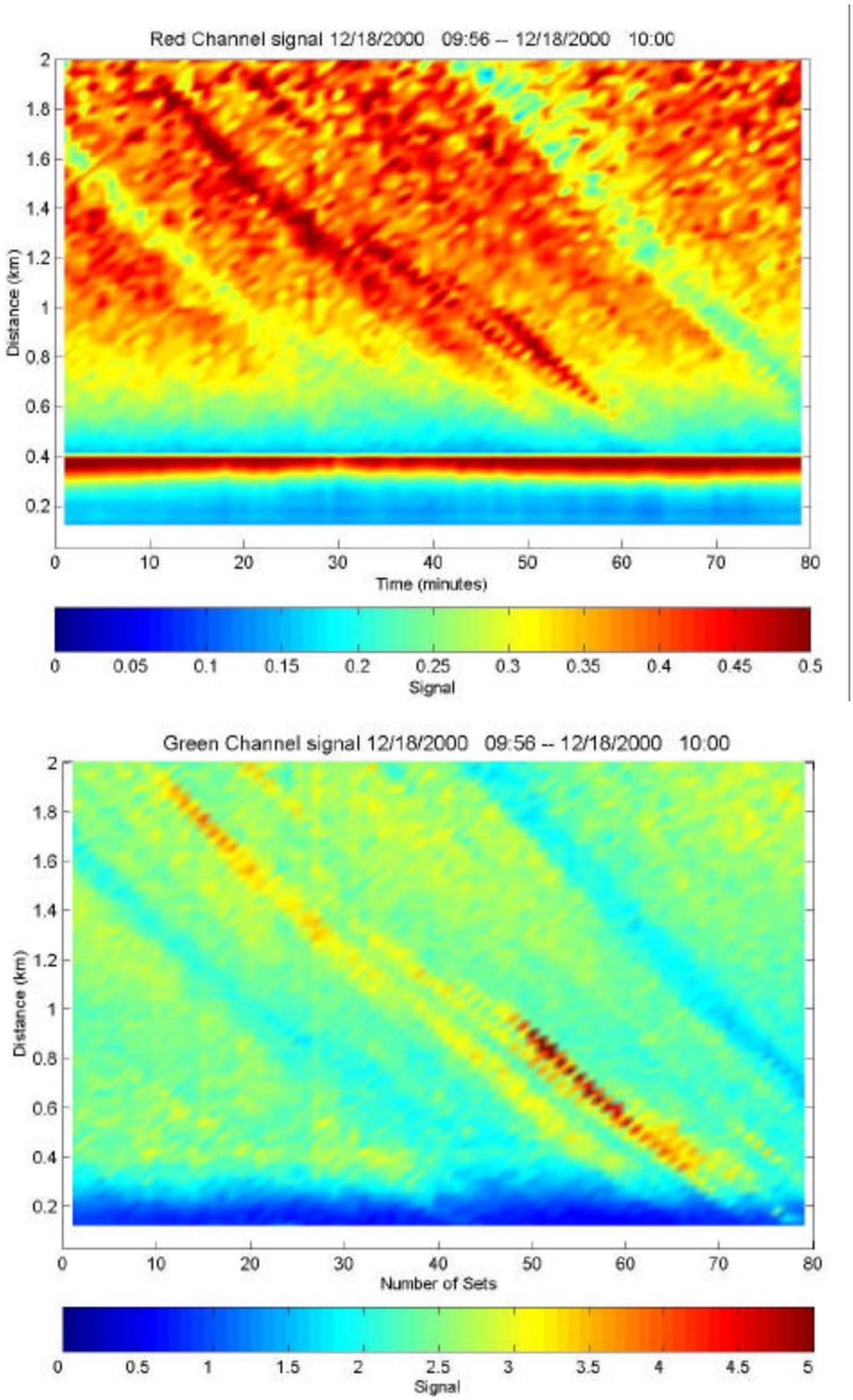

Figure 4.7. Horizontal scan profiles of raw data plots showing dust plumes were generated by the large wind shear at the surface during the Santa Anna on 18 Dec 2000.

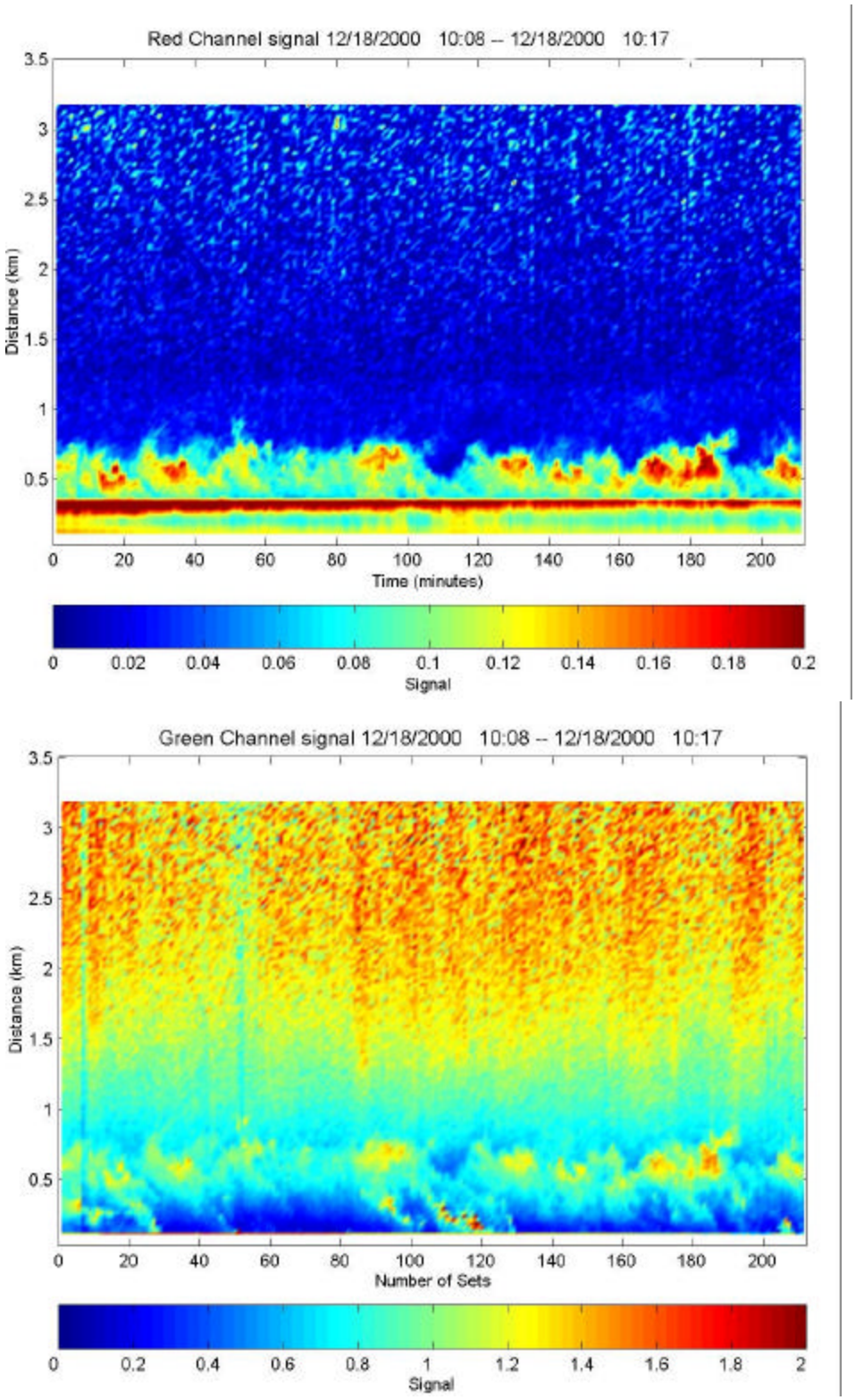

Figure 4.8 Vertical profiles show dust plumes between surface and 700 m. The raw signals have only been range corrected and thus the signal at higher altitude appears larger due to the effect of the telescope form factor (the red channel shows an instrument artifact near 400 m).

4.4.3 Chamber Test Results (Main Study – 2001)

Figure 4.9 shows an example of variation of lidar return signal after the sample dust was puffed into the chamber for Test #35 on 19 December 2001. Test #35 used a 0.7 µm calcium carbonate ($CaCO_3$) sample containing 800 mg of material. The raw data has been range corrected and normalized to remove molecular scattering and the telescope form factor. As shown in the figure, a strong backscatter signal is obtained from the material in the chamber, which is located about 566 meters from the lidar. The target board was placed behind the chamber, at a distance of 800 meters away from the lidar. At time 07:42:00, the chamber was closed and the lidar signal is blocked by the chamber. And for that reason, we don't have backscatter signal from the target board, which is beyond chamber. One minute later, (time 07:42:56), the chamber was opened and returns are obtained from both inside chamber and target board. As shown in the figure, the dust injected into the chamber settles out rapidly during the first minute after the chamber was opened.

Figure 4.10 shows comparison of DustTrak PM measurements with Climet Instrument particle size distribution on 19 December, 2001 during the several tests conducted in the early morning period 5:20-8:00 PST. The Climet PM result is calculated from size distribution data and is shown in Figure 4.10 (a). Since the Climet spectrum was obtained during a one minute sample period, the DustTrak data (obtained with a two second period) was averaged for the same one minute period to compare with the value reported by the Climet instrument, and the Climet results were integrated for particles less than 10 µm. The Climet size distribution instrument has the capability of measuring particle size concentrations for 16 size ranges from 0.7µm to 15µm, and the results can be used to calculate the integrated mass concentration of PM10 and PM2.5 for comparison with DustTrak PM measurements. An example of the comparison is shown in Figure 4.10 (a). Figure 4.10 (b) shows the linear regression comparison of the results in log scale from the average of the three DustTrak PM sensors and the Climet PM. The correlation coefficient is around 0.81 between the DustTrak and Climet measurements. As shown in Figure 4.10 (a), the

comparison between these results was quite good and generally agreed within 5%. These instruments are capable of measuring particles less than 20µm (Climet) and 10µm (DustTrak).

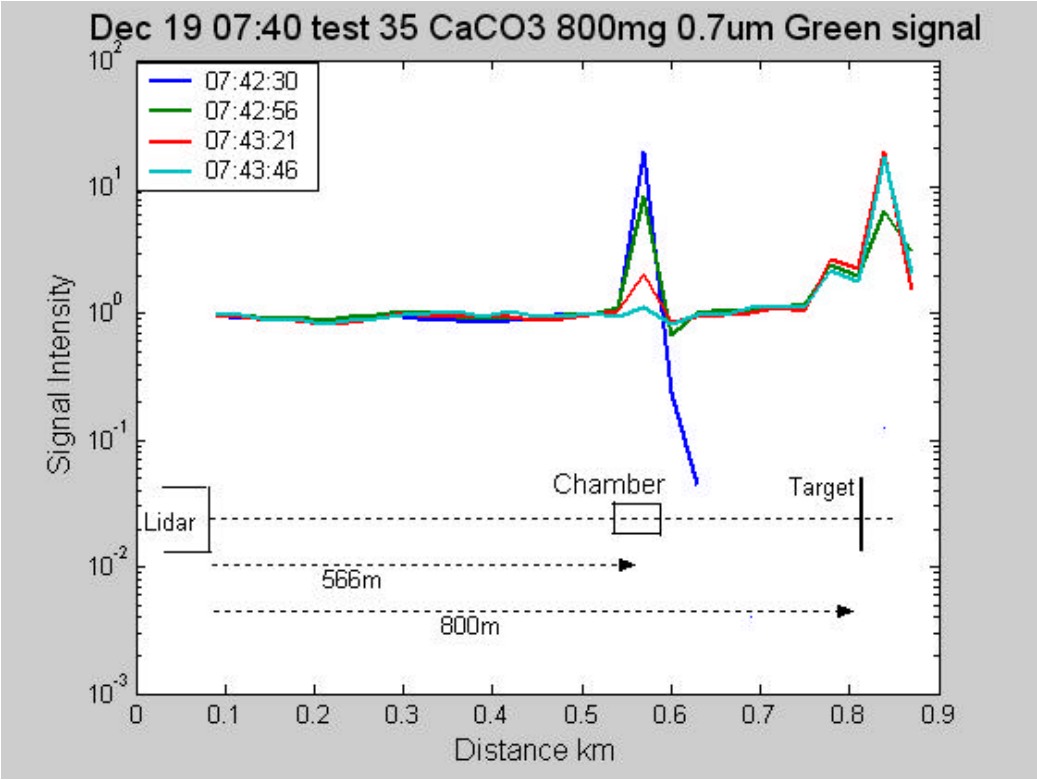

Figure 4.9. The lidar return signal at the visible wavelength resulting from a dust sample of 800mg of $CACO_3$ at size 0.7 µm during Chamber Test #35 19 December 2001.

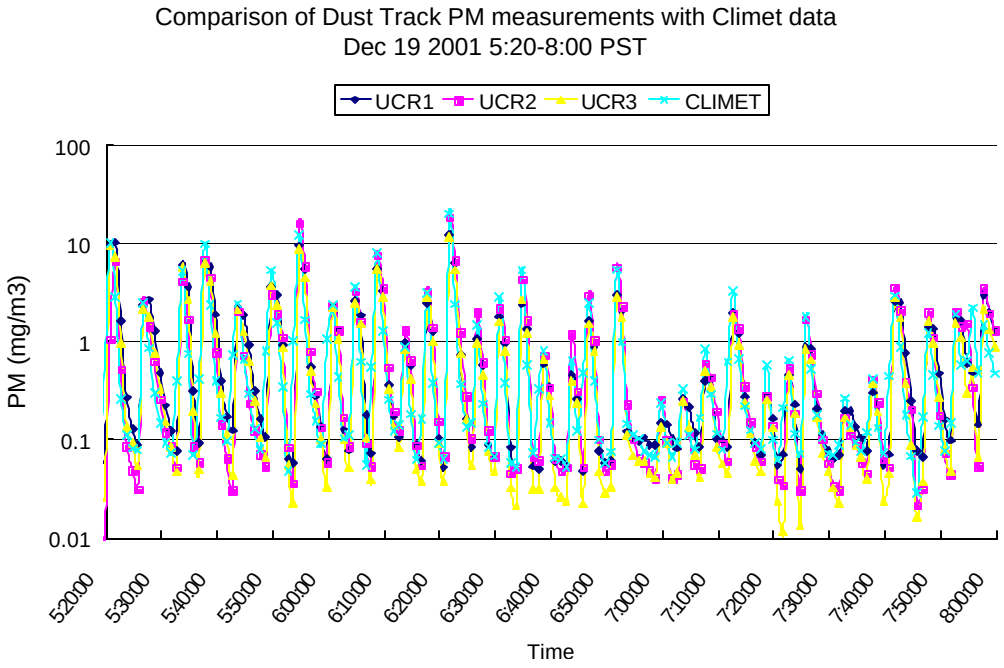

(a)

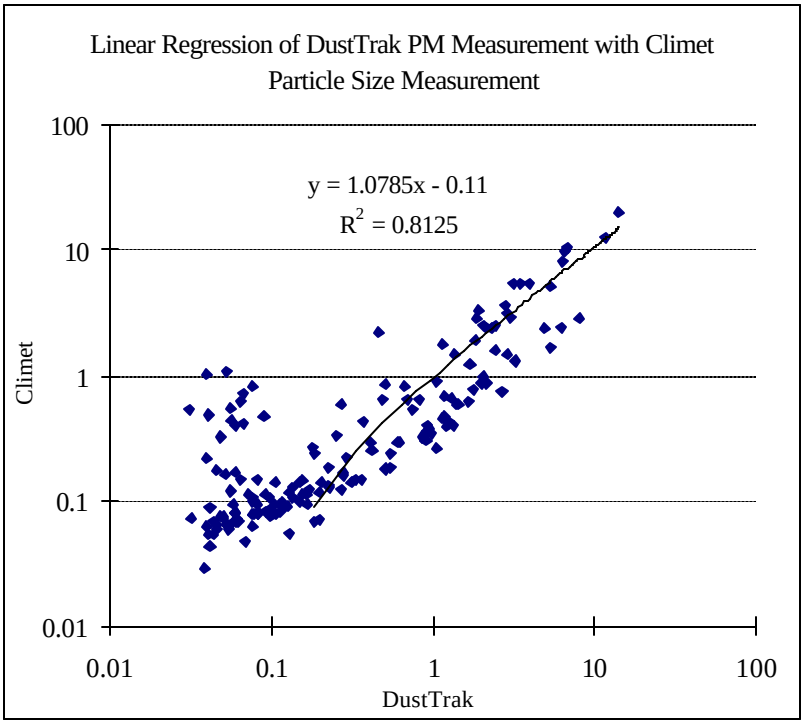

(b)

Figure 4.10. Summary of aerosol chamber tests on 19 December 2001 5:20-8:00. (a) Comparison of DustTrak PM measurement with Climet particle size distribution measurement, (b) Linear regression of averaged DustTrack PMmeasurement with Climet particle size distribution measurement.

Examples of the particle size spectra are shown in Figure 4.11 from the tests using

200 mg $CaCO_3$ crush samples and different soil types measured on 19 December 2001. It is apparent that the 0.7µm sample is an anomaly in this set because the observed signal is small. The low concentration is also observed in the DustTrak results which show excellent agreement for the integrated mass density of particles less than 10 µm from the Climet instrument. The lower particle concentration observed in the 0.7 µm tests is consistent with the idea that we are experiencing a loss of the small particles adhering to the plywood sides of the chamber, and thus being immediately lost from the volume as the circulating fans distributed the sample in the chamber. Examination of Figure 4.11 shows that the relative signal does change as expected for the other size distributions measured.

The results shown in Figure 4.12 provide the Climet particle spectra for the several types of soils measured during the chamber tests. Soil samples included local sifted field soil and soil samples from several California sites, including Shafter, Westside and Kearney locations. In addition, the results from 2 and 10 µm samples of $CaCO_3$, and samples of standard Arizona Road Dust were measured, and the results are shown in Figure 4.12. It is obvious that the $CaCO_3$ samples contain a larger relative concentration of the smaller particles than do the soil samples. Also the Arizona Road Dust contains a larger fraction of small particles than any of the other soil samples.

Examples of the particle size spectrum are shown in Figure 4.13 from the Climet instrument of the 0.7 µm $CaCO_3$ sample. A two component log-normal distribution has been fit to the measured spectrum. Also, the chamber measurements of the 0.7 µm sample depicted in Figure 4.13 are shown in Figure 4.14 with distributions for both mass density and number density. We used the particle spectrum shown in Figure 4.14 to calculate the expected optical signal and examined that case as the larger particle sizes are successively removed from the distribution in an analysis described below. The two component log-normal distribution fits of the particle size spectrum from the Climet instrument of the 2 µm, 4 µm and 10 µm $CaCO_3$ samples are shown in Figure 5.15, Figure 5.16 and Figure 5.17, respectively. Notice that the two component log-normal distribution has been shown in figures of each chamber tests.

These results from chamber tests will be used later in the analysis of field tests and for constructing a model for the settling of different size particles. As result of simulation, the size distribution model for 10 µm $CaCO_3$ sample is very close to the model for 4 µm. This is due to the larger than 10 µm particles inside the chamber settle out in less than 1 minute and is not detected by the particle size instrument. However, this will not take significant effect to our modeling result because the larger size particles contribute little to the scattering.

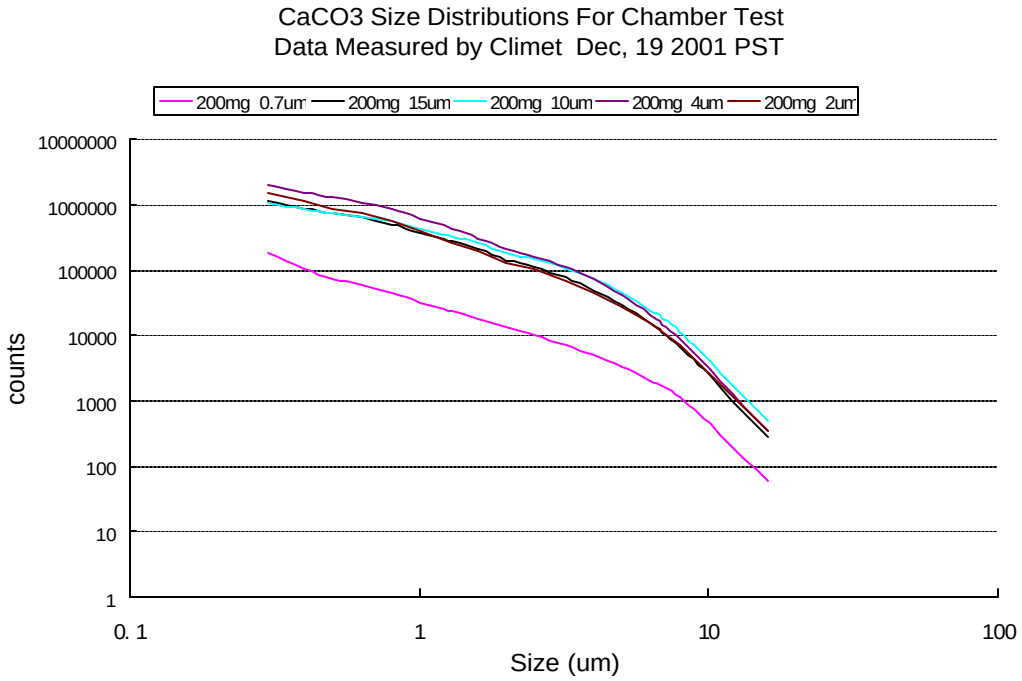

Figure 4.11. The Climet spectrum of the particle counts versus particle size for the several samples of different sizes of $CaCO_3$ power that were tested. Notice that the 0.7 µm case is an anomaly (see text) and the other samples do show a change that agrees with the increasing particle size in the samples.

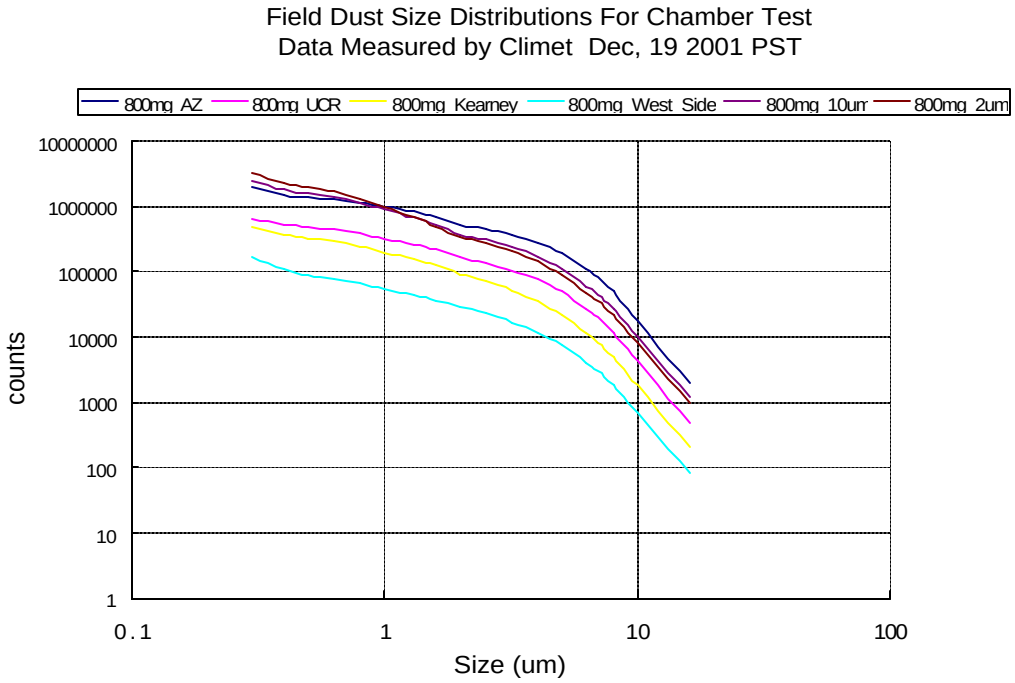

Figure 4.12. The Climet particle size spectra for the several different types of soil and powder tested are compared.

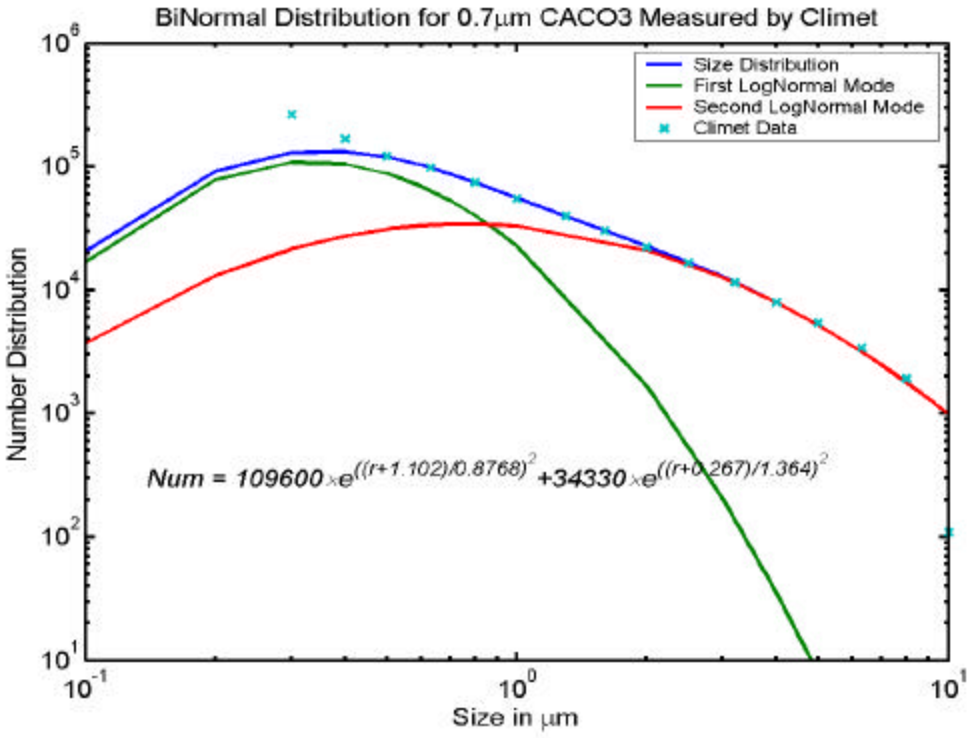

Figure 4.13. The log-normal distributions for a two component models are fit to the Climet instrument measured result for the 0.7 μm sample of $CaCO_3$.

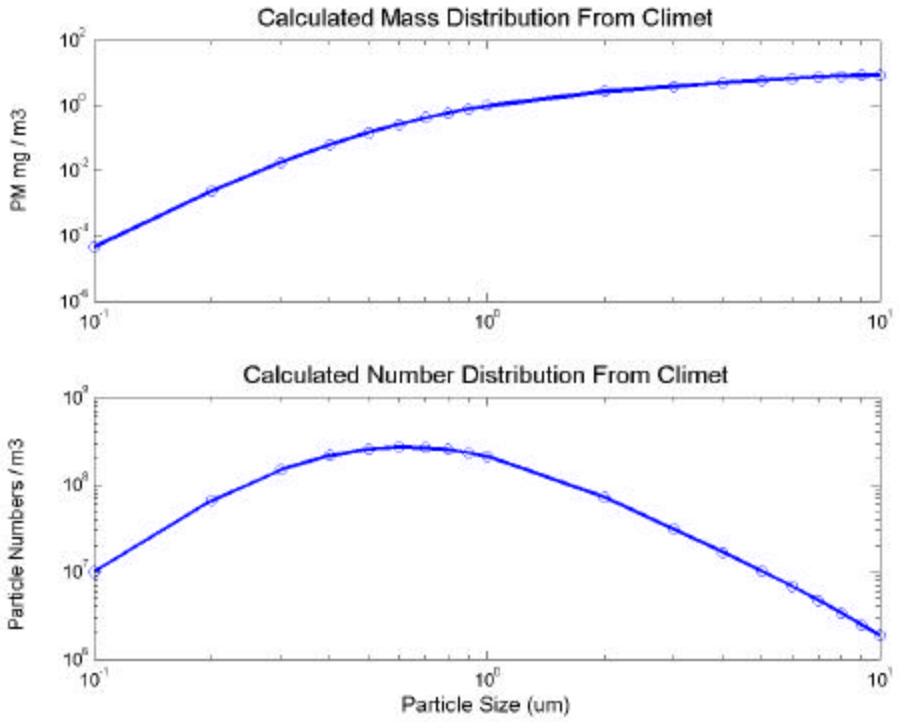

Figure 4.14. The Climet spectrum for the 0.7 µm sample of the $CaCO_3$ dust corresponding to Figure 4.12 displayed as number density and mass density.

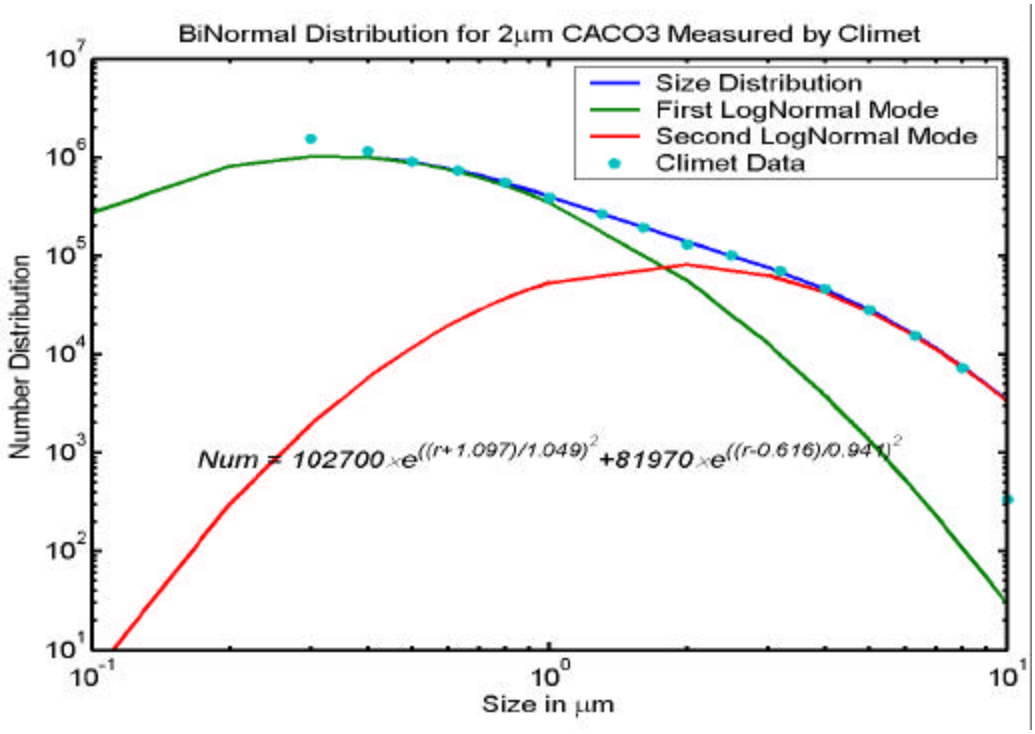

Figure 4.15. The log-normal distributions for a two component model are fit to the Climet instrument measured result for the 2 µm sample of $CaCO_3$.

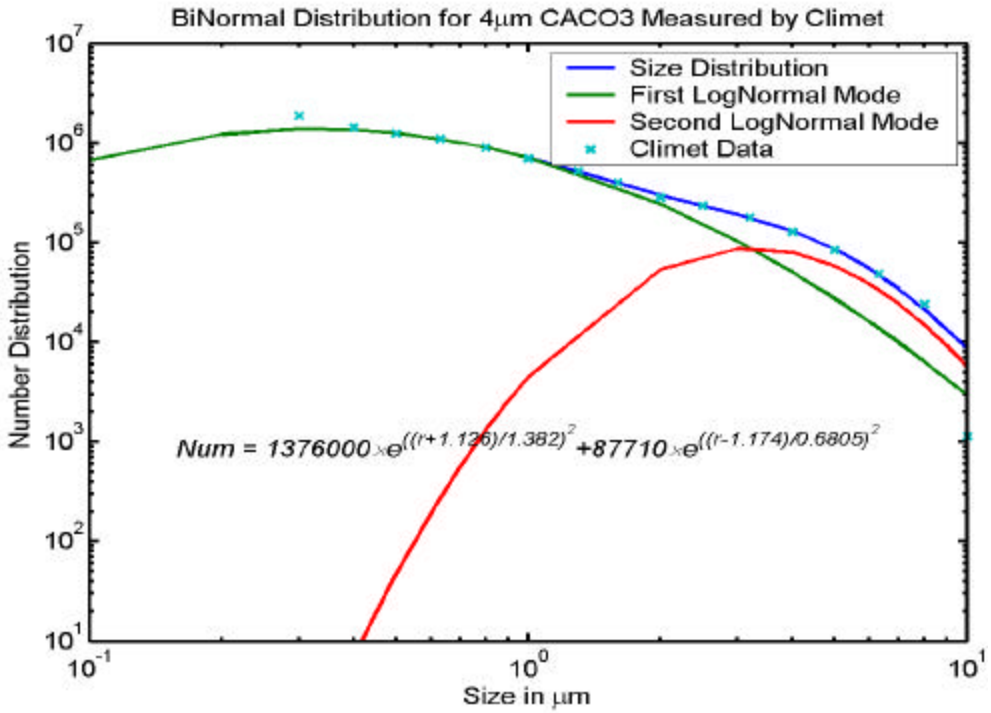

Figure 4.16. The log-normal distributions for a two component model are fit to the Climet instrument measured result for the 4 μm sample of $CaCO_3$.

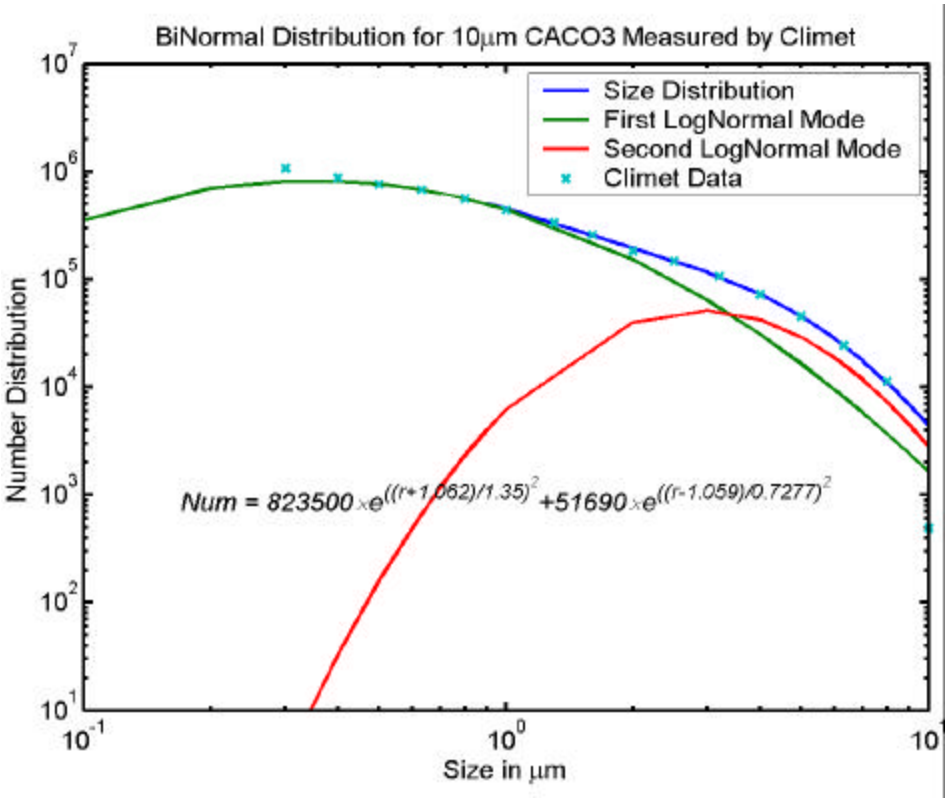

Figure 4.17. The log-normal distributions for a two component model are fit to the Climet instrument measured result for the 10 μm sample of $CaCO_3$.

The upper panel of Figure 4.18 shows the signal return from the closed end on the chamber near 05:44, 05:50 and 05:55. When the chamber is opened, the lidar signals from scatter by from the dust in the chamber and from the target board are observed. The fact that the return from the end of the closed chamber is less than the return from the target board is due to the higher reflectivity of the white target board. Since the chamber is only 10 meters in length (corresponding to only 1/3 of one range bin), the extinction signal is relatively weak and the hard target return is the only practical way to observe any extinction signal. Examination of the signals of the target board return shows that the extinction corresponding to the dust path can be detected but the signal is weak. For example, the upper panel of Figure 4.18 at 05:51 (test #11) shows an extinction signal corresponding to the same time as the larger return from the backscatter signal. The lower panel of Figure 4.18 shows the three DustTrak measurements (front, middle and back of chamber) together with the lidar signal return, which has been normalized using measurements of the clear atmospheric path before the test. The lidar signal in the chamber is high before opening due to the back scatter from a cardboard cover placed on the front of the chamber. The backscatter from the dust is measured when the path is open, however the concentration within the chamber volume is not sufficient to measure the path extinction in the signal using the target board. A comparison of these three tests (#10 - #12) shows some difference in the settling rate of the dust. The increase in signals with increasing sample size is easily observed.

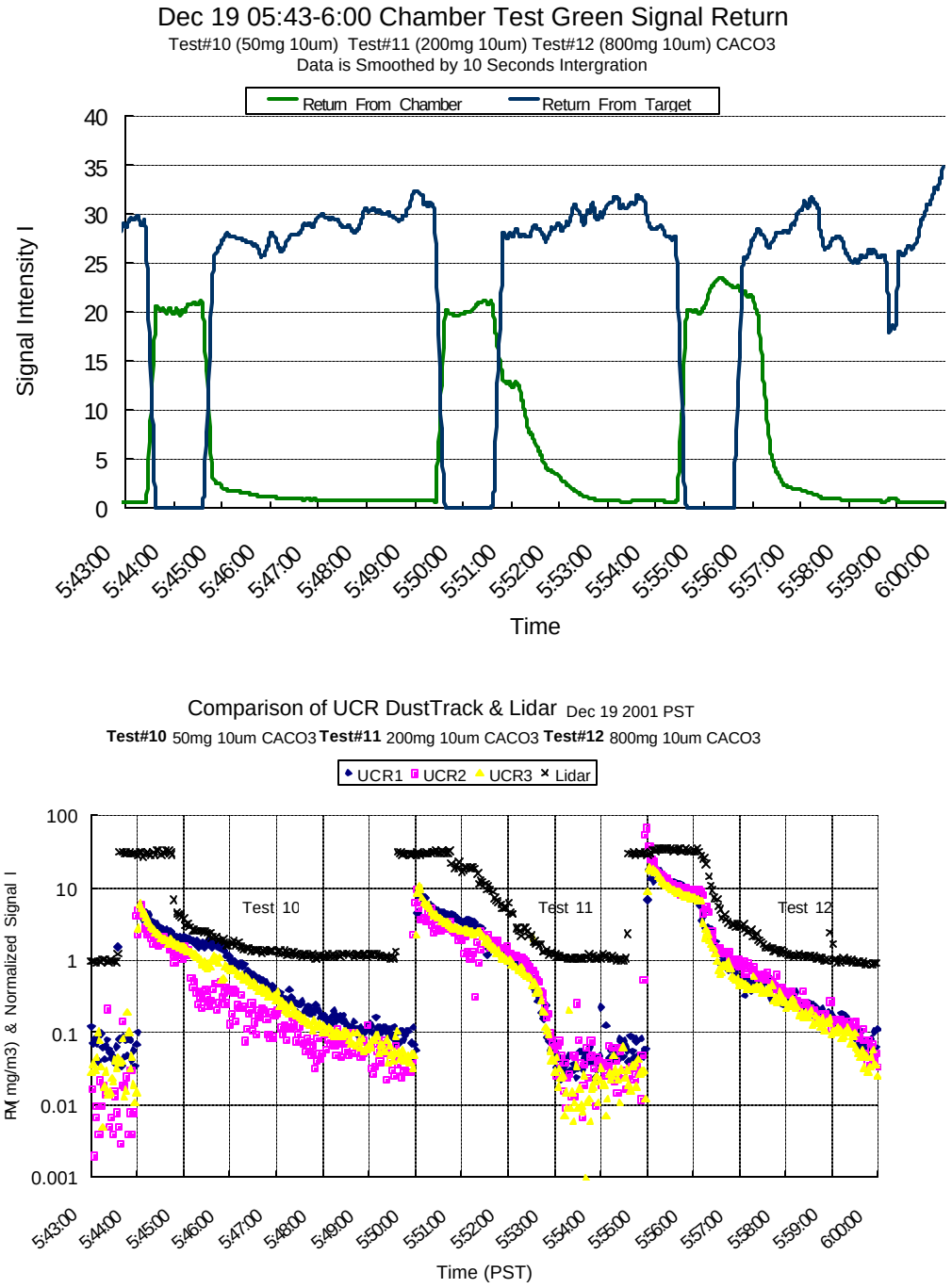

Figure 4.18. Chamber test measurements from Tests #10, #11 and #12 are shown. Upper panel shows the raw signal returns from the lidar at the range intervals corresponding to the chamber and the target board. The lower panel shows the signal from the DustTrak instruments and the normalized lidar return.

Ratio of the Red and Green Signal

The PDL Lidar uses two backscatter channels, one is the red signal at 1046nm, and the second is the green signal at 523nm. The ratio of the two return signals is used to investigate the concentration distribution and interpret information on the particle size.

Before comparing the results from two different wavelengths, the signal is normalized to remove system parameters. Since the experiment is carried out in a closed chamber, the signal return of one range bin before the chamber can be used as reference to normalize the signal. From the Lidar Equation in section 3.3, the signal return from inside chamber can be written as,

$$P(\lambda, z) = E_T(\lambda_T) x_T(\lambda_T) x_R(\lambda_R) \frac{ct}{2} \frac{A}{z^2} b(\lambda) \exp\left[-2\int_0^z a(\lambda, z')dz'\right] \tag{4.1}$$

The normalized chamber return of the two wavelengths are given by

$$P_N(\lambda_G) = \frac{P(\lambda_G, z_c)}{P(\lambda_G, z_c - d)} = \frac{(z_c - d)^2}{z_c^2} \frac{b(\lambda_G, z_c)}{b(\lambda_G, z_c - d)} \exp[-2a(\lambda_G)d] \tag{4.2}$$

$$P_N(\lambda_R) = \frac{P(\lambda_R, z_c)}{P(\lambda_R, z_c - d)} = \frac{(z_c - d)^2}{z_c^2} \frac{b(\lambda_R, z_c)}{b(\lambda_R, z_c - d)} \exp[-2a(\lambda_R)d] \tag{4.3}$$

where z_C represents the chamber position, d is the bin range, which is 33.33 meters for this experiment. $P(\lambda_R, z_c)$ and $P(\lambda_R, z_c - d)$ represent signal returns from chamber and one bin range before, respectively. The factor $\exp[-2ad]$ is the attenuation in one range bin, and it is negligible in this case. Since the dust scatter result is limited to the path in the chamber, $b(\lambda_G, z_c - d)$ and $b(\lambda_R, z_c - d)$ can be first considered to be due to molecular scattering only. Note that $P_N(\lambda)$ represents normalized signal. We have to normalize the signal to eliminate the system sensitivity to different wavelengths. Therefore, the scattering from different wavelengths can be compared to study the optical properties of particles. Then the signal ratio of the two wavelengths can be then written as,

$$\frac{P_N(\lambda_G)}{P_N(\lambda_R)} = \frac{b(\lambda_G, z_c)}{b(\lambda_R, z_c)} \frac{b_{mol}(\lambda_R)}{b_{mol}(\lambda_G)} \tag{4.4}$$

Note that the ratio of molecular scattering coefficient $\frac{b_{mol}(l_R)}{b_{mol}(l_G)}$ can be calculated by Mie scattering theory, the value is 16.

Theoretical calculation of the ratio of backscattering coefficient of 523nm and 1046nm is shown in Figure 4.19. Since the dust samples are rather size distributed spectra instead of single sizes, we applied Gaussian filter to smooth the result. If we made the assumption that the signal return path is clear, that is, only molecular scattering occurred outside chamber, then the normalized signal ratio will be very close to 1, when the chamber is clear. This assumption is not possible in the real world, because fine mode particles will stay in the air for relatively long time, and aerosol scattering must be taken into account even outside the chamber. Ratio of backscatter coefficient will be changed into $\frac{b(l_G,z)}{b(l_R,z)}\frac{b_{mol+aer}(l_R)}{b_{mol+ser}(l_G)}$. We have assumed that the aerosols outside chamber have a uniform distribution with particle size of 0.1μm. The reference value $\frac{b_{mol+aer}(l_R)}{b_{mol+ser}(l_G)}$, calculated by Mie scattering theory, will change to approximately 6.11 according to the assumption we made. This second assumption is proved later to be successful for representing the real situation in the chamber tests. The simulation result is shown in Figure 4.20. As indicated in the figure, if only fine mode aerosols (< 0.1μm) stay in the atmosphere, the ratio of the backscatter coefficient of 523nm and 1046nm is about 1.5.

The results of the ratio $\frac{P_N(l_G)}{P_N(l_R)}$ from chamber tests are shown in Figure 4.21. Here we have chosen the tests during the morning of December 19, 2001. The different sizes of $CaCO_3$ from 0.7μm, 4μm and 10μm tests were picked for comparison. After comparing with the theoretical result in Figure 4.20, we can observe the particle size change in the chamber as a function of time.

In Test #35, 0.7 μm particles were released, the backscatter ratio gradually decreases from 1.5 to about 0.5. After releasing, the particles starts to settle out, the

backscatter ratio gradually increases back to 1.5. If we compare it with the curve of the backscatter ratio in Figure 4.20, the value 1.5 represents a clear chamber, that is the time we start releasing. The value increasing from 0.5 to 1.5 represents the chamber clearing process and indicates that the larger particles, for example, this would be the case when those in the 0.3 μm to 1 μm range, settled out and only smaller sizes (< 0.3μm) remained in the chamber. The correlation of the ratio with the particle sizes can also be observed in Test #9, Test #11 and Test #6, which are 4 μm, 10 μm and 2 μm size releases, respectively. In Test #9, 4 μm particles were released, the backscatter ratio gradually decreases from 1.4 to about 0.4, then increases to around 0.7 and stay in this value for several minutes. In Test #11, 10 μm particles were released, the backscatter ratio gradually decreases from 1.5 to about 0.7, then suddenly decrease to the value below 0.1 after about 4 minutes. However, it is very hard to tell whether this decrease (< 0.1) is due to the larger size particles were observed, or off alignment of the laser beam. In Test #6, 2 μm particles were released, the backscatter ratio gradually decreases from 2.5 to about 0.5. We notice that the backscatter ratio is around 2.5 instead of 1.5 before release when the chamber is clean. This could be due to a problem when normalizing the signals caused by the assumption that the aerosols outside chamber have a uniform distribution with particle size of 0.1μm. The value of the normalized backscatter ratio for clear chamber will be larger if larger size particles exist outside chamber. During Test #35 of 0.7 μm release, the ratio increases back to 1.5 after around 4 minutes, that indicates the cleaning out procedure of released particle. However, the particle settling out procedure can not be observed during the other tests of larger size releases. This is consistent with the idea that the small particles adhere to the plywood sides of the chamber, and thus being immediately lost from the inside of the chamber.

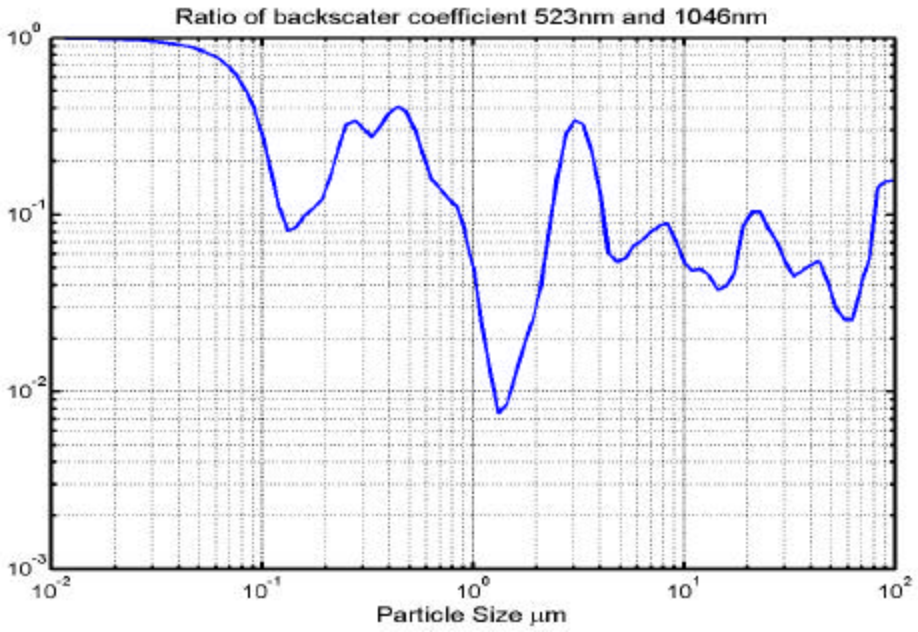

Figure 4. 19. Ratio of backscatter coefficient $\frac{b(l_G,z)}{b(l_R,z)}\frac{b_{mol}(l_R)}{b_{mol}(l_G)}$ after smoothing with a Gaussian filter assuming a clear optical path (no aerosol).

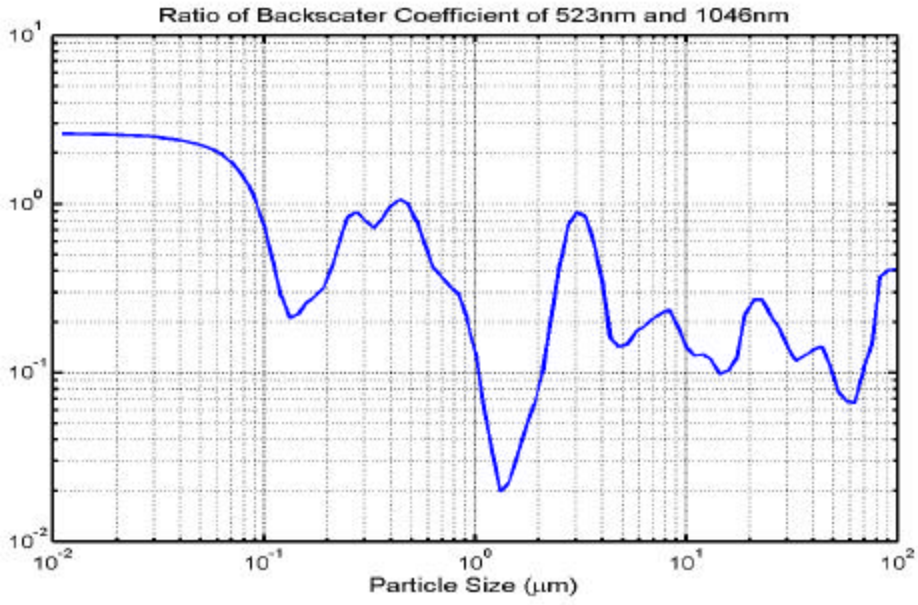

Figure 4. 20. Ratio of backscatter coefficient $\frac{b(l_G,z)}{b(l_R,z)}\frac{b_{mol+aer}(l_R)}{b_{mol+aer}(l_G)}$ after smoothing with a Gaussian filter assuming that there are fine mode aerosols in the optical path.

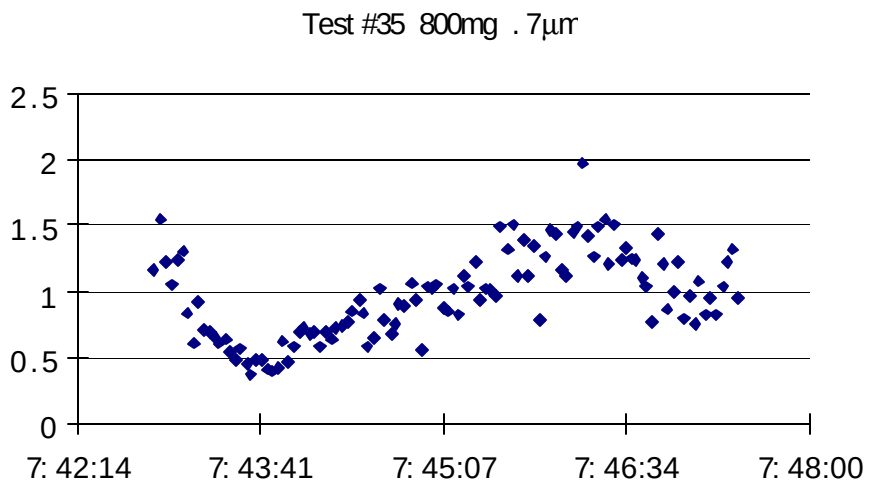

(a)

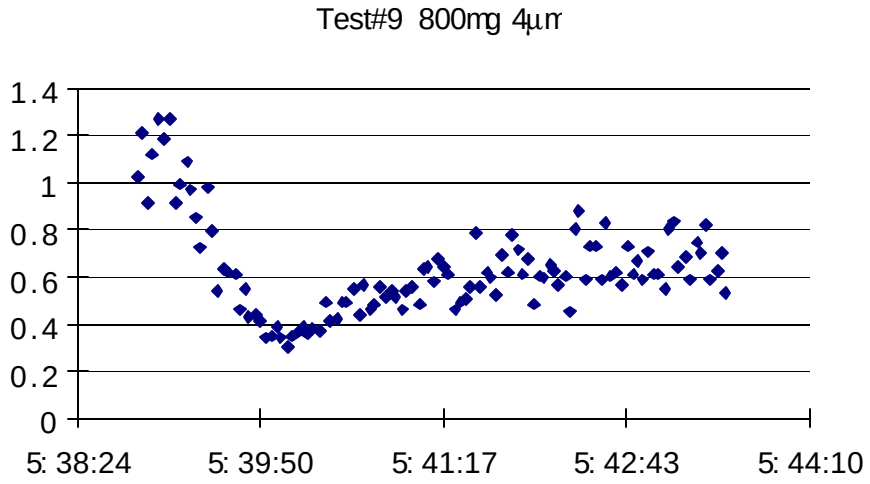

(b)

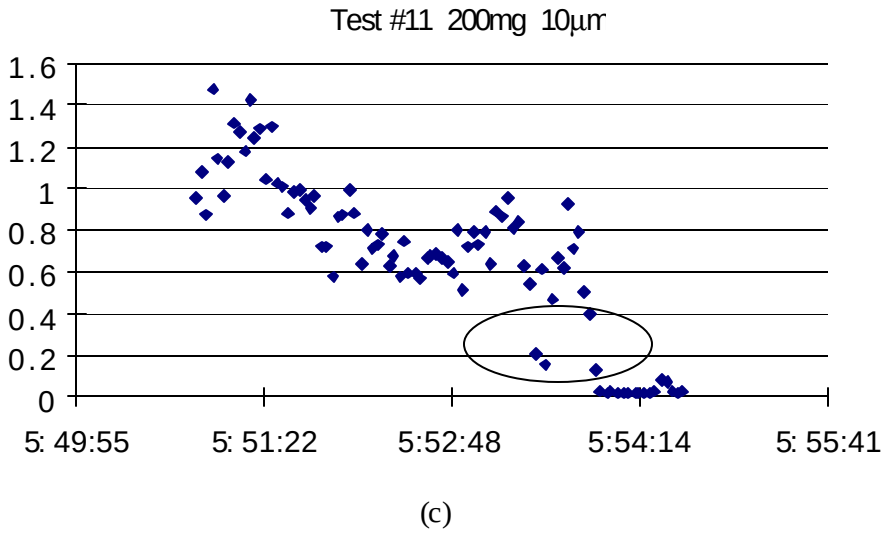

(c)

Figure 4.21. Ratio of the return signal of green and red channels from chamber tests during 19 December 2001: (a)Ratio of 0.7 µm; (b) Ratio of 4 µm; (c)Ratio of 10 µm.

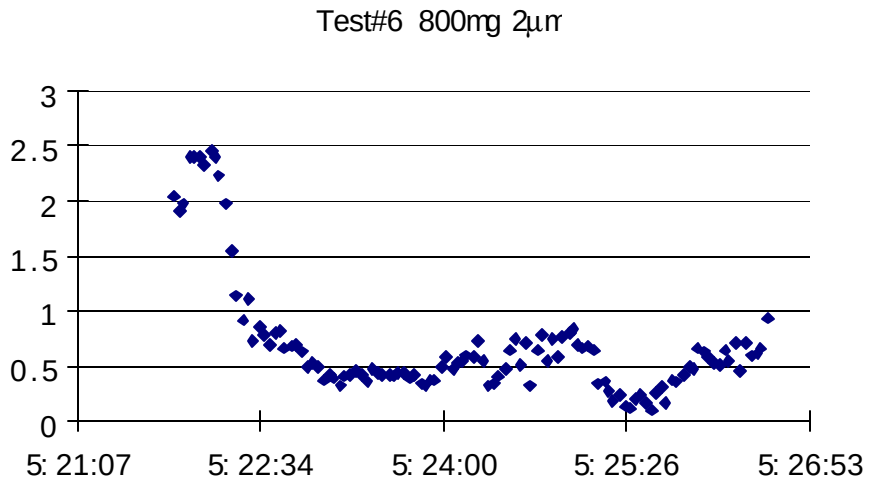

(d)

Figure 4. 21. Ratio of the return signal of green and red channels from chamber tests during 19 December 2001: (d) Ratio of 2 µm.

4.4.4 Dust generation test results

Pilot Study

The measurements from the tests performed during the pilot study have been used for a particularly interesting investigation. Figures 4.22 shows an example of the measurements from the two wavelengths, which display the result of the backscatter and the extinction of Test #4 which was 5 kilograms of local soil. The total amount of backscatter and extinction passing through dust plume can be observed, as illustrated in figure. The backscatter is larger for the red channel and the extinction is larger for the green channel. The fact that such striking differences exist provides support of the idea of using the lidar data to describe and characterize the changes in the distribution of airborne particulate matter.

It is generally difficult to obtaining quantified extinction profiles from signals of a backscatter lidar. However, the dust plume was tracked successfully by lidar and the total amount of backscatter and extinction of the plume can be observed, as shown the Figure 4.22. It is very important to quantify the total amount of both backscatter and extinction, because the combination can be used in describing the particle properties in

dust plume, and the result can be compared with model simulation. To better serve this purpose, the data has been normalized by referencing to the measurements of the clear atmospheric path just before the test, which is shown in Figure 4.23. There are two reasons that we need this normalization. First, the initial molecular scattering and aerosol scattering from the optical path is removed, and second, the effect of the telescope form factor is removed. The fact that the dust generator location is actually within the near field of optical path adds to the importance of the last point. All the lidar data analyzed for the dust generation tests have been normalized the same way for comparing with model simulation results.

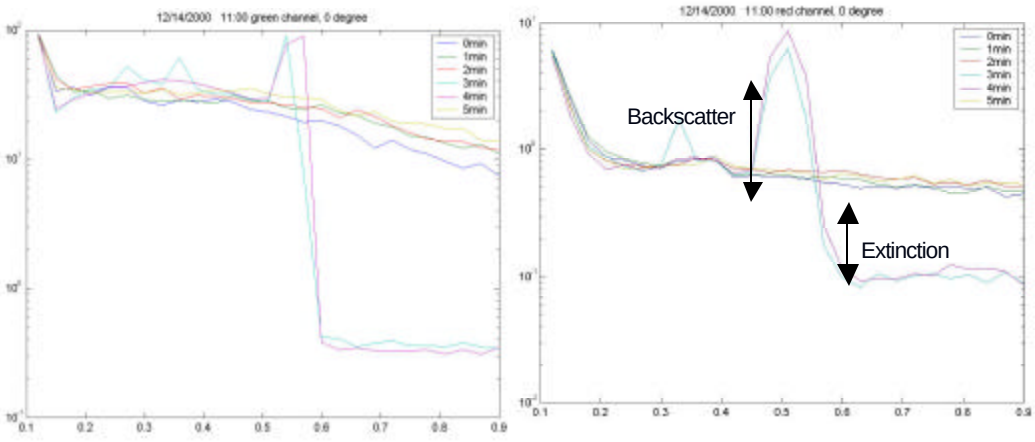

Figure 4.22. Examples of the raw data profiles from the lidar at the visible and NIR wavelengths during Test #4 on 14 December 2000 show the backscatter and extinction of dust plume at a range of about 500 m.

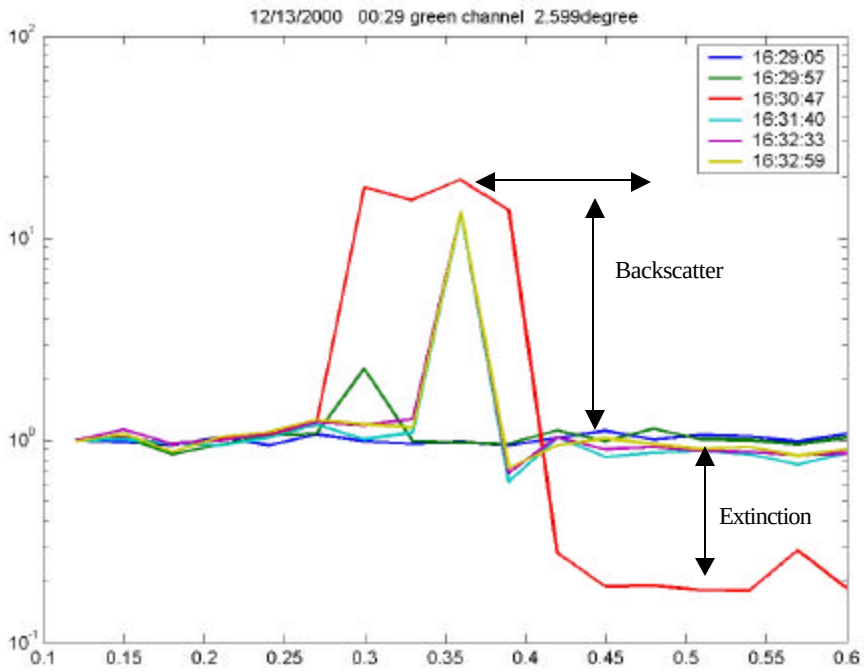

Figure 4.23. Example of data processing to quantify the total amount of backscatter and extinction.

Examples of the model simulations show various features of the optical scattering from the generated dust clouds in Figures 4.24, 4.25 and 4.26. The calculations in Figure 4.24 show the differences in backscatter and extinction signals as a function of the density of 10 µm particles. The calculation simulates a 200 m thick uniform dust cloud and provides values at 30 m intervals, which is same as the bin size of the lidar measurements. The upper panels show the calculations for the two wavelengths when the complex index of refraction is negligible and bottom two panels show the same cases when the complex index of refraction value is similar to that absorption expected for crustal earth samples. It is important to notice that the extinction only depends on the concentration of particles and not on the wavelength or absorption. However, the backscatter does depend strongly on the wavelength and on the complex index of refraction, but it does not depend on the particle density except for the amount of extinction when passing through the dust plume.

The calculations shown in Figure 4.25 demonstrate that the backscatter intensity dependance on the particle size. The relatively larger backscatter for the NIR

wavelength is expected based upon the fact that the longer wavelength allows the particles to remain longer in the Rayleigh scattering range, where the cross-section dependence, is proportional to r^6. Increasing the particle size increases the backscatter up to the point where the extinction from scattering loss results in an optical thickness that reduces the backscatter signal.

The simulation results showing more details of the dependence of the backscatter on the absorption due to increasing complex refractive index for the two wavelengths, and for different particle number densities are provided in appendix D.

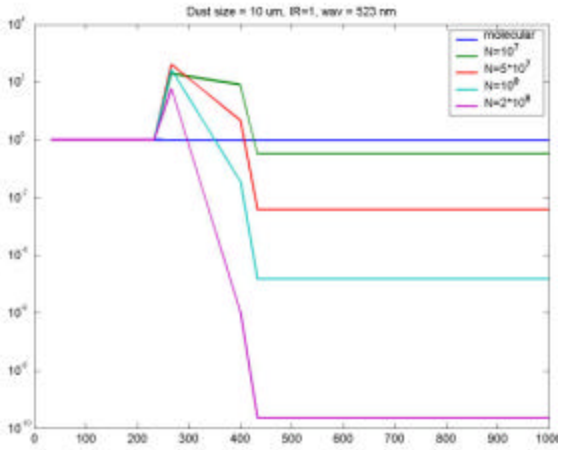

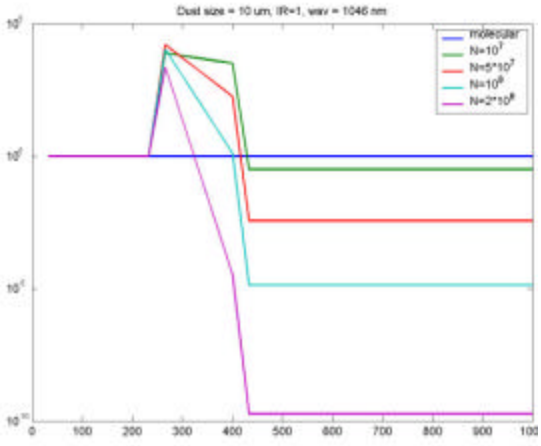

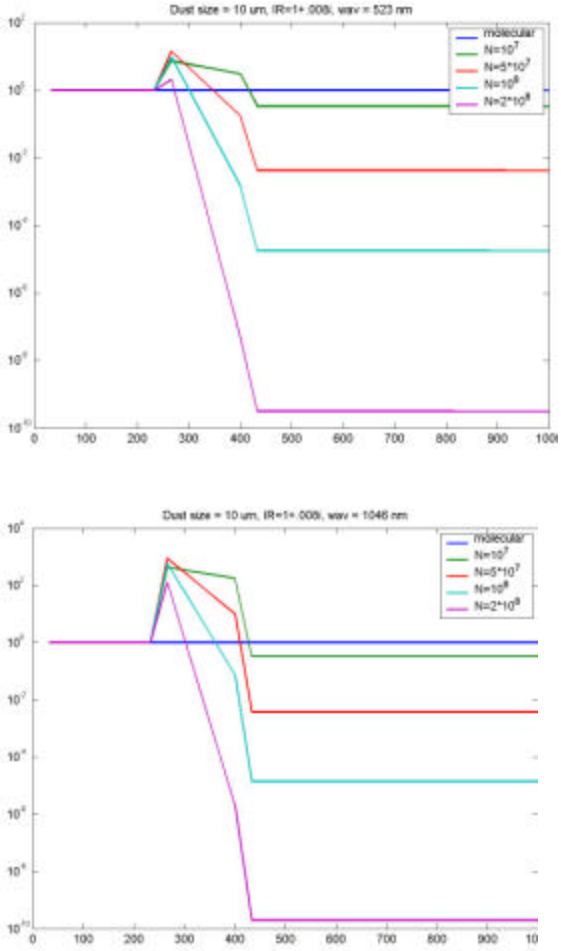

Figure 4.24. Simulation model of the scattering from 10 µm dust showing backscatter and extinction expected for both wavelengths at several different particle concentrations in the upper panels. The two lower panels show the same results, except they show dependence on complex index of refraction typical for crustal materials.

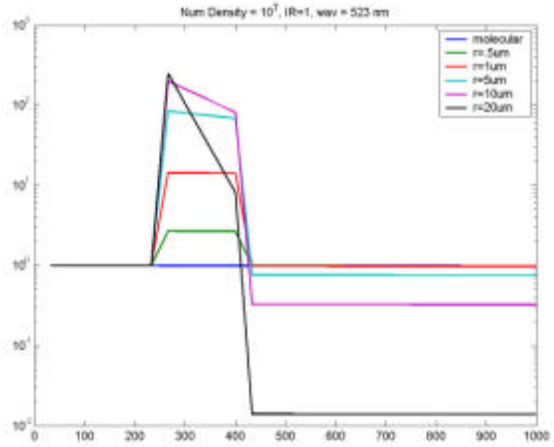
Num Density = 10^7, IR=1, wav = 523 nm
molecular
r=.5um
r=1um
r=5um
r=10um
r=20um

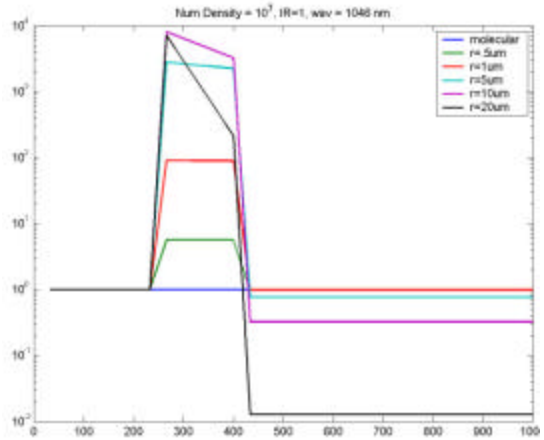
Num Density = 10^7, IR=1, wav = 1046 nm
molecular
r=.5um
r=1um
r=5um
r=10um
r=20um

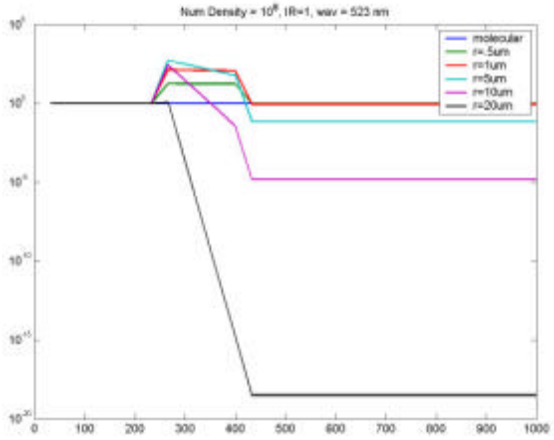
Num Density = 10^6, IR=1, wav = 523 nm
molecular
r=.5um
r=1um
r=5um
r=10um
r=20um

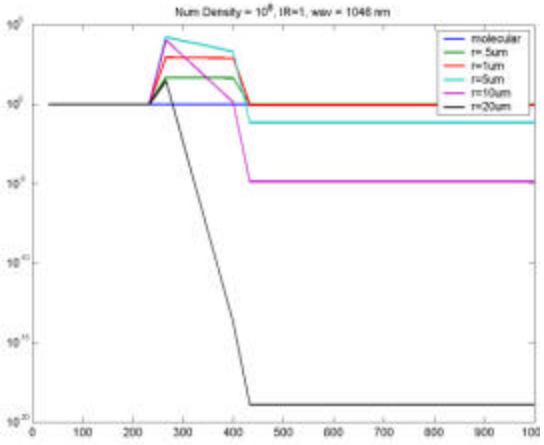

Figure 4.25. The calculations of the backscatter and extinction for the two wavelengths depending on the particle size. The upper panels show values for particle concentration of 10^7 m^{-3} and the lower panels show values for particle concentration of 10^8 m^{-3}.

The results from the pilot study have provided many interesting examples of backscatter and extinction that can be examined in the context of the simulation calculations above. The more difficult task is to use the field measurements to analyze the inverse problem and describe the particulate matter properties from the scattering profiles. The definitive solution of this latter task has begun, but it is beyond the scope of the present work. The present goal is to show how several tests can be interpreted with reference to the model simulations. Cases which represent small particle and large particle sizes are compared. The appendixes provide many other supporting results and a series of tests that were conducted.

The results shown in Figure 4.26 show the large range of changes in backscatter and extinction from changes in the concentration of particles during the generation of a very dense cloud from a spinning tire of a vehicle moving along a 50 m long North-South line. The results are plotted relative to the profile immediately before the test to show the dust characteristics more clearly. During the 45 second generation period, the extinction increased and then rapidly decreased again as the larger particles settled quickly, and the fine particle component is observed for a longer period of time. The small particle component is observed to continue to drift to

longer range while the larger particles, which are responsible for most of the extinction have settled out of the plume. If we compare the backscatter at around with the simulation result in Figure 4.25, it suggests that the observed scattering feature is due to relative large amount (> 10^7 /m^3 and < 10^8 /m^3)of large size particles (>10μm) in the air.

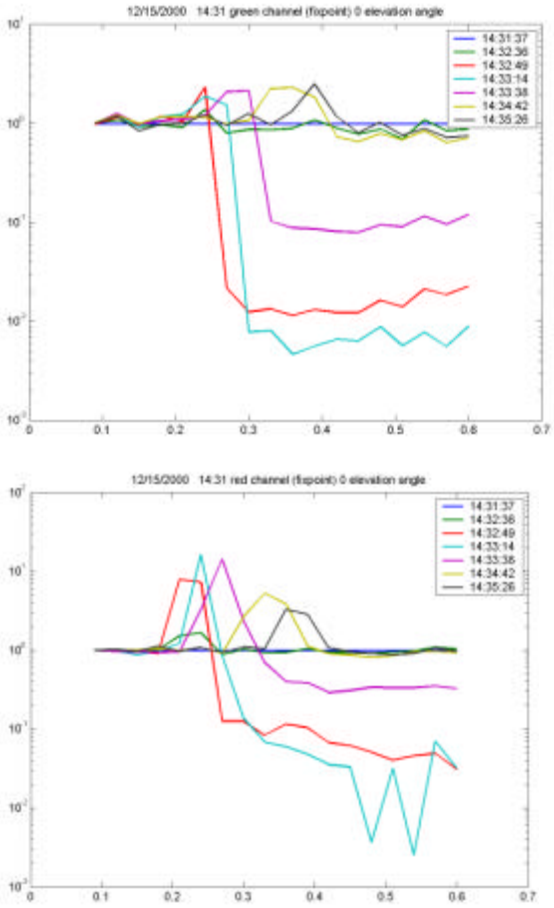

Figure 4.26. The backscatter and extinction at both visible and NIR wavelengths resulting from vehicle generated dust between 14:32:00 and 14:32:45 during Test #18 on 15 December 2000.

The result in Figure 4.27 shows a small puff of about 0.5 kg of sieved dirt from the field. The 0^o and $+10^o$ azimuth directions show the drift of the dust cloud to the right in the background wind. The feature at 450 m at $+10^o$ azimuth is due to scattering from a row of scrub bush and the -10^o azimuth plots show that no change is observed along a clear path. If we compare the backscatter at around 280m at 0^o

azimuth angle in Figure 4.27 with the simulation result in Figure 4.25, it suggests that the observed scattering feature is due to small amount (< 10^7 /m^3) of fine particles (<1μm) in the air.

Figure 4.28 shows the backscatter and extinction from the white powder (calcium carbonate) from Test #7. Because the atmospheric condition is very stable and calm during this test, we can set the direction of laser beam staring through the generated dust plume without scanning, which is better for studying the dissipating and settling procedures. The scattering peaks in both red and green signals at about 500 meters are due to scattering from a row of scrub bush, the scattering peaks at about 250 meters are due to generated dust plume. The result showing here is very interesting because the procedure of settling out of larger size particles can be clearly observed. We compared with the simulation results in Figure 4.25. The larger size particles (~ 10μm) which are responsible for most of the extinction settled out in 40 seconds, however, the smaller size particles (between 1 μm and 10 μm), which contribute to most of the scattering, will stay in the air for several minutes. The decrease of the backscatter signal after one minute is either due to the scattering from the fine mode particles (<1 μm), which will stay in the atmosphere for a longer time, or due to the scattering from the dissipated larger size particles.

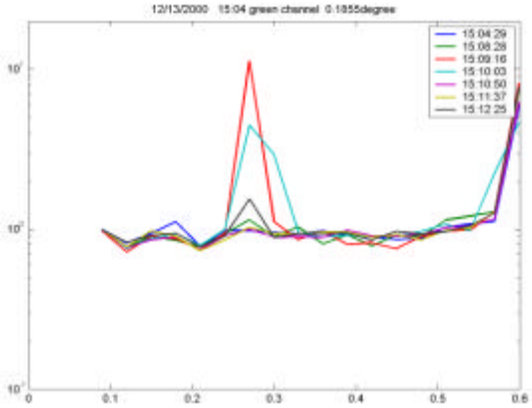

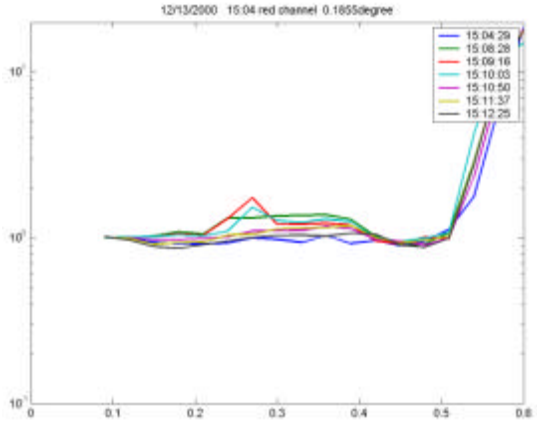
12/13/2000 15:04 red channel 0.1855degree
15:04:29
15:08:28
15:09:16
15:10:03
15:10:50
15:11:37
15:12:25

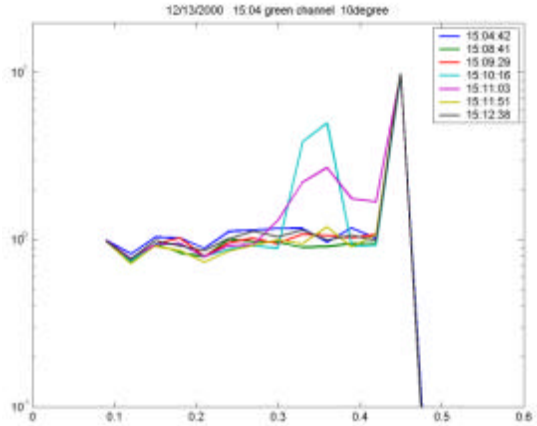
12/13/2000 15:04 green channel 10degree
15:04:42
15:08:41
15:09:29
15:10:16
15:11:03
15:11:51
15:12:38

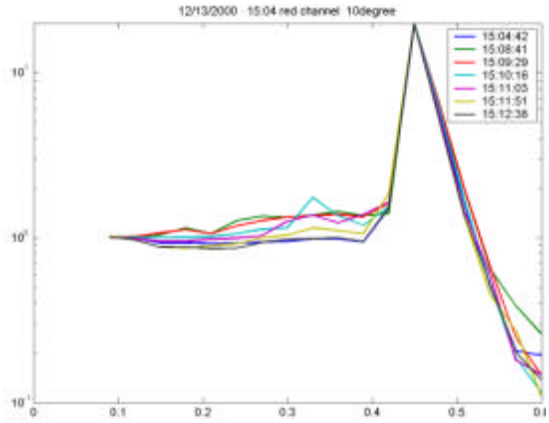
12/13/2000 15:04 red channel 10degree
15:04:42
15:08:41
15:09:29
15:10:16
15:11:03
15:11:51
15:12:38

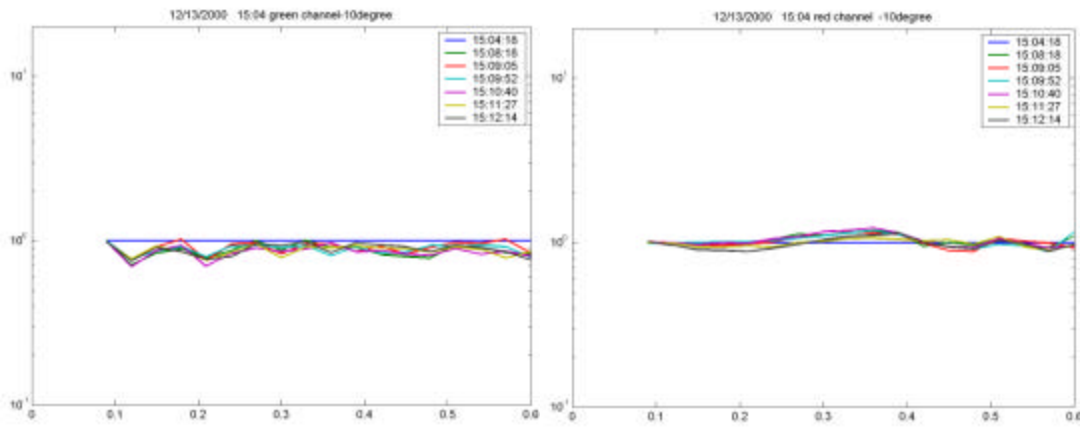

Figure 4.27. Results from Test #1, which was from a small puff of about 0.5 kg of sieved dirt from the field. The 0^{o} and $+10^{o}$ azimuth directions show the drift of the dust cloud in the background wind. The feature at 450 m at $+10^{o}$ azimuth is due to scattering from a row of scrub bush and the -10^{o} azimuth plots show that no change is observed along a clear path.

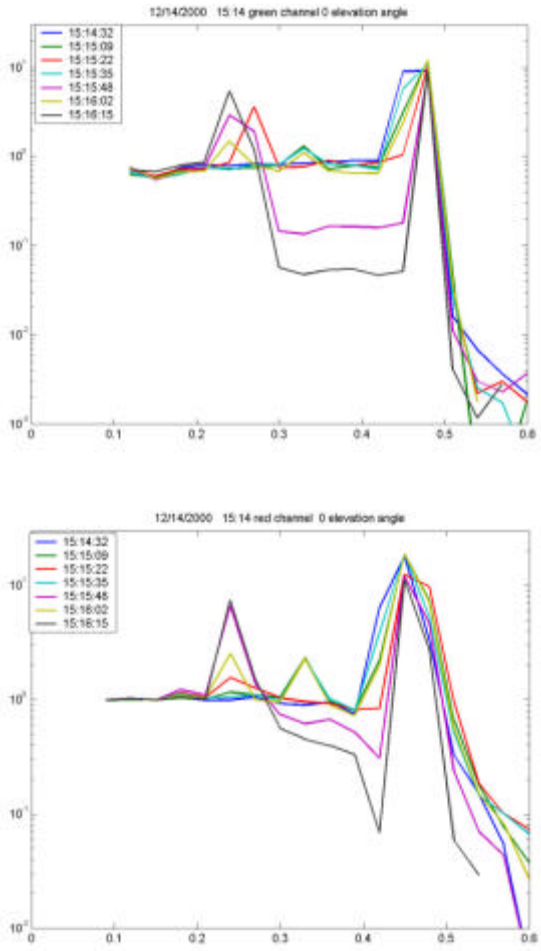

Figure 4.28. Results from Test #7 show the backscatter and extinction from the white

powder (calcium carbonate).

Main Study

The field test scenario of the main study is similar to the field tests conducted during pilot study, which has been described in Section 4.4.2. The primary results will be described using example which focus on the tests conducted on the morning of 19 December, 2001, because an interesting data set was obtained during this period when the atmospheric conditions were very stable. Therefore, it gives us a good opportunity to study the settling rate and transport of the generated dust plume and provides a much easier case to consider in comparing with the modeling calculations. In those tests, the lidar was set up and pointed to stare through the dust plume, at a height of about 3 meters above the ground. Additional measurements are presented in Appendix.

Figure 4.29 shows results of the signal returns from visible and IR wavelengths from Test #44 on 19 December, 2001, which was from a puff of about 600 g of 0.7 μm $CaCO_3$. The data has been normalized by reference to the measurements of the clear atmospheric path just before the test. It is easier to use normalized signal in modeling calculations because the normalized signal shows only the relative intensity difference of the dust plume relative to the clear atmosphere. Also, the telescope form factor from near field is removed by noemalizing the signal. Both the visible and IR returns show that the extinction from the dust plume decreases rapidly while the backscatter changes relatively slowly for a range of concentrations. The results in Figure 4.29 and Figure 4.30 show the changes in the relative effects of backscatter and extinction change as a function of time during the test. Notice that drift in position, and the rapid change in the extinction relative to backscatter denotes the settling out of larger particles. Figure 4.31 shows the 3-D contour plots of the signal returns from this same test. The 3-D plots are very useful for showing the dust plume evolution on the optical path as a function of time.

We have compared the results of Test #44 with results from model calculations in Figure 4.32. In our simulation, we assumed that the dust plume is generated at the

same location of the field test (dust generation location) with known thickness along optical path. The different particle sizes were truncated to simulate the loss of larger particles by settling from the optical path, step by step. The dust plume density can be calculated from the release size of the test and assumption of the volume of the plume. The simulation return signals from IR and VIS wavelengths were calculated using Mie scattering theory and compared with lidar results. The simulation results show a remarkable agreement with the measurements. In the analysis of chamber tests of Section 4.3.8, we have developed two-lognormal size distribution for 0.7 μm particles, which are shown in Figure 4.13 and 4.14. This size distribution model was used to describe the release in Test #44. The two-lognormal size distribution model is described by:

$$N(r) = F \cdot \left(10960 \cdot e^{\left(\frac{\ln(r)+1.102}{0.8768}\right)^2} + 3433 \cdot e^{\left(\frac{\ln(r)+0.267}{1.304}\right)^2} \right) \qquad (4.5)$$

where r represents particle size, F is a constant factor which is determined by density of dust plume relating to the release size. The factor F was chosen to make the amount of backscatter and extinction align with the experimental result, and is a crude estimate of the size of the dust plume.

Figure 4.32 shows the simulation result for Test #44. The simulation scenario is as follows: the dust plume is generated at the same location of the field test; the dust plume thickness is about 10 meters along optical path. In discrete steps, the particles with sizes larger than 5 μm, 1 μm, 0.9 μm, 0.8 μm and 0.7 μm are successively removed from the dust plume, respectively, to represent the settling out of the larger mass particles. The calculated signal estimates are shown in Figure 4.32. As shown in the figure, the backscatter remains relatively constant till the smallest size of 0.7 μm particles were removed from the plume, but the extinction drops very rapidly as the sizes larger than 1 μm particles were removed. Comparing the analysis of the simulation results and the backscatter and extinction results in Figure 4.30, we conclude that the larger particles (> 1 μm) settled out in 100 seconds, but it takes about 250 seconds untill the fine particles (~ 0.7 μm) settle or are transported out of the range.

It is very interesting to compare our result of settling rate with the result from particle settling rate by Seinfeld, which is shown in Figure 2.2. [Seinfeld and Pandis, 1998]. If we assumed a 1 meter range in our model, it takes about 1 hour for large particles (above 1 μm) to settle out of range from Seinfeld's model, which is much longer than we find. However, wind effect, turbulence and other atmospheric mechanisms are not considered in Seinfeld's model, and soil coagulation is difficult to estimate.

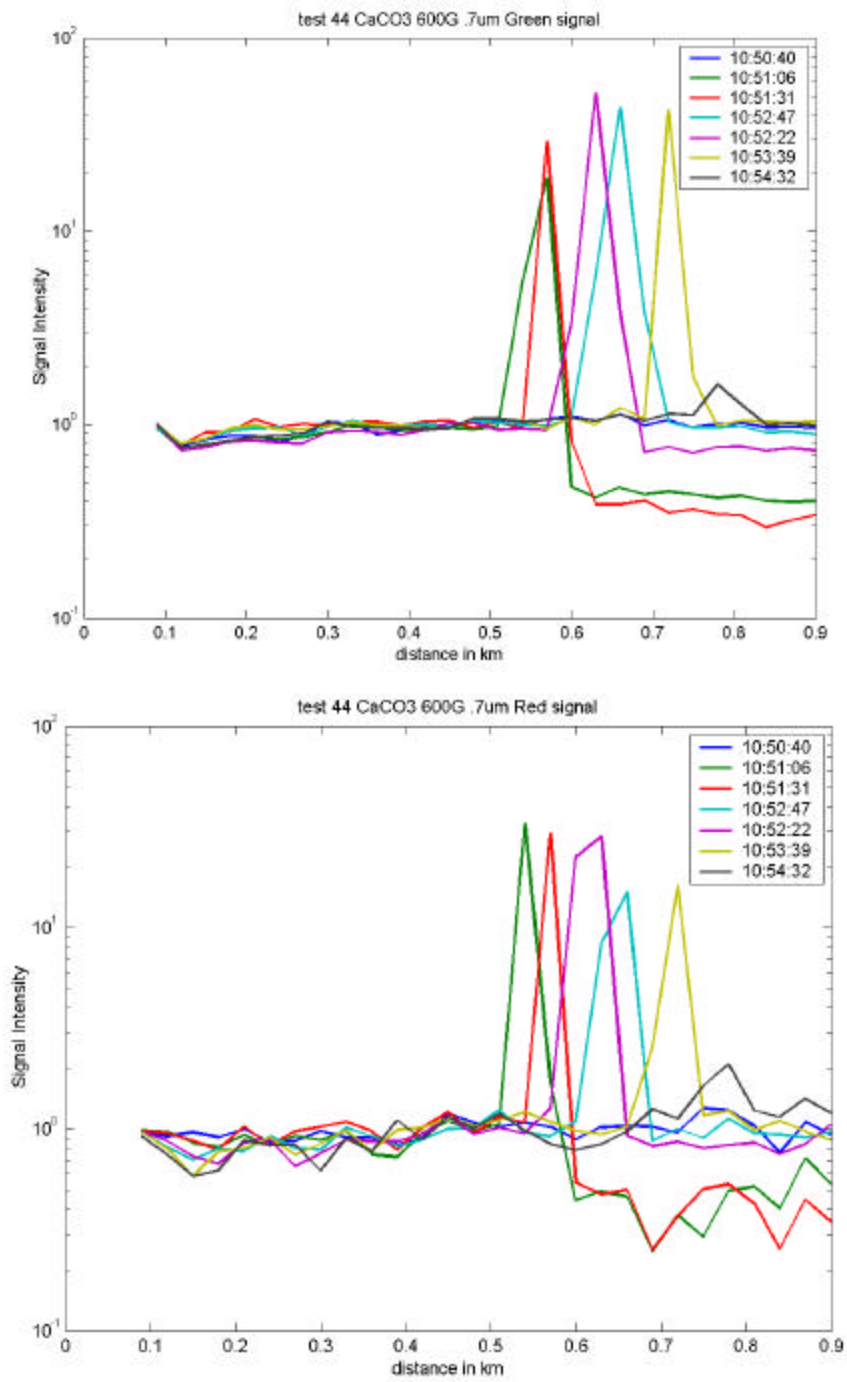

Figure 4.29 Results of the signal returns from (a) visible channel (b) IR channel from Test #44 on 19 December 2001, which was from dust generation of about 600 g of 0.7 μm $CaCO_3$.

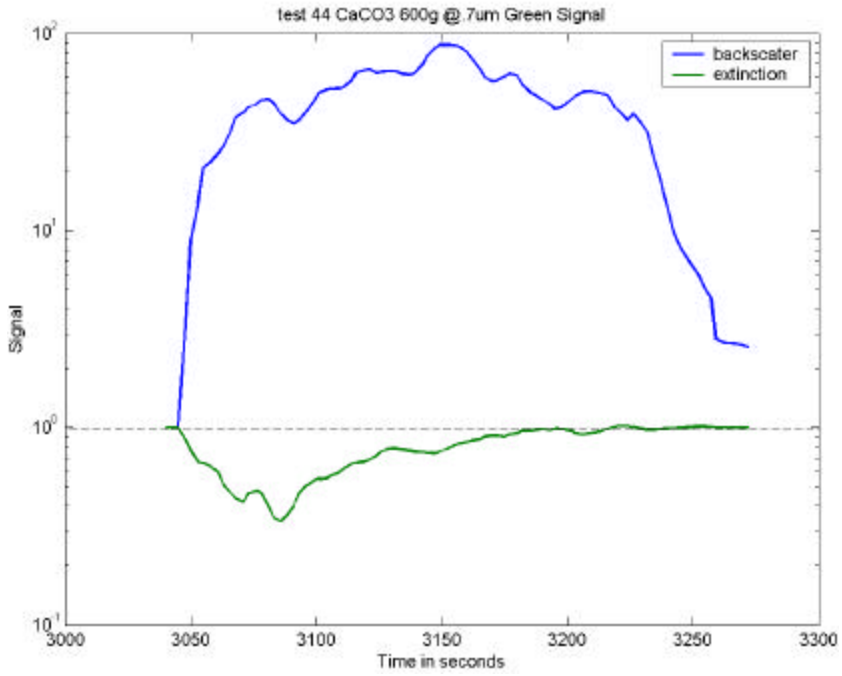

Figure 4.30. The backscatter and extinction from dust plume at the visible wavelength are function of time from Test #44 on 19 December 2001 for 600 g of 0.7 μm $CaCO_3$.

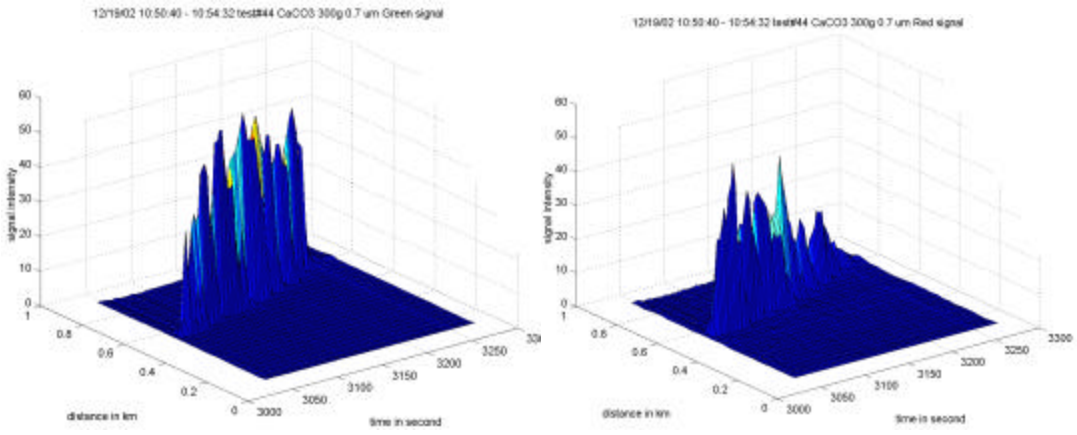

Figure 4.31. 3-D Contour plots of signal returns from (a) visible channel (b) IR channel from Test #44 on 19 December 2001, for 600 g of 0.7 μm $CaCO_3$.

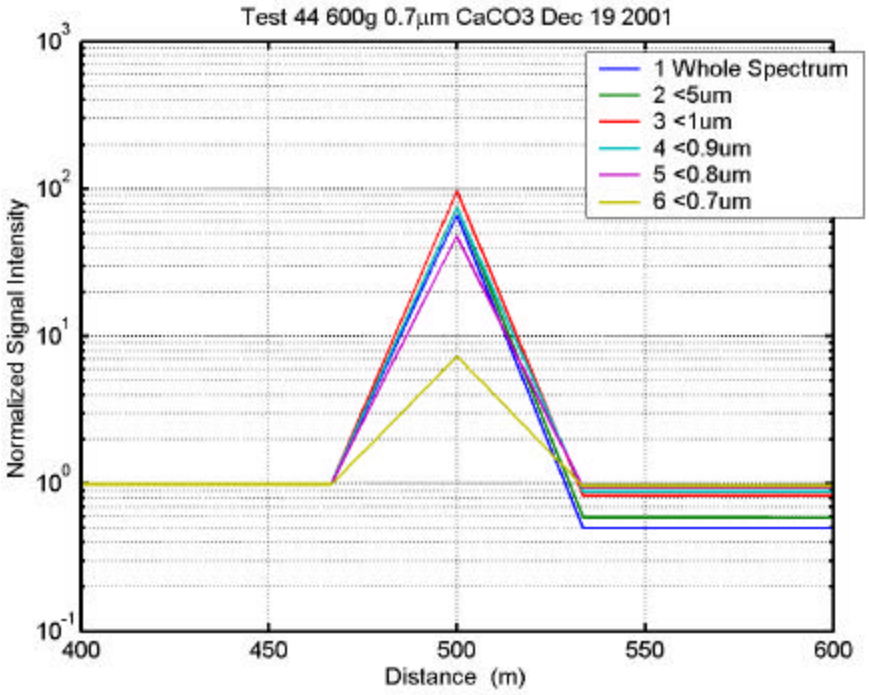

Figure 4.32. Model simulation results based upon truncation of particle spectrum from Test #44 on 19 December 2001, for 600 g of 0.7 μm $CaCO_3$.

Simulations for 4μm and 10 μm releases were also carried out which show close correspondence to the experimental data. Figure 4.33 shows results of the return signals from visible and IR wavelengths from Test #45 on 19 December, 2001, which was from a small puff of about 600 g of 2 μm $CaCO_3$. Figure 4.34 shows the variation in backscatter and extinction as a function of time during the same test. Figure 4.35 shows the 3-D contour plots of the signal returns from the Test #45. Also, the results of Test #45 are compared with results from model calculations.

Two-lognormal size distributions were developed for 4 μm particles, which are shown in Figure 4.16. The lognormal size distribution for two mode sizes, which represent the less than 10 μm particles and the fine particle powder, are used in the model as follows,

$$N(r) = F \cdot \left(102700 \cdot e^{\left(\frac{\ln(r)+1.097}{1.049} \right)^2} + 81970 \cdot e^{\left(\frac{\ln(r)-0.616}{0.941} \right)^2} \right) \qquad (4.6)$$

Figure 4.36 shows the simulation result for Test #45. The simulation results provide an excellent way of interpreting particle size information when comparing with the field test results. We have set up the simulation scenario so that the dust plume is generated at the same location as the field test and the dust plume thickness is chosen to be about 10 meters along the path. In discrete steps, the particles with sizes larger than 10 μm, 5 μm, 2 μm, 1 μm and 0.6 μm are sequentially removed from the dust plume to simulate the settling out of the large particles. The corresponding signal returns are shown in Figure 4.36. As shown in the figure, the backscatter signal remains almost constant until the 0.6 μm particles were removed from the plume. However, the extinction drops rapidly when larger particle sizes are removed. Comparing the analysis of the simulation results with the backscatter and extinction results in Figures 4.33 and 4.34, we conclude that the larger course mode particles (above 5 μm) settled out in about 20 seconds, but it takes longer about 100 seconds until the fine particles settle or transport out of the range.

Figure 4.37 shows results of the signal returns from visible and IR wavelengths from Test #43 on 19 December, 2001, which resulted from a small puff of about 600 g of 10 μm $CaCO_3$. Figure 4.38 shows the change of backscatter and extinction as a function of time during the same test. Figure 4.39 shows the 3-D contour plots of the signal returns from the Test #43. Also, we compared the results of Test #43 with results from model calculations, two-lognormal size distributions were developed for 10 μm particles, which is shown in Figure 4.17. The lognormal size distribution for two mode sizes, which represent the 10 μ particles and the fine particle powder, are used in the model as follows,

$$N(r) = F \cdot \left(82350 \cdot e^{\left(\frac{r+1.062}{1.35}\right)^2} + 51690 \cdot e^{\left(\frac{r-1.059}{0.7277}\right)^2} \right) \qquad (4.7)$$

Figure 4.40 shows the simulation for Test #43. The backscatter signal drops fast due to small amount of fine mode particles in the atmosphere relative to the larger particle sizes used in this test and this simulation result is important on interpreting particle size information when comparing with the field test results. We have set up

the simulation scenario so that the dust plume is generated at the same location as the field test and the dust plume thickness is chosen to be about 10 meters along the path. In discrete steps, the particles with sizes larger than 10 μm, 5 μm, 2 μm, 1 μm and 0.6 μm are removed sequentially from the dust plume to simulate the settling out of the large particles. The corresponding return signals are shown in Figure 4.40. As shown in the figure, the backscatter and the extinction both drop more rapidly as the particles of size greater than 5 μm were removed. This is different from previous two cases and is due to the large particle size of this release, not so many small particles remained after the course mode particles settled out. Comparing the analysis of the simulation results and the backscatter and extinction results in Figures 4.37 and 4.38, we conclude that the larger course mode particles (above 5 μm) settled out in about 50 seconds.

The model simulations in Figure 4.32, 4.36 and 4.40 represent the release of 600 g of $CaCO_3$ of different sizes 0.7 μm, 4 μm and 10 μm. The model calculations demonstrate that the backscatter and extinction intensity depend on the particle size, although the same mass density is assumed on optical path. The relative larger backscatter and smaller extinction are expected for 0.7μ release. The increase in particle size increases the extinction and decrease the backscatter intensity with fixed mass density. During 10 μμ release, the simulation shows the backscatter drops dramatically when larger size particles settle out of optical path. This is expected because most of the mass density falls out of the plume as the larger size particles settle.

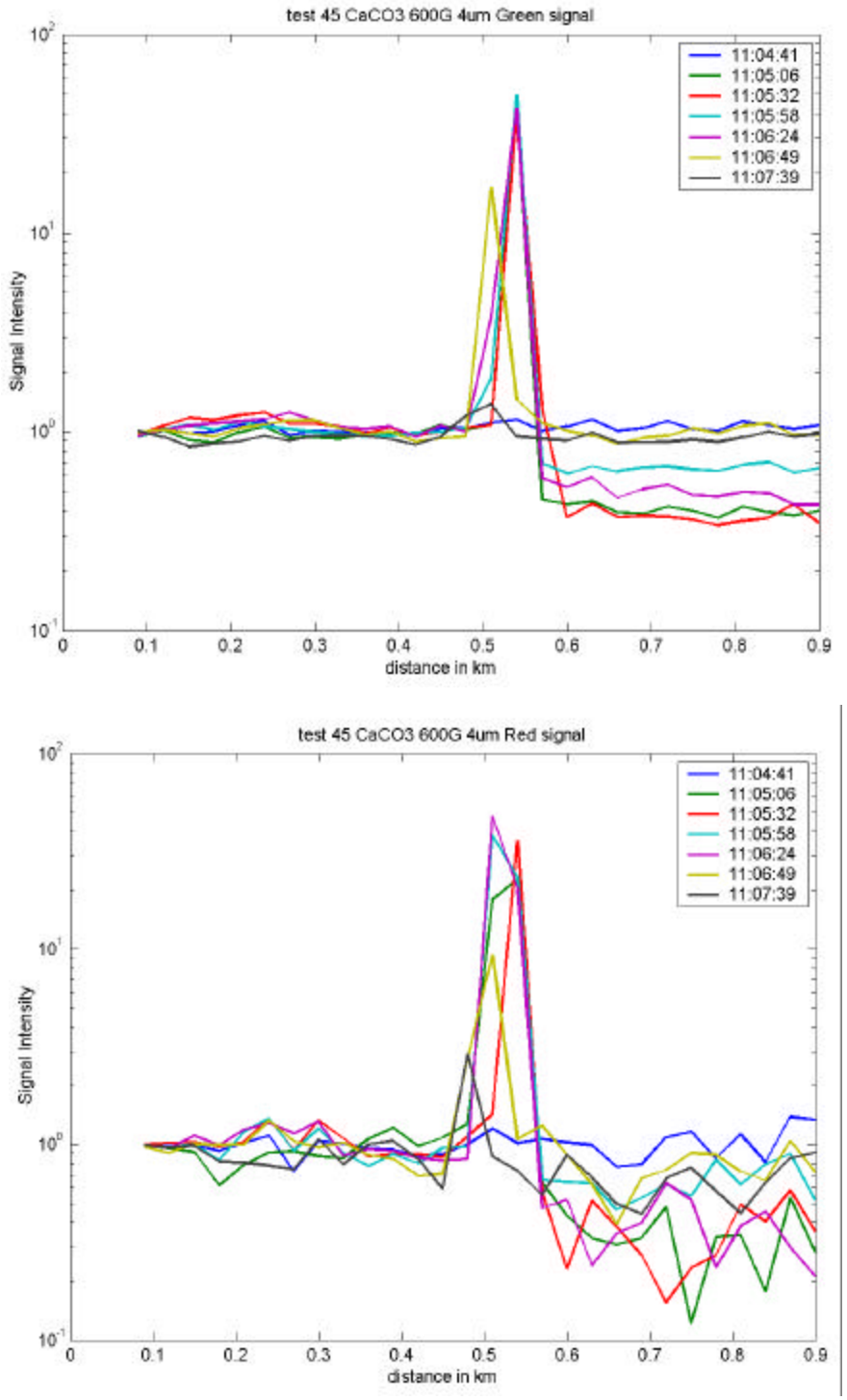

Figure 4.33. Results of the signal returns from (a) visible channel (b) IR channel from Test #45 on 19 December 2001, for 600 g of 4 µm $CaCO_3$.

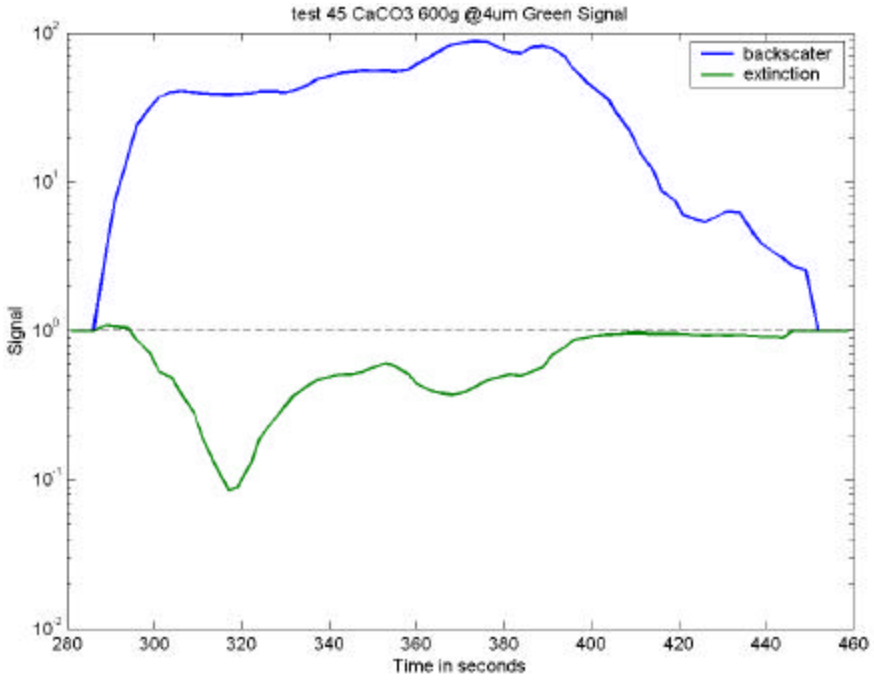

Figure 4.34. The backscatter and extinction from dust plume at visible wavelength along with time from Test #45 on 19 December 2001, for 600 g.

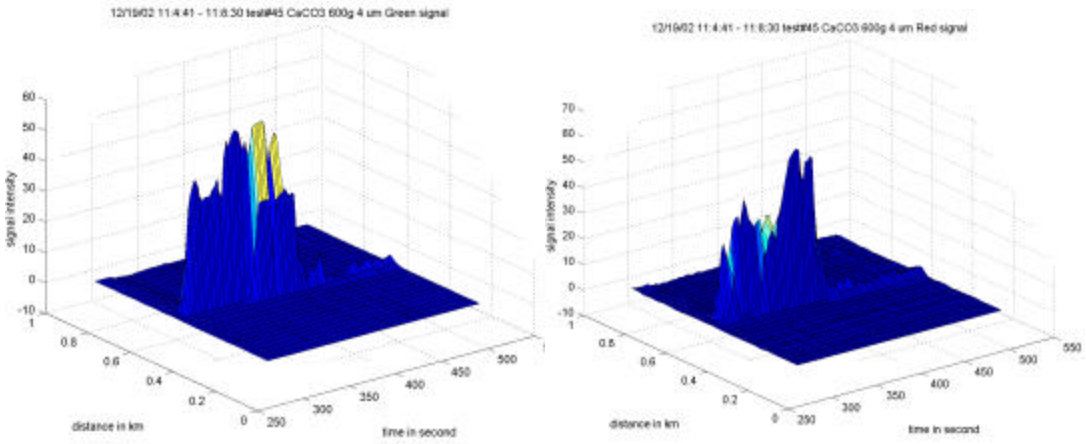

Figure 4.35. 3-D Contour plots of signal returns from (a) visible channel (b) IR channel from Test #45 on 19 December 2001, for 600 g of 4 μm $CaCO_3$.

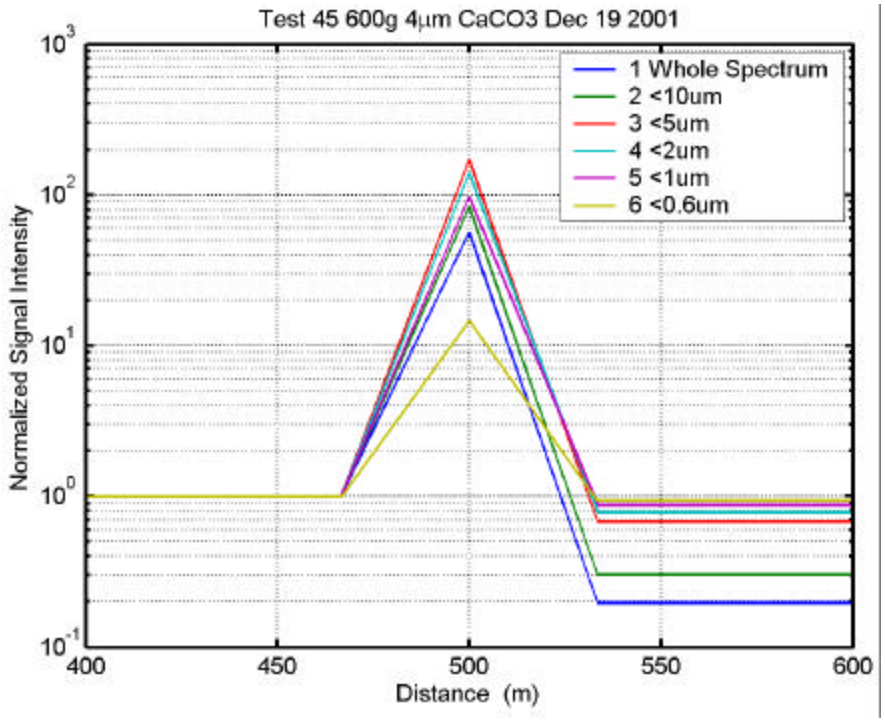

Figure 4.36. Model simulation results based upon truncation of particle spectrum from Test #45 on 12/19/2001, for 600 g of 4μm $CaCO_3$.

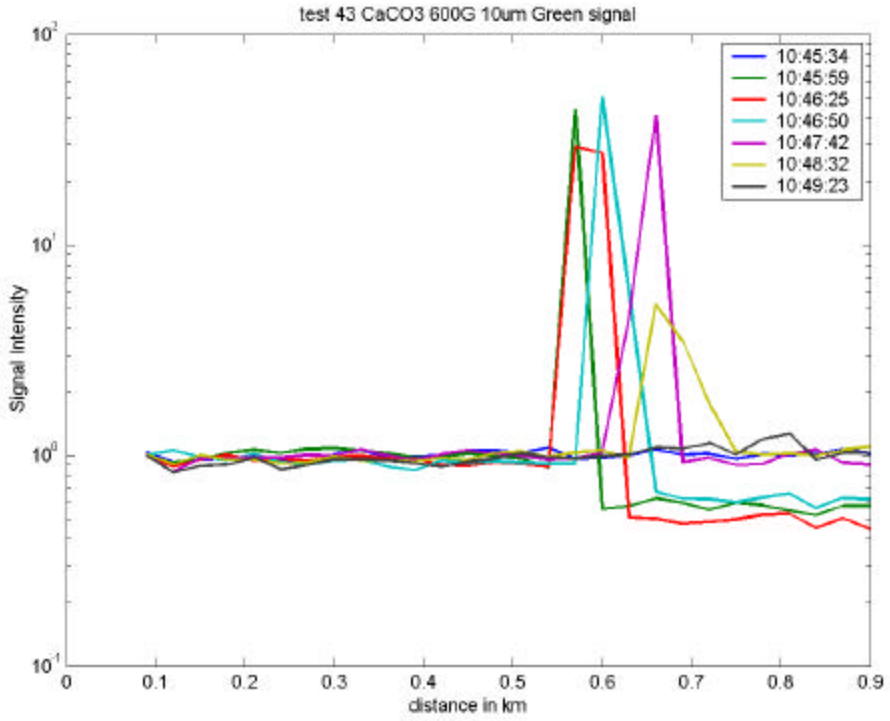

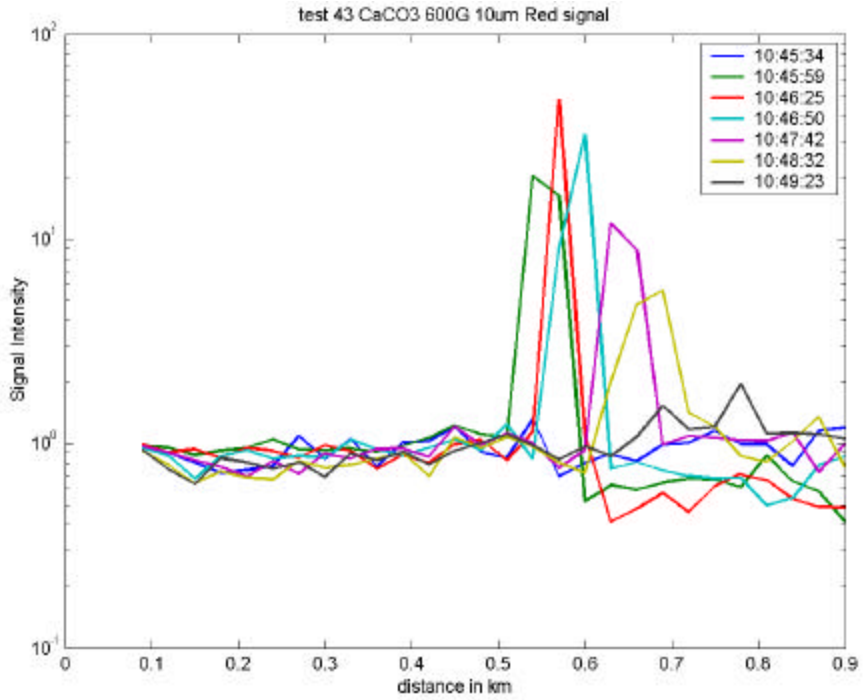

Figure 4.37. Results of the signal returns from (a) visible channel (b) IR channel from Test #43 on 19 December 2001, for 600 g of 10 μm $CaCO_3$.

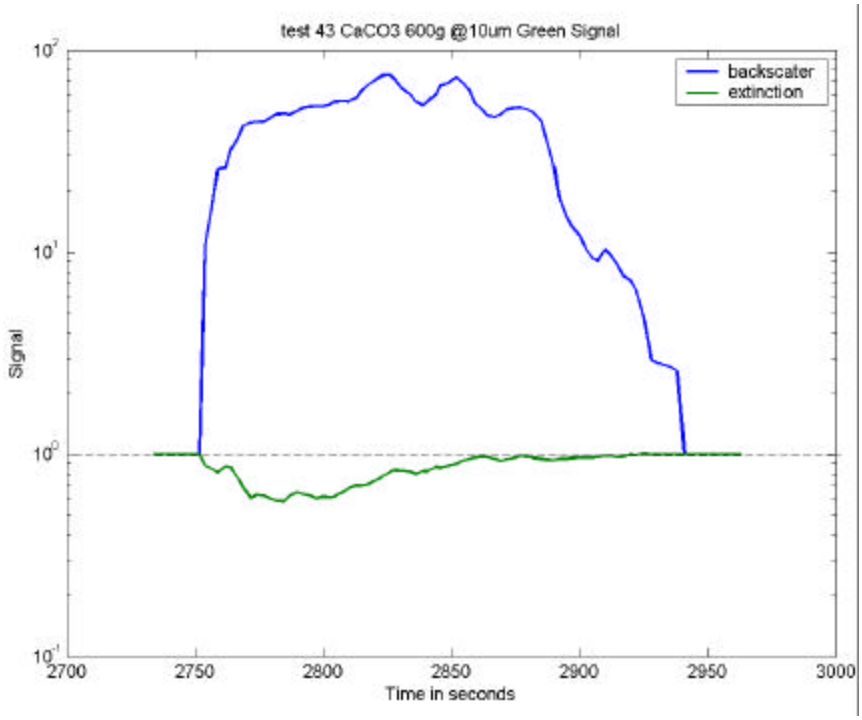

Figure 4.38. The backscatter and extinction from dust plume at visible wavelength along with time from Test #43 on 19 December 2001, for 600 g of 10 μm $CaCO_3$.

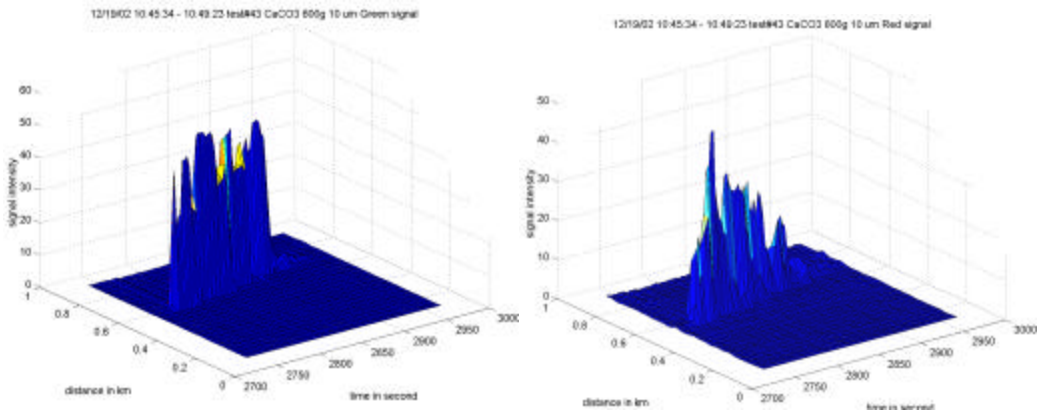

Figure 4. 39. 3-D Contour plots of signal returns from (a) visible channel (b) IR channel from Test #43 on 19 December 2001, for 600 g of 10 µm $CaCO_3$.

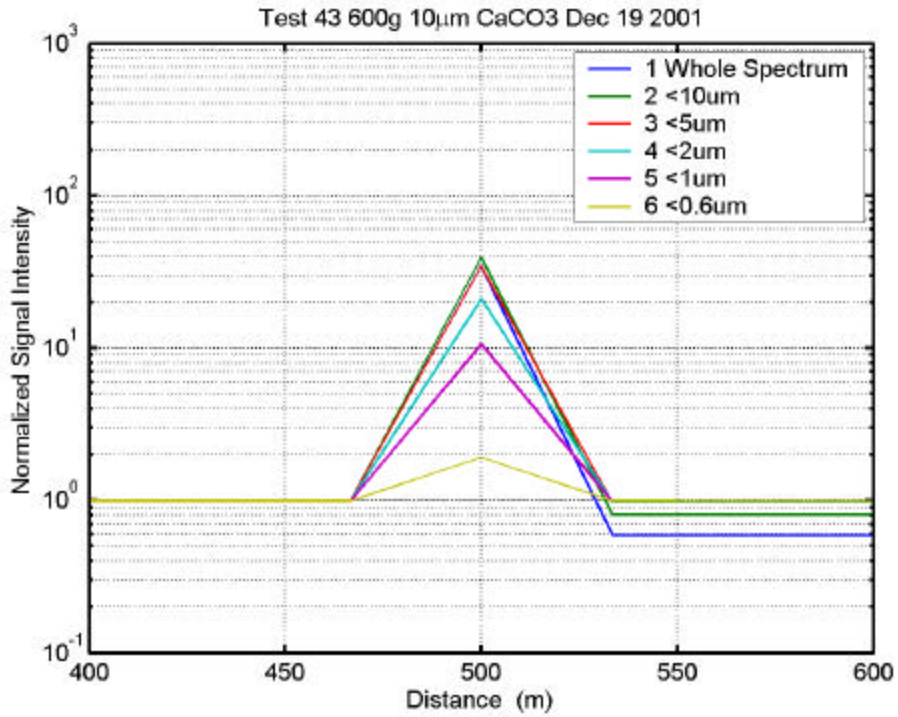

Figure 4.40. Model simulation results based upon truncation of particle spectrum from Test #43 on 19 December 2001, for 600 g of 10 µm $CaCO_3$.

4.5 Summary

In this chapter, we analyzed the lidar data of dust scattering from CA-Dust campaign and made comparison with model simulations based upon Mie scattering theory. Lidar data was compared with measurements by other instruments. The ratios of the backscatter signal from green channel (523 nm) and red channel (1046 nm) were studied to investigate the particle characteristics in artificial plumes of dust that we released into the atmosphere. During chamber test, particle size distribution models were constructed and used later to study the settling rate of different sizes of the dust particles. Model simulation results provide an excellent way to understand the signal variations measured by lidar. It has been observed in our study that the larger particles, which contain most of the PM mass, settle out of the air fairly quickly, however, the fine particles that contribute primarily to the backscatter remain suspended much longer. The results suggest that the rapid deposition of PM10 particles, and the relatively longer residence time of the optical plume associated with small particles (< 2m), may have led to overestimates of emission flux in the particle mass in plumes. This could explain the major discrepancy between the source estimates and the measured mass of soil particulates.

CHAPTER 5

NE-OPS Measurement Campaign

5.1 Introduction

The NARSTO-NE-OPS (North American Research Strategy for Tropospheric Ozone - North East - Oxidant and Particle Study) is a project dedicated to the investigation of the sources of chemical species and particulates during atmospheric pollution episodes. The program includes the instruments that are most useful for describing the evolution of pollution events and examining the controlling influence of local meteorology on the distributions of particulate matter and chemical species in the lower atmosphere. Local and regional meteorological factors are keys in the development and dissipation of pollution events since they greatly influence the formation of both aerosol particles and ozone. Distinguishing between the local and regional sources that generate pollution episodes is important when considering emissions control regulations. The vertical and horizontal transport of pollutants, which is mainly controlled by meteorological dynamical processes, is essential in describing population exposure and risk. The NARSTO-NE-OPS research program's goals are to address these issues by providing measurements of atmospheric properties and processes that can be used for testing and development of atmospheric pollution models. The lidar technique has the capability to provide real-time vertical profiles and time-sequence plots of atmospheric properties. The lidar is most useful for investigating the vertical and horizontal structure of the atmosphere. The research effort benefits from the wide range of measurements that are possible from the collaboration of a number of universities and agencies. The measurement campaigns have benefited from the opportunity to bring together the instruments and research capabilities of a number of investigators. The participants and their contributions are shown in Table 5.1

Table 5.1. List of Investigators in the NARSTO-NE-OPS Program

August 1998 NARSTO-NE-OPS Campaign

Penn State University - Russell Philbrick

Raman Lidar - Profiles of Specific Humidity, Temperature, Ozone, Optical Extinction (285, 530 and 607 nm)

Millersville University - Richard Clark

Tethered Balloon - 100 m^3 - 10 hr aloft with sensors at surface, 100 m, 200 m, and 300 m AGL

1) Personal Environmental Monitors (PEMS) 4 each - 4 L/min dry PM 10 hr sample
2) Diode laser scatterometer (Dust Traks) 1.7 L/min continuous data

Tethered Balloon - 7 m^3 - up/down scan to 300 m each hour

Meteorological properties: T, D, RH, wind speed and direction 1 m vertical resolution and O_3

Surface Measurements - O_3 and meteorological data

Meteorological Data Archive - Radar, Satellite Images, Surface Observations, Upper air data, ETA/RUC model output

Harvard School of Public Health - Petros Koutrakis and George Allen

Mass density of particulates: PM1, PM2.5, PM10, aerosol-size, EC/OC, sulfate, nitrate, toxics

Harvard University - Bill Munger

NOy concentrations and fluxes are used to infer the rates for NOx oxidation and deposition.

University of Maryland - Bruce Doddridge and Bill Ryan

Instrumented Aircraft Cessna 170: GPS, Ozone, Carbon Monoxide, temperature, humidity probe

Ozone and PM event forecasting, description of interesting episodes and meteorological modeling

Drexel University - Steve McDow

Organics in PM2.5 with GCMS analysis: non-polar components (alkanes, PAH), acids and diacids.

Polar Organics for GCMS with derivatization using PM10 with composite samples

June-August 1999 NARSTO-NE-OPS Campaign

Penn State University - Russell Philbrick

1) Raman Lidar - Profiles of Specific Humidity, Temperature, Ozone, Optical Extinction (285, 530 and 607 nm)

2) Radar-RASS - Wind velocity, Virtual Temperature

3) 10 m Tower - Temperature, dew point, relative humidity, wind velocity, wind gust, solar flux, atmospheric pressure, precipitation

Millersville University - Richard Clark

Tethered Balloon - 100 m^3 - 10 hr aloft with sensors at surface, 100 m, 200 m, and 300 m AGL

1) Personal Environmental Monitors (PEMS) 4 each - 4 L/min dry PM 10 hr integrated sample
2) Diode laser scatterometer (DustTraks) 1.7 L/min continuous data
3) VOC - Micro-orifice vacuum canister at surface and at 300 meters, 10 hour sample with GC/MS lab analysis

Tethered Balloon - 7 m^3 - up/down scan to 300 m each hour

1) Meteorological properties: T, D, RH, wind speed and direction 1 m vertical resolution
2) O_3 by KI oxidation method, 2-3 second time resolution (1 meter altitude)

Surface Measurements - O_3 and meteorological data

Meteorological Data Archive - Radar, Satellite Images, Surface Observations,

Upper air data, ETA/RUC model output

Harvard School of Public Health - Petros Koutrakis and George Allen

Mass density of particulates: PM_1, $PM_{2.5}$, PM_{10}, aerosol-size, EC/OC, sulfate, nitrate, toxics

Harvard University - Bill Munger

NOy concentrations and fluxes are used to infer the rates for NOx oxidation and deposition.

University of Maryland - Bruce Doddridge and Bill Ryan

Instrumented Aircraft Cessna 170 and Aztec: GPS, Ozone, Carbon Monoxide, temperature, humidity probe

Ozone and PM event forecasting, description of interesting episodes and meteorological modeling

Drexel University - Steve McDow

Organics in $PM_{2.5}$ with GCMS analysis: non-polar components (alkanes, PAH), acids and diacids using Hi-Vol 24 hour sample

Polar Organics for GCMS with derivatization using PM_{10} with composite samples

Brookhaven National Laboratory - Peter Daum, Larry Kleinman, Yin-Nan Lee, Stephen Springston

DOE G-1 Instrumented Aircraft - particulate and gas-phase chemistry

Brigham Young University - D. Eatough

Measurement of particle volatile mass component and identification of volatile species with RAMS and PCBOSS

Pacific Northwest National Laboratory - C. Doren, J. Allwine, J. Fast, C. Berkowitz

Radiosondes - Pressure, temperature, humidity 0-15 km at Philadelphia, Radar-RASS instrument at West Chester, 12 ozonesondes at Philadelphia

Argonne National Laboratory - R. Coulter, J. Gaffney, N.A. Marley

Radiosondes, SODAR and Chemistry Laboratory at Centerton NJ

N. Carolina A&T State University - D. Dunn

Remote sensing with lidar and SODAR

N. C. State University - H. Hallen

Laser remote sensing, particle optical scattering properties

July 2001 NARSTO-NE-OPS Campaign

Penn State University - Electrical Engineering - Russell Philbrick

1) Raman Lidar - Profiles of Specific Humidity, Temperature, Ozone, Optical Extinction (285, 530 and 607 nm)

2) Radar-RASS - Wind velocity, Virtual Temperature

3) 10 m Tower - Temperature, dew point, relative humidity, wind velocity, wind gust, solar flux, atmospheric pressure, precipitation

4) Radiosondes - Pressure, temperature, humidity 0-15 km

Penn State University - Meteorology - Bill Ryan and Nelson Seaman

Ozone and PM event forecasting (with Univ. Maryland) and modeling, description of episodes

Millersville University - Richard Clark

Tethered Balloon - 100 m^3 - 10 hr aloft with sensors at surface, 100 m, 200 m, and 300 m AGL

1) Personal Environmental Monitors (PEMS) 4 each - 4 L/min dry PM 10 hr integrated sample

2) Diode laser scatterometer (DustTraks) 1.7 L/min continuous data

3) VOC - Micro-orifice vacuum canister - surface and 300 meters, 10 hour sample GC/MS analysis

Tethered Balloon - 7 m^3 - up/down scan to 300 m each hour

1) Meteorological properties: T, D, RH, wind speed and direction 1 m vertical resolution

2) O_3 by KI oxidation method, 2-3 second time resolution (1 meter altitude)

Surface Gas and Particles - O_3, $NO/NO_2/NO_X$, SO_2, CO, 3λ Nephelometer

Meteorological Data Archive - Radar, Satellite Images, Observations, Upper air data, ETA/RUC model output

Harvard School of Public Health - Petros Koutrakis, George Allen and Mark Davey

Particle Size and Count: 0.02 to 0.6 :m electrostatic classification, 0.7 to 15 :m time of flight, $PM_{2.5}$ CAMM, Black carbon soot aethalometer, sulfate from HSPH thermal conversion method, EC/OC analyzer

Particulate10-hour Day/Night Samples: HEADS for acid gases [HNO_3, HONO, SO_2], NH_3, and sulfate/nitrate/strong aerosol acidity EC/OC on quartz filters with DRI's TOR analysis, $PM_{2.5}$ and PM_{10} from Harvard impactors with Teflon filters and gravimetric analysis daily, Hivolume OC speciation sampler, HSPH PUF substrate collection; Drexel University filter analysis

Harvard University - College of Engineering - Bill Munger

NOy concentrations and fluxes are used to infer the rates for NOx oxidation and deposition.

University of Maryland - Bruce Doddridge, Russ Dickerson, Lung-Wen (Antony) Chen, Emily Tenenbaum, Aztec aircraft on board instrument rack:

1) Modified Radiance Research Particle_Soot Absorption Photometer
2) Garmin recording GPS_90 Global Positioning System
3) Thermo Environmental Instruments (TEI) Model 49 Ozone
4) Modified TEI Model 43CTL Sulfur Dioxide
5) Modified TEI Model 48 Carbon Monoxide instrument
6) TSI Model 5363 3-wavelength integrating nephelometer

Univ Maryland & NASA Goddard

AERONET (Aerosol Robotic Network) data available include AOT at 1020, 870, 670, 500, 440, 380, and 340 nm plus precipitable Water (cm). Column averaged SS albedo and size number distributions will be calculated from the data.

Drexel University - Prof. Steve McDow, Min Li

1) Organics in $PM_{2.5}$ - GCMS analysis; non-polar components (alkanes, PAH) acids and diacids; Using sample from Tuch TE-1202 Hi-Vol Sampler - 24 hour integration

2) Polar Organics for GCMS with derivatization - Using Anderson PM_{10} with composite weekly samples

3) Metals in Inductively Coupled Plasma Mass Spectrometer (ICPMS); Low volume teflon membrane filter; Using daily 24 hour sample

Clarkson University - Phil Hopke and Alex Polissar

1) $PM_{2.5}$ with 0.5 hr resolution using RAMS, TEOM and 3OC

2) $PM_{2.5}$ with 1hr resolution using CAMM's instrument

3) Nephelometers - one with and one without dryer

EPA - RTP & **Texas Tech University** - Bill McClenny (EPA), Sandy Dasgupta, Jianzhong Li, Rida Al-Horr (Texas Tech)

1) Fluorescence Detector H2O2 HCHO MHP NH3 with 10 min resolution

2) Ion Chromatography (15 min time resolution) Sulfur Dioxide, Nitric Acid, Nitrous Acid, HCl, Oxalic Acid, Oxalate, Nitrate, Nitrite, Sulfate, Chloride, Ammonium

Brookhaven National Lab

Investigators: Larry Klineman, Linda Nunnemacker, Xiao-Ying Yu, Yin-Nan Lee, Stephen Springston

1) IC measurements of cations: Na+, K+, NH4+, Ca2+
2) IC measurements of anions:SO42-, NO3-, Cl-, NO2-, oxalate
   IC measurements of TOC in solutions with time resolution of 6 min
3) 3-channel Nox (1 min average)
   NO continuous 10 ppt DL
   NOx continuous 20-30 ppt DL
   NOy/NOy* (switching each minute) ~75 PPT DL
4) Carbon Monoxide - non dispersive infra-red (30 sec response) ~50 ppb DL (1-5 min avg)

5) Ozone - ultraviolet absorption (10 sec response)~ 5 ppb DL (1-5 min avg)
6) Sulfur Dioxide - Pulsed fluorescence (30 to 60 sec response time) ~ 30-50 ppt (1-5 min avg)

Carnegie Mellon University - Spyros Pandis
TSI-SMPS 0.02 to 0.6 um, electrostatic classification, run dry

Philadelphia Air Management Services - Fred Hauptman, Lori Condon (AMS)
Speciation Air Sampling System - $PM_{2.5}$ mass, trace metals, organic and elemental carbon, sulfate, nitrate, and other ions/elements

EPA-RTP (NERL-Atmospheric Chemistry and Physics Branch)
Investigators: Edward Edney, Ron Speer, Walt Weathers (EPA); Tad Kleindienst, Shawn Conver, Eric Corse (ManTech Environmental Technology, Inc.)
1) Integrated EC/OC sample: Triple quartz filters, Thermo-Optical Technique.
2) Liquid Water Content of $PM_{2.5}$, Inorganic Anions, Diacids: Teflon filter collection; liquid water analyzer, IC analysis.
3) IR analysis of $PM_{2.5}$: Low pressure impactor-Reflectance FTIR (size cut points 4, 2, 1, 0.5, 0.25, 0.13, 0.063 :m)
4) Detailed Organic Analysis (1): Extractable organic denuder (Aromatic and natural hydrocarbon oxidation products and other polar compounds)
5) Detailed Organic Analysis (2): Carbon-based organic denuder

5.2 Extinction Profiles

The results described here are taken from lidar measurements during the NE-OPS campaigns 1998, 1999 and 2001, and comparisons are made with data obtained by several other instruments at the same time and location.

Figure 5.1 and Figure 5.2 show examples of the typical raw lidar turn signals at 607 nm, 530 nm and 284 nm, together with the corresponding raw lidar aerosol extinction profiles measured. The results shown in Figure 5.1 are taken from measurements on 10 July 1999 02:00-03:00 UTC, which was a time when the atmosphere was relatively clean. The standard deviation of the statistical error is included to show the data accuracy. The blue, green and red curves represent the return signal at 284nm, 530nm and 607nm, respectively. These three wavelengths are used to measure the optical extinction profiles. The magenta curve represents the scale height of the atmospheric density, which is a decreasing exponential function. The pressure scale height is determined from the gravitational distribution by using the hydrostatic equation. The number density scale height only differs from the pressure scale height by the effect of the temperature profiles. However, the temperature gradient of the lower atmosphere is a rather slowly varying profile. The largest changes in the lower atmosphere temperature occur during the formation of the nocturnal inversion, because the thermodynamic structure in the troposphere is mostly dependent upon solar heating of the surface. The number density scale height profile

shown in Figure 5.1(a) is a typical example which corresponds to a linear temperature model. The model profile is normalized to lidar return signal at ground level for comparison. The slope of the lidar returns will be parallel to the slope of scale height where the optical extinction is negligible. The differences in the slope between lidar returns and the molecular scale height provide a measure of the aerosol extinction (scattering and absorption), and the molecular extinction (scattering and absorption) of chemical species in the atmosphere. Figure 5.1(b) shows the extinction at the three different wavelengths 284 nm, 530 nm, and 607 nm measured during the same time period. The extinction was calculated using the algorithm discussed in Chapter 2. Aerosol scattering is the primary contribution to the optical extinction profiles at the visible wavelengths of 530 nm and 607 nm. The extinction values at visible wavelengths are much less than at the 284 nm channel because of the larger cross-section at ultraviolet wavelengths due to scattering by molecules and aerosols, and due to absorption by ozone. Extinction due to molecular scattering is easily calculated and that signal is removed to examine the aerosol scattering properties. At visible wavelengths, the difference from the density scale height is primarily due to aerosol scattering. Extinction values due to absorption by both molecules and aerosols at the 530nm and 607nm wavelength is generally considered to be small and in most cases it is negligible. For example, the largest absorption is due to ozone Chappuis band absorption at the visible wavelengths, and it corresponds to less than 0.001 km^{-1} for ozone concentrations of 50 ppb. The measurements provide profiles of extinction due to aerosol scattering at 530 nm and 607 nm. However, we can not neglect the ozone absorption at the wavelength of 284 nm. The extinction profile at 284 nm, which is shown in Figure 5.1, includes both the aerosol extinction and ozone absorption. We will discuss the effect of ozone absorption later in this chapter. The results in Figure 5.2 are measurements on 25 July 2001 at 01:00-02:00 UTC, and provide another example of comparison of raw data and extinction profiles. In both Figure 5.1 and Figure 5.2, the relatively high extinction values at visible wavelengths at altitude below 500 m are due to the night time boundary layer. In Figure 5.2(b), the small extinction values (about 0.02 above 2 km) from visible channels at 530 nm and 607 nm indicate clear atmospheric conditions. Note that in the clear atmosphere above 2 km shown in Figure 5.2 (a), the slope of the 530 and 607 profiles is parallel with the neutral density scale height.

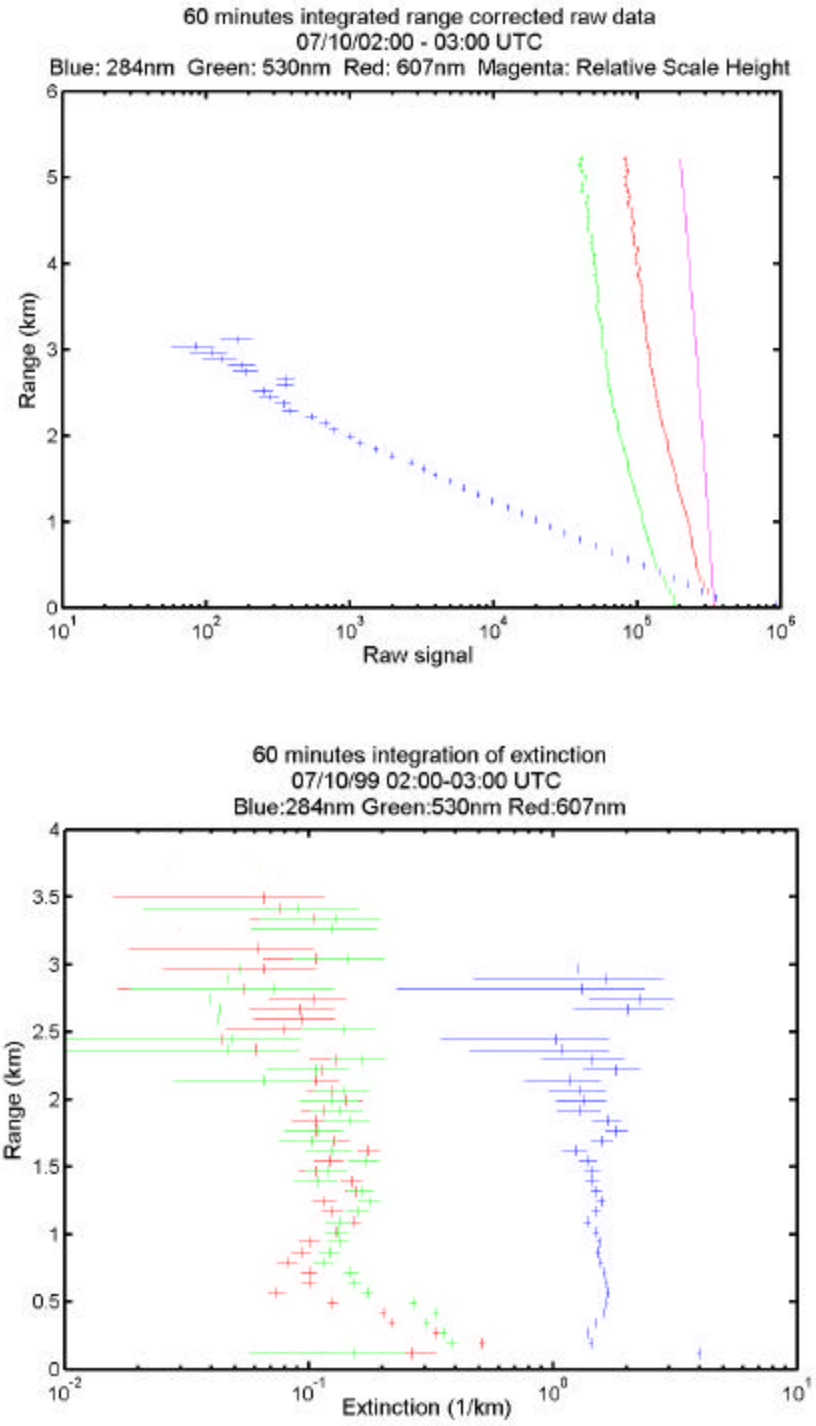

Figure 5.1. (a) Examples of 60 minutes integration of range corrected raw data from lidar return signal of 607nm, 530nm and 284nm taken from NEOPS 99. (b) Examples of 60 minutes integration of extinction profiles from the same time period.

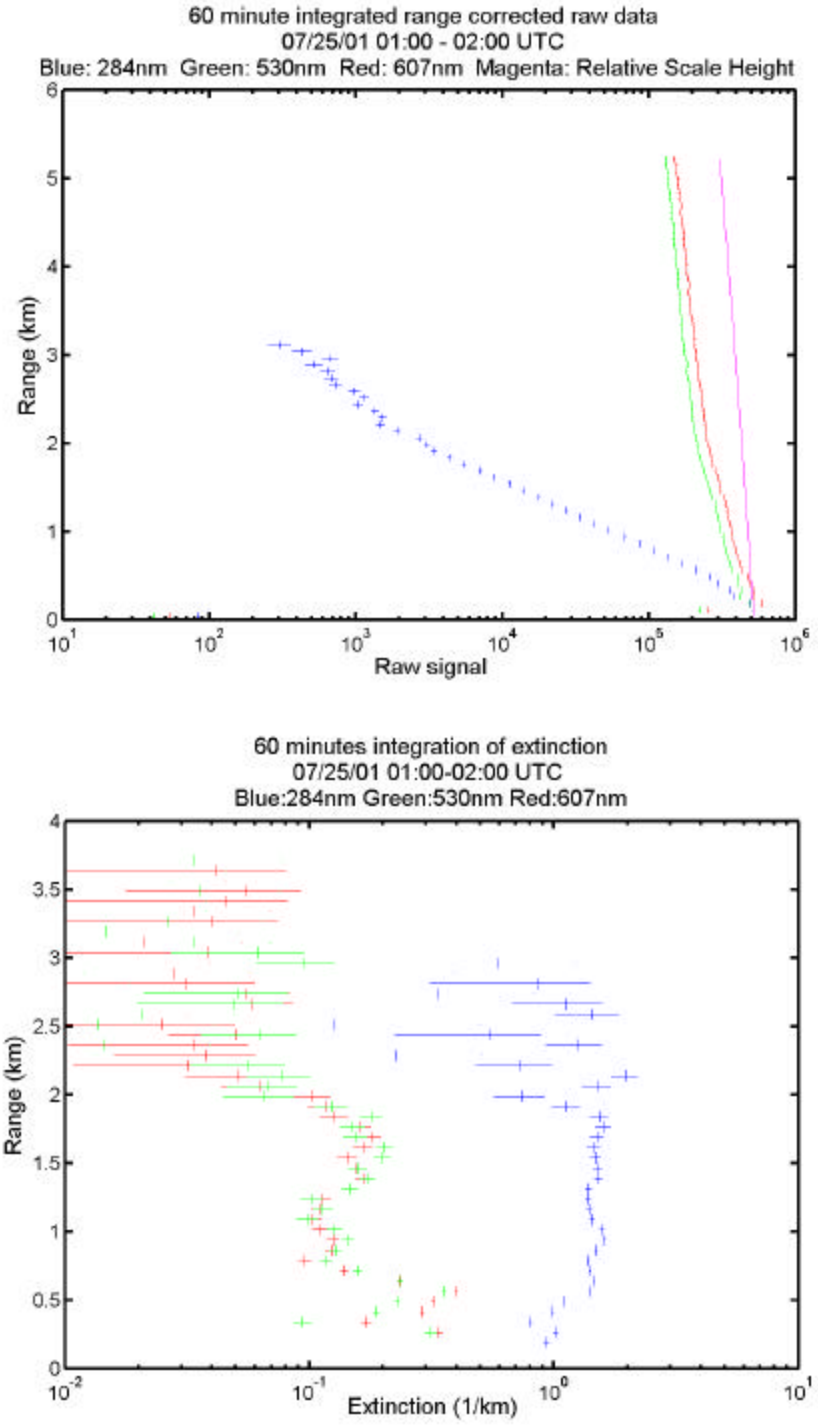

Figure 5.2. (a) Examples of 60 minutes integration of range corrected raw data from lidar return signals of 607nm, 530nm and 284nm taken from NEOPS 2001. (b) Examples of 60 minutes integration of extinction profiles from the same time period.

5.3 Effect of Ozone Absorption on Extinction

LAPS can measure three extinction profiles at these wavelengths of 284, 530 and 607 nm. The absorption can be considered negligible at visible wavelengths, 530 nm and 607 nm, but the ozone absorption coefficient at ultraviolet wavelength is large. At the transmit wavelength of 266 nm and return at 284 nm, the absorption due to Hartley band absorption is quite significant. To investigate the aerosol extinction at UV wavelengths, we need to remove the ozone absorption from the total extinction profile.

The Hartley absorption band of ozone is shown in Figure 5.3 with the Raman wavelengths indicated. The figure shows the absorption cross sections at 284 nm (nitrogen Raman scattering) and 266 nm (transmit wavelength), which are actually measured to be 0.2854×10^{-17} cm^2 and 0.85×10^{-17} cm^2, respectively.

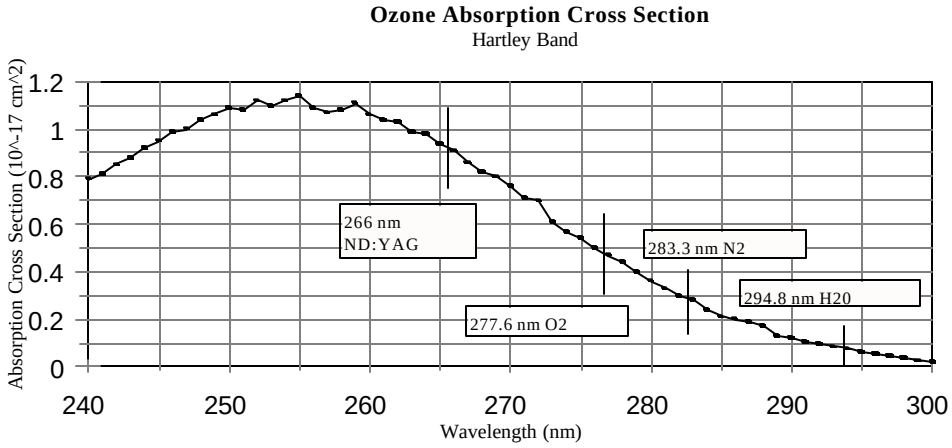

Figure 5.3. Hartley band absorption cross-section of ozone is shown with wavelengths associated with the lidar's 266 nm transmission and its associated Raman-shifted wavelengths used to measure ozone concentration [Philbrick 1998a using the data of Inn, et. al., 1953].

Figure 5.4 (a) and (b) shows an example from measurements on 21 August 1998 for a 60 minute integrated profile of ozone and the corresponding extinction profile at UV wavelengths. We choose this time period because it represents a typical pollution episode when precursor materials were transported into the region and thermally dissociated in the higher temperatures of the surface layer as it was mixed down. Figure 5.4 (c) shows the corresponding water vapor mixing ratio profile during

a 6 hour time period from 6:00 to 12:00 UTC. We observed from the water vapor time sequence that there is a water vapor layer at 1 km above the ground between 10:00 and 11:00 UTC, which corresponds to the peak at 1 km in extinction and ozone results. Specific humidity is a good tracer of the optical extinction in regions where hydroscopic aerosols make up a significant fraction of the particulate matter. An increased extinction can correspond to an increase both in ozone absorption and PM scattering. High ozone concentrations contribute significantly to the extinction, for example, 100 ppb contributes about 0.8 km^{-1}. As we have described in Section 3.4, the ozone profile can be calculated from LAPS by differentiating the ratio of signals from the vibrational Raman shift of oxygen/nitrogen (277 nm/284 nm). We can obtain the aerosol extinction at 284 nm by subtracting the ozone absorption from the total extinction profile. But this method is not applicable sometimes due to large errors in ozone calculation, where increased errors in the ozone are caused by the differential algorithm. The calculation of the corrected extinction can be obtained directly from the ratio of signals (277 nm / 284 nm).

Figure 5.5 (a) shows another example of extinction profiles on 08 July 1999 02:00-03:00 UTC. The small extinction values from visible channels (530 nm and 607 nm) indicate that it is a clear night. The difference between the aerosol extinction and total extinction at 284nm shows the effect of ozone on extinction in the UV region. However, above 1 kilometer altitude the extinction value at 284 nm is relatively large compared with the small values of extinction at 530 nm and 607 nm. It indicates that there is a haze layer or sub-visual cloud above 1 kilometer altitude, the particles in this layer are small enough that the extinction is more sensitive at the short wavelengths compared to the visible wavelengths. Figure 5.5(b) shows the time sequence water vapor mixing ratio measurements during that night. The figure shows a water vapor cloud layer above 1 kilometer which thickens after 1:00 UTC. The relatively small extinction at visible wavelengths indicates that this cloud layer would not be observed visually.

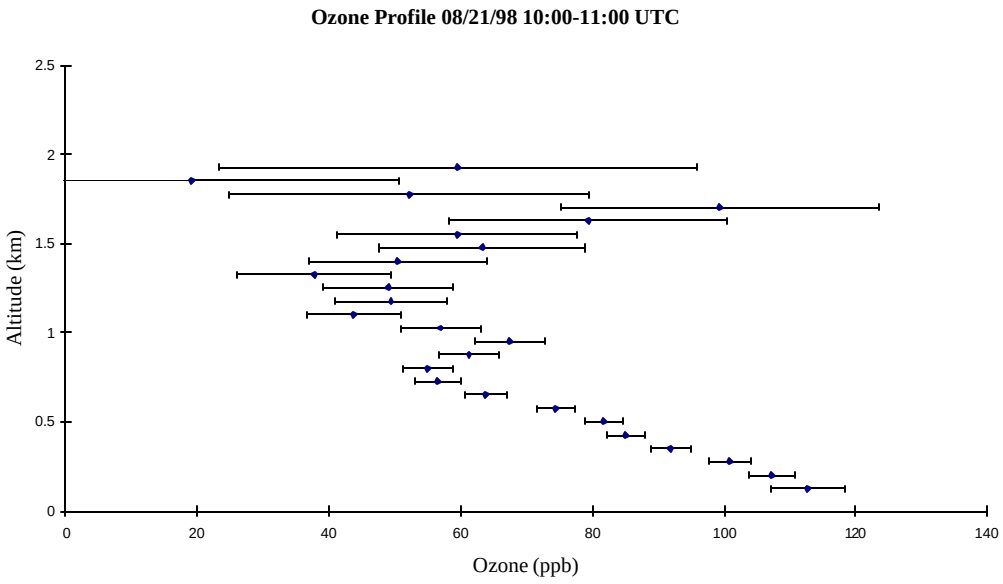

(a) Ozone profile

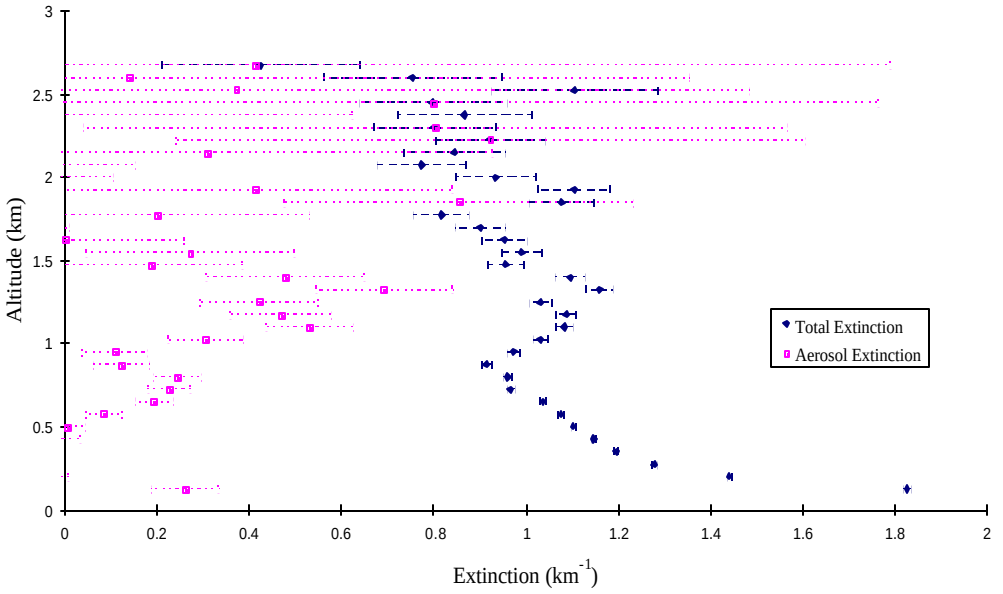

(b) Extinction profile

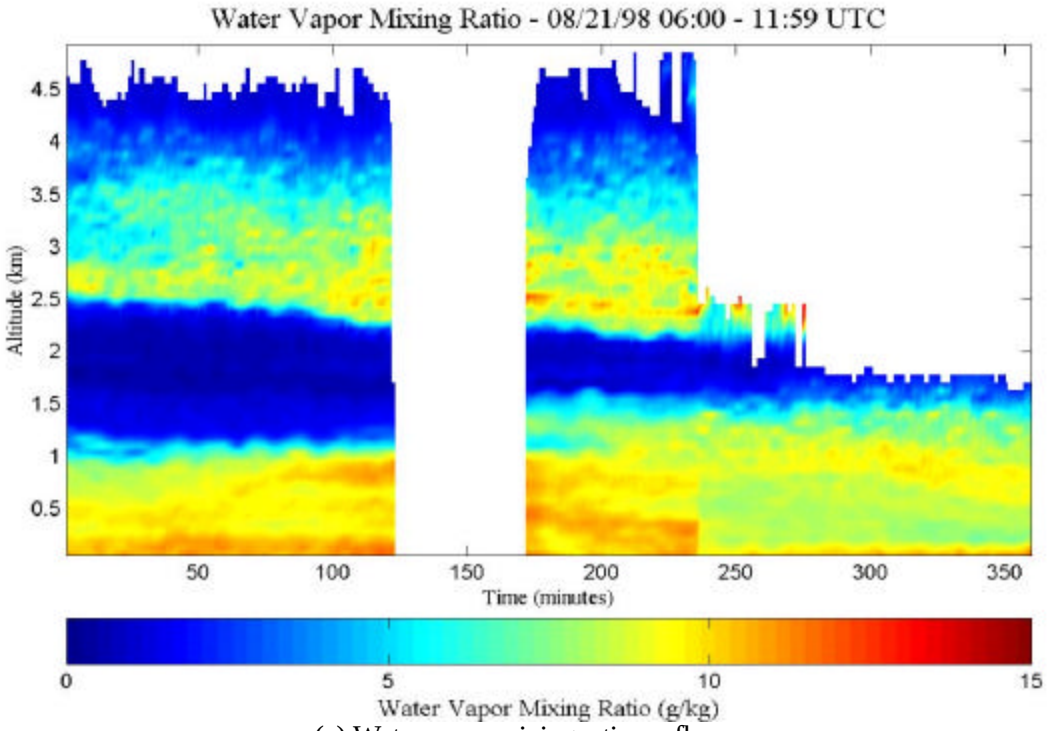

(c) Water vapor mixing ratio profle

Figure 5.4. Raman lidar 60 minutes integration of (a) ozone, and (b) total extinction and aerosol extinction profiles at 284nm on 21 August 1998 10:00 – 11:00 UTC, (c) time sequence water vapor mixing ratio on 21 August 1998 06:00 – 12:00 UTC.

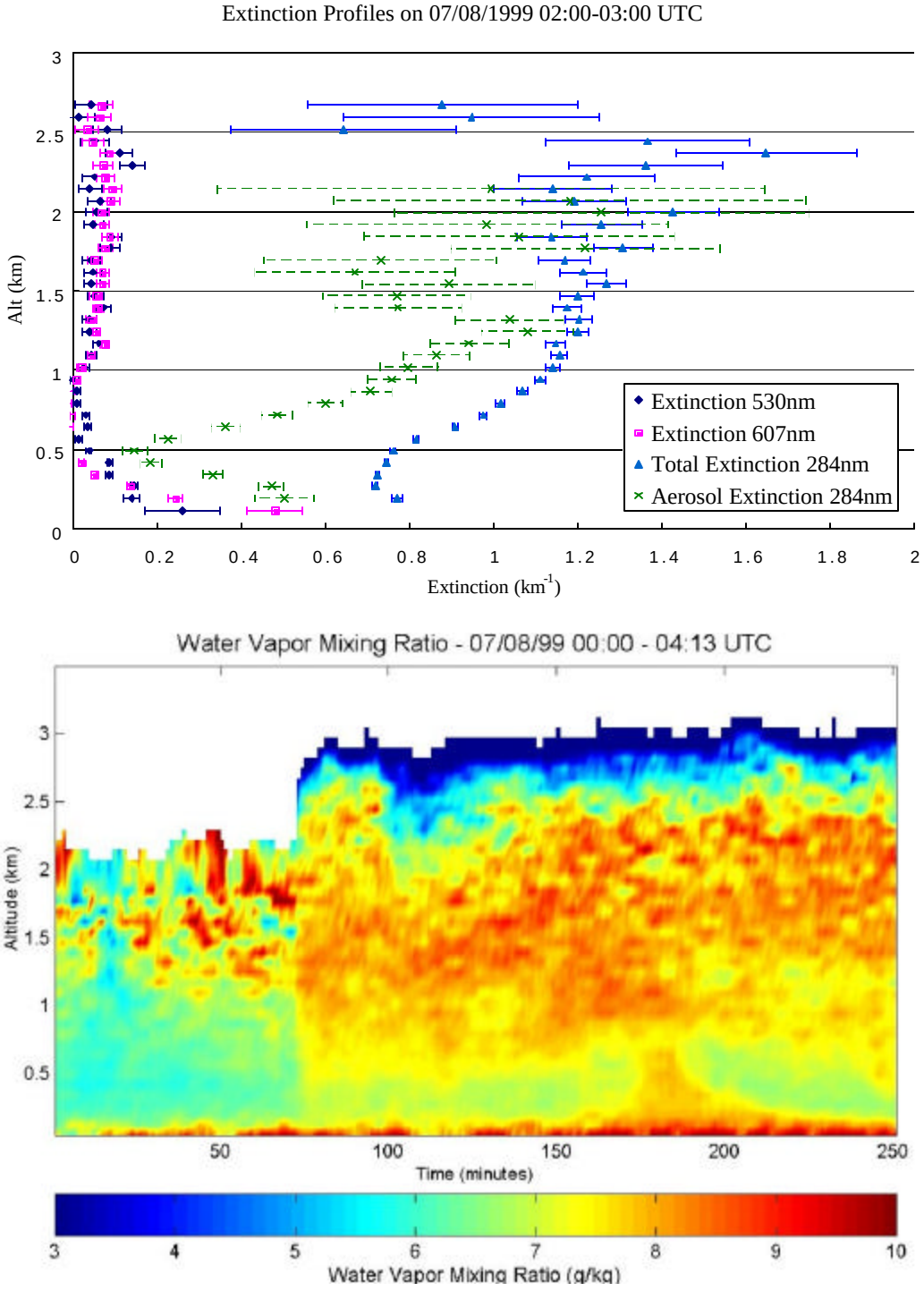

Figure 5.5. (a) 60 minutes integration of extinction profiles at 284nm, 530nm and 607nm on 08 July 1999 02:00 – 03:00 UTC (b) Time sequence water vapor profile on 08 July 1999 00:00 – 4:13 UTC.

5.4 Effect of Relative Humidity on Extinction

Water is an important component of atmospheric aerosols. Most of the water associated with atmospheric particles is chemically unbound. At very low relative humidity, atmospheric aerosol particles are solid. As the relative humidity increases, the particle remains solid and water vapor may attach to gradually form large particles until the relative humidity reaches a threshold value characteristic of the aerosol composition. At this relative humidity, the solid particle absorbs water, producing a saturated aqueous solution. The relative humidity at which this phase transition occurs is known as deliquescence relative humidity [Seinfeld, 1998 pp 508]. The relative humidity for deliquescence of some chemical species common in atmospheric aerosols is given in Table 5.2. The most abundant chemical species in the aerosols of the Eastern United States have the threshold of deliquescence at a relative humidity of about 80% [Seinfeld, 1998 pp 508].

The accumulation mode is described by the accumulation of ultra fine particles (<0.1 μm) to form larger particles. Particles tend to coagulate at high relative humidity, above the critical saturation ratio of the particle. Water vapor content and temperature are the important factors in determining the optical extinction because of the humidity influence on the size distribution of the particulate matter. Extinction is thus strongly correlated with relative humidity. A number of data sets have demonstrated that there is a sharp change in extinction at around the deliquescence point. This point corresponds to a relative humidity of about 80% for sulfate aerosols. Particle sizes in the accumulation mode (0.1 to 2μ) are most easily detected with lidar. Figures 5.6 and 5.7 show low altitude extinction from the 284nm channels for various periods compared with relative humidity.

Table5.2. Deliquescence Relative Humidity of Some Chemical Species at 298K

Salt	DRH (%)
KCl	84.2 ± 0.3
Na_2SO_4	84.2 ± 0.4
NH_4Cl	80.0
$(NH_4)_2SO_4$	79.9 ± 0.5
NaCl	75.3 ± 0.1
$NaNO_3$	74.3 ± 0.4
$(NH_4)_3H(SO_4)_2$	69.0
NH_4NO_3	61.8
$NaHSO_4$	52.0
NH_4HSO_4	40.0

Sources: Tang (1980) and Tang and Munkelwitz (1993).

Figure 5.6(a) shows the rise and fall in extinction corresponding to the relative humidity transitions, through the threshold of 80 %. The extinction increases from less than 1 km^{-1} to 5 km^{-1} as the relative humidity increases to values greater than 80%. Figure 5.6(b) (c) and (d) show the vertical profiles of water vapor mixing ratio, relative humidity and extinction respectively. In Figure 5.6(d) we can see the corresponding rise in extinction near the ground. Another time period showing a similar atmospheric effect is presented in Figure 5.7. Figure 5.7(a) shows the fall in extinction corresponding to the relative humidity falls in the early morning, through the threshold of 80 %. Figure 5.7(b) (c) and (d) show the vertical profiles of water vapor mixing ratio, relative humidity and extinction respectively. In Figure 5.7(d) we can see the corresponding rise and decrease in extinction near the ground. For both these time periods we can clearly see the strong correlation between extinction and relative humidity. However, we observed a variation in extinction which is not corresponding to the change in relative humidity during the afternoon of 1 August 1600 – 2200 UTC in Figure 5.7(a). The variation in extinction at 284 nm is observed to be due to the increase of ozone density in the afternoon. The peak value of this 80 ppb ozone should increase the extinction by 1 km^{-1}. The ground ozone measurement by Millersville University from the same time is shown in Figure 5.7(e).

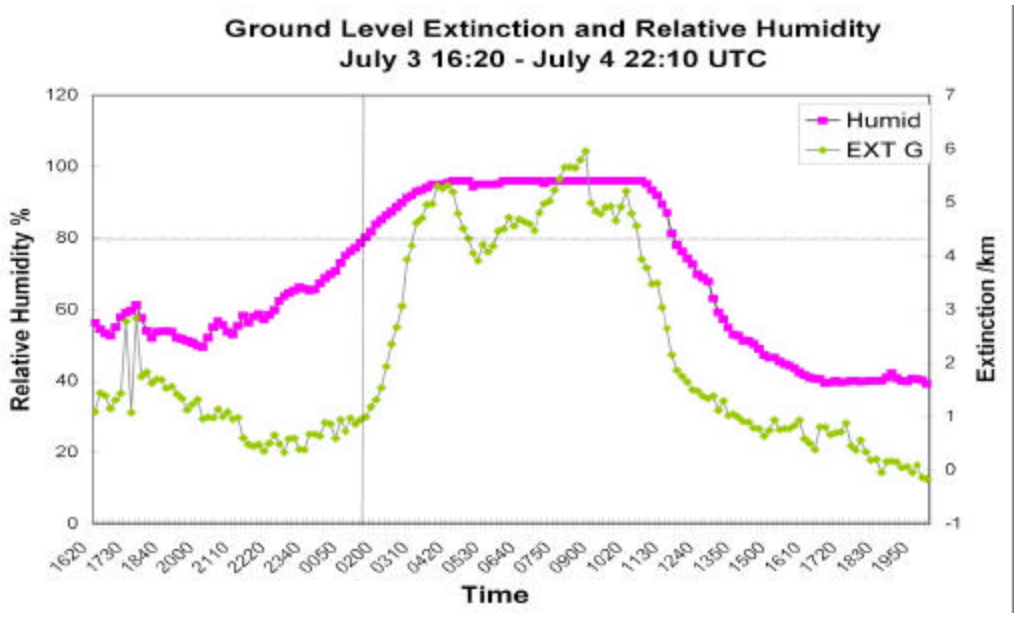

(a)

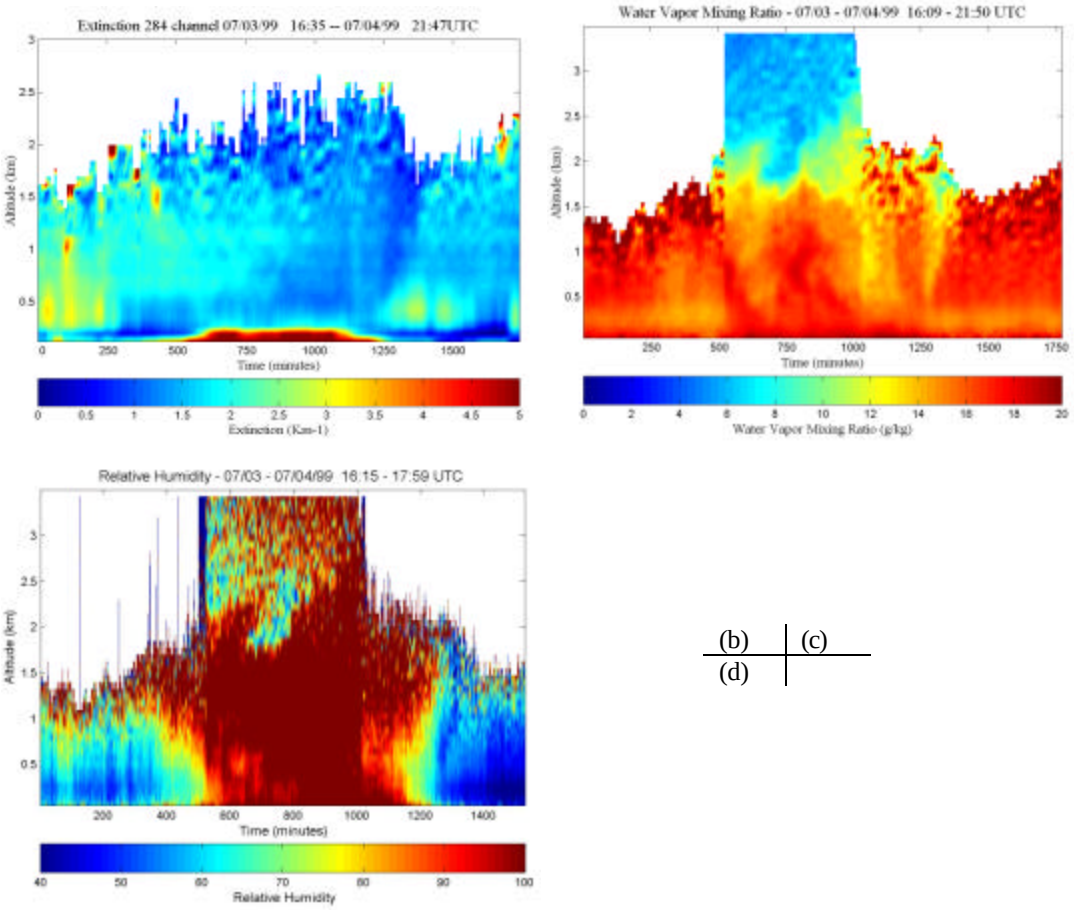

(b) | (c)
(d) |

Figure 5.6. (a) Ground level extinction and relative humidity, and (b) Water vapor mixing ratio, (c) Relative humidity, (d)Vertical extinction profile, for the time period 07/03/99 16:20 – 07/04/99 22:00 UTC.

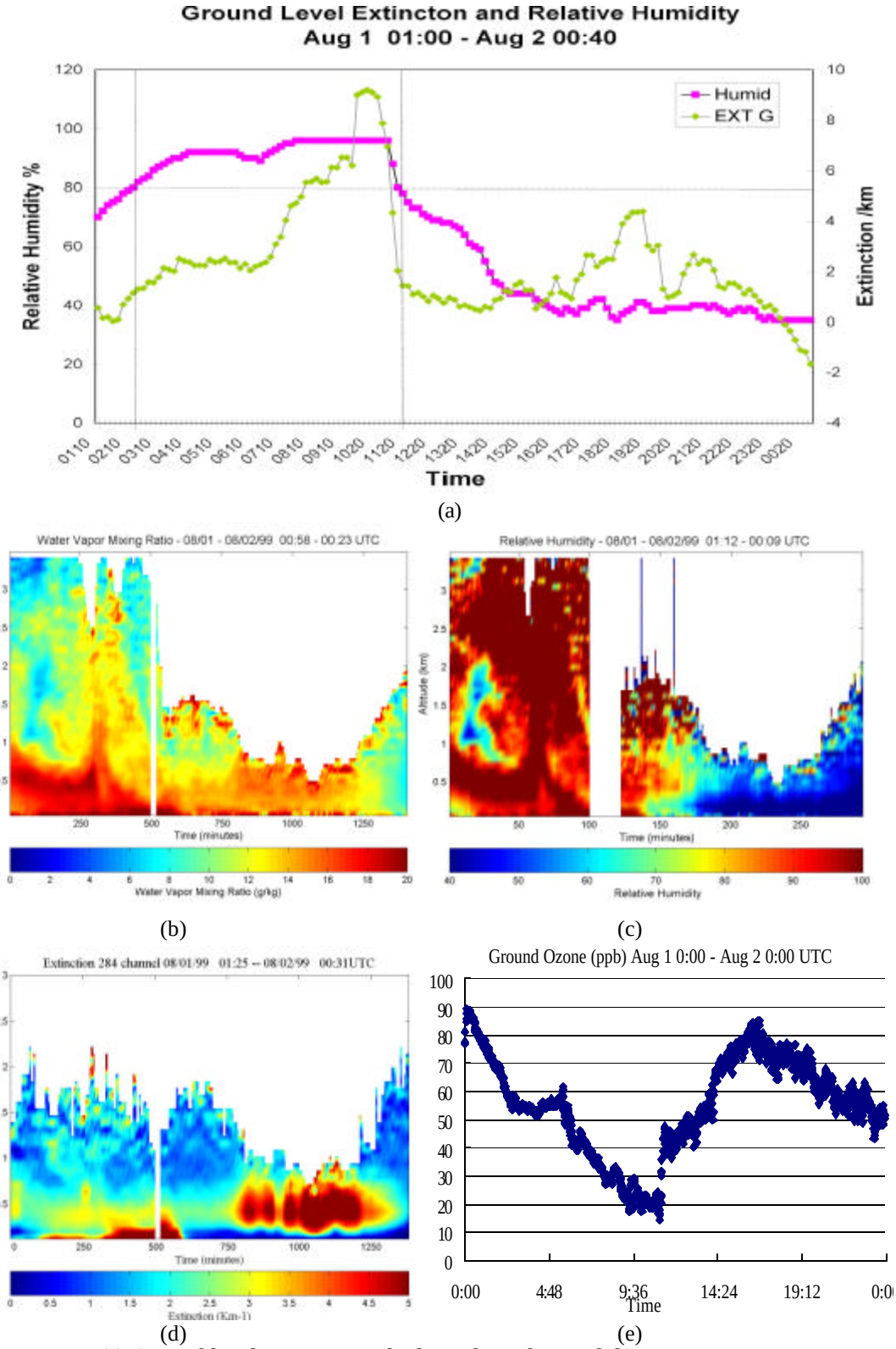

Fig. 5.7. (a) Ground level extinction and relative humidity, and (b) Water vapor mixing ratio, (c) Relative humidity, (d)Vertical extinction profile, (e) Ground ozone measurement from Millersville University for the time period 08/01/99 01:10 – 08/02/99 00:40 UTC.

The lidar measures profiles of water vapor mixing ratio and temperature which can be used to calculate the relative humidity profiles. However, the LAPS lidar is only capable of measuring night time temperature profiles because these measurements are made using the visible channels. To calculate the daytime relative humidity, a simple linear temperature model has been applied which adequately represents the daytime temperature profile most of the time,

$$T(z) = T_0 + 273 - 6.85 \cdot z \tag{5.1}$$

where z is the altitude in kilometers and T_0 is the ground temperature in Celsius measured by LAPS ground sensor. Although this is the simplest model, it has been proven accurate enough for our calculation of the daytime temperature profile. The RASS sounding provides another method to obtain the temperature measurements. In Figures 5.8(a) and 5.9(a), the profiles of LAPS data (blue curves) show 30 minutes integration temperature profiles of rotational Raman compared with the model temperature (red curves) during nighttime. The nighttime temperature profiles shown here are expected to exhibit poorer correlation with the simple model than the daytime profile because of the temperature variations of the nocturnal inversion. The daytime temperature profile is governed by the buoyant forcing of the warmer layer below and thus follows a profile with a constant gradient from the surface.

The pressure profiles as a function of altitude can be calculated as follows,

$$P(z) = P_0 \cdot \exp(-\frac{z}{H(z)}) \tag{5.2}$$

P(z) represents the pressure as a function of altitude, P_0 is the pressure at ground measured by LAPS ground sensor, and *H(z)* is scale height defined by $H(z) = RT(z)/g$. R = 287.05 $Jkg^{-1}K^{-1}$ is the gas constant for dry air. The relative humidity can be calculated as follows from the ratio of the actual, E_{act}, to saturated, E_{sat},

$$Esat(z) = 6.112 \cdot \exp(17.62 \cdot (\frac{T(z)}{T(z) + 243.5})) \tag{5.3a}$$

$$Eact = Wat(z) \cdot P(z)/0.622/1000 \tag{5.3b}$$

$$RH = \frac{Eact}{Esat} \cdot 100 \tag{5.3c}$$

where *Wat(z)* represents water vapor mixing ratio in g/kg, and *RH* is the relative humidity in percentage.

Figures 5.8(b) and 5.9(b) show the results calculated from Equation 5.1 – Equation 5.3. Although the temperature profiles calculated from linear model can not perfectly fit the profiles from LAPS measurements, the linear model has been proved in these results to be accurate enough to show the structure of variation in the relative humidity in atmosphere. These cases comparing the nighttime conditions actually represent worse cases, because the daytime temperature profile generally has more uniform gradient from the surface up through the troposphere because of convective mixing.

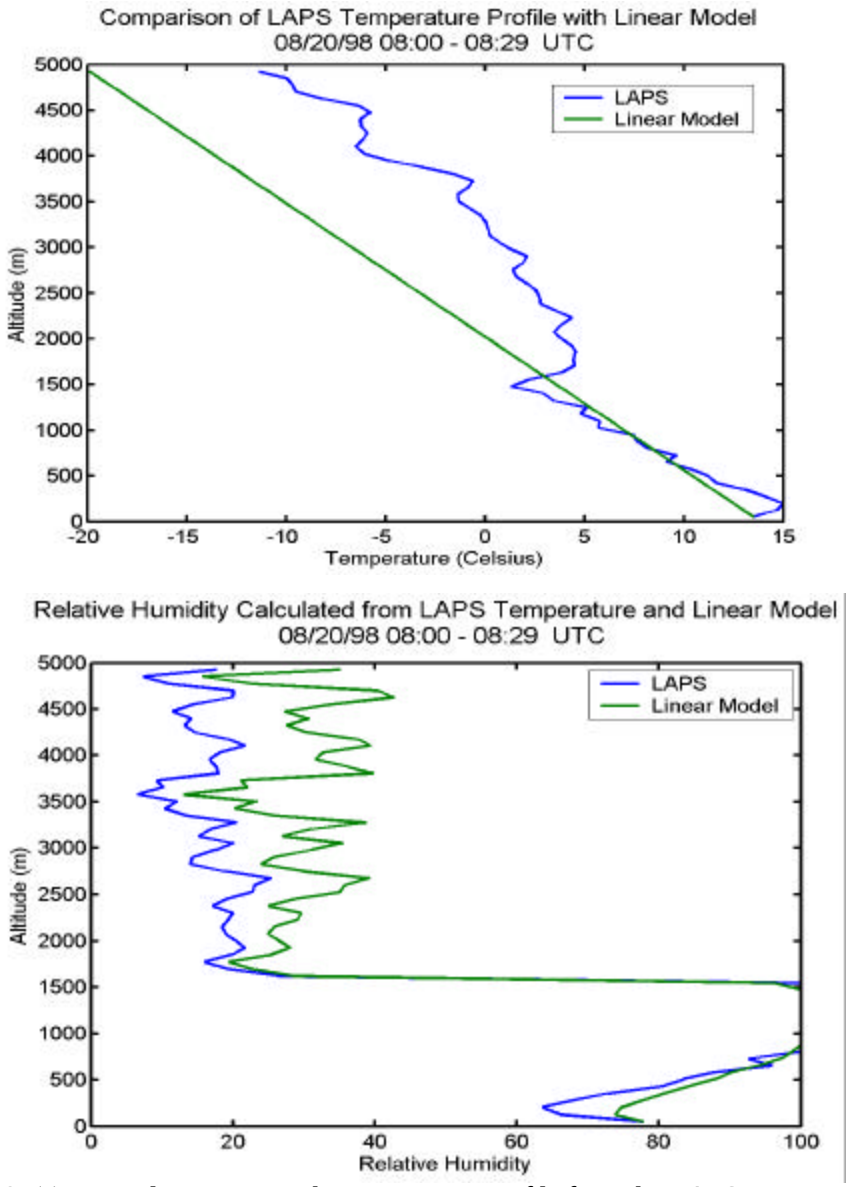

Figure 5.8. (a) Example comparing the temperature profile from the LAPS measurement with the linear model in Equation 5.1 on 20 August 1998 08:00 – 08:29 UTC. (b) Calculated relative humidity from the LAPS temperature profile and from the linear model at the same time period.

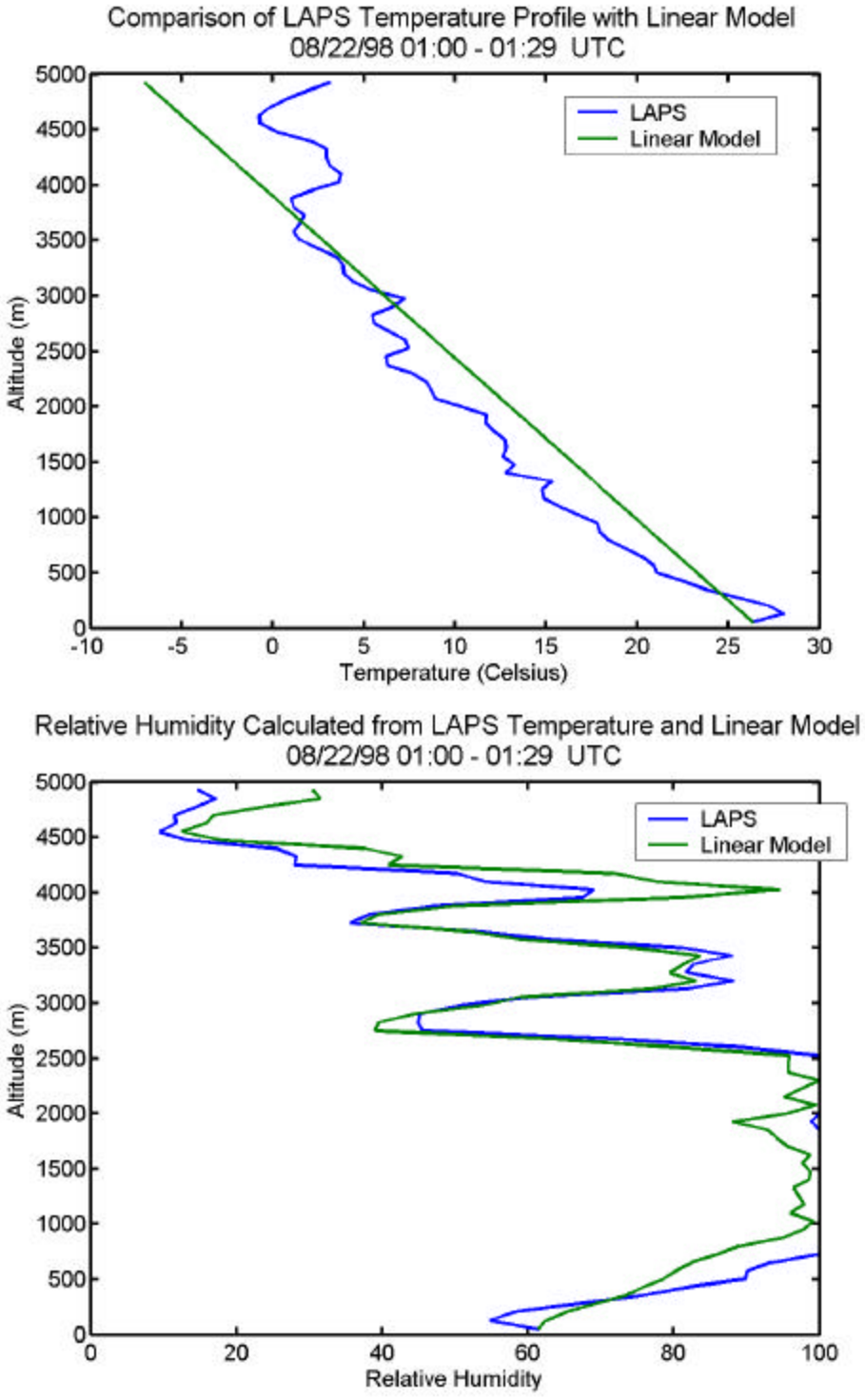

Figure 5.9. (a) Example comparing the temperature profile from the LAPS measurement with the linear model in Equation 5.1 on 21 August 1998 01:00 – 01:29 UTC. (b) Calculated relative humidity from the LAPS temperature profile and from the linear model at the same time period.

5.5 A Pollution Episode Analysis

The results shown in Figure 5.10 are taken from the time period of the major air pollution episode that occurred in the region during the summer of 1998. A set of 24 hour time sequences, which depict the water vapor, ozone and optical extinction for the period from 12 hours UTC on 21 August to 12 hours UTC on 22 August 1998, capture some interesting features of an air pollution episode. An elevated layer, which is observed to mix down with the rising boundary layer at 17 UTC (1 PM local), appears to trigger an air pollution event which results in high concentrations of ozone and airborne particulate matter.

The measurements of the profiles of water vapor, ozone and optical extinction at 284 nm are shown for a 24 hour period on 21 and 22 August 1998. The water vapor mixing ratio and relative humidity results are shown for 1 minute time steps with 5 minute smoothing. The results of relative humidity and specific humidity (water vapor mixing ratio) show the convective plumes as they move past the vertical beam of the lidar during the morning hours of 21 August. Between 1600 and 1700 UTC (12 - 1 PM local time), the elevated layer meets and mixes with the rising boundary layer. Back trajectories of the air mass show that it originated in the mid-west industrialized region. The ozone and optical extinction measurements show an interesting response to the arrival of the air mass which initiates the air pollution event with increases in ozone and PM due to the precursor chemicals contained in the air mass. The extinction profile shown here is the total extinction, which includes significant ozone absorption. During the nighttime period, shown near the middle of the second panel, the background wind began to dissipate and redistribute the ozone and particulate matter. As shown in the time sequence of relative humidity, the RH value is almost 100 percent for the lower atmosphere from ground to 2km during the night of August 22. However, the extinction follows the specific humidity during the same time, and indicates that the specific humidity is a good tracer of the dynamics and thus describes the location of the PM particles. Since the region contains maximum relative humidity, the aerosol particles distributions will grow to equilibrium size wherever the particles are located, thus the optical extinction and the specific humidity are well correlated.

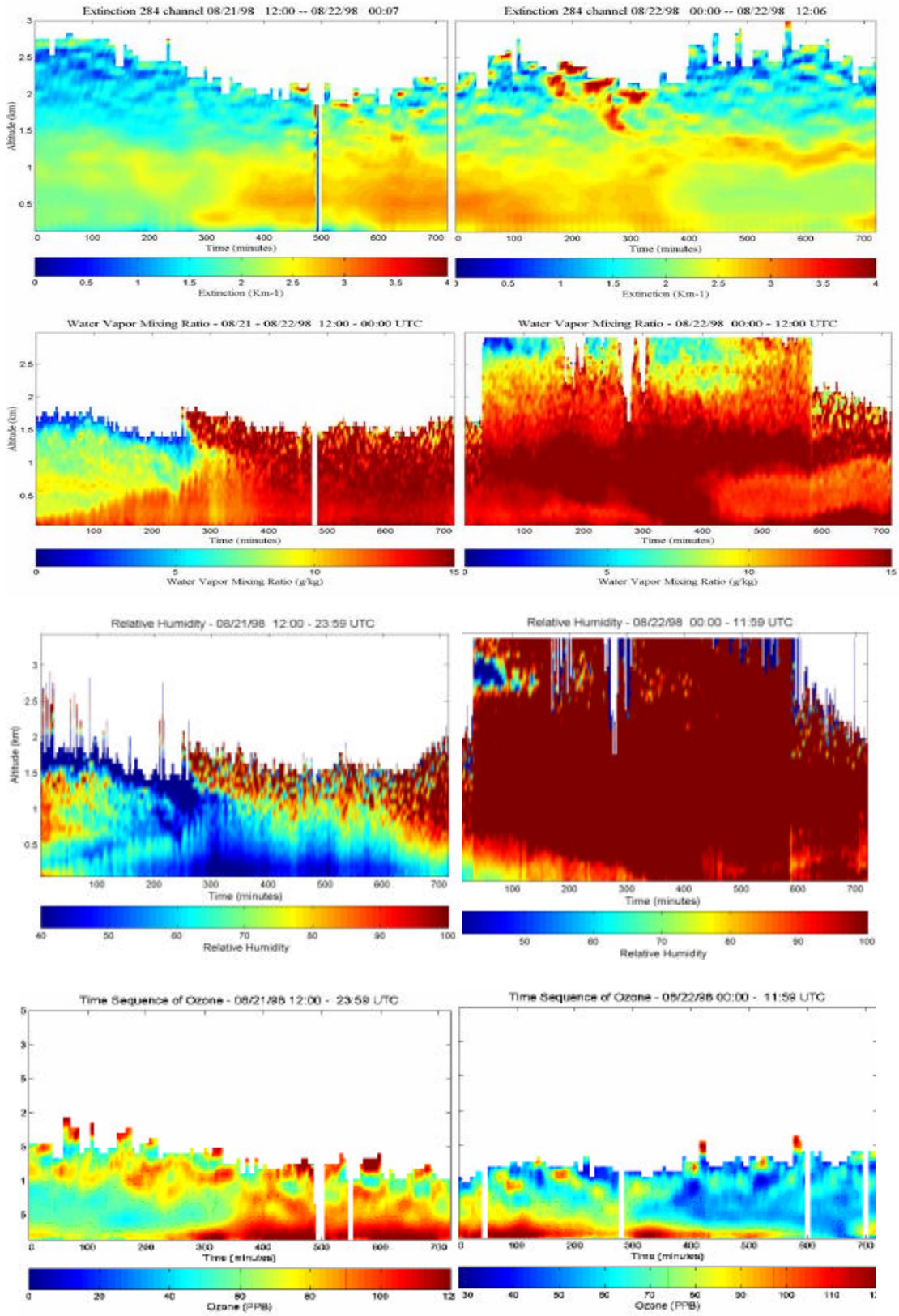

Figure 5.10. Pollution episode study for the time period from 12 hours UTC on 21 August to 12 hours UTC on 22 August 1998.

5.6 Aerosol Variations at Sunrise and Sunset

Figure 5.11 and 5.12 show examples of the variations in the aerosol density that have been found to occur at around sunset and sunrise, respectively. Frequent variations in aerosol concentration were observed in a number of data sets during the summer of 1998 and 1999. An increase in optical extinction was observed with some regularity during the morning hours, following sunrise, which may be associated with the daily rise in temperature and humidity or changes in aerosol sources from vehicular traffic and industrial activity. Also, we observed that the optical extinction profiles show a decrease in the extinction with the onset of night time. This again could be attributed to the decrease in the level of human activity, the cessation of convective activity, and/or condensation and settling out of the hydroscopic aerosols at sunset. Soon after sunset, much of the moisture that was distributed by convective turbulent activity shrinks into a nocturnal boundary layer which is only 200 to 400 meters thick, and much of the water content condenses and settles to the surface. The extinction from airborne particulate matter also follows the redistribution associated with the collapse of the convective boundary layer. Water vapor content and temperature are important factors in determining the optical extinction because of the humidity influence on the size of the aerosols, and thus on the optical extinction. The increase and decrease of ozone of about 80 ppb are also observed during the same time periods, that will contribute about the value of 1 km^{-1} to the extinction. This value is not very significant comparing to the peak value of the extinction, which is about 5 km^{-1}.

The results in Figure 5.11, 5.12 show examples time sequences of the Raman lidar extinction profiles at sunrise and sunset, respectively. At sunrise, the moisture which was condensed on the surface during the night is rapidly transferred back into the atmosphere. As the convective activity builds up from the surface heating, the moisture is uniformly mixed through the boundary layer. Human activity also adds fresh particulate matter from mechanical generation of coarse particles and combustion sources for fine particles. The boundary layer frequently exhibits a layer of optical extinction near the top of the layer where the relative humidity is maximum. The convective activity mixes the fine particles and water vapor rather uniformly, however the lower temperature at the top of the mixed layer results in higher relative humidity that condenses and coalesces the particles to form a population of larger particles, thereby increasing the optical extinction.

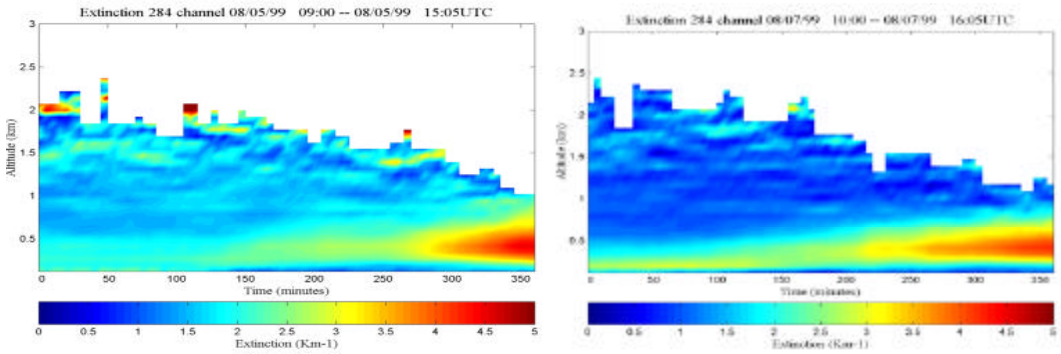

Figure 5.11. Examples of optical extinction time sequence from Raman lidar results at 284 nm which show variations in extinction near local sunrise.

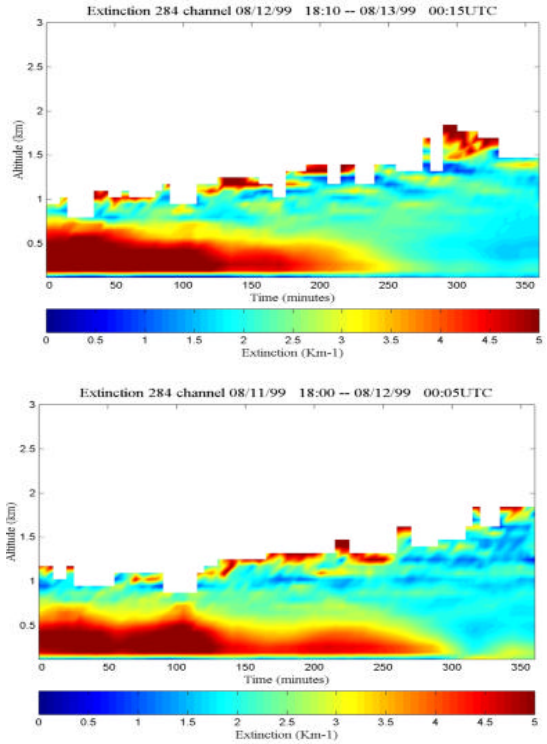

Figure 5.12. Examples of optical extinction time sequence from Raman lidar results at 284 nm which show variations in extinction near local sunset.

During NE-OPS summer 1999 and 2001 campaigns, the rawinsonde sounding technique was used to establish the background meteorology conditions and to provide data to verify the lidar calibration constants. Twenty sondes were relased in 1999 and twelve sondes were released in 2001 to measure the temperature, relative

humidity, pressure and wind speed and the results were compared with lidar measurements. The time sequence of lidar profiles provides more useful and accurate picture of atmospheric structure than single instrumented balloon flights. The summary and comparison of the sonde measurements with lidar is shown in appendix E.

5.7 Correlations of Extinction with PM Measurements

During the NE-OPS summer campaigns of 1998, 1999 and 2001, several research groups measured the particulate matter at the site. Harvard School of Public Health (HSPH) obtained continuous measurements of the surface level particulate matter during each campaign. During summer 1998, $PM_{2.5}$ was sampled using the CAMMS and TEOM instruments, and PM_{10} was sampled using a TEOM instrument. The measurements were obtained continuously from August 3 to August 22 with 10 minute averaging. For several weeks during 1999, the volatile aerosol mass components were measured by Brigham Young University using RAMS and PCBOSS instruments. During summer 1999, $PM_{2.5}$ was sampled using CAMMS continuously from June 28 to August 15 with 10 minute averaging. During summer 2001, $PM_{2.5}$ was sampled using CAMMS continuously from July 1 to August 7 with 10 minutes averaging, particle size distribution was sampled from July 1 to August 1. During the 1999 and 2001 summers, The $PM_{2.5}$ was measured using an optical scatterometer (DustTrak) by Millersville University.

Figure 5.13 shows the summary of PM measurement results by the Harvard School of Public Health during summer NEOPS campaigns in 1999 and 2001. Figure 5.13 (a) shows the summary of ground $PM_{2.5}$ and ozone measurements by HSPH during the summer of 1999. PM measurements were simultaneously performed at the same site location. The summary of PM measurements results from HSPH and Millersville University, and ozone results are shown in Figure 5.13(b). These graphs show that the values of ambient mass concentration measured by Millersville University are higher than the measurement results from HSPH. Measurement of the 'wet mass', particles include the ambient water vapor and represent the optical properties measured by the lidar. Summary of other PM measurements are shown in appendix F.

Particles with diameters less than 2 μm, corresponding to the accumulation range, typically arise from condensation of low volatility vapors and from coagulation of smaller particles in the nuclei range or from the accumulation range. The latter is usually the most important mechanism since the coagulation rates for the particles in the nuclei range with the larger particles in the accumulation range are often much

larger than for self coagulation. Because of the natures of their source, particles in accumulation range generally contain far more organics and soluble inorganics such as, NH_4^+, NO_3^-, SO_4^{2-} [Albritton, et.al., 1998]. Sulfate, in particular, represents a large fraction of particulate matter [Hidy, et.al., 1998]. Since the high ozone concentration always reflects high chemical reactivity, the high SO_4^{2-} with low SO_2 and high O_3 are observed during the summer, due to the active SO_2 oxidation rates. PM levels are strongly correlated with ozone and other pollutants. The variations of PM are used to describe the evolution of the pollution episodes during the campaigns.

During the campaign of 2001, Millersville University used a tethered sonde to measure particulate matter at altitudes 100 m, 200 m, 300 m and at the surface. Figure 5.14 shows sample results of the measurement on two days in July 2001. From both Figure 5.14(a) and Figure 5.14(b), a lot of structure in the time sequence of aerosol concentration is observed at altitudes inside nighttime boundary layer. It is useful to compare model simulations with lidar measurements, because the traditional measurements are all taken at surface. After the time 1000 UTC (6AM local time), we observes the process of mixing of aerosols by surface heating after sunrise, which results in a more uniform concentration of aerosols in the lower atmosphere. The surface measurements taken by Millersville University using a DustTrak are compared with the measurements taken by the CAMMS instrument of HSPH in Figure 5.15. There is a major difference in the measurement method, HSPH measures the 'dry mass', which means that the PM density has been passed through a drier before sampling, and the DustTrak measures the 'ambient mass', which is the measure with water still attached to the particle surface.

Figure 5.15 shows an example that compares wet mass, dry mass and relative humidity at the surface over a period of two days. The relative humidity data shown was taken using the sensor on the top of the LAPS instrument. As shown, the wet mass concentration is strongly correlated with the changes in relative humidity while the dry mass concentration stays fairly constant. The large variations in the ambient mass variation with rising relative humidity may be associated with changes in the signals measured by the optical scatterometer as the deliquesce of the aerosol changes it optical scattering characteristics.

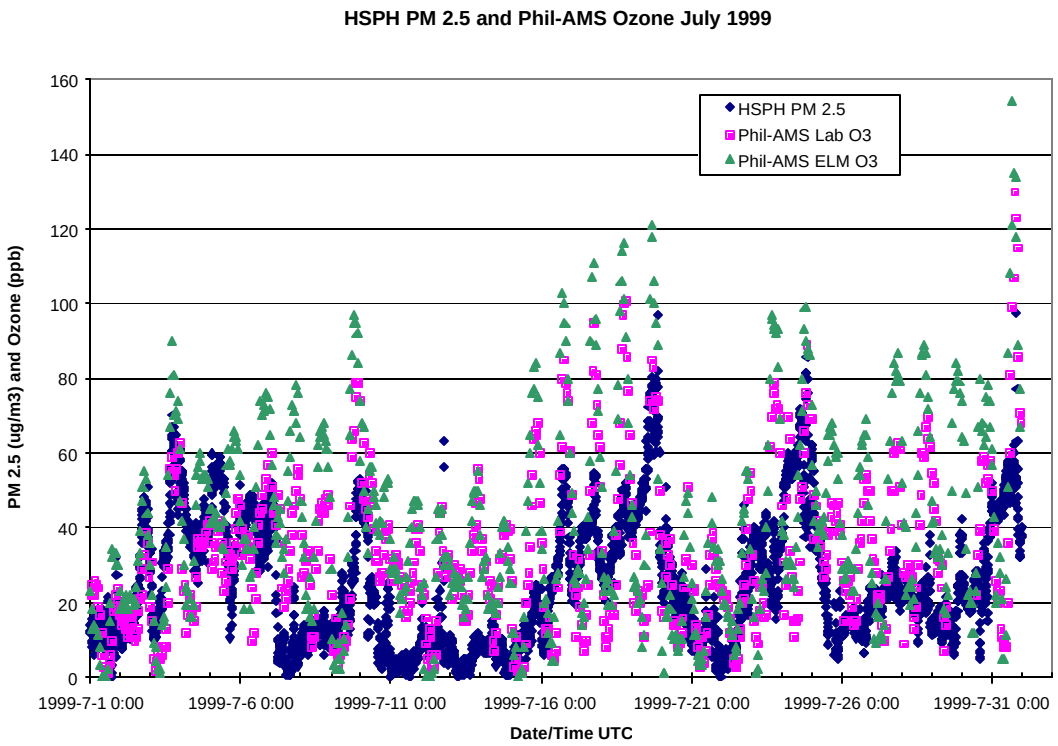

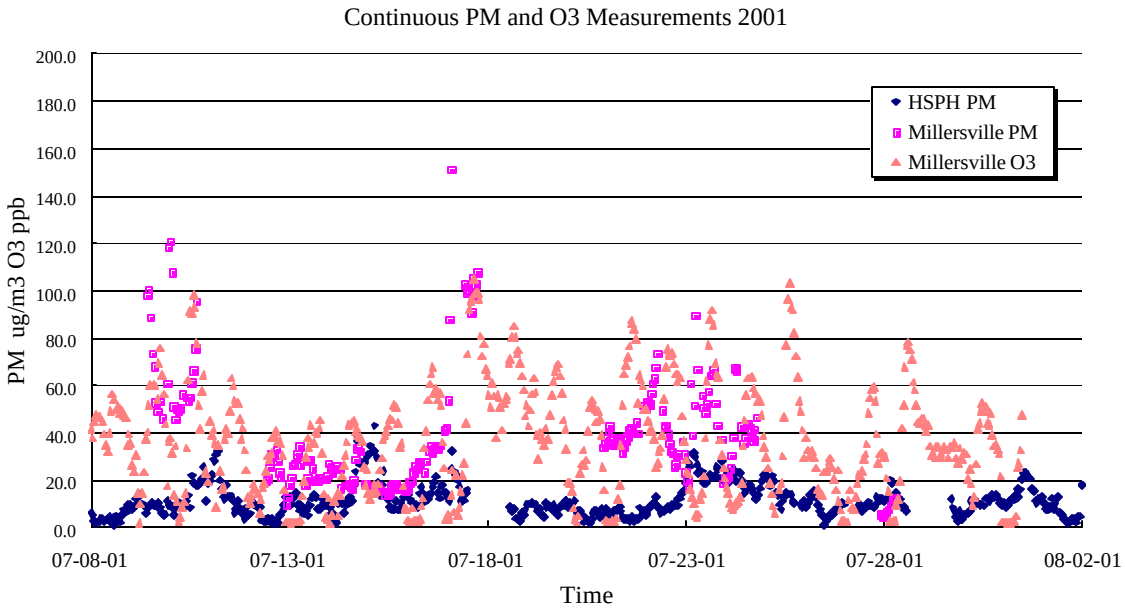

Figure 5.13. (a) Summary of PM and O3 measurements by HSPH during NEOPS 1999 summer campaign, (b) Summary of PM measurement by HSPH during NEOPS 2001 summer campaign.

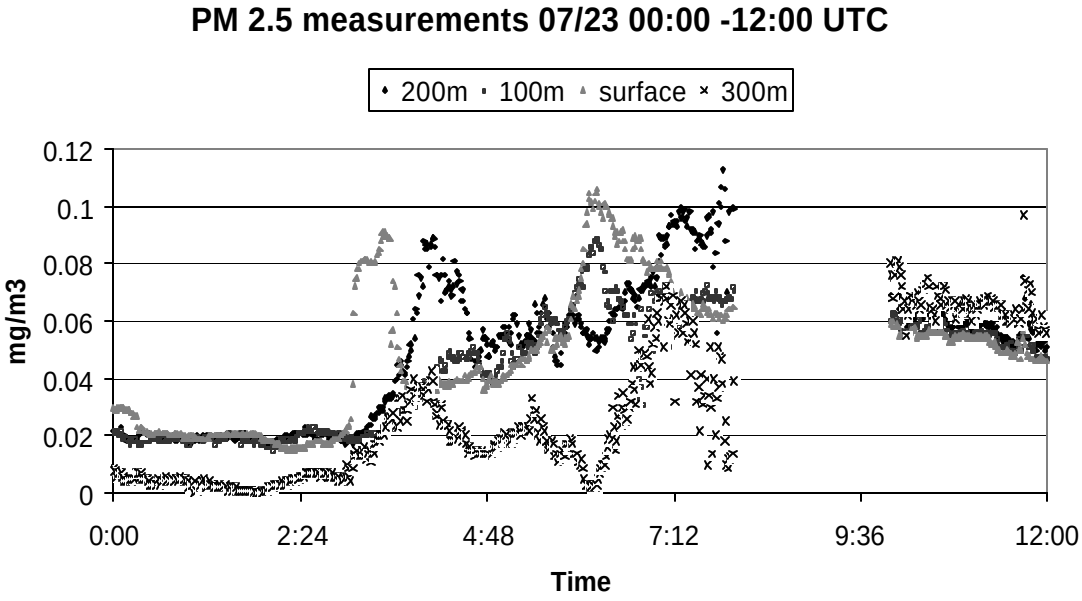

(a)

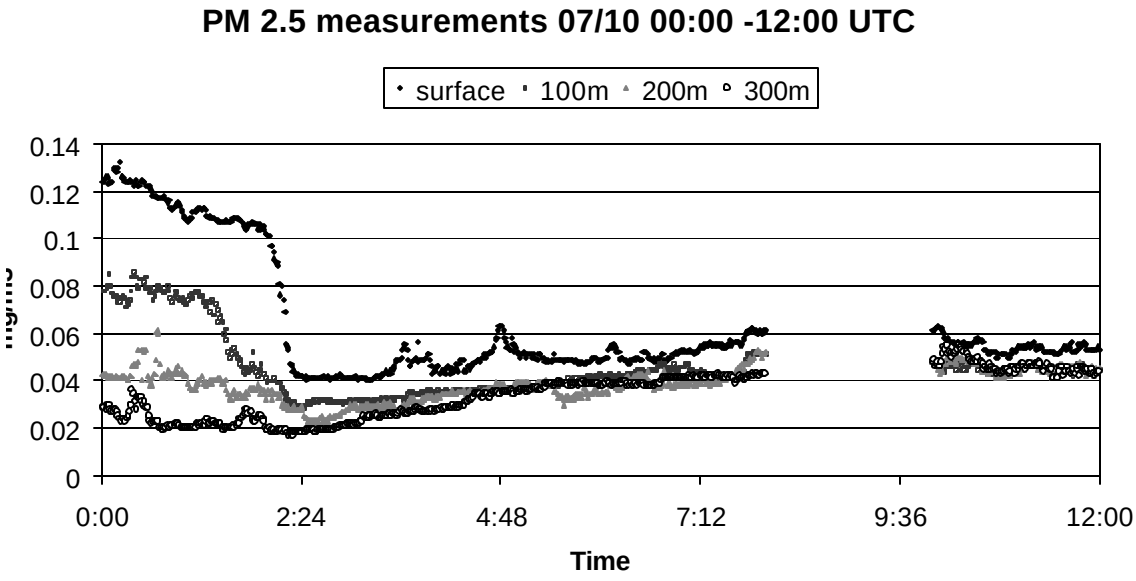

(b)

Figure 5.14. Tethered Sonde data shows comparison of PM measurements from Tethered Sonde at surface and at altitude 100 m, 200 m, and 300 m on two days of July 2001 [Rich Clark, Millersville University].

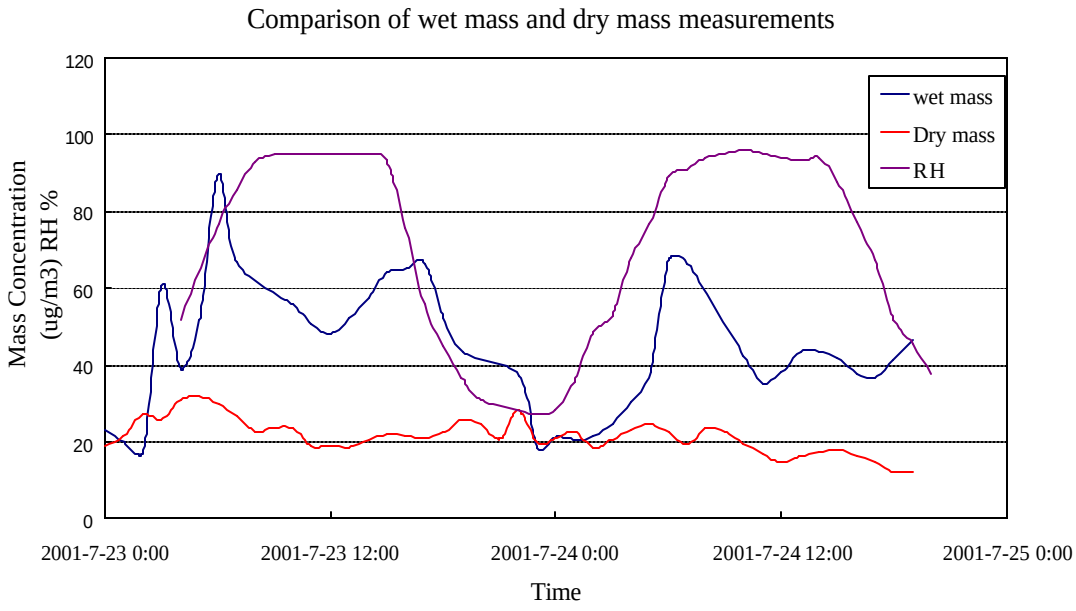

Figure 5.15. Comparison of ambient (wet mass) and dry mass with relative humidity measurements on 23 and 24 July 2001.

A sequence of plots of extinction and particulate matter measurements are shown in Figure 5.16, 5.17 and 5.18. Both the extinction and particulate matter were averaged for a 60 minute periods in these results. Due to the telescope form factor, the extinction may have a large error below 800 meters and so we have chosen to use the extinction at 800 meters to represent the surface conditions on the assumption that the atmosphere is uniform through the boundary layer. This approximation serves to show the relationship between the PM and the optical extinction.

Figure 5.16 (a) shows the comparison of ground PM measurements from HSPH with optical extinction at 284 nm measured by LAPS from 19 August 1998 to 22 August 1998. The scale for PM mass concentration is shown in left vertical axis, and the scale for optical extinction is shown on the right hand side. The PM measurements are strongly correlated with optical extinction. Figure 5.16 (b) shows the line regression of $PM_{2.5}$ with optical extinction. Figures 5.17 and 5.18 show two other examples of comparison from campaign of 1999, which also show strong correlations between PM and optical extinction. Detail analysis and modeling of the relation between particulate matter and optical extinction will be discussed later in this chapter.

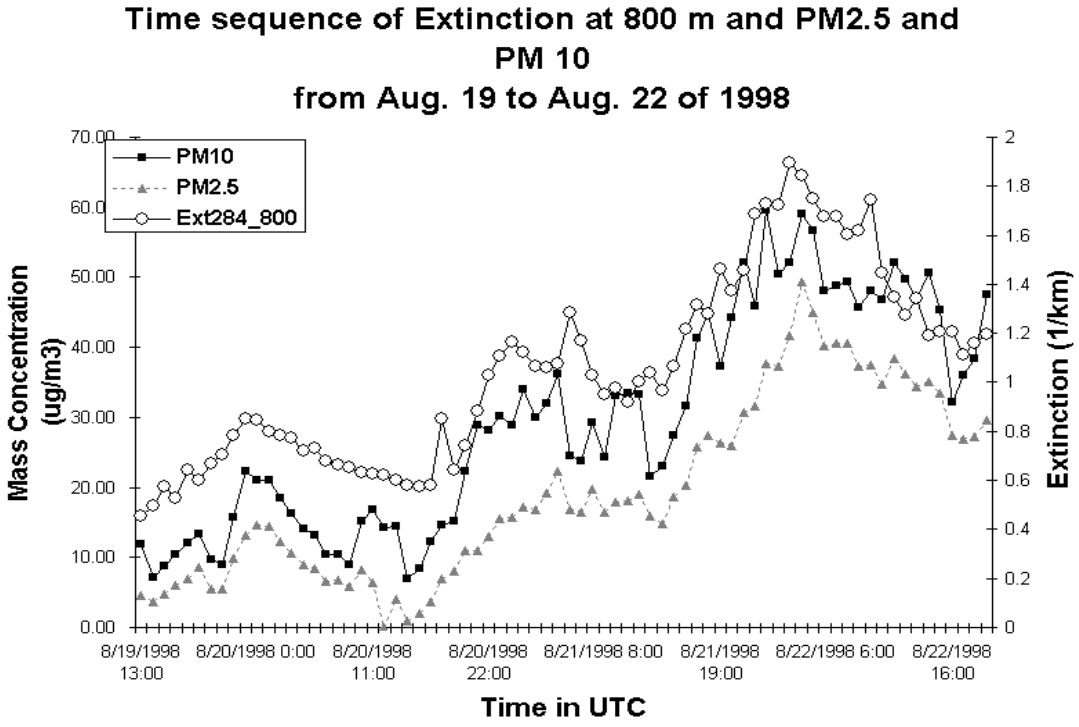

(a)

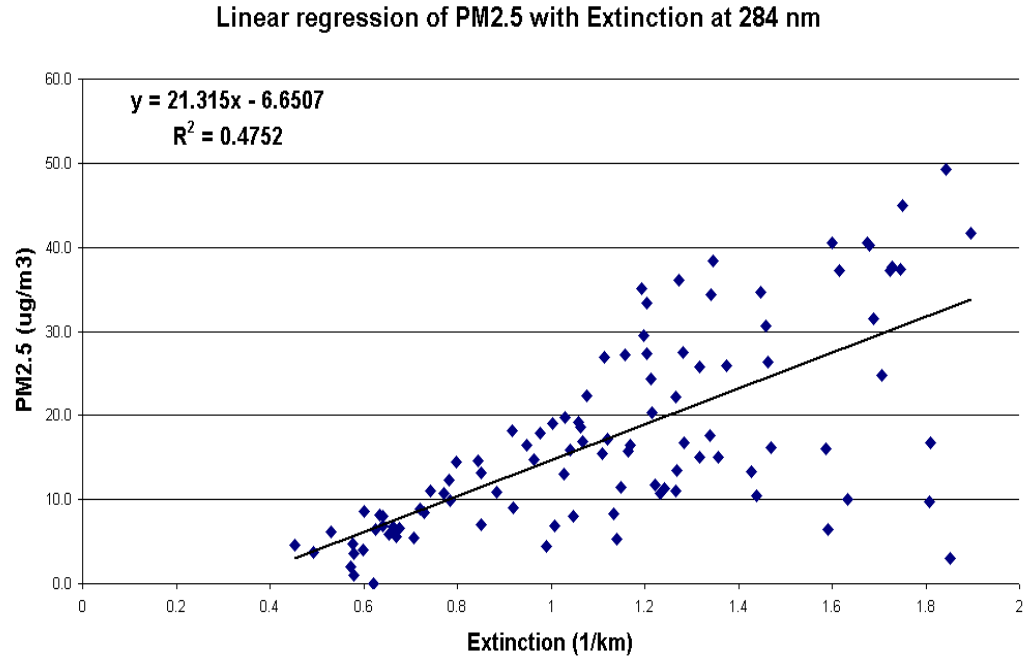

(b)

Figure 5.16. Comparison of PM concentration with Extinction at 284 nm, August 15 to August 22, 1998. (a) Comparison of PM_{10}, $PM_{2.5}$ with optical extinction; (b) Linear regression of $PM_{2.5}$ with optical extinction.

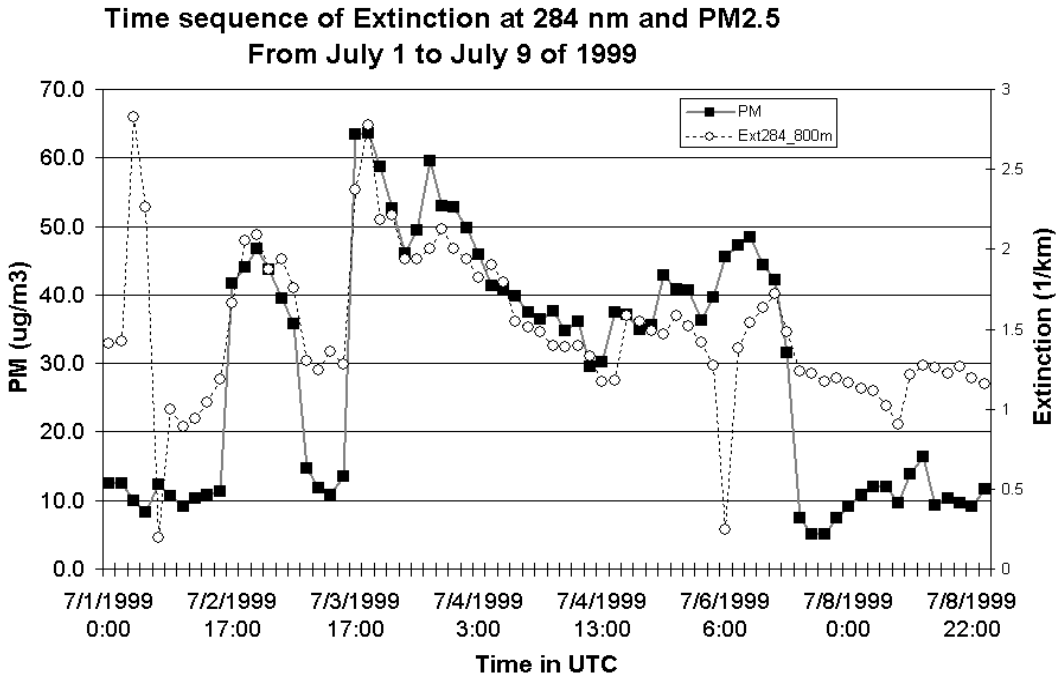

(a)

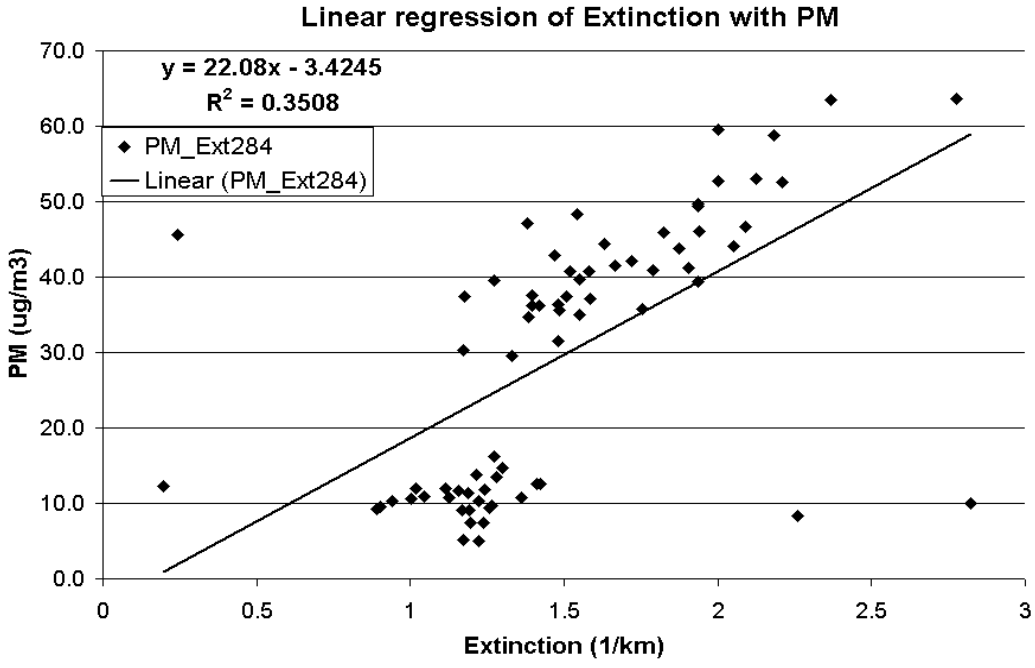

(b)

Figure 5.17. Comparison of $PM_{2.5}$ mass concentration with optical extinction at 284 nm, July 1 to July 9, 1999. (a) Comparison of $PM_{2.5}$ with optical extinction; (b) Linear regression of $PM_{2.5}$ with optical extinction.

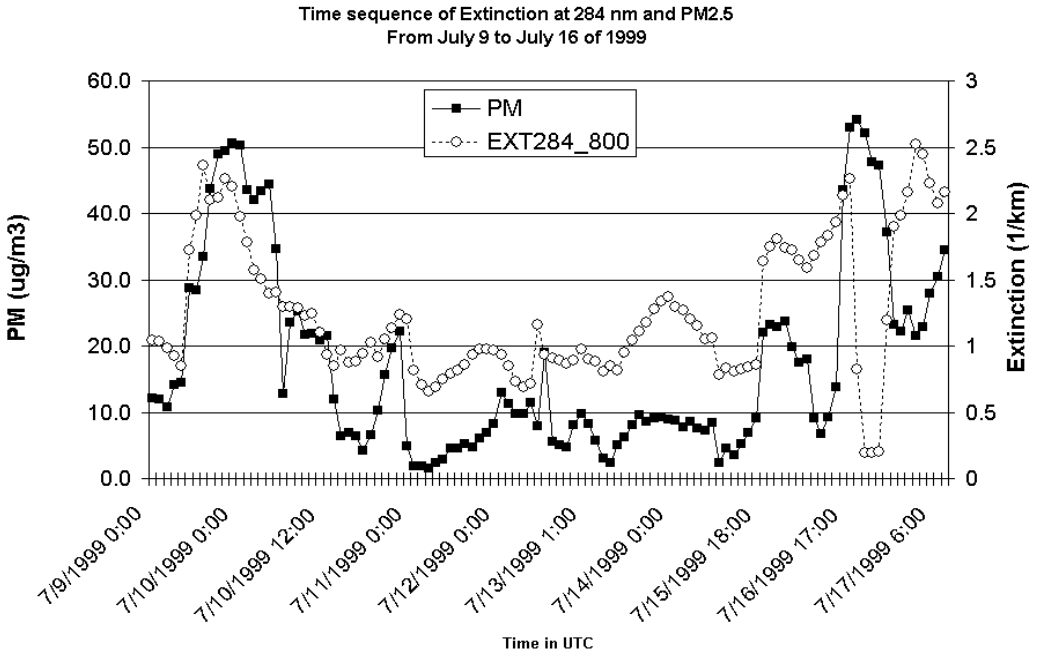

(a)

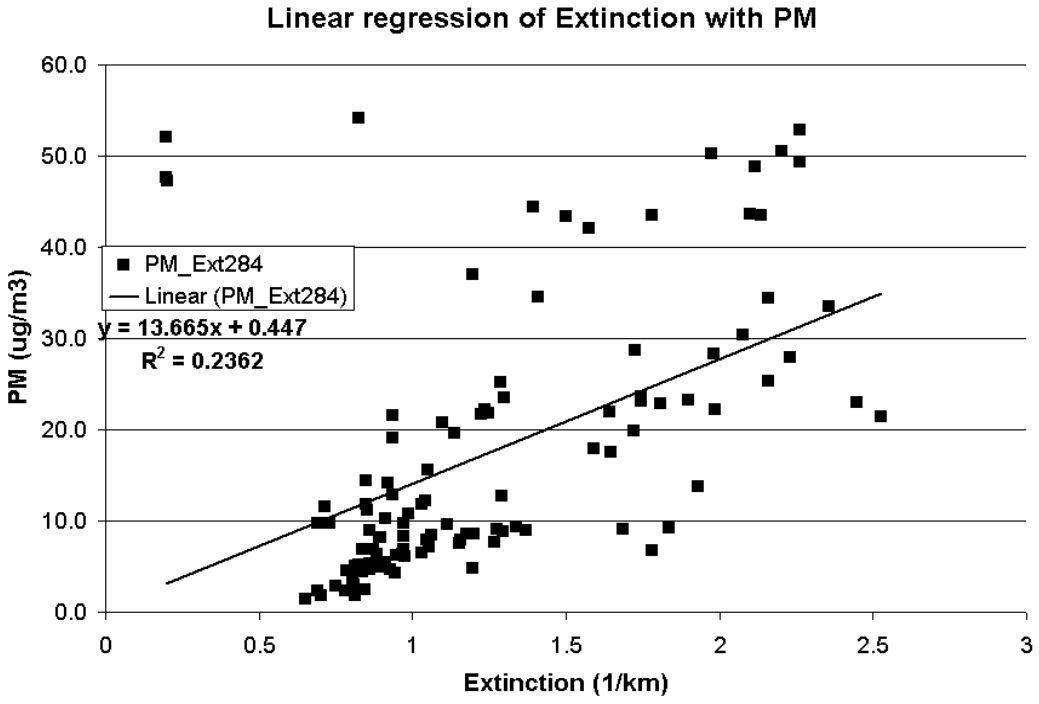

(b)

Figure 5.18. Comparison of $PM_{2.5}$ mass concentration with optical extinction at 284 nm, July 9 to July 22, 1999. (a) Comparison of $PM_{2.5}$ with optical extinction; (b) Linear regression of $PM_{2.5}$ with optical extinction.

A simple model has been built to study the relationship between particulate matter and optical extinction. In this model, we have assumed that the particulate matter in the atmosphere is composed of non-absorbing particles with mono-distributed size. This means that the size distribution of particles in atmosphere is determined by only 2 parameters, size and number density. These two parameters are dependent on each other if we fix either the total mass or volume concentration. We have used this model in Chapter 4 to simulate the backscatter signal from PDL Lidar. Although it is only an approximation for particles in atmosphere, it was shown in Chapter 4 to be effective and useful tool. Therefore, we attempt to predict optical extinction from $PM_{2.5}$ measurements by applying this model with an appropriate particle size assumption.

The variations of optical extinction with particle size at different $PM_{2.5}$ concentrations are shown in Figure 5.19, the model simulation results. The blue, green and red curves represent the different PM concentrations of 100 μg/m3, 50 μg/m3 and 10 μg/m3, respectively. As shown, with fixed total PM concentration, we had higher extinction with smaller particle sizes, because that would correspond to many more scattering particles.

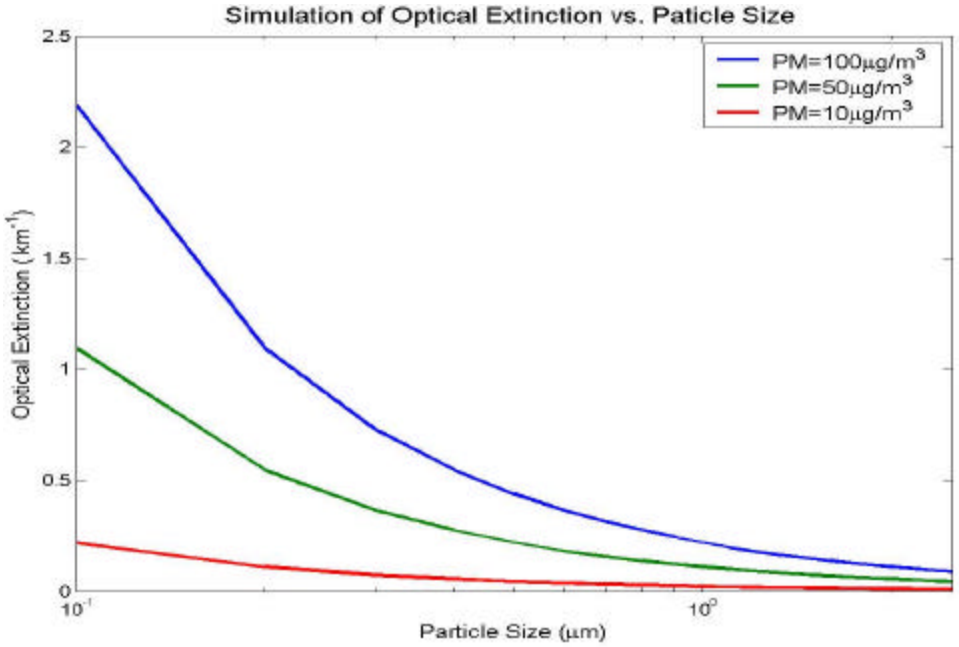

Figure 5.19. Optical extinction versus particle size at several different $PM_{2.5}$ concentrations.

Our goal is to roughly approximate the optical extinction that would be observed corresponding to the measured PM. It is difficult to predict the characteristic of water vapor attaching to the particles in atmosphere, so we choose the 'wet mass' PM data from Millersville University instead of 'dry mass' to use in our model calculations. Figure 5.20 shows an example of the model calculated from 10:00 on 9 July 2001 to 16:00 on 10 July 2001 UTC, all the measurements have been integrated over 60 minutes to reduce errors and to permit easier comparisons. In the size distribution model, the average size of particles has been estimated to be around 0.7 μm, this is not exact but is very close to typical atmosphere. Therefore, the Mie scattering coefficient at 248 nm can be calculated from the 'wet mass' $PM_{2.5}$ data measured by the tethered balloon at 300 meters above ground, and the absorption coefficient at 284 nm is estimated from the ozone concentration taken by the ground ozone sensor from Millersville University. The simulation result of total optical extinction at 284 nm, which is the sum of absorption and Mie scattering coefficient, is indicated by the blue dots in Figure 5.20(a). The red dots represent the optical extinction at 284 nm at the same altitude. We observed that the calculation and the measured values agree during the early and late portion of the interval. However, model calculations of extinction are lower than expected from 18:00 on 9 July 2001 to 6:00 on 10 July 2001 UTC, this is due to a aloft absorbing layer of ozone that was present. As shown in Figure 5.20(b), from the night of 9 July to the morning of 10 July, there is an ozone layer above the ground from the altitude of 200 meters to 800 meters. Since our model calculation used the measurements from the ground sensor to estimated absorption at 300 meters, the calculation will be lower than the measurements due to this high ozone layer. In Figure 5.20(b), the ozone concentration of the layer is about 120 ppb, which is corresponding to optical extinction value of 1 km^{-1} at 284 nm. This is very close to the difference between the model simulation result and lidar extinction measurement.

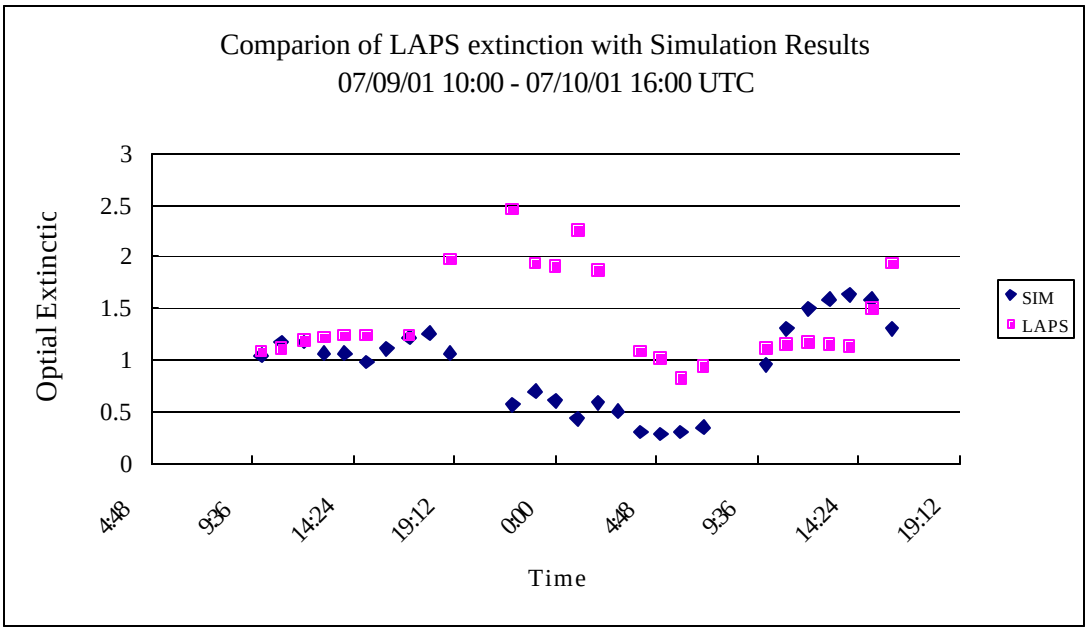

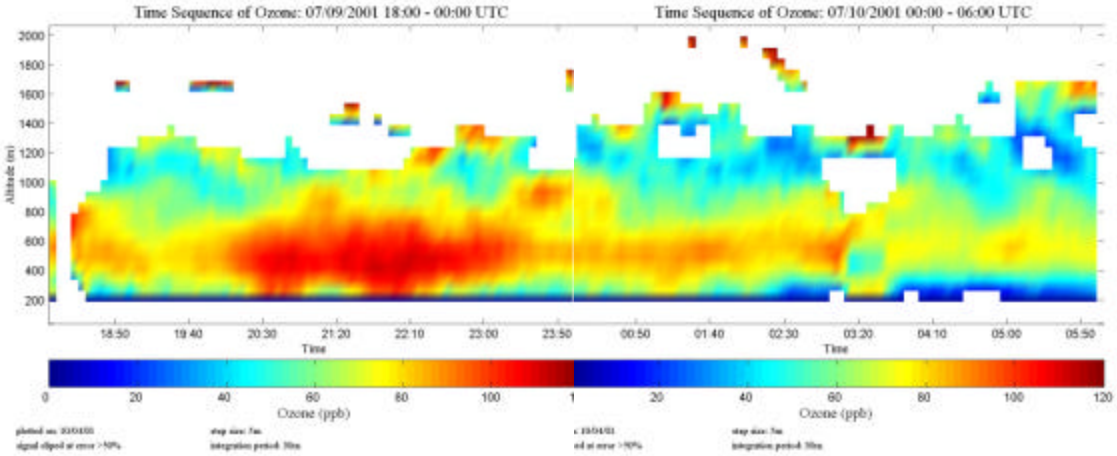

Figure 5.20. (a) Comparison of LAPS extinction measurements at 284nm with calculation results from Millersville University $PM_{2.5}$ ambient mass measurements at 300 meters on 9 July 2001 10:00 UTC – 10 July 2001 16:00 UTC. (b) Time sequence of LAPS ozone measurements characteristic.

Figure 5.21 shows another model calculation result from the campaign of 1999 which is more sophisticated because we compared LAPS extinction with 'dry mass' PM measurement instead of 'wet mass'. During the summer of year 1999, the PM was only measured as 'dry mass' by Harvard School of Public Health. This increases our difficulty in predicting the optical extinction because the atmospheric aerosols have water vapor attached to its surface, which changes the optical extinction value as the particle size changes. Therefore, we attempt to estimate the relations between 'dry'

particles and 'wet' particles in atmosphere. In Section 2.3, we described models related to this subject. In general, the relation between 'wet' and 'dry' particles can be described as,

$$\frac{WetMass}{DryMass} = 1 + Er_{dry} EH\left(\frac{RH}{1-RH}\right) \tag{5.4}$$

E and ρ_{dry} are constants, EH is defined as composite function which varies with relative humidity (RH).

Figure 5.21 (a) shows a several day sequence of the nighttime extinction at 600 meters with the estimated ozone absorption coefficient. The optical extinction is measured by LAPS and the ozone extinction is calculated from the values measured by the ground ozone sensor from Millersville University. This result shows the effect of ozone absorption on the extinction. The ozone absorption can be removed from the optical extinction to obtain the aerosol extinction. Figure 5.21(b) show the comparison of aerosol extinction profile with the PM 'dry mass' measurements. The scale for PM concentration is shown on the left vertical axis and the scale for extinction is shown on the right vertical axis. The comparisons show some correspondence, however the PM concentration does not follow the variation of extinction during the night of 11 July and day of 12 July. The comparison of relative humidity profile with PM 'dry mass' measurements were shown in Figure 5.21(c). It may suggest that the discrepancy in Figure 5.21 (b) is due to the effect of relative humidity. We introduced composite functions in our model calculation to further analyze this discrepancy. Figure 5.21(d) shows several composite functions from different references, which is also shown in Table 2.2. However, since the processes of water attachment to the particle surface is very complicated, and varies with atmosphere conditions, none of the composite functions are claimed to be accurate enough to be used as a reference. When we applied those composite functions into our model calculation, the output optical extinctions and the LAPS measurement results are shown in Figure 5.21 (e). It looks like the composite function from measurements of Lowenthal et al. (1995) is the closest to our LAPS's optical extinction results.

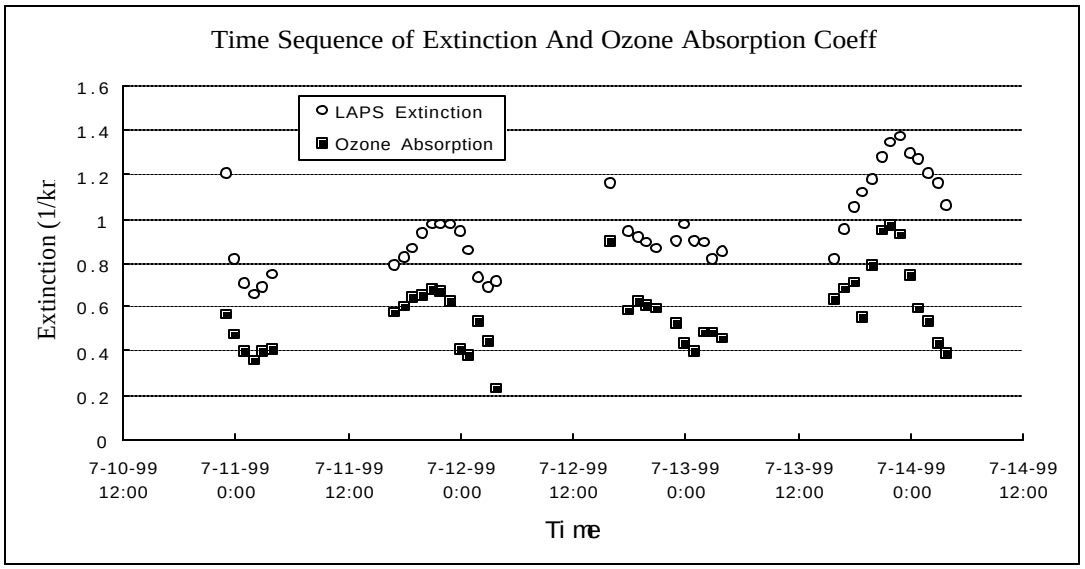

Time sequence of Extinction at 284 nm and PM2.5
From July 11 to July 14 of 1999

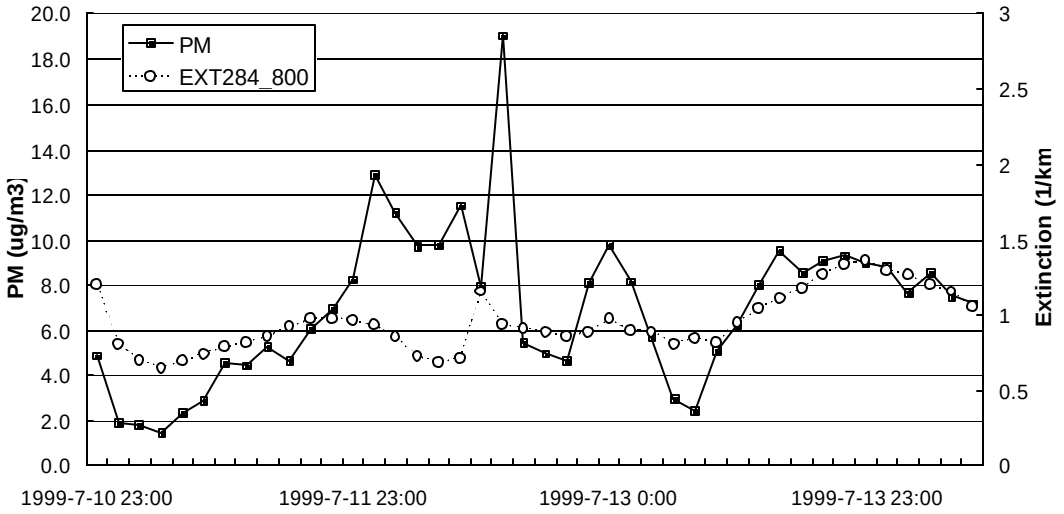

Time sequence of Relative Humidity and PM2.5
From July 11 to July 14 of 1999

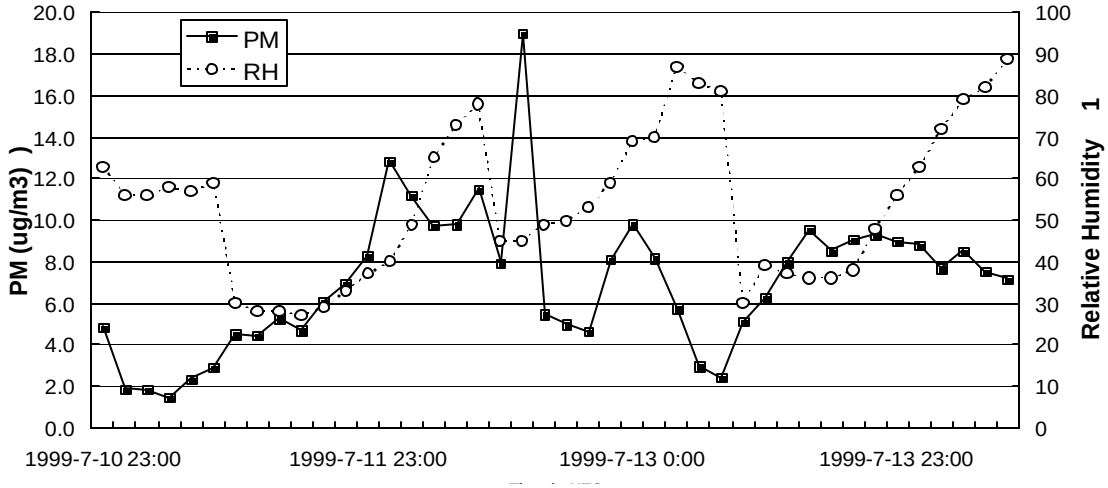

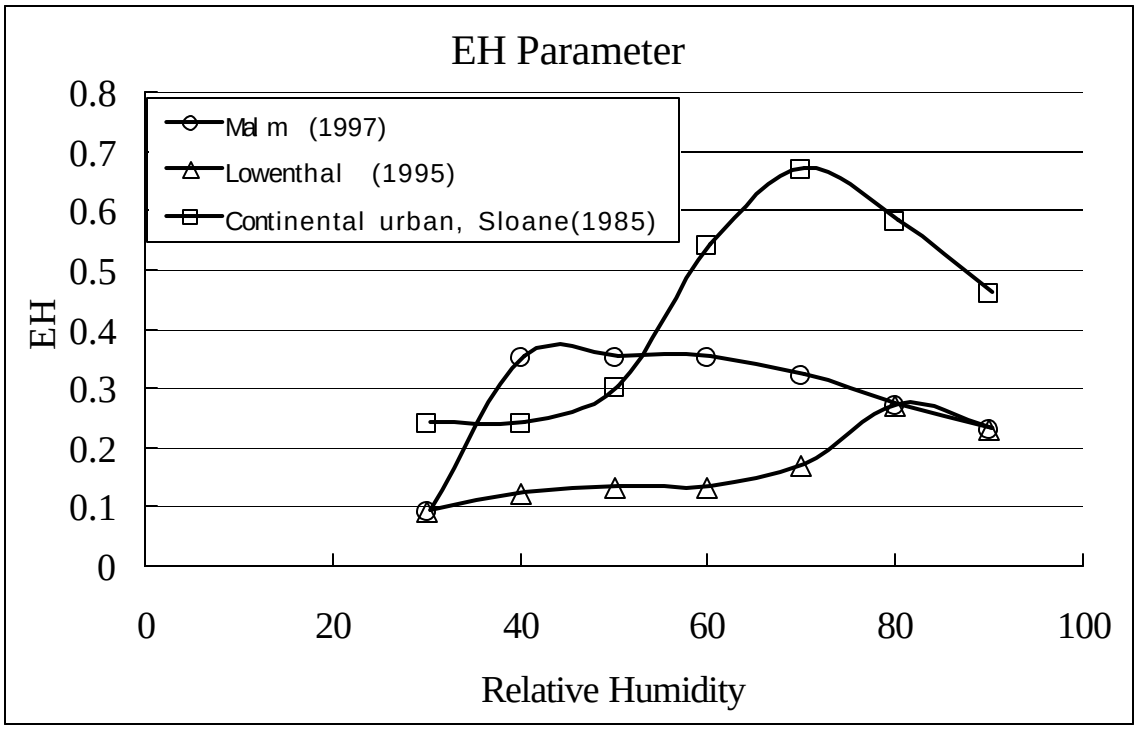

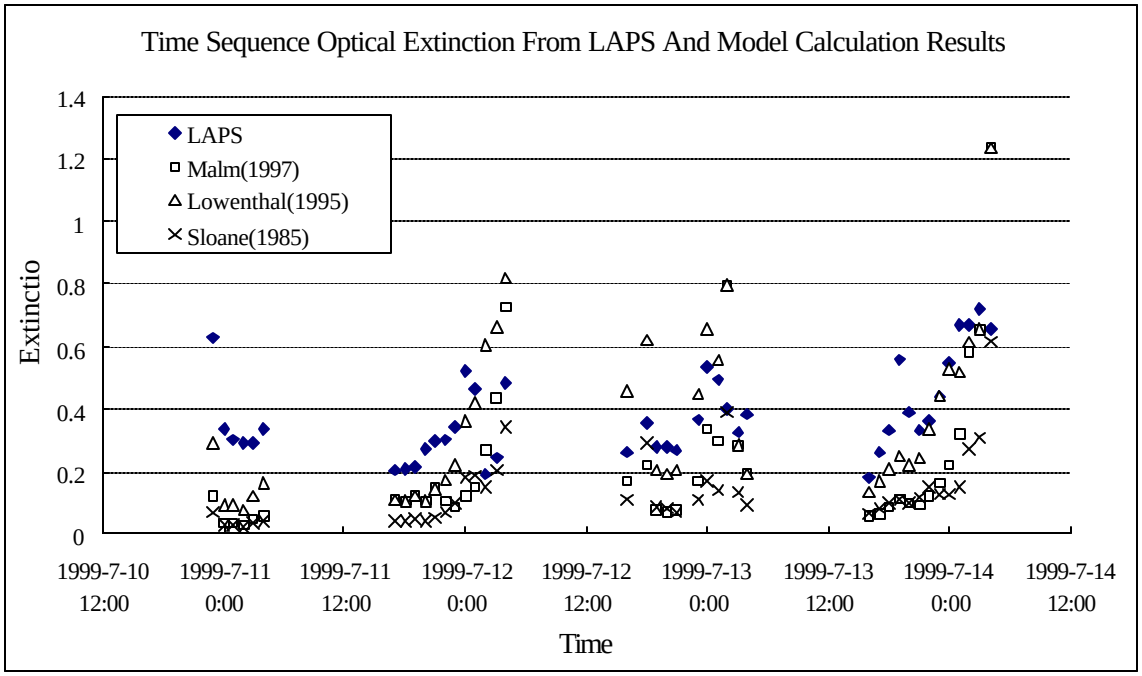

Figure 5.21. (a) Comparison of extinction at 600 meters with the estimated ozone absorption coefficient, optical extinction is measured by LAPS, ozone concentration is measured by ground ozone sensor from Millersville University. (b) Comparison of $PM_{2.5}$ with optical extinction. (c) EH parameters from different references (d) Time sequence optical extinction from LAPS and model calculation results.

5.8 Ratio of Extinction of Different Wavelengths

LAPS Raman lidar system has a distinct advantage that it can measure optical extinction profiles at several different wavelengths simultaneously. It is important to examine the ratio of aerosol extinction profiles at different wavelengths to interpret information on the particle size.

Figure 5.22 (a) presents the model results for volume extinction coefficients for several kinds of atmospheric conditions. Rayleigh scattering shows that the scattered intensity should be inversely proportional to the fourth power of the wavelength when the particle size is small comparing to wavelength. Under haze conditions, the wavelength dependence of aerosol scattering is almost inversely proportional to the wavelength. While inside cloud, the aerosol scattering is almost independent to the wavelength changes [Wright, et al. 1975]. The model calculation of the ratio of extinction coefficients at 530 nm and 284 nm is presented in Figure 5.22 (b). In our calculation, we consider only spherical particles using Mie theory. The simulation result shows that the ratio of the extinction coefficients of 530 nm and 284 nm is close to value 0.08 for fine mode particles when the particle size is relatively small, which follows the Rayleigh's theory. The ratio is size dependent for accumulation mode particles with size range from 0.1 μm to 1μm. For the larger size particles referred as coarse mode particle, the ratio of the extinction coefficient is size independent and approaches the value 1.

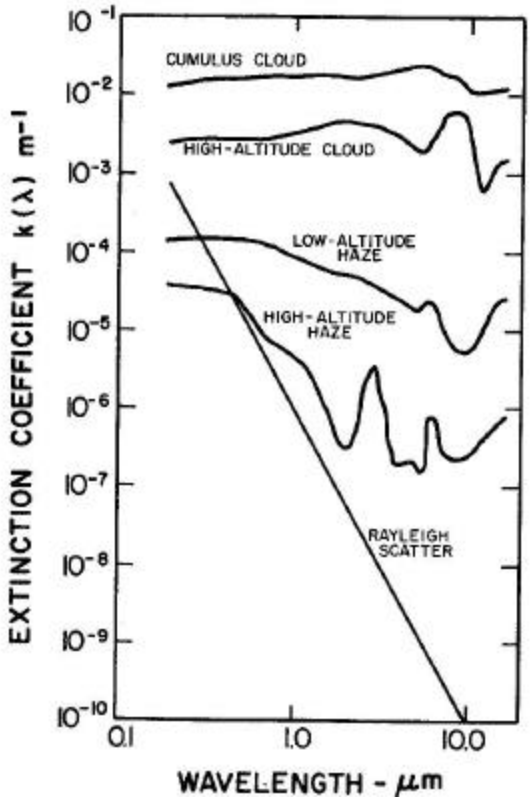

(a)

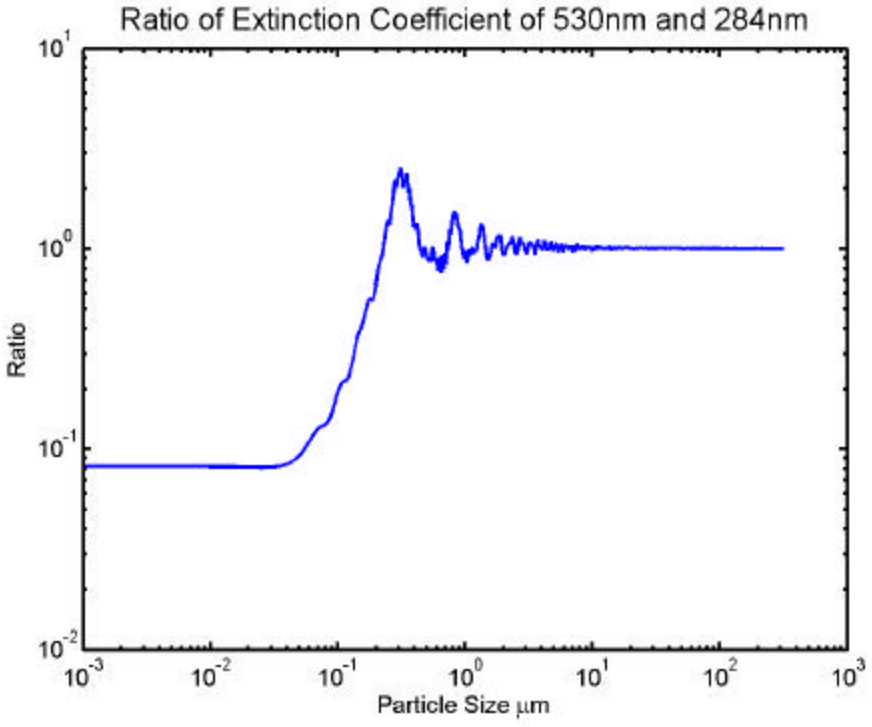

(b)

Figure 5.22. (a) Aerosol extinction coefficient as a function of wavelength for different atmospheric conditions. [Wright et al, 1975]. (b) Ratio of extinction coefficient of 284 nm and 530 nm as a function of particle size calculated using Mie theory.

A time period was chosen when there is an aerosol cloud layer passing through the laser path. The analysis of the ratio of the extinction coefficient of 530 nm and 284 nm shows the result relative to interpretation of the particle size information inside the cloud layer. Figure 5.23 (a) shows the time sequence plot of extinction at the night of July 11 1999. A cloud passed though the laser beam at 2 km between 0230 UTC and 0300 UTC. Figure 5.23 (b) shows the 30 minute integration of extinction profiles at 530nm and 284nm during the time the cloud passing through. Figure 4.24 (c) shows the ratio of the extinction coefficients from the result in Figure 5.23 (b). The ratio is very close to 1 inside the cloud at 2 km altitude, which follows the conclusion in Figure 5.22 and suggests that the cloud is formed by relatively large size particles (>1μm). Also, the ratio is close to 1 near the ground. It indicates the higher aerosol concentration at lower altitude.

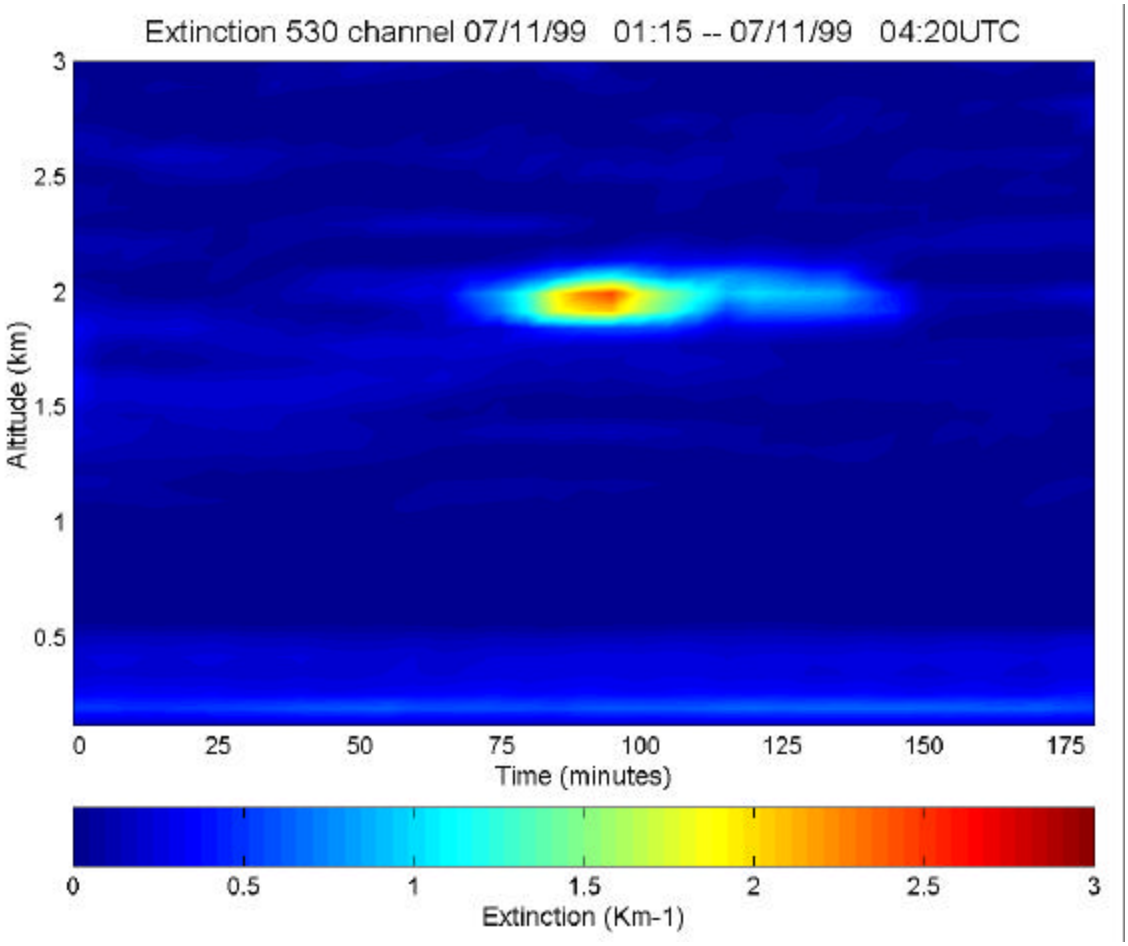

(a) Time sequence plot of extinction at 530 nm.

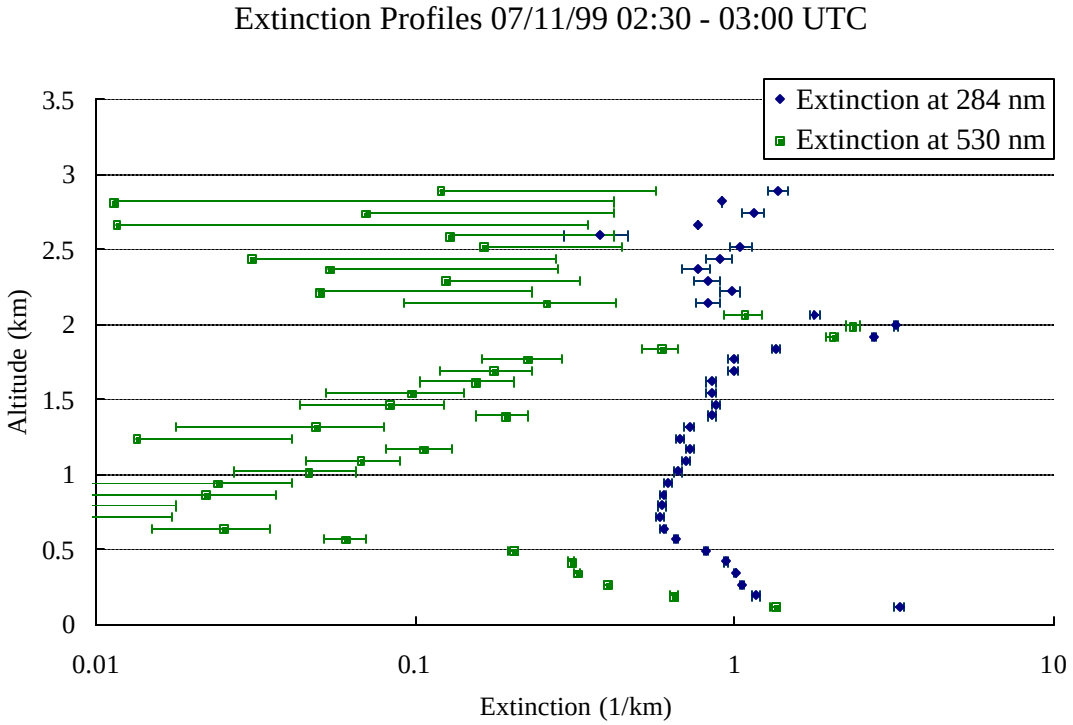

(b) Extinction profiles of 284nm and 530nm.

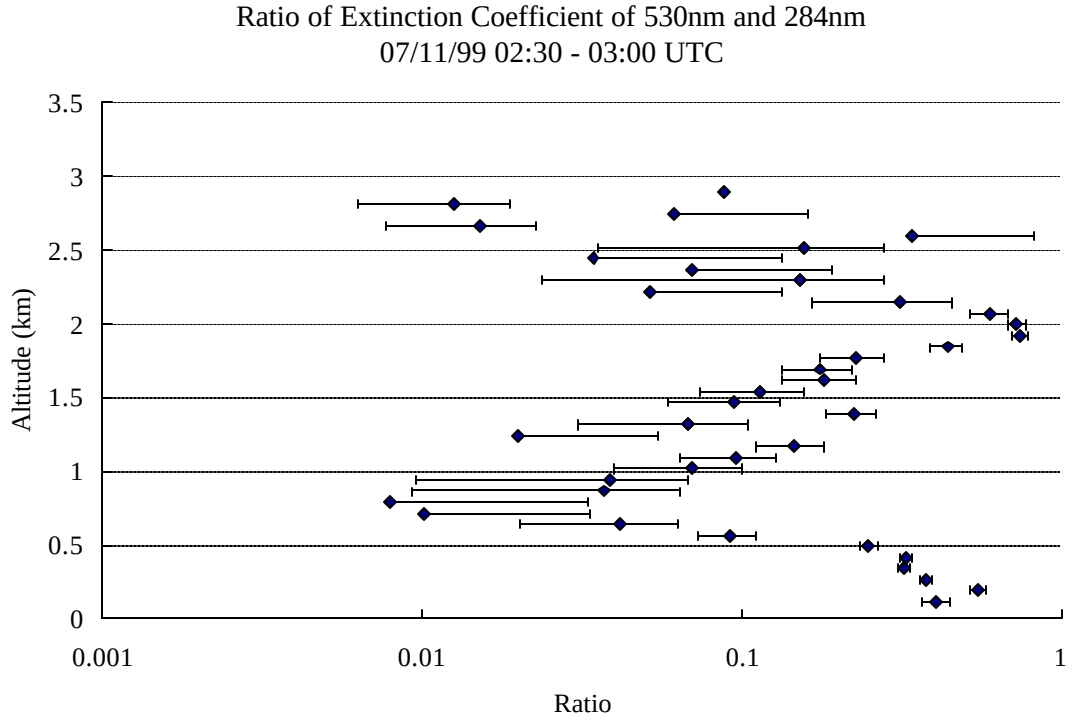

(c) Ratio of extinction coefficient of 530 nm and 284 nm.

Figure 5.23. Analysis of the ratio of extinction coefficient of 530 nm and 284 nm on July 11 1999 02:30 – 03:00 UTC.

5.9 Summary

In this chapter, we analyzed the data of Raman scattering lidar of NE-OPS campaign. Lidar data were compared and validated with measurements by other instruments. An algorithm was developed which removes the molecular extinction and ozone absorption to obtain aerosol extinction profiles for the study of airborne particulates. We have learned that the low altitude extinction profile measured by Raman lidar corresponds with the extinction from surface PM mass concentration. The relationship between extinction and relative humidity has been demonstrated experimentally and modeled. The effect of water vapor attached to surface of particles was examined by using particle growth function. Further model calculations were carried out for interpreting atmospheric aerosol size information. Model simulations have been presented to explain the relationship between extinction and PM concentration. Ratio of the extinction coefficient from different wavelengths shows unique information about particle sizes, which can not be obtained from single extinction profile.

These results show that we can describe the vertical distribution of the airborne particulate matter using Raman lidar and thereby describe the evolution of air pollution episodes more accurately.

CHAPTER 6

Conclusions

6.1 Summary of Accomplishments

Little work has been done to take advantage of the scientific benefit that can be gained from the applications of laser remote sensing techniques to investigate airborne particulate matter. The purpose of this thesis was to improve our knowledge on airborne particulate matter by developing algorithms and techniques for measurements of atmospheric optical extinction in the troposphere for different types of lidar. Models were constructed to relate the optical extinction and backscattering to particle characteristics and to other types of PM measurements. To achieve this goal, a range of technologies available in the area of laser remote sensing have been used to study the optical properties of atmosphere, including Rayleigh scattering, Mie scattering and Raman scattering. We analyzed the data measured by Raman lidar during NE-OPS campaigns during 1998, 1999 and 2001; and the data measured by Mie scattering lidar during campaign of California DUST project from the filed tests in 2000 and 2001. The major accomplishments are summarized below.

6.1.1 Algorithm Development

The ultraviolet aerosol extinction algorithm and telescope form factor for LAPS, the Penn State Raman Lidar, have been developed and tested. Also, an algorithm has been developed to decide the aerosol extinction and backscatter from backscatter lidar that propagates through a dust plume.

UV Extinction Algorithm for Raman Lidar

Previous efforts by Penn State lidar group have developed extinction algorithms at visible wavelengths for Raman lidar. However, the continuous measurement of extinction at visible wavelength is limited to nighttime measurements. To extend these measurements, an extinction algorithm for UV wavelengths has been developed

that can be used continuously over 24 hours. The molecular extinction at visible wavelengths is about 0.015 km^{-1} at 530nm at ground, and is negligible compared to values of aerosol extinction normally observed. However it is not negligible at UV wavelengths, where it is about 0.1 km^{-1} at 284nm at ground. Another important attenuation factor at the UV wavelength region is the ozone absorption. The ozone absorption coefficient profile can be calculated from the ozone density profile, which is obtained by taking the ratio of vibrational Raman shifted signals of oxygen/nitrogen (277/284 nm) from the LAPS measurements. To obtain aerosol extinction at UV wavelength, the molecular extinction and ozone absorption were removed.

Telescope Form Factor for LAPS

The telescope overlap factor limits the data accuracy of lidar measurements in the near field below 800 m. Previous attempts to develop the geometrical overlap correction method to calibrated telescope form factor have been presented by Penn State researchers, and other research groups, but we have found they are not generally applicable approaches. A new experimental approach has been developed to obtain the telescope form factor that shows very good results. Also, a new geometric calibration method of telescope form factor has been introduced and compared with the experimental result. The combination of experimental approach and geometric calibration provides a good approach, not only for the form factor calculation, but also for the lidar system alignment and calibration procedures for use during future campaigns.

Extinction Algorithm for Backscatter Lidar

Mie scattering simulations of lidar performance have been used to study the atmospheric meteorological properties and characterize the fate (deposition and transport) of PM emissions originating from the mechanical disturbance of surface soil during the California dust project. Previous work shows that it is very difficult and usually not possible to quantify the optical properties from backscatter signals of lidar.

However, we have demonstrated that the amount aerosol extinction and backscatter can be measured when the signal passes through a dust plume.

6.1.2 Model Simulations

The relation between Raman lidar extinction, relative humidity and PM mass measurements were measured and modeled. The results show that we can describe the vertical distribution of the airborne particulate matter using Raman lidar and thereby describe the evolution of air pollution episodes more accurately. The modeling results from California Dust campaign shows that the rapid deposition of PM_{10} particles, and the relatively longer residence time of the optical plume associated with small particles (< 2μm), may have led to overestimates of airborne particle mass in plumes. This could explain the major discrepancy between the source estimates and the measured mass distributed from entrainment of soil particulates.

Micro-Pulse Lidar

The micro-pulse backscatter lidar provides a newly demonstrated capability to examine the properties of the aerosols in plumes when a profile of background atmospheric scattering is available for normalization of the plume signal. This information is important for the study of PM transport and describes the fate of generated plumes from entrainment of surface soil, as discussed in Chapter 4. In this chapter, we analyzed the lidar data of dust scattering from CA-Dust campaign and made comparison with model simulations based upon Mie scattering theory. A soil particle size distribution model has been constructed successfully from lidar results and compared with results from other particle size instruments. The model calculations have been designed to simulate various features of the optical scattering from dust clouds. Therefore, we used the field measurements to analyze the inverse problem and describe the particulate matter properties from the optical scattering measurements. Model simulation results provide an excellent way to understand the signal variations measured by lidar. It has been observed in our study that the larger particles, which contain most of the PM mass, settle out of the air fairly quickly.

However, the fine particles contribute primarily to the backscatter, and remain suspended much longer. The results suggest that the rapid deposition of large particles (PM_{10}), and the relatively longer residence time of the optical plume associated with small particles (< 2μm), may have led to overestimates of airborne particle mass in plumes. This could explain the major discrepancy between the source estimates and the measured mass distributed from entrainment of soil particulates.

Raman Lidar

The relationship between Raman lidar extinction and PM measurements were quantified in Chapter 5. It has been shown in this thesis that the variations of optical extinction are useful in understanding the evolution of pollution events. The relationship between extinction and relative humidity has been measured experimentally and modeled. The effect of water vapor attached to surface of particles was examined by using particle growth function. Low altitude extinction profiles measured by Raman lidar are demonstrated to compare well with the surface PM mass concentration. Model simulations have been presented to explain this correspondence and quantify the relation between extinction and PM mass concentration. Ratio of the extinction coefficient at different wavelengths shows unique information on particle size, which can not be obtained from single extinction profile. These results show that we can describe the vertical distribution of the airborne particulate matter using Raman lidar and thereby describe the evolution of air pollution episodes more accurately.

6.1.3 Ratio of Signals from Different Wavelengths

The ratio of the backscatter signal and ratio of extinction profiles from Raman lidar at multiple wavelengths were analyzed to show unique information about particle characteristics, which can not been obtained from the single wavelength profiles.

Micro-Pulse Lidar

The ratios of the backscatter signal from green channel (523 nm) and red channel (1046 nm) of backscatter lidar were compared with simulation results to investigate the particle characteristics in Chapter 4. During the measurements, the correlation of the ratio with the particle sizes was observed that clearly shows the particle size changes in the dust plume.

Raman Lidar

LAPS Raman lidar system has a distinct advantage that it can measure optical extinction profiles at several different wavelengths simultaneously. Model simulations show that the ratio of extinction is size dependent for accumulation mode particles with size range from 0.1 μm to 1μm; while for the larger size particles referred as coarse mode particle, the ratio is size independent and approaches to the value 1. When an aerosol cloud layer is present in the laser path of Raman lidar, the analysis of the ratio of the extinction coefficient of visible (530 nm) and ultraviolet (284 nm) wavelengths shows a striking result as the aerosol size changes in the cloud layer.

6.2 Future Work

Raman lidar has proven to be a very effective instrument for measuring the optical extinction profiles. Investigation of optical extinction using the Raman lidar technology improves our understanding of the distribution of airborne particles. During NE-OPS campaign, we have compared optical extinction measurements from lidar with PM measurements from other instruments. The comparisons show good agreement and correspondence, however, more information is needed to obtain better understanding of physical properties which determine the quantity and distribution of particulate matter and its optical properties in the atmosphere. For example, if the particle size distribution information can be obtained at the same time and volume, we could develop a better model that better describe atmospheric conditions and better quantify the relationship between optical extinction and PM measurements.

In our model calculation, Mie theory is primarily used for optical scattering

calculations because we have made the basic assumption that the particles we considered are spherical. It has been shown in this thesis that Mie theory explains most of our experimental results very well, particularly when we are modeling the hydroscopic particles under high relative humidity in atmosphere. However, we know that Mie theory is not applicable to atmospheric scattering under certain circumstances, such as desert and dry urban environments where T-matrix or other more sophisticated scattering theory will be required.

During the California-Dust campaign, several problems were addressed using the data set that included features associated with modeling the Mie scatter lidar for our experiment arrangement. We addressed the problem of distortion by the telescope form factor when using near field lidar profile. The effects of instrument limitations were minimized by forming a ratio to describe the dust cloud observed relative to a background profile obtained just before each test. The scanning of the digital camera image made it difficult to characterize the spatial evolution of a dust cloud because of the slow scanning speed of the instrument compared with the fast settling rate of the dust plume. These problems can be reduced in future experiments by improvements in the experiment arrangement.

REFERENCE

Albritton, Daniel L., and Daniel S. Greenbaum, "Atmospheric Observations: Helping Build the Scientific Basis for Decisions Related to Airborne Particle Matter," *Proceedings of the PM Measurements Research Workshop*, Chapel Hill, North Carolina, July 22-23, 1998.

Almeida, G.A, P. Koepke, and E.P. Shettle, *Atmospheric Aerosols,* A. Deepak Publishing, Hampton, Virginia, 561 p., 1991.

Arya, S.P. *Air pollution meteorology and dispersion*. Oxford, 1999

Ansmann, A., U. Wandinger, M. Riebesell, C. Weitkamp, and W. Michaelis. Independent Measurement of Extinction and Backscatter Profiles in Cirrus Clouds by using a Combined Raman Elastic-Backscatter Lidar. *Applied Optics*. 31:7113, 1992.

Balsiger F. and C. R. Philbrick, "Comparison of Lidar Water Vapor Measurements Using Raman Scatter at 266nm and 532 nm," in *Applications of Lidar to Current Atmospheric Topics,* SPIE Proceedings Vol. 2833, 231-240 1996.

Barber, P.W. and R.K. Chang, *Optical Effects Associated with Small Particles,* World Scientific, Singapore, 336 p., 1988.

Barber, P .W .and S.C. Hill, *Light Scattering by Particles: Computational Methods*, World Scientific Publishing, Singapore, 261 p., 1990.

Bergin, M. H., J. A., Ogren, S. E., Schwartz, and McInnes, L. M.. Evaporation of ammonium nitrate aerosol in a heated nephelometer: implications for field measurements. *Environ. Sci. Technol.* 21:2878-2883, 1997.

Bohren, C. F. and D. R. Huffman. *Absorption and Scattering of Light by Small Particles*. Wiley-Interscience Publication, 1983.

Bullrich, K. Scattered radiation in the atmosphere. *Adv. Geophys.* 10:99-260. 1984

Charlson, R. J., N. C. Ahlquist , and H. Horvath. On the generality of correlation of atmospheric aerosol mass concentration and light scatter. *Atmos.Environ.* 2:455-464, 1968.

Charlson, R. J.. Atmospheric visibility related to aerosol mass concentration: A review. *Environ.Sci.Technol.* 3:913-918, 1969.

Chow, J. C., J. G.Watson, D. H. Lowenthal, R. Hackney , K. Magliano, D. Lehrman, and T. Smith, Temporal variations on $PM_{2.5}$, PM_{10}, and gaseous precursors during the 1995 integrated monitoring study in central California. *J. Air & Waste Manage. Assoc.* 49:PM-16-24, 1999

Clarke A.D., Aerosol light absorption by soot in the remote environments, *Aerosol Sci. Technol.*, 10,161-171,1989.

Crow, E.L. and K. Shimizu, *Lognormal Distributions*, Marcel Dekker, New York City, 387 p., 1988.

Cowherd, C (1998). Particulate Matter from Roadways. *Final Report to the Colorado Department of Transportation*.

Cowherd, C; Muleski, G; and Grelinger , M.A.; (1998a) Potential Biases in $PM_{2.5}$ Emission Factors for Fugitive Dust Sources. *Presentation at the AWMA 91st Annual Meeting*, San Diego CA.

Cowherd, C; Grelinger, M.A.; and Morris, S.S; (1998b)Analysis of Road Dust Re-Suspension at a Hot Spot in Anchorage. *Presentation at AWMA 91st Annual Meeting,* San Diego CA.

Dave, J. Subroutines for computing the parameters of the electromagnetic radiation scattered by a sphere. Report No. 320-3237, IBM Scientific Center, Palo Alto CA, 65pp, 1968.

Dave, J. Effect of coarseness of the integration increment on the calculation of the radiation scattered by polydisperse aerosols. *Appl.Opt.* 8:1161-1167, 1969.

Davies, C.N. "Size Distribution of Atmospheric Particles", *Journal of Aerosol Science*, Vol. 5, pp. 293-300, 1974.

Deepak, A., editor, *Atmospheric Aerosols: Their Formation, Optical Properties, and Effects,* Spectrum Press, Hampton Virginia, 480 p., 1982.

Drake, R.L., J.M. Hales, J. Mishima and D.R. Drewes. Mathematical models for atmospheric pollutants. Appendix B: Chemical and physical properties of gases and aerosols. Electric Power Research Institute, EPRI EA-1131, 1979.

Dutcher, D. D., K.D. Perry, and T. A. Cahill, Water and volatile particulate matter contributions to fine aerosol gravimetric mass. in: *Visual Air Quality: Aerosols and Global Radiation Balance,* pp. 991-999, Air and Waste Management Association, Pittsburgh, Pa, 1997.

Dzubay, T. G., R. K. Stevens, C. W. Lewis, D. H. Hern, W. J. Courtney, J. W. Tesch, and M. A. Mason, Visibility and aerosol composition in Houston, Texas. *Environ.Sci.Technol.* 16:514-525, 1982.

Eldred, R. A., T. A. Cahill, and R. G. Flocchini, Composition of $PM_{2.5}$ and PM_{10} aerosols in the IMPROVE network. *J. Air & Waste Manage, Assoc.* 47: 194-203, 1997.

Environmental Protection Agency (EPA). *Atmospheric Observations: Helping Build The Scientific basis For Decisions related to Airborne Particulate Matter.* Report of the PM Measurements research Workshop, Chapel Hill, North Carolina, 1998.

Esposito, S. T. *Applications and Analysis of Raman Lidar Techniques for Measurements of Ozone and Water Vapor in the Troposphere*. Masters Thesis, Department of Electrical Engineering, Pennsylvania State University, 1999.

H. J. Ettinger, and G. W. Royer, Visibility and mass concentration in non-urban environment. *JAPCA* 22:108-111, 1972.

Farmer, W. M. *The Atmosphere Filter Volume I, Sources* JCD Publishing, 2001

Fitz, D., D. Pankratz, R. Philbrick, and G. Li: AEvaluation of the Transport and Deposition of Fugitive Dust Using Lidar,@ *Proc. Environmental Protection Agency's 11th Annual Emission Inventory Conference: Emission Inventories-Partnering for the Future*, Atlanta GA, 2002.

Fuller, K. A., Malm, W. C., and Kreidenweis, S. M. Effects of mixing on extinction by carbonaceous particles. *J.Geophys.Res.* 104:15,941-19,954, 1999.

Garthman, S.G., A time dependent oceanic aerosol model, *Tech. Rep.* 8536, 35 pp. Nav. Res. Lab., Washington, D.C., 1982.

Garthman, S.G., *Navy Hygroscopic Aerosol Model: Hygroscopic Aerosol*, A. Deepak, Hampton, Va., 1984.

Gillespie, J. B. and J. D. Lindberg, Seasonal and geographic variations in imaginary refractive index of atmospheric particulate matter. *Appl.Opt.* 12:2107-2111, 1992.

Handbook of Chemistry and Physics, 61h edition 1986-1987, R.C. Weast (editor in chief), M.j. Astle, W .H. Beyer (associate editors), CRC Press, Inc., Boca Raton, FL, 1986

Handbook of Optics, Vol. I, Fundamentals, Techniques, and Design, 1"dedition, M. Bass (editor in chief), E. W .Van Stryland, D.R. Williams and W .L. Wolfe (associate editors), McGraw-Hill Inc., New York City, 1995.

Handbook of Optics, VoL II, Devices, Measurements and Properties, 2"d edition, M. Bass (editor in chief), E. W. Van Stryland, D.R. Williams and W.L. Wolfe (associate editors), McGraw-Hilllnc., New York City, 1995.

Hanel, G. The real part of the mean complex refractive index and the mean density of samples of atmospheric aerosol particles. *Tellus* 20:371-379, 1968

Hanel, G. and K. Bullrich, Calculations of the spectral extinction coefficient of atmospheric aerosol particles with different complex refractive indices. *Letter. Phys. Atmos.* 43:202-207, 1970.

Hanel, G. The properties of atmospheric aerosol particles as functions of the relative humidity at thermodynamic equilibrium with the surrounding moist air. *Adv. Geophys.* 19:73-188, 1976

Hasan, H. and T. G. Dzubay, Apportioning light extinction coefficients to chemical species in atmospheric aerosol. *Atmos.Environ.* 17:1573-1581, 1983

Heintzenberg, J. and R. J. Charlson, Design and Applications of the Integrating Nephelometer: A Review. *J.Atmos.Oceanic Technol.* 13:987-1000, 1996.

Hering, S. and G. Cass, The magnitude of bias in the measurement of $PM_{2.5}$ arising from volatilization of particulate nitrate from teflon filters. *J. Air & Waste Manage, Assoc.* 49: 725-733, 1999.

Hidy, G. M., P. M. Roth, J. M. Hales and R. Scheffe , Oxidant Pollution And Fine Particles: Issues And Needs. *NARSTO Critical Review Series*, 1998, http://odysseus.owt.com/Narsto/

Hill, S. C., C. Hill, and P. W. Barber, Light scattering by size/shape distributions of soil particles and spheroids. *Appl.Opt.* 23:1025-1031, 1984

Hobbs, P .V., editor, *Aerosol-Cloud-Climate Interactions,* Academic Press, San Diego, 233 p., 1993.

Hoppel, W.A., Measurements of the size distribution and CCN supersaturation spectrum of submicron aerosols over the ocean, *Atmos. Sci.,* 9, 41-54, 1979.
Hoppel, W.A., G.M. Frick, and J.W. Fitzgerald, Marine boundary layer measurements of new particle formation and the effects nonprecipiting clouds have on aerosol size distribution, .1: *Geophys. Res.,* 99, 14,443- 14,459, 1994.

Husar, R. B. and S. R.. Falke, The relationship between aerosol light scattering and fine mass. Report No. CX 824179-01. Center for Air Pollution Impact and Trend Analysis, St. Louis, MO. Prepared for U.S. Environmental Protection Agency, Research Triangle Park, NC, 1996.

Jaggard, D. L., C. Hill, R. W. Shorthill, D. Stuart, M. Glantz, F. Rosswog, B. Taggart, and S. Hammond, Light scattering from particles of regular and irregular shape. *Atmos.Environ.* 15:2511-2519, 1981.

Jenness J. R., Jr., Daniel B. Lysak, Jr., and C. R. Philbrick, Design of a Lidar Receiver with Fiber-optic Output. *Applied Optics*. 36:4278, 1997.

John, W., S. M. Wall, J. F. Ondo, and J.L. Winklmayr, Modes in the aerosol size distribution of atmospheric inorganic aerosol. *Atmos.Environ.* 24:2349-2359, 1990.

Kerker, M. The Scattering of Light and Other Electromagnetic Radiation. Academic Press, New York. 1969.

Kretzschmar, J. G. Comparison between three different methods for measuring suspended particulates in air. *Atmos.Environ.* 9:931-934. 1975.

Kyle, Thomas. G., *Atmospheric Transmission, Emission, and Scattering*. Butterworth-Heinemann Publishing, 1991.

Lewis, C. W. On the proportionality of fine mass concentration and extinction coefficient for bimodal size distributions. *Atmos.Environ.* 15:2639-2646. 1981.

Li., G, G.S. Chadha, K.R. Mulik, and C.R. Philbrick, "Characterization of Properties of Airborne Particulate Matter from Optical Scattering Using Lidar," *Proceedings of the A&WMA Specialty Conference and Exhibition, PM2000: Particulate Matter and Health*, Charleston, South Carolina, January 24-28, 2000, pp. 4ASP1: 8-10.

Li., G, G. Chadha and C.R. Philbrick, "Characterization of properties of airborne particulate matter from optical scattering using lidar," *Aerosol Science and Technology*, 2000.

Li., G, G.S. Chadha and C.R. Philbrick, "Lidar Measurements Describe Distribution of Airborne Particulate Matter," *Proceedings of the 20th International Laser Radar Conference*, Vichy France, 2000.

Li., G, S.N. Kizhakkemadam and C.R. Philbrick, "Optical Scattering by Airborne Dust Particles," *24th Annual Review of Atmospheric Transmission Models ARFL Transmission Meeting*, Hanscom AFB, MA6-8 June 2001.

Li., G, and C.R.Philbrick, "Ramman Lidar Measurements of Airborne Particular Matter," *Proceedings of the Fourth Conference on Atmospheric Chemistry: Urban, Regional, and Global-Scale Impacts of Air Pollutants*, Orlando, Florida, January 13-17, 2002, 7.7 pp.135

Li., G, S. J. Verghese and C. R. Philbrick "Airborne Dust and Aerosols Description Using Lidar Backscatter" *25th Annual Conference on Atmospheric Transmission and Radiance Models*, Lexington, MA, 25-27 June 2002.

Li., G, C.R. Philbrick, "Lidar Measurements of Airborne Particulate Matter" *Proceedings of the 2003 SPIE – the international society for optical engineering*, Hangzhou, China, 24-25 October 2002.

Lilienfeld, P. Nephelometry, an ideal PM-2.5/10 method, *Particulate Matter: Health and Regulatory Issues VIP-49,* pp. 211-225, Air and Waste Management Association, Pittsburgh, Pa., 1997. 1995.

Lowenthal, D. H., C. F. Rogers, O. Saxena, J. G. Watson, and J. C. Chow, Sensitivity of estimated light extinction coefficients to model assumptions and measurement errors. *Atmos.Environ.* 29:751-766. 1995.

W. C. Malm, J. F. Sisler, D. Huffman, R. A. Eldred, and T. A. Cahill, Spatial and seasonal trends in particle concentration and optical extinction in the United States. *J.Geophys.Res.* 99:1347-1370. 1994.

Malm, W. C., J. V. Molenar, R. A. Eldred, and J. F. Sisler, Examining the relationship among aerosols and light scattering and extinction in the Grand Canyon area. *J.Geophys.Res.* 101:19,251-19,265. 1996.

Malm, W.C. and Kreidenweis, S.M. The Effects of Models of Aerosol Hygroscopicity on Estimated Scattering Efficiencies. *Presented at the Air & Waste Management Association's 89th Annual Meeting*, Nashville, TN, 1996.

Malm, W. C. and S. M. Kreidenweis, The effects of models of aerosol hygroscopicity on the apportionment of extinction. *Atmos.Environ.* 31:1965-1976. 1997.

Malm, W. C. and M. L. Pitchford, Comparison of calculated sulfate scattering efficiencies as estimated from size-resolved particle measurements at three national locations. *Atmos.Environ.* 31:1315-1325. 1997.

McCartney, E.J., *Optics of the Atmosphere -Scattering by Molecules and Particles*, John Wiley & Sons, New York City, 408 p., 1976.

McMurry, P. H., W. D. Dick, P. Saxena, and S. Musarra, Mie theory evaluation of species contributions to visibility reduction in the smoky mountains: results from the 1995 SEAVS study. in: *Visual Air Quality: Aerosols and Global Radiation Balance*, pp. 394-399, Air and Waste Management Association, Pittsburgh, Pa. 1997.

Magari, S.R., R. Hauser, J. Schwartz, P.L. Williams, T.J. Smith, and D.C. Christiani: AAssociation of Heart Rate Variability with Occupational and Environmental Exposure to Particulate Air Pollution,@ *Circulation* 104, 986-991, 2001.

Measures, R. *Laser Remote Sensing-Fundamentals and Applications*. Krieger, 2002.

Mishchenko, M. I., L. D. Travis, R. A. Kahn, and R. A. West, Modeling phase functions for dustlike tropospheric aerosols using a shape mixture of randomly oriented polydisperse spheroids. *J.Geophys.Res.* 102:16,831-16,847. 1997.

Mie, G. Beitraege zur Opitek trueber Medien, speziell kolloidaler Metalosungen. *Ann. Phys.*, 25:377-445. 1908.

Molenar, J. V. Analysis of the real world performance of the Optec NGN-2 ambient nephelometer. in: *Visual Air Quality: Aerosols and Global Radiation Balance*, pp. 243-265, Air and Waste Management Association, Pittsburgh, Pa., 1997.

Moore, T., M. Fitch, J. Adloch, and P. Lahm, Effects of filtering out rapid transitory changes in optical visibility data: extrapolating the results of a case study analysis from the Grand Canyon National Park to selected class I areas in the western United States. presented at: *PM2000 Particulate Matter and Health – The Scientific Basis for Regulatory Decision-making Specialty Conference & Exhibition.* Air and Waste Management Association, Pittsburgh, Pa., 2000.

Morawska, L., G. Johnson, Z. D. Ristovski, and V. Agranovski, Relation between particle mass and number for submicrometer airborne particles. *Atmos.Environ.* 33:1983-1990, 1999.

Mulik, K. R., G. Li, G. S. Chadha, S. Mathur, C. R. Philbrick, *Evolution of Air Pollution Events Determined From Raman Lidar.* Extended Abstracts Book- PM2000:Particulate Matter and Health. 4ASP2, 2000.

Novitsky, Edward J., *Multistatic Lidar Profile Measurements of Lower Tropospheric Aerosol and Particulate Matter*. Ph.D thesis, Department of Electrical Engineering, Pennsylvania State University, 2002.

O'Brien, M. D. T. D. Stevens, and C. R. Philbrick, "Optical Extinction from Raman Lidar Measurements," in *Optical Instruments for Weather Forecasting*, SPIE Proceedings Vol. 2832, 45-52, 1996.

Ouimette, J. R. and R. C. Flagan, The extinction coefficient of multi-component aerosols. *Atmos.Environ.* 16:2405-2419, 1982.

Patterson, E. M. Optical properties of the crustal aerosol: relation to chemical and physical characteristics. *J.Geophys.Res.* 86:3236-3246, 1981.

Peters, A., D.W. Dockery, J.E. Muller, and M.A. Mittleman: AIncreased Particulate Air Pollution and the Triggering of Myocardial Infarction,@ *Circulation* 103, 2810-2815, 2001.

Philbrick, C. R(1998a). "Investigations of Factors Determining the Occurrence of Ozone and Fine Particles in Northeastern USA," *Proceedings of the Air &Waste Management Symposium on Measurement of Toxic and Related Air Pollutants*, pg. 248-260, 1998.

Philbrick, C. R.(1998 b). Raman Lidar Capability to Measure Tropospheric Properties. *Proceedings of the Nineteenth International Laser Radar Conference,* NASA Langley Research Center, Hampton, VA, NASA Conf. Publ. 207671, p. 289 - 292.

Philbrick, C. R. and D. B. Lysak, Jr. (1998 a). Atmospheric Optical Extinction Measured by Lidar. *NATO-RTO Meeting Proceedings I , E-O Propagation, Signature and System Performance Under Adverse Meteorological Conditions*. 40:1-7, 1998.

Philbrick, C. R. and D. B. Lysak, Jr.(1998b). "Optical Remote Sensing of Atmospheric Properties," *Proceedings of the Battlespace Atmospheric and Cloud Impacts on Military Operations (BACIMO),* AFRL-VS-HA-TR-98-0103, pg 460-468, 1998.

Philbrick, C.R "Lidar Measurements of Water Vapor Concentrations in the Troposphere," *Proceedings of IGARSS'94 (International Geophysics and Remote Sensing Symposium)* at UCLA in Pasadena CA, August 1994, Vol IV, pg 2043-2045, 1994 .

Philbrick, C. R., G. Li and J. Collier, "Profiling Atmospheric Optical Properties", *25th Annual Conference on Atmospheric Transmission and Radiance Models*, Lexington, MA, 25-27 June 2002.

Poner, J.N., A.D. Clarke, G. Ferry, and R.F. Pueschel, Aircraft studies of size dependent aerosol sampling through inlets, *J. Geophys. Res.*. 87, 3815-3824, 1992.

Prospero, J.M., R.A. Glaccum, and R. T. Nees, Atmospheric transportation of soil dust from Africa to South America, *Nature*. 289, 570-572, 1981.

Pruppacher, H.R., and J.D. Klett, *Microphysics of Clouds and Precipitation,* D. Reidel, Nowell, Mass., 1980.

Reist, P.C., *Introduction to Aerosol Science,* Macmillan, New York, 1984. Remer. L.A., Y.J. Kaufman, and B.N. Holben, The size distribution of ambient aerosol particles, in *Biomass Burning and Global Change,* edited by J.S. Levine, MIT Press, Cambridge, Mass., 1996.

Richards, L. W., S. B. Hurwitt, C. McDade, T. Couture, D. Lowenthal, J. C. Chow, and J. Watson, Optical properties of the San Joaquin valley aerosol collected during the 1995 integrated monitoring study. *Atmos.Environ.* 33:4787-4795, 1999.

Robinson, E. The effects of air pollution on visibility. In *Air Pollution* , A. C. Stern, ed. Vol. 1, 2nd edition, Chapter 11 pp. 349-99, Academic Press, NY, 1968.

Rogers, R.R., and M. K. Yau, *A Short Course in Cloud Physics,* 3rd edition, Pergamon Press, Oxford, 290 p., 1989.

Rosen, J. M., R. G. Pinnick, and D. M.Garvey, Nephelometer optical response model for the interpretation of atmospheric aerosol measurements. *Appl.Opt.* 36:2642-2649, 1997.

Ruskin, R.R. and W.D. Scott. Weather modification instruments and their use. In *Weather and Climate Modification*, ed. W.N. Hess. J. Wiley, New York, p. 181, 1974.

S. Rajan, T. J. Kane and C. R. Philbrick, "Multiple wavelength Raman Lidar Measurements of Atmospheric Water Vapor," *Geophys. Res. Let.* 21, 2499_2502, 1994.

Saltzman, E.S., D.L. Savoie, J.M. Prospero, and R.G. Zika, Atmospheric methansulfonic acid and non-sea-salt sulfate at Fanning and American Samoa, *Geophys. Res. Lett.*. 12, 437-440, 1985.

Saxena, P., L.M. Hildemann, P.H. McMurry, and J.H. Seinfeld, Organics alter hygroscopic behavior of atmospheric particles. *J. Geophys. Res.* 100:18,755-18,770, 1995

Savoie, D.L., J.M. Prospero, and R. T. Nees, Washout ration of nitrate, non-sea-salt sulfate, and sea salt on Virginia Key, Florida, and on America Samoa, *Atmos. Environ.*. 21, 103-112,1987.

Schutz, L., Long-range transpon of desen dust with special emphasis on the Sahara, *Ann. N. Y. Acad. Sci.*, 338, 5 15-532, 1980.

Seinfeld, J.H. and S.N. Pandis, *Atmospheric Chemistry and Physics. From Air Pollution to Climate Change*, John Wiley & Sons, Inc., New York City, 1326 p., 1998.

Shaw, G.E., Consideration on the origin and propenies of the Antartic aerosol. *Rev Geophys.*. 17, 1983-1998, 1979.

Shettle, E. P. and R. W. Fenn, Models of the aerosol of the lower atmosphere and the effects of humidity variations on their optical properties. *Air Force Geophysics Laboratory Report*, AFGL-TR-79-0214, September 1979.

Sloane, C. S. Optical properties of aerosols – comparison of measurements with model calculations. *Atmos.Environ.* 17:409-416, 1983

Sloane, C. S. Optical properties of aerosols of mixed composition. *Atmos.Environ.* 18:871-878, 1984.

Sloane, C. S. Effect of composition on aerosol light scattering efficiencies. *Atmos.Environ.* 20:1025-1037, 1986.

Sloane, C.S. and G.T. Wolff. "Prediction of Ambient Light Scattering using a Physical Model responsive to Relative Humidity: Validation with Measurements from Detroit." *Atmospheric Environmen*t, 19:669-680 (1985).

Stevens, T. D. and C. R. Philbrick, "Particle Size Distributions and Extinction Determined by a Unique Bistatic Lidar Technique," *Proceeding of IGARSS96 Conference on Remote Sensing for a Sustainable Future (International Geophysics and Remote Sensing Symposium)* at Lincoln NB, May 1996, Vol II pg 1253-1256, 1996.

Stevens, T.D *Bistatic Lidar Measurements of Lower Tropospheric Aerosols*, PhD Thesis for Penn State University, Department of Electrical Engineering, May 1996.

Tang, N., Deliquescence propenies and particle size change of hydroscopic aerosols in *Generation of Aerosol*, 153 pp., Butterworth- Heinemann, New Mass., 1980.

Tang, .N., and H.R. Munkelwitz, Aerosol growth studies, III, Ammonium bisulfate aerosols in a moist atmosphere, *J. Aerosol Sci*, 1 321-330, 1977.

Tang, I. N. Chemical and size effects of hygroscopic aerosols on light scattering coefficients. *J.Geophys.Res.* 101:19,245-19,250, 1996.

Thomas, A. and J. Gebhart, Correlations between gravimetry and light scattering photometry for atmospheric aerosols. *Atmos.Environ.* 28:935-938, 1994.
Twomey, S., *Atmospheric Aerosols*, 302 pp., Elsevier Sci., New York, 1977.

u.s. Standard Atmosphere, 1976, U.S. Government Printing Office, Washington, D.C., 227 p., 1976.

VanCurren, T. Spatial factors influencing winter primary particle sampling and interpretation. *J. Air & Waste Manage. Assoc.* 49:PM-3-15, 1999.

Watson, J.G., D.L. Blumenthal, J.C. Chow, C.F. Cahill, L.W. Richards, D. Dietrich, R. Morris, J.E. Houck, R.J. Dickson, and S.R. Andersen. 1996. Mt. Zirkel Wilderness Area reasonable attribution study of visibility impairment—Volume II: Results of data analysis and modeling. *Prepared for Colorado Dep. of Public Health and Environ.*, Denver, CO. Desert Res. Inst., Reno, NV.

Watson, J.G., and J.C. Chow. 1994. Clear sky visibility as a challenge for society. *Ann. Rev. Energy Environ.* 19:241–266.

Watson, J.G., J.C. Chow, and C.A. Frazier. 1999. X-ray fluorescence analysis of ambient air samples. p. 67–96. *In S. Landsberger and M. Creatchman (ed.) Elemental analysis of airborne particles*. Gordon and Breach, Newark, NJ.

Watson, J.G., J.A. Cooper, and J.J. Huntzicker. 1984. The effective variance weighting for least squares calculations applied to the mass balance receptor model. *Atmos. Environ.* 18:1347–1355.

Waggoner, A. P. and R. E. Weiss, Comparison of fine particle mass concentration and light scattering extinction in ambient aerosol. *Atmos.Environ.* 14:623-626, 1980.

Waggoner, A. P., R. E. Weiss, N. C. Ahlquist, D. S. Covert, S. Will, and R. J. Charlson, Optical characteristics of Atmospheric aerosols. *Atmos.Environ.* 15:1891-1909,

Watson, J.G., and J.C. Chow: AReconciling Urban Fugitive Dust Emissions Inventory and Ambient Source Contribution Estimates: Summary of Current Knowledge and Needed Research,@ Document No. 61110.4D2, Desert Research Institute, Reno NV, September 3, 1999

Mauderly, J., L. Neas, and R. Schlesinger: APM Monitoring Needs Related to Health Effects,@ *Proc. PM Measurements Workshop*, EPA Report No. 2, Chapel Hill, NC, pp 9-14, July 1998.
Whitby, K.T. *Modeling of atmospheric aerosol particle size distributions*. Particle Technology Lab. Publ. 253, University of Minnesota, Minneapolis, 1975.

Whitby, K. T. The physical characteristics of sulfur aerosols. *Atmos.Environ.* 12:135-139, 1978.

White, W. H. On the theoretical and empirical basis for apportioning extinction by aerosols: A critical review. *Atmos.Environ.* 20:1659-1672, 1986.

White, W.H., and P.T. Roberts. 1977. On the nature and origins of visibility-reducing aerosols in the Los Angeles air basin. *Atmos. Environ.* 11:803–812.

White, W. H. (1990a). The components of atmospheric light extinction: a survey of ground level budgets. *Atmos.Environ.* 24a:2673-2679, 1990.

White, W. H. (1990b). Appendix H Dry Fine-Particle Scattering Efficiencies, p 24-H1: In - Visibility: Existing and historical conditions – Causes and effects. *State Sci. and Technol. Rep. 24,*. Natl. Acid Precip. Assess. Program, Washington, D. C, 1990.

White, W. H., E. S. Macias, R. C. Nininger, and D. Schorran, Size-resolved measurements of light-scattering by ambient particles in the southwestern U.S.A. *Atmos.Environ.* 28:900-921, 1994

Willeke, K. and K. T. Whitby, Atmospheric aerosols: size distribution interpretation. *JAPCA.* 25: 529-534, 1975

Willeke, K. and J. E. Brockman, Extinction coefficient for multimodal atmospheric particle size distributions. *Atmos.Environ.* 11: 995-999, 1977.

Wilson W. E. and H. H. Suh, Fine Particles and Coarse Particles: Concentration Relationships Relevant to Epidemiologic Studies. *Journal of Air & Waste Management Association* 47:1238-1249, 1997.

Whitby, K.T., R.B. Husar and B.Y.H. Liu, "The Aerosol Distribution of Los Angeles Smog", *Journal of Colloid and Interface Science*, Vol. 39, No. 1, pp. 177-204, 1972.

Whitby, K.T., "The Physical Characteristics of Sulfur Aerosols", *Atmospheric Environment*, Vol. 12, pp. 135-159, 1978.

Wright, M. L., E. K. Proctor, L. S. Gasiorek, and E. M. Liston, A Preliminary Study of Air-Pollution Measurement by Active Remote Sensing Techniques, NASA CR – 132724, 1975.

Zhang, X.Q., B.J. Turpin, P.H. McMurry, S.V. Hering, and M.R. Stolzenburg. 1994. Mie theory evaluation of species contributions to 1990 wintertime visibility reduction in the Grand Canyon. *J. Air Waste Manage*. Assoc. 44:153–162.